# A portable artificial kidney system using microfluidics and multi-step filtration


Bac Van Dang

**School of Mechanical and Manufacturing Engineering**

**University of New South Wales, Australia**

A thesis in fulfilment of the requirements for the degree of

Doctor of Philosophy

February 2021

*This page is intentionally left blank.*

# Thesis/Dissertation Sheet

| | | |
|---|---|---|
| Surname/Family Name | : | **Dang** |
| Given Name/s | : | **Bac** |
| Abbreviation for degree as give in the University calendar | : | **PhD** |
| Faculty | : | **Engineering** |
| School | : | **Mechanical and Manufacturing Engineering** |
| Thesis Title | : | **A Portable Artificial Kidney System Using Microfluidics and Multi-step Filtration** |


**Abstract 350 words maximum: (PLEASE TYPE)**

Natural kidney filtration is a compact, multi-step filtration process which passes wastes and exceeded fluids via microscale vessels in glomerulus and tubules. The principal renal replacement therapy (RRT), commonly called dialysis, is a single-step filtration process based on diffusion to replace kidney failure. Conventional dialysis is limited in its effectiveness (not a continuous treatment), its impact on quality of life (typically requiring patients to spend several days per week in a clinic), and its cost (large systems, requiring frequent membrane replacement).

This thesis is an investigation into the feasibility of using microfluidics and membrane technology to create portable alternatives to dialysis systems. It starts with a comprehensive review of the state-of-the-art in portable artificial kidneys, microfluidics, membrane science, and other related fields. An innovative, multi-step process was designed to mimic kidney filtration using two membranes; one to filter out large particles and one to remove urea and recycle water, thus mitigating the need for a dialysate system. The underlying physics (the mixing and shear stress) of the mechanisms which could enhance filtration performance at microscale was then studied.

It was found that by adding microspacers into narrow-channel flows, it is possible to significantly enhance filtration. Optimized 3D-printed spacer designs (e.g., a 'gyroid' spacer) showed flux enhancement of up to 93% (compared to a plain channel) when using a plasma mimicking solution. The use of different blood and plasma mimicking solutions also suggested a prior step to separate large biological components (e.g., cells, proteins) is helpful to reduce cell contact and fouling in membrane filtration. The potential use of microfluidic diode valves and micropumps for pressure and flowrate regulation in the proposed small-format system was discussed. Membrane processes which mimic the filtration function of the tubules and have the potential for integration into portable systems (e.g., reverse osmosis and membrane distillation) are demonstrated to be useful potential alternatives to dialysis in toxin removal and in returning clean water to the blood stream.

*This page is intentionally left blank.*

# Inclusion of Publications Statement

Thesis Title and Abstract | Declarations | **Inclusion of Publications Statement** | Corrected Thesis and Responses

UNSW is supportive of candidates publishing their research results during their candidature as detailed in the UNSW Thesis Examination Procedure.

Publications can be used in the candidate's thesis in lieu of a Chapter provided:

- The candidate contributed **greater than 50%** of the content in the publication and are the "primary author", i.e. they were responsible primarily for the planning, execution and preparation of the work for publication.
- The candidate has obtained approval to include the publication in their thesis in lieu of a Chapter from their Supervisor and Postgraduate Coordinator.
- The publication is not subject to any obligations or contractual agreements with a third party that would constrain its inclusion in the thesis.

☑ The candidate has declared that **some of the work described in their thesis has been published and has been documented in the relevant Chapters with acknowledgement**.

A short statement on where this work appears in the thesis and how this work is acknowledged within chapter/s:

> My literature review in Chapter 2 of the thesis is mainly comprised of a review paper that I contributed to and published in the journal: IEEE Reviews in Biomedical Engineering. The results used in Chapter 4 has been published in the journal: Separation and Purification Technology. The results from the journal papers in ACS Sensors and Sensors & Actuators: B. Chemical are contained in Chapter 5 of the thesis. Acknowledgement of the works of collaborators and other authors has been made in the Acknowledgement section.

## Candidate's Declaration

**I declare that I have complied with the Thesis Examination Procedure.**

# Originality Statement

‘I hereby declare that this submission is my own work and to the best of my knowledge it contains no materials previously published or written by another person, or substantial proportions of material which have been accepted for the award of any other degree or diploma at UNSW or any other educational institution, except where due acknowledgement is made in the thesis. Any contribution made to the research by others, with whom I have worked at UNSW or elsewhere, is explicitly acknowledged in the thesis. I also declare that the intellectual content of this thesis is the product of my own work, except to the extent that assistance from others in the project's design and conception or in style, presentation and linguistic expression is acknowledged.’

Signed ……

Date 28/06/2021 ……

## Copyright Statement

‘I hereby grant the University of New South Wales or its agents a non-exclusive licence to archive and to make available (including to members of the public) my thesis or dissertation in whole or part in the University libraries in all forms of media, now or here after known. I acknowledge that I retain all intellectual property rights which subsist in my thesis or dissertation, such as copyright and patent rights, subject to applicable law. I also retain the right to use all or part of my thesis or dissertation in future works (such as articles or books).

For any substantial portions of copyright material used in this thesis, written permission for use has been obtained, or the copyright material is removed from the final public version of the thesis.’

Signed ……

Date 28/06/2021 ……

## Authenticity Statement

‘I certify that the Library deposit digital copy is a direct equivalent of the final officially approved version of my thesis.’

Signed ……

Date 28/06/2021 ……

# Abstract

Natural kidney filtration is a compact, multi-step filtration process which passes wastes and exceeded fluids via microscale vessels in glomerulus and tubules. The principal renal replacement therapy (RRT), commonly called dialysis, is a single-step filtration process based on diffusion to replace kidney failure. Conventional dialysis is limited in its effectiveness (not a continuous treatment), its impact on quality of life (typically requiring patients to spend several days per week in a clinic), and its cost (large systems, requiring frequent membrane replacement).

This thesis is an investigation into the feasibility of using microfluidics and membrane technology to create portable alternatives to dialysis systems. It starts with a comprehensive review of the state-of-the-art in portable artificial kidneys, microfluidics, membrane science, and other related fields. An innovative, multi-step process was designed to mimic kidney filtration using two membranes; one to filter out large particles and one to remove urea and recycle water, thus mitigating the need for a dialysate system. The underlying physics (the mixing and shear stress) of the mechanisms which could enhance filtration performance at microscale was then studied.

It was found that by adding microspacers into narrow-channel flows, it is possible to significantly enhance filtration. Optimized 3D-printed spacer designs (e.g., a 'gyroid' spacer) showed flux enhancement of up to 93% (compared to a plain channel) when using a plasma mimicking solution. The use of different blood and plasma mimicking solutions also suggested a prior step to separate large biological components (e.g., cells, proteins) is helpful to reduce cell contact and fouling in membrane filtration. The potential use of microfluidic diode valves and micropumps for pressure and flowrate regulation in the proposed small-format system was discussed. Membrane processes which mimic the filtration function of the tubules and have the potential for integration into portable systems (e.g., reverse osmosis and membrane distillation) are demonstrated to be useful potential alternatives to dialysis in toxin removal and in returning clean water to the blood stream.

*This page is intentionally left blank.*

# List of Publications

## Journal Articles

### Directly Related Publications

1. **Dang, B.V.,** Taylor, R.A., Charlton, A.J., Le-Clech, P. & Barber, T., "Towards portable artificial kidneys: The role of advanced microfluidics and membrane technologies in implantable systems", *IEEE Reviews in Biomedical Engineering* 13, 261–279 (2019).

2. **Dang, B.V.**, Charlton, A.J., Li, Q., Kim, Y.C., Taylor R.A., Le-Clech, P., Barber, T., "Can 3D-printed spacers improve filtration at the microscale?", *Separation and Purification Technology*, 256, 117776 - 117776 (2020).

3. **Dang, B.V.** †, Hassanzadeh-barforoushi, A. †, Syed, M., Yang D., Kim, S., Taylor, R.A., Liu, G., Liu, G., Barber, T., "Microfluidic actuation via 3D-printed molds towards multiplex biosensing of cell apoptosis", *ACS Sensors*. 4, 8, 2181–2189 (2019), selected as cover († Authors contributed equally).

### Related Publications

4. Kim, G., **Dang, B.V.**, Kim S.-J., 'Stepwise waveform generator for autonomous microfluidic control'*, Sensors Actuators B. Chem.* 266 614–619 (2018).

5. Kim, Y.C., **Dang, B.V.**, Taylor R.A., Barber, T., "Controlled Generation of Single Microbubbles" submitted to *International Journal of Engineering Science* (2020).

## Conference Papers

6. **Dang, B.V.**, Charlton, A.J., Li, Q., Taylor, R.A., Barber, T., "A 3D-printed microfiltration unit for improving hemofiltration efficiency: Effects of spacer designs on fluid management", the 10th *ANZ Nano and Microfluidics Symposium (ANZNMF 2019)*, 1-3.07.2019, Wollongong, NSW, Australia.

7. **Dang B.V.**, Hassanzadeh-barforoushi, A. †, Syed, M., Yang, D., Kim, S., Taylor, R.A., Liu, G., Liu, G., Barber, T., "Microfluidic Actuation Via 3D-printed Molds: Towards *Multiplexed Biosensing", The Biomedical Engineering Society ANNUAL MEETING (BMES 2019),* 16-19.10. 2019, Philadelphia, USA.

# Acknowledgements

This thesis has been conducted in the context that I went to kidney and dialysis department at the local hospital, seeing and talking with people on the brick of dying with end-stage chronic kidney failure. The target of the thesis is to provide a systematic approach for developing portable artificial kidneys from an engineering perspective, with the hope to encourage researchers from the fields of medicine, microfluidics, membranes, and related disciplines to work together to create portable artificial kidneys that support patients on dialysis in the near future. By answering some background questions, it is expected to add a brick to the foundation of knowledge in this field and to broaden humanity's understanding horizon.

Firstly, I would like to offer my sincere gratitude to my supervisor, Prof. Tracie Barber, for her time, effort and brilliant supervision. Tracie thank you for your patience and for helping me with the critical thinking of what is important and what is not, for scheduling and for the endless support with your talented ideas, hilarious sharing and equipment supports. You make me feel safe, encouraged at all time and support in every way that make all this possible. You are the best primary supervisor I can have.

I would like to thank my co-supervisor, Prof. Rob Taylor, who always offer tremendous helps in technical details. Rob, thank you for your patience and for your creative ideas. I admire the way you think, the way you sharpen the logics in my writing, the responsibility, and the depth of your thinking towards applications.

A particular thanks to my co-supervisor, Dr. Qiyuan Li, for his genuine support in challenging membrane experiments and in logical writing. Also, a sincere thanks to my beloved and amazing colleagues and personalities, Doctors: Pujith Vijayaratnam (P. J.), Amin Hassanzadeh-Barforoushi, Maira Syed, Joseph Kim, Mehdi Rafeie, Mahdi Motamedi, Alexander Charlton, Olivia Ng, Sanjiv Gunasekera, Xinxing Chen, Yani Zhang, Andre Aquino, Jie Yi, Ky Nguyen, Son Tong, Amr Omar and Sharmila Kayastha for your companionship and encouragement over the course of my PhD. In the difficult PhD time, I used to say, "I'm still alive" when you asked, "How are you?", and thankfully until this moment, the answer remains the same.

Thanks to Dr. Tamsin Peters, Benjamin Willis, Dr. Eldad Ben-Ishay, Joe Tscherry, Terry Flynn, Mr. Martyn Sherriff for helpful lab guidance and technical supports. Also, thanks to Prof. Anne Simmons, Dr. Sam Mallinson, Prof. Guozhen Liu, Prof. Pierre Le-Clech (UNSW), and the nephrologists, nurses, and doctors at the Prince of Wales Hospital for important technical guidance and lab equipment.

Thanks to the University of New South Wales, Australian Commonwealth Government, Australian Government Research Training Program Scholarship for providing financial support and facilities throughout my PhD.

A special thanks to my beloved parents for your unconditional love, care, and patient supports throughout my life. You are the greatest gifts that I have. Thanks to my brothers, sisters, nieces, my uncles and aunties and good friends for all your love and caring throughout my long journey of studying; without those supports I could never accomplish my PhD today.

Ultimately, thanks to God, who has blown the Spirit of joy, passion, and diligence in me. I have the low starting point from countryside of my homeland Vietnam and had no attention before to study in this overwhelmingly great country and education of UNSW and Australia. The PhD journey was extremely difficult sometimes, but with the hope in Him, I gain renewed Christian's strength, humbleness, and wisdom. It is to him I dedicate this thesis.

# Table of Contents

# Table of Figures

# Nomenclature

| | |
|---|---|
| AK | Artificial Kidney |
| AKI | Acute Kidney Injury |
| BMS | Blood Mimicking Solution |
| BUN | Blood Urea Nitrogen |
| BSA | Bovine Serum Albumin |
| x | Cartesian Direction |
| y | Cartesian Direction |
| z | Cartesian Direction |
| CB | Cell-based |
| cm | Centimeter |
| $L_c$ | Characteristic (Channel) Length |
| CKD | Chronic Kidney Disease |
| CFD | Computational Fluid Dynamics |
| CAD | Computer Aided Design |
| CNC | Computer Numerical Control |
| $C$ | Concentration |
| CP | Concentration Polarization |
| $\theta$ | Contact Angle |
| CHD | Conventional Hemodialysis |
| Da | Dalton |
| DAQ | Data Acquisition |
| °C | Degree Celsius |
| $\rho_w$ | Density of Fluid |
| DLD | Deterministic Lateral Displacement |
| D | Diffusion Coefficient |
| $\mu$ | Dynamic Viscosity |
| ESRD | End Stage Renal Disease |

| | |
|---|---|
| $E$ | Energy Consumption |
| $Q_H$ | Energy for Heating |
| $Q_C$ | Energy for Cooling |
| $T$ | Experimental Temperature |
| XHD | Extreme High Definition |
| $T_F$ | Filtration Time |
| $Q$ | Flow Rate |
| $u$ | Flow Velocity in *x*-Direction |
| $v$ | Flow Velocity in *y*-Direction |
| $w$ | Flow Velocity in *z*-Direction |
| $\rho$ | Fluid density |
| $\nu$ | Fluid Kinematic Viscosity |
| GOR | Gained Output Ratio |
| GBM | Glomerular Basement Membrane |
| GFR | Glomerular Filtration Rate |
| g | Gram |
| $H_{ct}$ | Hematocrit |
| HD | Hemodialysis |
| Hgb | Hemoglobin |
| HB | Herringbone |
| $H$ | Height (Channel) |
| HFM | Hollow-fiber Membrane |
| HHD | Home hemodialysis |
| HPLC | High-Performance Liquid Chromatography |
| $D_h$ | Hydraulic Diameter of a square cross-section flow channel |
| $Q_{RO}$ | Hydraulic Pumping Power |
| iAK | Implantable Artificial Kidneys |
| iRAD | Implantable Renal Assist Device |
| $\Delta t$ | Interval of Time |
| kg | Kilogram |

| | |
|---|---|
| LOC | Lab-on-a-chip |
| LEP | Liquid Entry Pressure |
| L | Liter |
| $m$ | Mass |
| $\dot{m}$ | Mass flux |
| Max | Maximum |
| $\bar{V}$ | Mean Fluid Velocity |
| $Q_{mean}$ | Mean Volumetric Flow Rate |
| MD | Membrane Distillation Membrane Technology |
| m | Meter |
| $H$ | Microchannel Height |
| $L$ | Microchannel Length |
| $W$ | Microchannel Width |
| MF | Microfiltration |
| $\mu L$ | Microliter |
| $\mu m$ | Micrometer |
| µAK | Micro-scale Implantable Devices |
| mL | Milliliter |
| mm | Millimeter |
| ms | Millisecond |
| Min | Minimum |
| Min | Minute |
| MWCO | Molecular Weight Cut-off |
| MJM | Multi-jet Manufacturing |
| NF | Nanofiltration |
| $nm$ | Nanometer |
| N | Newton |
| NCB | Non-cell-based |
| NC | Normally Closed (Valve) |
| NO | Normally Open (Valve) |

| | |
|---|---|
| NMR | Nuclear Magnetic Resonance |
| Δπ | Osmotic Pressure |
| $P_{TH\text{-}O}$ | Opening Threshold Pressure |
| r | Particle Radius |
| Pa | Pascal |
| $L_P$ | Permeability |
| PBS | Phosphate Buffered Saline |
| PMS | Plasma Mimicking Solution |
| PVA | Poly- (Vinyl Alcohol) |
| PDMS | Polydimethylsiloxane Polymer |
| PES | Polyethersulfone |
| PEG | Polyethylene Glycol |
| PET | Polyethylene Terephthalate |
| PP | Polypropylene |
| PTFE | Polytetrafluoroethylene |
| PVDF | Polyvinylidene Difluoride |
| pAK | Portable Artificial Kidney |
| pH | Power of Hydrogen (Acidity Measurement Unit) |
| $p$ | Pressure |
| $\Delta P$ | Pressure Drop/ Loss |
| $P_I$ | Pressure Inlet (Feed Pressure) |
| $P_O$ | Pressure Outlet |
| $P_M$ | Pressure at Permeate Side |
| R | Radius |
| RBC | Red Blood Cell |
| RGB | (Red, Green, Blue) Components of a Color |
| $R$ | Rejection Rate (salt/urea) |
| $R^2$ | Regression R-Squared Value |
| RRT | Renal Replacement Therapy |
| RAD | Renal Tubule Assist Device |

| | |
|---|---|
| RO | Reverse Osmosis Membrane Technology |
| $rpm$ | Revolutions per Minute |
| $Re$ | Reynolds Number |
| s | Seconds |
| $\gamma$ | Shear Rate of Fluid |
| $\tau$ | Shear Stress |
| SNM | Silicon Nanopore Membrane |
| SMF | Spacer-integrated Microfluidic Filtration Device |
| MXene | The materials consist of few-atoms-thick layers of metal carbides |
| $P$ | Thermodynamic Pressure |
| 3D | Three Dimensional |
| $t$ | Time |
| $\Delta t$ | Time-step size |
| TMP | Transmembrane Pressure |
| TOC | Total organic carbon |
| 2D | Two Dimensional |
| UF | Ultrafiltration |
| UV | Ultraviolet |
| UMS | Uremic Plasma Mimicking Solution |
| $V$ | Velocity Vector |
| VMD | Vacuum-based Membrane Distillation system |
| $\mu$ | Viscosity of Fluid |
| $Q$ | Volumetric Flow Rate |
| WSS | Wall Shear Stress |
| $\lambda$ | Wavelength of Light |
| WAK | Wearable Artificial Kidney Devices |
| WBC | White Blood Cell |
| $W_C$ | Width (Channel) |
| $J$ | Permeate Flux |
| $\nabla$ | Gradient Operator |

| | |
|---|---|
| M1 | Membrane 1 |
| M2 | Membrane 2 |

*This page is intentionally left blank.*

# Chapter 1

## Introduction

Kidney failure is a growing global health issue, with up to 10 million people around the globe needing renal replacement therapy (RRT)) [1]. Although dialysis, kidney transplants, and other RRT options are available, a “next generation” of artificial RRT devices is needed to provide continuous treatment and much higher quality of life for patients.

The leading treatment for kidney failure is hemodialysis (i.e. ~70% of end stage renal disease (ESRD) patients, about 2 million people are able to access regular hemodialysis treatments in 123 countries [1], [2]). Hemodialysis requires patient’s blood flow to be circulated through an external filtration system which contains a bundle of hollow fiber membranes to remove waste products (and a co-flow of a dialysate solution which replaces any lost fluids and electrolytes). Hemodialysis treatments typically take three (or more) hours and are done three times per week in a clinic, which severely limits quality of life. Since this process intends to supplement/replace the filtration function of the kidney, hemodialysis does a good job of removing toxic substances. Hemodialysis is also widely available (e.g. much more available than peritoneal dialysis and kidney transplants) as it has a high overall survival rate and is independent from amount of kidney donor [3], [4]. However, hemodialysis is not a continuous treatment and it cannot replace the kidney’s transport, metabolic, and endocrine functions [5]. A clinical setting is required for monitoring of the patient’s condition and to ensure the replacement fluids are clean and well-regulated (e.g., balancing glucose, potassium, sodium, and bicarbonate levels).

In the attempt to move beyond traditional dialysis treatments, a considerable amount of research has gone into the development of artificial devices which are portable [6]–[8] or implantable [9]–[12] through miniaturization, for both ‘cell-based’ (CB) and ‘non-cell-based’ (NCB) approaches. The motivation for developing artificial portable RRT devices is that they could be designed to work continuously, possibly in a dialysate-free mode, and that they could even replace the other kidney functions (i.e., metabolic and endocrinologic) [13], [14]. This would enable patients to have more freedom and mobility and a closer match to a fully functioning kidney.

Over the last several years, microfluidics technologies have been rapidly developing to meet the challenges of applications ranging from inkjet printheads, DNA chips to lab-on-a-chip and point-of-care applications [15]–[18]. As an ideal functional unit/ platform for biological testing, microscale versions of many biomedical devices (e.g. multiplex biosensors, organ-on-a-chips, and cell separators) have proven to be at least as effective as their macroscale counter parts [18]–[20]. To date, though, only a limited amount of work has gone into using microfabrication and microscale devices for RRT [13], [21].

Since artificial kidney research is a mature field, this thesis only focuses on how the emerging field microfabrication and microfluidics might be leveraged to achieve near-term solutions to improve current baseline treatment methods for RRT. Thus, the aim of this study is *to investigate new micro-engineered membrane filtration mechanism for the near-term artificial kidneys*. *It includes designing and experimental analyzing the support of microfluidics, membrane, and related advances in developing the system*. To achieve this aim, this thesis is an examination of the state-of-the-art in the literature for RRT and followed by detailed design, testing, and simulations of promising new microscale compartments which could form the basis for the next generation of artificial kidneys.

As such, this thesis is presented in 7 Chapters. Chapter 2 of this thesis will review the existing literature to lay the groundwork for the fundamentals of kidney filtration, how traditional methods work, and the ongoing trends for artificial kidneys. It compares and contrasts the state-of-the-art in cell-based and non-cell-based approaches. Building upon the research gaps identified in Chapter 2, Chapter 3 proposes a new design (that is potentially portable) and some fabrication techniques, along with the methods for computational and experimental analysis used in this study. Chapter 4 will zoom in on ways to achieve high filtrations rates in small-scale devices. In particular, it investigates the use of microscale spacers in artificial kidney's filtration, from a heat and mass transfer perspective. In Chapter 5, the additional knowledge of using valves for controlling the fluidic system towards portable or implantable device will also be discussed. In Chapter 6,

potential filtration mechanisms which do not need a supplemental dialysate solution will be investigated. In particular, membrane processes which remove urea while pulling water back to the main flow using reverse osmosis or membrane distillation will be explored. And, finally, Chapter 7 provides a broader analysis on the future of such portable artificial kidneys, followed by a conclusion of the study, with a summary of the author's contributions to the field of artificial kidneys.

# Chapter 2

# Literature Review

## Chapter Overview

*Portable or implantable devices to support or replace native organs have seen successes in artificial limbs, urinary bladders, ears, eyes, hearts and lungs (to varying degrees of functionality) [22]–[25], yet the artificial kidneys remain elusive. The complexity and compactness of the native kidney (as a waste filter and a regulator of blood components, including proteins and hormones) make it inherently difficult to replicate.*

*This Chapter will provide a basic overview of how the kidney works and the status quo in renal replacement therapies. It will also review the on-going research in advanced renal replacement solutions as well as the remaining challenges. Based upon these findings, the most promising near-term solutions will be highlighted for the next generation of portable and implantable artificial kidneys.*

*Note: The content in this chapter has been previously published in IEEE Reviews in Biomedical Engineering;* ***Dang, B. V****, Taylor, R. A., Charlton, A. J., Le-Clech, P. & Barber, T., 'Towards portable artificial kidneys: The role of advanced microfluidics and membrane technologies in implantable systems', IEEE Rev. Biomed. Eng. 13, 261–279 (2019). DOI: 10.1109/RBME.2019.2933339.*

## 2.1 Kidney Filtration: A Brief Overview

Within a compact 120-230cm$^3$ volume, the kidney contains over a million functional units, called nephrons (Fig. 2-1A) [26]. The nephrons filter out nano-sized waste products from the blood while maintaining water, minerals, hormones, and pH levels. Since a number of waste products must be continuously filtered (i.e. urea, creatinine, and uric acids with sizes of about 60, 113 and 168 Daltons (Da), respectively) from useful substances (i.e. water, glucose and albumin which are 18, 180 and 66,500 Da, respectively), each of the nephrons of the kidney can be thought of as a highly sophisticated, selective filter [27]. To accomplish these functions, each nephron is comprised of two main parts—a glomerulus and a tubule—each of which performs separate, specific tasks. Taken together, the kidney is an astonishingly compact, anti-fouling/clogging system which can operate continuously for decades, on very little driving pressure (~55 mmHg or ~7.3 kPa) [28]!

### 2.1.1 The Glomerulus

The glomerulus is the first stage of the nephron and it is responsible for ultra-filtration of the blood. Mechanically, it is essentially a filter which only allows molecules with a molecular weight of < 68,000 Da and a hydrodynamic diameter of < 5–7 nm to pass through to the tubule part [29]. The glomerulus also exhibits charge specificity in that negatively charged particles are rejected (i.e., albumin, which has ~66,500 Da molecular weight and a ~3.6 nm effective diameter). Geometrically, the glomerulus is essentially a very thin-walled ball filled with fenestrated capillaries. This allows the glomerulus to be a very compact filter since it has an average diameter of 200μm and a mean filtration surface area of 0.136 mm$^2$ [30]. Blood flows into the glomerulus from the afferent arteriole and out through the efferent arteriole. Even though the scale is small, the hydrostatic pressure drop (e.g. the working pressure) between these is a minimal ~55mmHg in total, which is just enough to overcome the glomerular colloid osmotic pressure (~30mmHg) and the back pressure of the capsule (~15mmHg) [28].

The glomerular membrane (the boundary of glomerulus capillaries) is composed of three layers: endothelial cells, the glomerular basement membrane (GBM), and epithelial cells of Bowman's capsule (a spherical-shaped balloon-like structure) (Fig. 2-

1B). On the intraluminal side of the capillary, endothelial cells cover 80% of the capillary surface to create a pore size of 70-100nm. On the other side, podocytes (the largest cell in the glomerulus) cover 90% of the epithelial surface, forming a slit diaphragm which creates high resistance to the fluid coming to the urinary space and a pore size of 25-60nm [31]. Sandwiched between the endothelium and podocytes, the GBM is a three-layer gel (lamina densa, lamina rara externa, lamina rara interna), with a total thickness of ~300nm. The excess anionic residues (carboxyls and sulfates) presented in the glycoproteins and proteoglycans impart a net negative charge (as mentioned above) to the GBM, which not only supports the selectivity of the GBM, but also serves to keep the surrounding gel in an expanded and porous state due to mutual repulsion [5], [27]. This prevents clogging of the gel which is an important characteristic of the membrane.

As mentioned above, only very small molecules can cross the GBM with the liquid flow—along with some bigger proteins which can also get across via diffusion [32]. From a nominal incoming renal blood flow of 1000 mL/min (i.e. ~20% of the total cardiac output), the glomerular filtration rate (GFR) of two healthy kidneys is about 120 mL/min (or 173L/ day), while over 800 mL/min returns to the blood stream (Fig.2-1C).

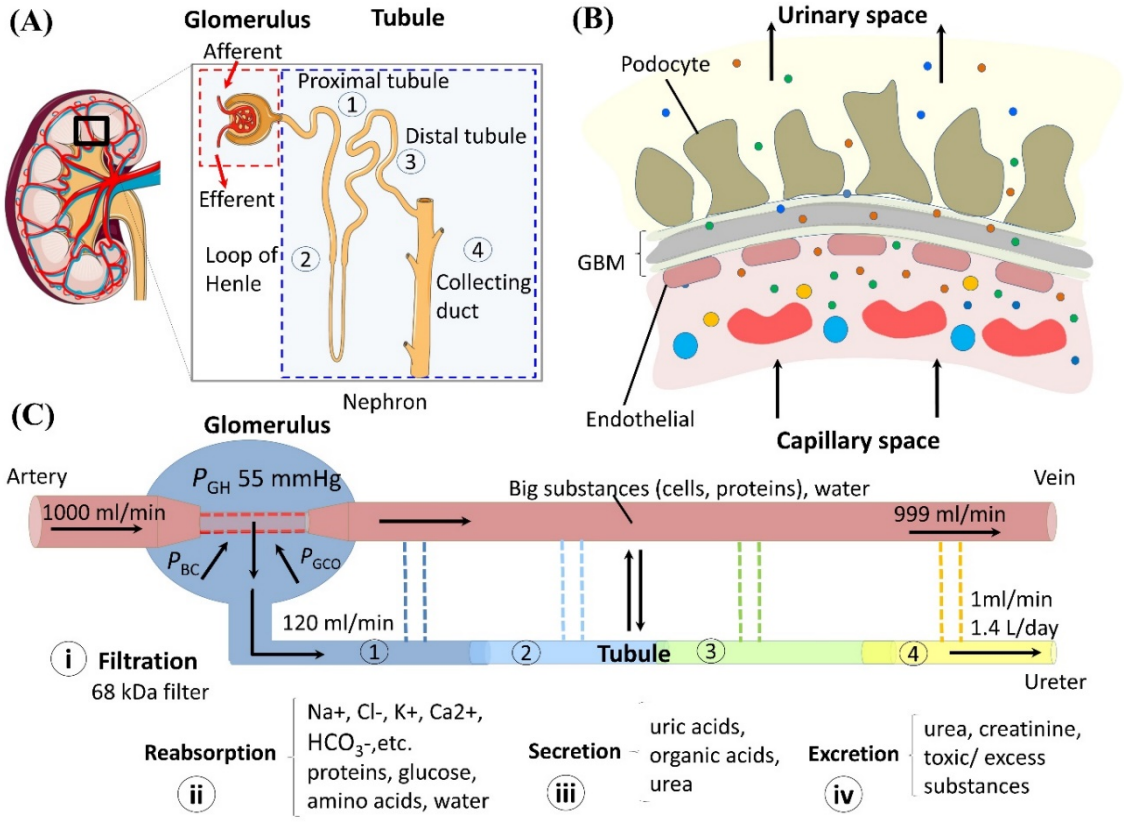


**Figure 2-1 Kidney filtration mechanisms.** (A) Kidney and the nephron. Images reprinted and modified with permission from Servier Medical Art (http://smart.servier.com/) under a Creative Commons Attribution 3.0 International License. (B) Glomerulus and its membrane. (C) Pressure and flowrate in glomerular filtration and the tubules functions.

### 2.1.2 The Tubule

The tubule is the second stage of the nephron and the filtrate from the glomerular part becomes the input into the proximal convoluted tubule. As a whole, the tubule enables key minerals (including a significant amount of water) and molecules to re-enter the blood stream, regardless of their smaller sizes compared to some excess substances which are then discharged with urine. The secreted substances include uric acid, some organic acids, and excess ions. The tubule consists of a proximal convoluted tubule, a Henle loop, a distal convoluted tubule, and a final collecting duct (Fig.2-1A). The most important filtered solutes are reabsorbed at proximal tubule (about 65% of $Na^+$, $K^+$, $Cl^-$ and water; ~70% $Ca^{2+}$, ~80% of $HCO_3^-$ and $PO_4^{2-}$; ~100% of glucose and amino acids) [33], while tubule's other components do the balance of the filtration. By its end, the tubule separates water, amino acids, glucose, potassium, chlorine, and other important

substances (for reabsorption) from creatinine, urea, some water, secreted acids, and other waste products (for excretion) [27] (Fig.2-1C).

Impressively, the tubule reabsorbs over 99% of the 173 L/day filtrate received from the glomerulus, and excretes out toxic substances with urine at a rate of 1.4 L/day to the bladder [31]. Apart from the selective filtration, the tubule is also responsible for the transport of enzymes (solute carriers, active transport ATP-biding cassette transporters, etc.), endocrine activity, and other homeostatic and metabolic functions of the kidney. Due to these biological functions, it is a high challenge to replace the tubule by an artificial filter.

## 2.2 Coping with Kidney Failure

### 2.2.1 Kidney Disease Coping Battle Status

Medical treatment is needed for both acute kidney injury (AKI) (rapid loss of function) and for chronic kidney failure (CKD) (slow loss of function) when the GFR of the kidney drops to 30 mL/min (25% of the normal value of ~120 mL/min) [34], [35]. A further reduction of the GFR to less than 15 mL/min is indicative of kidney failure, also known as end stage renal disease (ESRD) [36].

**Table 2-1. Basic parameters of a body with normal kidneys**

| **Parameters** | **Normal range** |
|---|---|
| Renal Blood Flow | 1000-1100 mL/min |
| Glomerular Filtration Rate (GFR) | 90 to 120 mL/min/1.73 $m^2$ * |
| Creatinine Clearance | 88 to 128 mL/min for female, 97 to 137 mL/min for male |
| Urine Albumin | 0-8 mg/dL |
| Blood Urea Nitrogen (BUN) | 7–20 mg/dL |
| Hematocrit (Hct) | 36 to 48% for female, 40 to 54% for male |
| Hemoglobin (Hgb) | 12–16 g/dL for female, 14–18 g/dL for male |
| Glucose (in blood) | Less than 100 mg/dL |
| Sodium (in blood) | 135-145 mEq/L |
| Potassium (in blood) | 3.6-5.2 mEq/L |
| Calcium (in blood) | 8.5-10.2 mg/dL |

* 1.73$m^2$ is an average body surface area of an adult. Data is collected from [27], [30], [37]

Once the kidneys have failed, a form renal replacement therapy (RRT) is needed for survival. As shown in Fig. 2-2A, there are 4.9-9.7 million people need RRT, but only ~2.62 million people are receiving RRT worldwide [1]. Although an estimated 40% of ESRD cases are caused by (largely preventable) Type 2 diabetes [38], [39], there is no escaping the fact that kidney failure is on the rise. At present most people receiving RRT are located in high income countries [40] but economically developing countries in Africa and Asia have a high, unserved population facing kidney failure [41], [42]. For the United States alone, the population requiring RRTs is approaching 1 million, with ~5% annual growth in recent years (see Fig. 2-2B) [43].

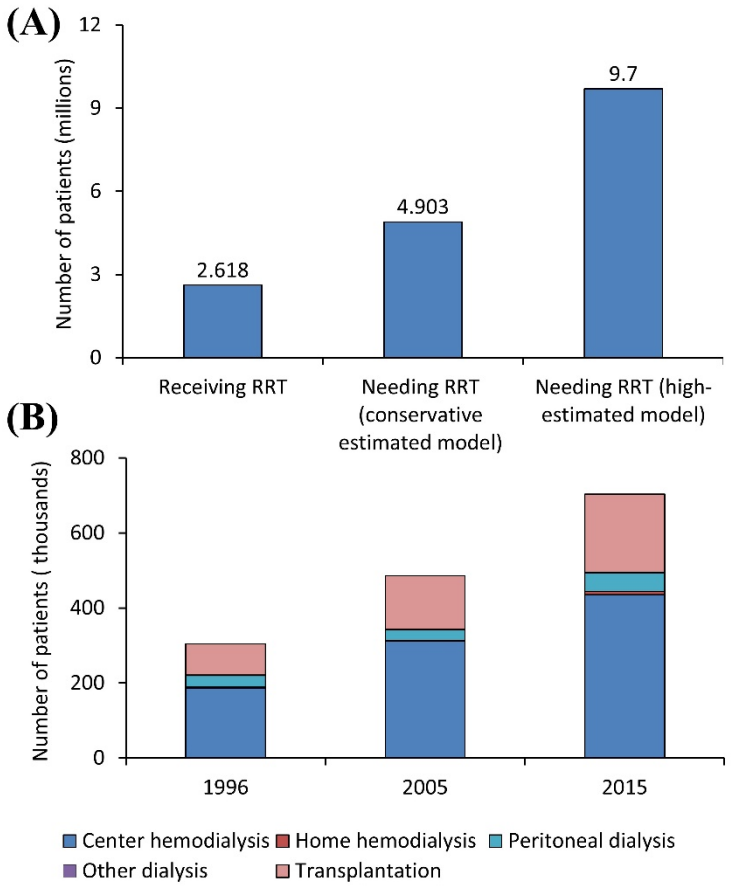


**Figure 2-2. Kidney failure treatment status.** (A) Worldwide kidney failure patients receiving RRT and estimates of practical demand. Data in 2010, adapted from [1]. (B) ESRD prevalent cases, by modality, in the U.S. population, 1980-2015. Data adapted from the United States Renal Data System 2017 [24].

As shown in Fig. 2-3, RRT can be roughly divided into non-cell-based (NCB) treatments and cell-based (CB) replacement therapies, noting that a few RRT methods provide a mix of NCB and CB mechanisms. Transplantation (a CB therapy) offers the best survival

and quality of life outcomes among therapies [44], [45], but it only supplies less than 10% of the practical demand due to the scarcity of donor kidneys [4]. There were about 89,800 kidney transplants globally in 2016; whereas, in United States alone there were approximately 94,817 patients awaiting kidney transplants as of July, 2019 [46]. Thus, the vast majority of ESRD patients rely upon dialysis.

Peritoneal dialysis (a mixed CB and NCB method) has comparatively lower mortality rates among dialysis methods in the first 2-3 years, however, serious problems arise over time with abdominal infection, low toxic clearance [47], [48], and obesity (from glucose intake) [49] in the following years of treatment. Hemodialysis (HD–a NCB therapy) utilizes synthetic semipermeable membranes to essentially do the job of the glomerulus part of the kidney [50], [51]. As the leading kidney failure treatment method (~70% of ESRD patients receiving RRT in 123 countries [1], [2]), HD has advantages of higher toxic clearance and higher overall survival rate compared to peritoneal dialysis [3].

### 2.2.2 Limitations of Hemodialysis

Despite its widespread use, HD is far from a perfect treatment. Typically, HD is not continuous since it is performed 3 days/week for 3 – 5 hours/day. A growing body of evidence indicates that for best performance, dialysis should be done nearly continuously [52]–[56], which is difficult with the traditional in-center HD method. Home-based dialysis therapies can be completed on a more continuous basis [57]–[59], but these systems place a large burden on the caregivers of the patient.

As the original, and most successful, NCB technique, modern HD therapies typically use hollow-fiber membrane (HFM) bundles (e.g. which contains thousands of porous tubes, each with a certain diameter (e.g. 200 μm), and thickness (e.g. 30 μm) [51]. The total filtration area of the HFM used in the dialyzer normally ranges 0.5–2.1 $m^2$, however, it is not suitable for an portable device due to miniaturization ability [60]. Besides, another fundamental problem is membrane fouling, which necessitates frequent membrane replacement [9].

HD can partly perform the tubule's functions using dialysate, but cannot replace its transport, metabolic, and endocrinologic functions [5]. With the use of dialysate, it

requires large volumes of clean water in relatively large filtration components. Therefore, the potential for straight-forward miniaturization of artificial kidney systems are limited. In addition, maintaining and operating HD machines remains difficult [61] and the required arteriovenous fistula creation and frequent needle access to perform dialysis can lead to damage and bloodstream infections [62]. Moreover, long-term HD is associated with blood pressure variability [63], iron overload [64], microbubble complications [65], depression [66] and low quality of life [67], [68].

### 2.2.3 The Next Generation of RRT

In the attempt to move beyond traditional dialysis treatments, the development of artificial devices which are portable [6], [7] or implantable [10]–[12], [69] has been increasingly considered in recent years, for both CB and NCB approaches (see the bottom green and pink boxes in Fig. 2-3). These essentially enable continuous treatment, which is linked to better outcomes. CB systems seek to fulfil tubular reabsorption, secretion, transport, and endocrinologic functions by either integrating natural cell-based components into an artificial device [9], [70] or creating bioengineered kidneys from stem cells [10], [11]. NCB systems developed based on dialysis fulfil the lack of tubular reabsorption function by using engineered materials with high urea adsorptive capacity, such as activated carbon [14] or titanium carbide (MXene) [8] and trigger the development of dialysate-free, anti-clogging devices [12]. This works tend to reduce the dependence on dialysate (e.g. up to 144 liters of dialytic water is typically needed to make up for lost volume during a 4-h dialysis treatment at 600 mL/min [9]).

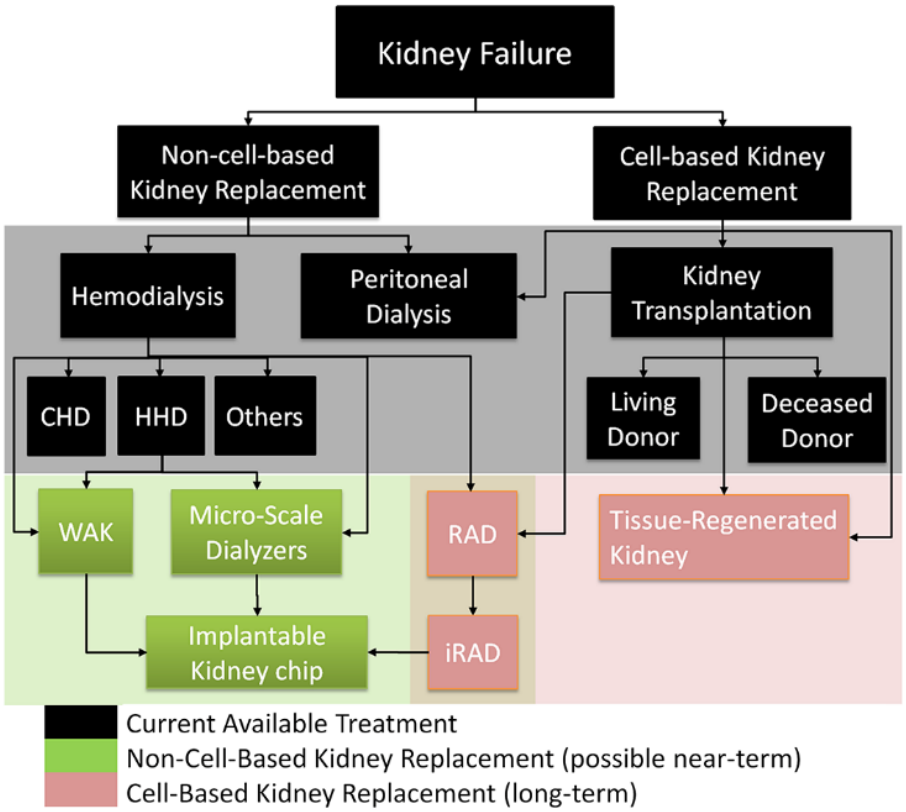


**Figure 2-3. Current therapies and on-going research to cope with kidney failure**

Ideally, an implantable/portable device should be small—of the order of a real kidney (i.e., ~120-230 mL)—so that it can be embedded as an auxiliary or primary filtration component. This small-scale requirement suggests that microfluidic technologies can be applied to develop artificial kidney components. As will be discussed below, several advances have been made in the field of microfluidics which could be useful in the next generation of artificial kidneys (e.g. integration of new materials and designs) [12], [71]–[73]. At the same time, membrane science has advanced to a level where self-cleaning and biocompatible membranes might be integrated at the microscale for NCB artificial kidney systems [74]. In addition, the combination of these technologies in silicon nanopore membrane (SNM) filters for animal trials [75]–[77], in the anti-fouling and biomolecule cleaning devices [78], [79] and the widening uses of membrane-embedded lab-on-a-chip systems [17], [80] also suggested that membrane-integrated microfluidic devices can be functional units for the further development of portable kidney devices.

As shown on Fig. 2-3, the general picture is that several research angles are being pursued in parallel to deal with kidney failure, but based on our review of the literature NCB artificial devices (e.g., the green box in Fig. 2-3) represent the best chance for near term solutions with the contribution of microfluidics, membrane and related fields. And that—if well developed—a fully implantable artificial kidney device (iAK) would have big advantages over conventional dialysis treatments because it would enable continuous toxic clearance, reduce (or eliminate) the number of hospital days for dialysis and would provide improved freedom and quality of life for millions of patients around the world.

## 2.3 Cell-based Kidney Replacement Research

Cell-based therapies can be categorized by the amount of biological material used in the device. For example, while transplants and stem-cell grown artificial kidneys are 100% biological, there are some 'hybrid' approaches like renal tubule assist devices (RAD) and implantable renal assist devices (iRAD) which use a mixture of synthetic membrane and CB material. The following sections will briefly discuss the CB options.

### 2.3.1 Bioengineered Artificial Kidneys

Bioengineering (whole) kidney from stem cells has represented the ultimate goal of artificial kidneys for at least 40 years [81]. However, only in recent years have some concrete steps been taken toward the realization of this technology [81]–[84]. Tissue-regeneration by recellularization (where cells are removed from native cadaveric kidney extracellular matrix to provide a scaffold for the stem cell growth process) has emerged as the leading CB candidate [85]–[87]. This approach seeks to create a bioengineered graft which has the kidney's full architecture and function. After obtaining native kidney cells from patients and a cadaveric kidney, this approach involves three basic steps: (1) Decellularization – the extracellular matrix is isolated to preserve the biomechanical properties and protein characteristics [88], [89]; (2) Cell growth –endothelial and epithelial cells are repopulated into the scaffold; and (3) Transplantation – the bioengineered kidney is grafted back into the patient.

In theory this three-step process seems straightforward, but, in practice, it has proven difficult to implement. In a study involving 12-week-old male Sprague-Dawley rats, macromolecular sieving, glucose and electrolyte reabsorption were partially restored regenerated kidney constructs provided good urine production (1.2 ± 0.1 µl/min) and clearance of metabolites without bleeding or graft thrombosis [11]. Regenerated kidneys represent the Holy Grail of RRT since they can provide high performance, high quality of life, and high survival rates, while eliminating the need for a living organ donor.

***Challenges***

While regenerated kidneys are promising, the GFR of regenerated kidneys is usually lower than cadaveric kidney transplants and a few other issues also remain, such as cell growth and functionality. It should be noted that due to the anatomically complicated structure of the kidney, with its extensive net of capillaries, millions of glomeruli, ~20 different specialized cell types, and the communication of resident cells with each other, it is difficulty to properly replicate all the renal functions with replacement cells [90]. Some key remaining challenges in regenerated kidneys involve improving the cell seeding efficiency, upscaling of the organ culture process and developing its transport characteristics [60]. The length and diameter of the acellular nephrons also pose a major bottleneck to cell seeding from the urinary side. This creates a situation where some engineering trade-offs must be managed. For example, tubule elasticity and permeability increase with decellularization, whereas vascular resistance (and the resulting graft perfusion) is a function of the final tubular diameters [11]. Additionally, it has been observed that significant thrombosis can occur within the vasculature of the scaffold [91]. Several other issues also beset the development of regenerated kidneys, such as finding a reliable cell sources [92], determining the optimal growth conditions for stable cell expansion, maintaining cell viability in the matrix [93], and several ethical challenges. Thus, translation of this technology beyond proof-of-principle tests will require extensive further work, particularly in the optimization of cell-seeding protocols for human-sized scaffolds. In addition, isolation, differentiation, expansion and biocompatibility of the required cell types must be demonstrated at clinically relevant scales [11]. Finally, because the use of cadaveric human kidney will

always be in limited supply, non-human (e.g. derived from animal using semi-xenotransplantation technology) [94]–[96] and artificial (e.g. 3D-printed) scaffolds must be found. Among that, 3D-printed organ is likely a golden goal [97]–[99]. Despite the bright future for this type of technology, it may still require decades worth of effort to achieve effective bioengineered artificial kidneys for human transplantation.

### 2.3.2 Renal Tubule Assist Device (RAD)

In 1999, Humes proposed a hybrid bioartificial kidney which essentially adds a tissue-engineered component to a conventional dialysis unit [100]. The RAD aims to ensure the normal tubule functions are maintained by seeding a HFM membrane with renal tubule cells. This cell layer provides both a mechanical scaffold and an immune barrier. It is typically added in series with the normal hemofiltration cartridge. Thus, the overall system is designed to mimic the nephron, with the hemodialyzer serving as an artificial glomerulus followed by the RAD which provides most of the functionality of the tubule. The processed luminal ultrafiltrate from the RAD is discarded to waste and the processed blood is returned to the patient [9]. The device was fabricated over the course of a ~14-day seeding process, wherein billions of porcine renal proximal tubule cells were deployed into the cartridge to achieve confluent monolayers with a concentration of ~3.5 x $10^5$ cells/$cm^2$ [100].

A modern RAD tested on uremic dogs enables 40-50% of the sodium and water to be reabsorbed – an amount similar to a normal nephron [101]. RAD systems have also been shown to provide good active transport of potassium, bicarbonate, glucose, and significant improvements in multiple physiological parameters (e.g. cardiovascular stability, ammonia excretion, glutathione metabolism, and 1,25-dihydroxyvitamin D3 production) were observed in RAD- treated animals compared to acellular RAD controls [100]. Based on these results, clinical evaluations have begun for using RAD in the treatment of severely ill patients with acute renal failure [102]. In fact, a RAD has been the only bioartificial kidney device that has been successfully used in humans so far [103]–[106]. The USA Food and Drug Administration approved Phase I clinical trials of RAD treatments for 10 critically ill patients with AKI and multi-organ failure at two institutions [103]. Six of the 10 treated patients survived past 30 days. Four others died

due to hypotension, arterial blood gases, toxic affection and other factors related to organ failure. The Phase I clinical study demonstrated that RAD therapy was safe for use for up to 24 hours and that the cell device retains viability, durability, and functionality throughout the therapy. Also, it suggested that RAD can provide differentiated metabolic and endocrinologic activities. In the Phase IIa clinical trial involving 58 patients (ages 18–80) with AKI at 12 clinical sites, RAD treatments were used for up to 72 hours [104]. RAD therapy provided a statistically significant mortality benefit at 28 days compared to standard continuous hemofiltration, 33% versus 61%, respectively. RAD therapy was also found to be associated with more rapid recovery of kidney function for critically ill patients with AKI.

***Challenges***

Although the RAD approach has shown promise, there are still several critical challenges preventing these devices from being widely deployed. One major challenge is in obtaining a long-term viable, well-distributed, monolayer of cells within the hollow fibers of the RAD cartridge [100]. With membrane surface areas as large as 0.7 $m^2$, a single RAD device requires on the order of $10^8$ cells. If we envisage mass-production of these devices, a reliable, consistent, pathogen-free, and cost-effective cell source and cell growth process must be identified. Difficulties in the manufacturing process of these devices have been noted by Hume et al. [9]. Upon evaluation of these RAD units, challenges were discovered in monolayer confluency and metabolic activity only six months after initial device construction. Additionally, a Phase IIb clinical trial had an unexpectedly high survival rate of patients treated with a control RAD (without seeded cells) [106], so more study is needed to confirm its effectiveness. It should be noted that recent progress has been made in seeding [107], [108], culturing cells on membranes [109] and immunomodulatory therapy [110], but to evolve it needs a great effort to overcome the challenges [60].

### 2.3.3 Implantable Renal Assist Device (iRAD)

Based on the progress and promise of RAD systems, Roy and Fissell's group has been working towards developing a miniaturized, implantable RAD device [72]. This approach uses some of the recent advances in microelectromechanical technology to

create an iRAD [111]–[113], consisting of 2 main segments, both of which use SNM membranes (with a pore size of 5 nm and less than 1% variability) [114]. As with the macro-scale RAD, the first segment mimics the glomerulus (no cells) and the second segment is seeded with renal epithelial cells to mimic tubules. The first segment of the device was tested in a pilot study with dogs [75], where the cartridges were connected to the aorta and the inferior vena cava, with the filtrate drained to collection pouches positioned in the peritoneum. The animals treated for 3-4 days had filtration volumes similar to predictions, but the device started showing defects (fractures) for longer treatment periods (5-8 days). Additional tests are needed to determine the optimal membrane characteristics [115], [116] and to identify tubule functions and limiting factors in long-term implantation [60]. However, the initial results show that this pump-free SNM membrane can work using the small arterial-venous pressure differential, achieving a filtration rate of 5 mL/ min/$m^2$ for 4-8 days [75].

***Challenges***

The iRAD has not yet been approved for clinical testing in humans. Since an iRAD uses the same CB methodology as the RAD, it will face similar cell manufacturing challenges, perhaps compounded by the compact scale [9], [117]. Further, since the device will be placed inside the body, a critical choice must be made between using autologous or nonautologous human cells. Nonautologous cells must overcome the host's immunologic rejection processes but expanding the patient's own autologous cells in large enough quantities brings its own difficulties. Another difficulty with an implantable device is that the cells must stay viable and clog-free for the long term with retrievability and maintenance after implantation being a concern [9]. Ensuring adequate nutrient and oxygen delivery to the cellular implant can also be a challenge, although some studies have shown this is possible for short-term cell therapy utilizing hollow-fiber bioreactors in an extracorporeal blood perfusion circuit [60]. Also, for long-term implant, anti-fouling membranes must be identified.

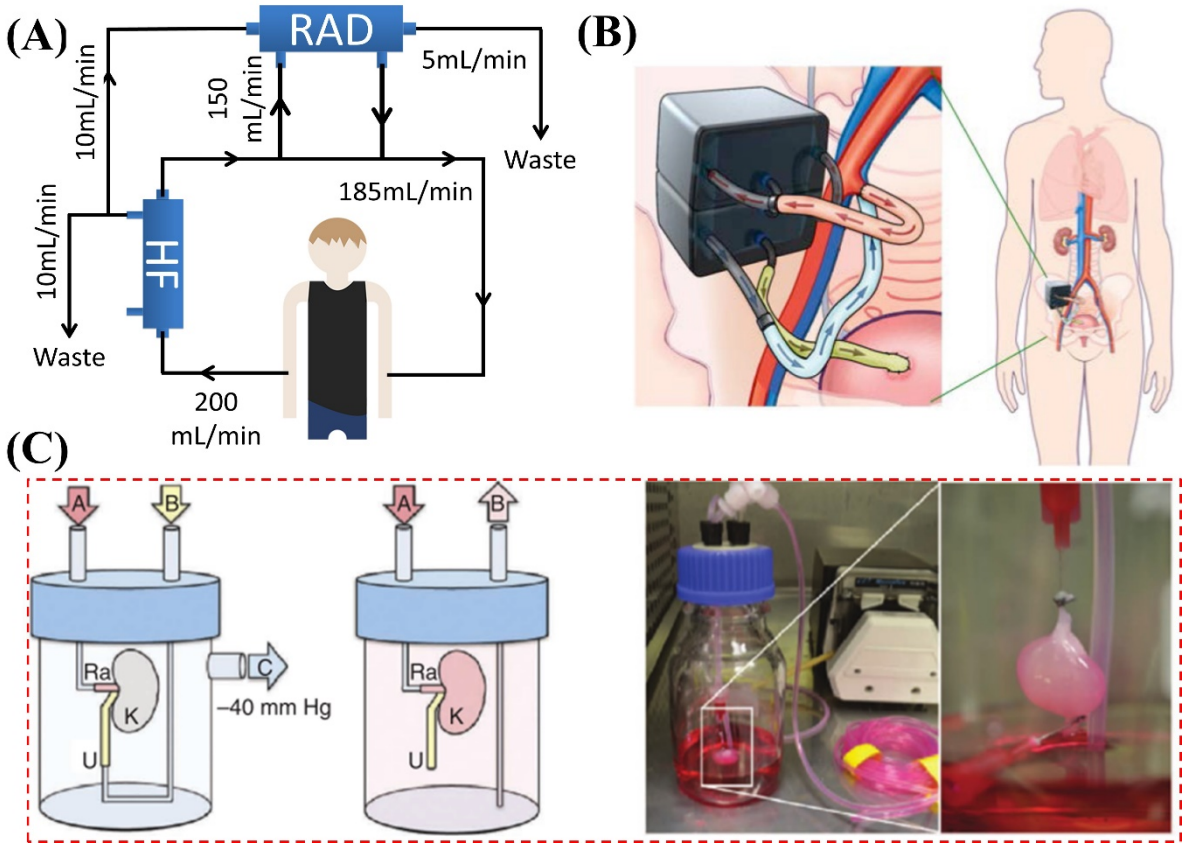


**Figure 2-4. Cell-based kidney replacement research.** (A) RAD clinical trial on human. Image's idea adapted from [103]. (B) Proposed implantable device iRAD [9]. Reprinted by permission from Springer Nature, H. D. Humes, D. Buffington, A. J. Westover, S. Roy, and W. H. Fissell, "The bioartificial kidney: Current status and future promise," Pediatr. Nephrol., vol. 29, no. 3, pp. 343–351, copyright 2014. (C) Cell seeding and whole-organ culture of regenerated kidneys [11]. Reprinted by permission from Springer Nature, J. J. Song, J. P. Guyette, S. E. Gilpin, G. Gonzalez, J. P. Vacanti, and H. C. Ott, "Regeneration and experimental orthotopic transplantation of a bioengineered kidney," Nat. Med., vol. 19, no. 5, pp. 646–651, copyright 2013.

## 2.4 Non-Cell-based Kidney Replacement Research

As explained above, cell-based therapies have shown some promising progress. However, like bioengineered replacement kidneys, the success of these therapies depends overcoming cell-related problems (e.g., cell seeding techniques, cell viability, differentiation, cell sourcing and complicated behavior control), which will take several years – if not decades – to resolve. Therefore, advanced non-cell-based devices could represent alternative near-term solutions, with several approaches under development. These can be roughly categorized as near-term, incremental extensions (or miniaturizations) of the traditional dialysis system and as innovative approaches which may take several years of development/integration.

### 2.4.1 Wearable Artificial Kidney Devices (WAK)

With evidence favoring continuous dialysis treatments over conventional periodic (thrice-weekly) dialysis treatments [52], [55], [56], significant research effort has gone into developing wearable artificial kidneys (WAK). The driving concept of WAK technology is to simply shrink the dialysis machine to create a portable device. Standard HD machines use roller pumps to generate large counter-current blood and dialysate flows. However, since a wearable artificial kidney device (WAK) must be lightweight and battery-powered, these must be replaced with micropumps [6], [118]. The devices that have been reported to date in the literature are indeed lightweight (~5kg) [119], wearable, and continuous. For example, one WAK device was trialed in pigs [120]. Ultrafiltration rates of up to 700 mL/h were enabled with an average of 106 mL/h [120]. Salt was removed at the rate of 0.95 g/h and no complications were observed during the 8-hour trial.

In a similar study, five ureterally ligated anesthetized pigs were dialyzed for 8 hours with a WAK running on two 9-volt batteries. In this study, a creatinine clearance level of 27.0 ±4.0 mL/min was reached [121]. A human study of six volume-overloaded patients treated for 6 hours was also reported to achieved safe and efficient use without complications [6]. It should be noted that in this human trial, treatment was discontinued in one patient due to a clotted catheter. Blood flow averaged 116mL/min and the ultrafiltration rate ranged from 120–288mL/h with about 150mmol of sodium removed (~1.5 g/h). Blood pressure, pulse, and biochemical parameters remained stable with no significant hemolysis or complications. In a later study, the WAK was trialed in eight humans for periods varying between 4 and 8 hours [119]. All patients were able to sleep, walk around, sit, eat, and drink without hindrance. Urea clearance was found to be 22.7 ±5.2 mL/min and creatinine clearance was 20.7 ±4.8 mL/min (~18% of normal kidneys). Additionally, this WAK is able to provides effective clearances of ß2-microglobulin and phosphate, by analogy, middle-molecule clearances [122]. From a practical point of view, the sorbents and battery life would be expected to last for at least 24 hours, allowing a simple daily exchange [117]. These successes indicate that a WAK represents a near-term solution which can have a large positive

impact on the quality of life of patients in terms of freedom of movement, less dietary restrictions, and an expected reduction in morbidity [123].

***Challenges***

Several challenges with a WAK exist, including: cost, continuous blood access and infection issues, catheter clotting, and $CO_2$ bubble formation in the dialysate circuit as using active carbon for urea reabsorption [121], [124]. In addition, questions remain about whether WAK can be worn over prolonged periods given the limited battery life and the fouling potential of the membrane, as well as the potential for low toxic clearance (observed in some ESRD patients) and vascular disease [121]. Moreover, although ultrathin silicon membranes have higher packing fractions that traditional HFM membranes [125], further miniaturization of the WAK device without increased pumping power requirements remains a challenge.

### 2.4.2 Micro-scale Artificial Kidney Devices (μAK)

Multi-layer cell-based microfluidic devices have been developed to evaluate kidney function [126], tubular reabsorption [127], and as an iRAD-like microfluidic system comprising dialysis and secretion components for a bioassay of kidney clearance [128]. These studies suggest that the micro-structures can overcome large size and detached structure of the traditional hollow fiber dialyzer while incorporating an ECM-coating on the membrane's surface is able to reduce protein adsorption and cell attachment on the surfaces.

Alternatively, simpler NCB microfluidic devices (microdialyzers) can be fully optimized to serve as a micro-scale artificial kidney (μAK) or functional kidney units. For example, some microfluidic systems have been developed with similar membrane-embedded multi-layer structures to study anti-fouling for a portable hemodialysis device [78], [129], particle deposition during ultrafiltration [80], and sample preparation and electrophoretic separation of proteins in urine [130]. Interestingly, Miki's group proposed a dialysate-free micro-scale kidney device [12], [71]–[74]. They investigated biofouling such as thrombus, coagulation and protein adhesion on the sidewall of the microfluidic channels in such devices. Their micro-dialysis device includes micro-

machined stainless steel channels and carbon films coated with nano-porous polyethersulfone (PES) membranes [72]. Water-permeability, channel geometry, and surface treatments were evaluated. Hemofiltration (only the glomerulus' filtration without dialysate) was considered to be advantageous over traditional HD (i.e. glomerulus filtration and the transport of ions with dialysate) [131]. The authors argue that although the device does not allow counter current flow of low-molecular weight ions and molecules to be diffused into the body, these can be replaced later by medication and diet [12]. Their results also showed that biofouling is mainly caused by the surface conditions and that a very smooth surface (formed by electrolytic etching) could effectively prevent biofouling. An animal test was done with 32–36-week-old, Sprague-Dawley rats with renal failure. In this study, the rats were anesthetized and tested with 3 devices for 5 hours of treatment. The filtrate was collected every 15 minutes and 5mL of saline was injected to maintain blood pressure. The rats connected to the system with renal failure showed only a 7.4% increase creatinine after 5 hours compared to a 100% increase in the control group without the treatment [12].

Recently, the pioneers in implantable kidney research, Roy and Fissell's group also conducted studies and animal tests on iRAD filtration without seeding cells [75]–[77]. In their microfluidic devices, which utilized a silicon membrane, the diffusion, permeability and selectivity, thrombosis, and platelet stress accumulation were all found to be promising. The diffusive clearance of thin, flat sheets of SNM membrane (pore size of ~10nm and a porosity of 1%) allows ~50 mL/min/$m^2$ creatinine clearance with the transmembrane pressure of 130 mmHg (arterial-venous pressure difference). To improve upon this further, Kim et al. implemented a new technique of reducing membrane support structure's thickness from 400µm to 100 µm and achieved a two-fold improvement of clearance to roughly 110 mL/min/$m^2$ in vitro and extracorporeal testings in pigs on prototype membranes [76]. Meanwhile, pump-free operation of the SNM hemofiltration cartridge was observed to remain thrombus free for 8 days with aspirin as an anticoagulant and polyethylene glycol (PEG) as a coating material [75]. In a separate study by Buck et al., platelet stress accumulation was reduced by using parallel microfluidic blood flow paths, rather than a serpentine design [77]. These works showed the potential of using SNM membrane in portable kidney devices.

***Challenges***

Although µAK are promising, several challenges must still be overcome. To be truly implantable they must be designed to work under low glomerular hydrostatic pressure (of just above 7kPa) or they must be integrated with micro-pumps (which are also under development [132]), to obtain the needed pressures within a compact, implantable system. Advanced coating materials must also be implemented to resist thrombosis and fouling. More importantly, if dialysate is avoided and the devices are not able to perform tubular functions, a pathway needed to be identified to replace lost ions and minerals (including water) and other tubular functions. It should be noted that many these issues can potentially be mitigated by diet, proper drugs, and periodic clinical treatments [12].

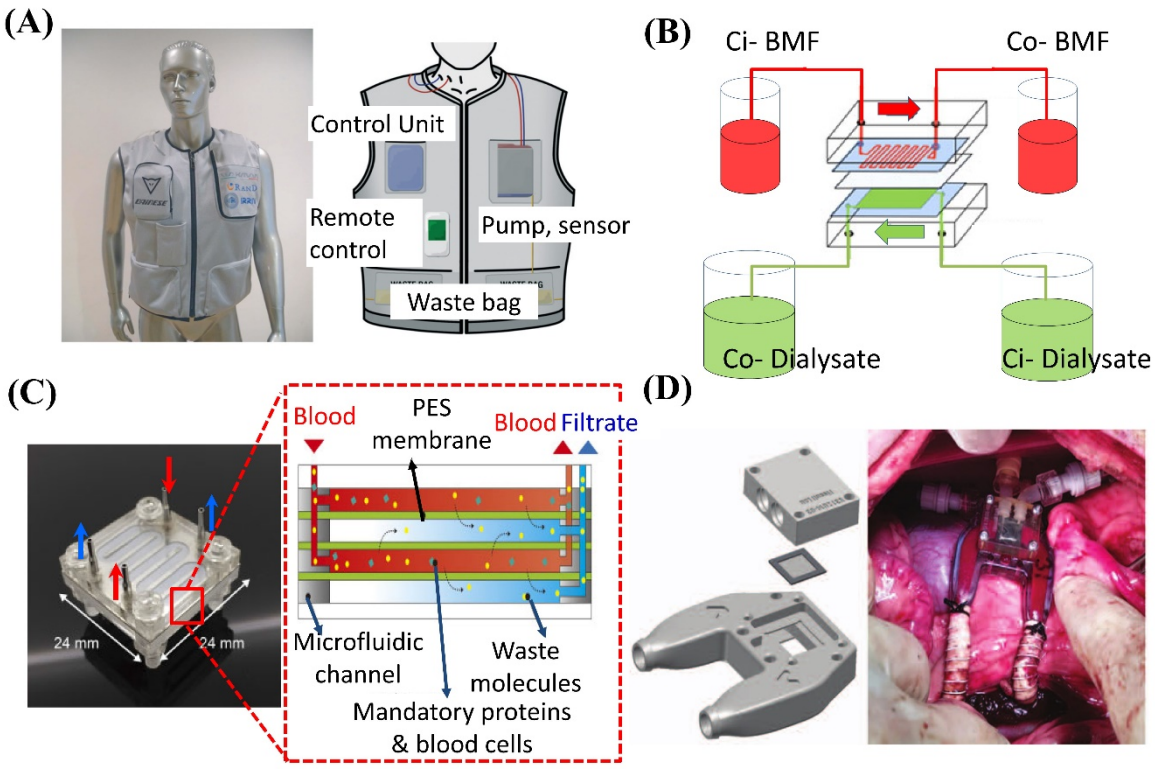


**Figure 2-5. Non-cell-based kidney replacement research.** (A) WAKMAN project, a complete system using WAK [116]. Reprinted by permission from Ronco, C., Davenport, A., Gura, V. "The future of the artificial kidney: moving towards wearable and miniaturized devices". Nefrologia 31, p. 9–16, copyright 2011. (B) A microfluidic platform for portable hemodialysis devices. Image's idea adapted from [70]. (C) Microdialysis dialysate-free system (microdialyzer) [65]. Reprinted and modified by permission from Japan Society of Applied Physics (JSAP), Ota, T., To, N., Kanno, Y., Miki, N., "Evaluation of biofouling in stainless microfluidic channels for implantable multilayered dialysis device" Jpn. J. Appl. Phys. 56, copyright 2017. (D) First implantation of silicon nanopore membrane hemofilters on dogs [67]. Reprinted by permission

from Wolters Kluwer Health, Inc., C. Kensinger et al., “First implantation of silicon nanopore membrane hemofilters” ASAIO J., vol. 62, no. 4, pp. 491–495, copyright 2016.

## 2.5 Comparison of Methods and Research Gap

Based on the all the progress discussed above, there are clearly many pathways towards artificial kidneys. These are summarized and compared with respect to their function and state of development in Table 2-2A. It can be seen that there are numerous challenges remaining in both CB and NCB approaches. Based on filtration capability of reported research devices (compiled in Table 2-2B), the NCB are closer to meeting the flow and filtration rate requirements of artificial kidneys. Based upon this logic, the following section provides more details on potential development path for NCB solutions.

**Table 2-2A. Summary table of artificial kidneys research**

| Content | *Cell-based Kidney Replacement* | | | *Non-cell-based Kidney Replacement* | |
|---|---|---|---|---|---|
| | **Regenerated kidney** | **Renal Assist Device (RAD)** | **Implantable Renal Assist Device (iRAD )** | **Wearable artificial kidney (WAK)** | **Micro-scale implantable kidney device (μAK)** |
| Mechanism | Stem cell-based bioengineered graft from cadaveric kidneys | Hemofilter seeded with renal tubule cells | Extention of RAD, used nanosilicone membranes | Miniaturized dialysis machine, battery-powered | Micro-scale dialysis system based on microfluidics (for implantation) |
| Functions | Glomerulus and tubule | Glomerulus and tubule | Glomerulus and tubule | Predominantly glomerulus | Predominantly glomerulus |
| % Cell | 100% | 0-<100% | 0-<100% | 0% | 0% |
| Animal tests? | Yes | Yes | Not yet | Yes | Yes |
| Animal test details | 68 kidneys in 12-week-old rats using decellularization | 12 uremic dogs (6 without, 6 with cell-treated RAD) | No results available | (i) Ultrafiltration was performed on 9 pigs ; (ii) Similar study was carried on 5 anesthetized pigs | Female Sprague-Dawley 32–36-week-old rats tested with 3 devices for 5h |
| Animal test results | Regenerated kidneys provided urine after transplantation in vivo | Sodium and water reabsorbed, up to 40-50% | No results available | No complications observed. Ultrafiltration rates of up to 700 mL/h, creatinine clearance of 27.0 ±4.0 mL/min | Rats showed only 7.4% creatinine increase (compared to 100% of rat with renal failure) |
| Clinical trial? | Not yet | Yes | Not yet | Yes | Not yet |
| Clinical trials details | No results available | (i) Phase I: 10 patients at 2 centers; (ii) Phase IIa: 58 patients at 12 centers; (iii) | No results available | (i) 6 patients are treated<br>(ii) In the next study, WAK was tried in 8 humans | No results available |

| | | | | | |
|---|---|---|---|---|---|
| | | Phase IIb: 24 patients at 15 centers | | | |
| Clinical Results | No results available | (i) Phase IIa RAD had a mortality benefit; (ii) Phase IIb had unexpectedly high survival rate in control filters | No results available | No complications, high quality of life, and effective middle-molecule clearances | No results available |
| Working duration | No results available | Up to 72h continuous RAD treatment | No results available | Up to 8h. Sorbent and battery life >24 h | No results available |
| Future Challenges | (i) Cell seeding issues; (ii) Cost; (iii) Cell control and biocompatibility | (i) Cell-related problems (cell sourcing and distribution, viability, compatibility); (ii) Treatment outcomes; (iii) Membrane clogging issue | (i) Cell-related problems; (ii) Membrane clogging issue; (iii) Treatment outcomes; (iv) Miniaturization | (i) Low clearance; (ii) Continuous blood access & catheter issues; (iii) $CO_2$ bubbles generated in sorbent. (iv) Miniaturization | (i) Low clearance; (ii) Lack of tubule functions; (iii) Membrane clogging issues (iv) Miniaturization |
| References | [10], [11], [133] | [9], [100], [101], [103]–[105] | [9], [60], [69], [75] | [6], [119]–[121], [124] | [12], [71], [72], [76], [77] |

**Table 2-2B. Filtration comparison of cell-based and non-cell-based implantable devices with hemodialysis and natural kidney**

| **Criteria** | **Natural kidney** | **Hemodialysis** | *Cell-based devices* | | *Non-cell-based devices* | |
|---|---|---|---|---|---|---|
| | | | **Regenerated kidney** | **iRAD** | **SNM without cells** | **Micro-scale device (μAK)** |
| Filtration rate | 90-120 (mL/min) | _ | 1.2 ± 0.1 (μL/min) | _ | 27.8 (mL/min/ $m^2$) (in vivo) | 8.3 (mL/ min/ $m^2$) (in vivo) |
| Blood flow (mL/min) | 1000-1100 | 200-400 | _ | _ | 120 | 100 |
| Driving pressure (mmHg) | 55 | 270 | 80 | _ | 103 | 55-80 |
| Creatinine clearance | 88 to 137 (mL/min) | 130-230 (mL/min/m2) | 1.3 ± 0.2 (mg/dL) | _ | 109±14 (mL/min/m2) (in vitro) | suppressed the increase of creatinine by 92.6% in test |
| Reabsorption rate ( mL/min) | ~119 | 0 | depends on cells | depends on cells | depends on absorptive materials | depends on absorptive materials |
| Working duration | _ | Several hours | _ | _ | 8 days | 28 days |
| Animal test | _ | Yes | Yes | Not yet | Yes | Yes |
| Clinical test | _ | Yes | Not yet | Not yet | Not yet | Not yet |
| References | [31] | [51] | [11] | [69] | [75], [76] | [12] |

### 2.5.1 Extrapolation of the Major Challenges and Possible Solutions

Wearable devices (WAK) serve as a possible near-term solution, however the dialysate system will also need to be miniaturized. While maintenance and replacement of the dialysate are relatively easy in a WAK, several of its major challenges arise from the need to carry the bags for urine and dialysate; blood access, infection and quality of life issues together with $CO_2$ bubbles generated in sorbent and clearance issues. Recent works have shown promise in overcoming the vascular access issue by integration of macromolecules that reduce the risk of thrombosis and infection on a needle-free device (similar to a chronic central venous catheter) [134] and development of a new non-$CO_2$-produced urea reabsorption method by using two-dimensional titanium carbide (MXene) [8] instead of previous materials such as zeolite, charcoal, activated carbon [14].

As shown in Fig. 2-6, NCB hemodialysis (and its miniaturized version, WAK) uses a simple one-stage filtration using (most commonly) hollow-fiber or tubular membranes. In contrast, the cell-based implantable iRAD (and its original RAD system) requires a two-stage (filtration and reabsorption) device which mimics the natural kidney. In trying to complete the whole job of the kidney, iRAD devices probably face more challenges (due to the integration of living cells) than the more simplistic WAK (see Fig. 2-6). It reveals a possibility to have a non-cell-based multi-step filtration mechanism to bridge between Fig. 2-6A and 2-6B cases. Bioengineered (whole) artificial kidney from stem cells, is the highest goal as its filtration mechanism is as same as a native kidney.

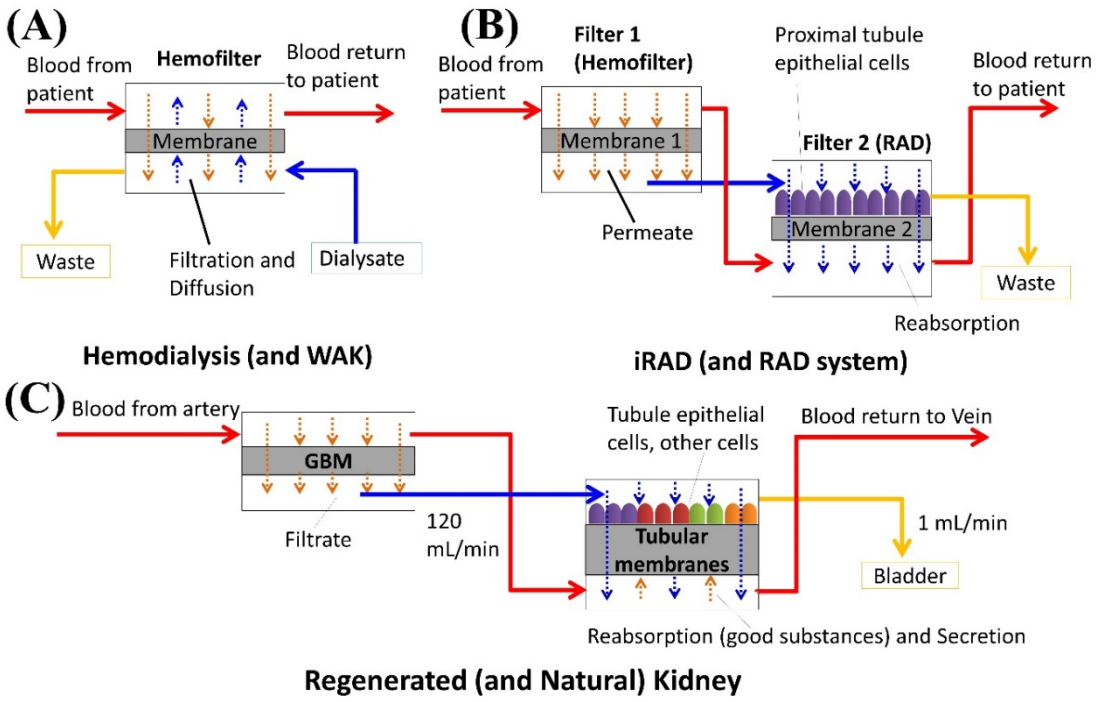


**Figure 2-6. Kidneys schematics.** (A) Hemodialyis and wearable artificial kidney (WAK) systems. (B) The proposed implantable renal assist device (iRAD) and the original RAD system. (C) Regenerated and natural kidneys.

Based on the presented in Table 2-2B and Fig. 2-7A (below), active NCB devices could potential meet most of the performance requirements of the kidney, if state-of-the-art from the fields of microfluidics and membrane systems and related technologies were integrated for this application. This study proposes a general approach (in Fig. 2-7B) that could be employed to develop the next generation of NCB devices. To be achieved for implantable kidneys, the devices must be: (1) Small at the size of natural kidneys, (2) Ultrafiltration rate to reach ~ 120 mL/min, (3) A self-cleaning dialyzer/ membrane, (4) Biocompatible and (5) Dialysate-free system.

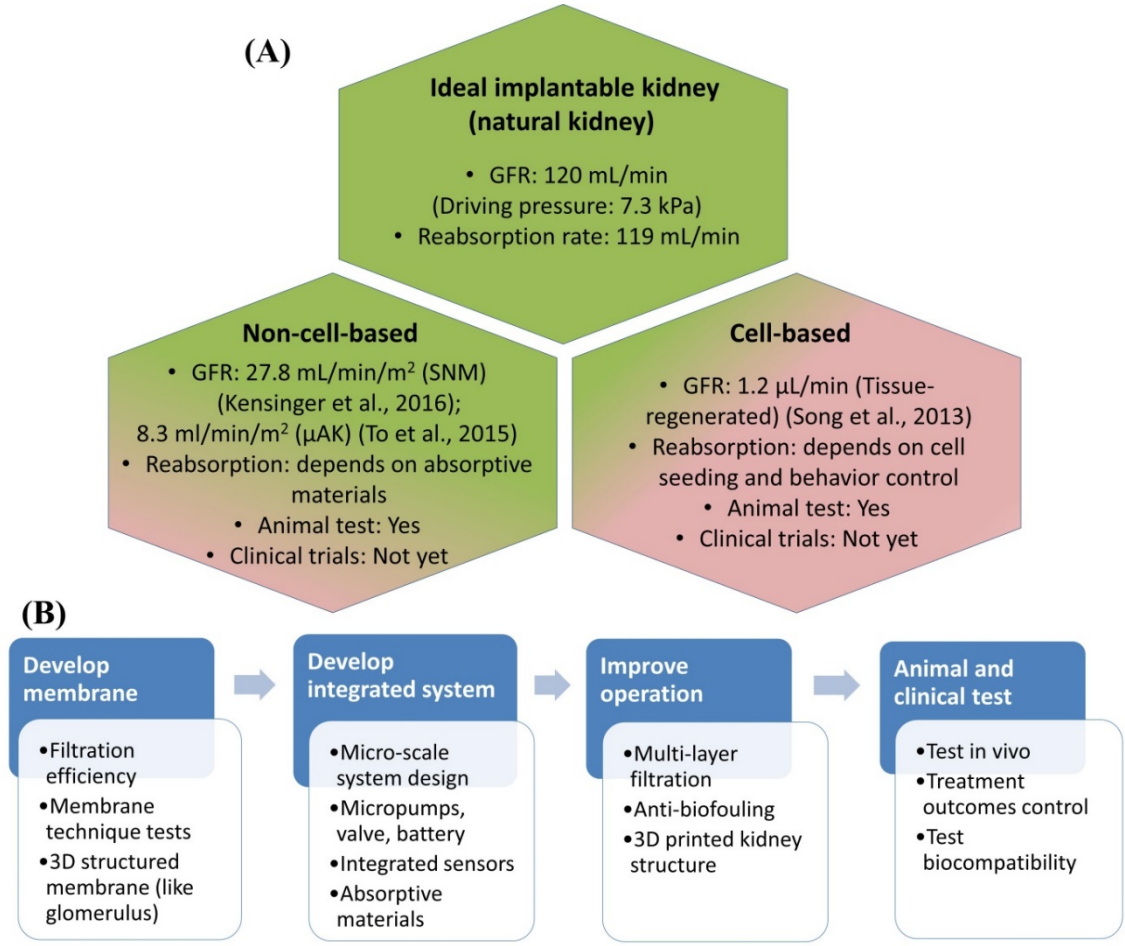


**Figure 2-7. Roadmap for device development** (A) Non-cell-based device can represent near-term solution. (B) Roadmap for non-cell-based device towards proposed implantable artificial kidney

## 2.6 Advances in Microfluidics and Fabrication Technology

### 2.6.1 Microfluidics Functional Unit Solution

So far, the proposed NCB implantable devices are membrane-embedded microfluidic dialysate-free systems [12]. They also have some problems with low toxic clearance and membrane fouling. Since natural pressure limitations also represent a constraint (e.g. low glomerular hydrostatic pressure of ~ 7.3kPa) for implantable systems, implantable devices might depend on the development of soft and safe micro-pumps [135]. Note that pumping power depends on the membrane selection and is also affected by the proposed dialysate-free mechanism. A further major challenge is to achieve an ions-and-water balance in the patient for hemofiltration system by replacement fluid, drugs or diet, due to a potential loss of important ions and minerals, without a dialysate [131].

The target filtration size of an artificial kidney device should remove components including urea (60 Da), creatinine (113 Da) and uremic components (~500 Da) as shown in Fig. 2-8. Unfortunately, the size of these waste components falls between other components which need to stay in the blood stream. This makes a (dialysate-free) single ultrafiltration unit unsuitable. Instead a selective filter system is required—e.g. perhaps a three microchip system as shown in Fig. 2-8. This type of solution—neglecting the challenges of CB techniques—may require a multi-disciplinary approach from medicine, microfluidics, membrane science, micro- and nanofabrication, and electronics. Thus, in the next part, we analyze the potential for bringing together knowledge from each of these fields to support iAK devices.

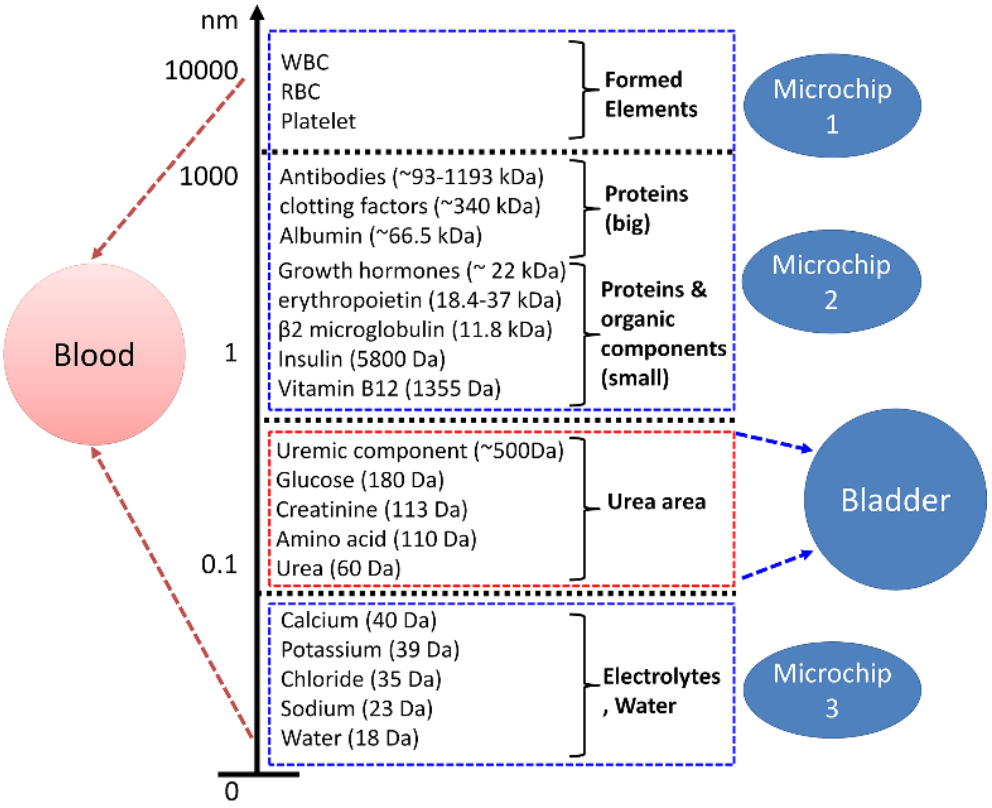


**Figure 2-8. Clearance target sizes and a proposed strategy**

## 2.6.2 Microfluidics Advances

Several organ-on-a-chip systems have been created using micro engineering approaches including kidney-on-a-chip devices [136]–[141]. Interestingly, there are similarities between these platforms and current iAK devices such as µAK [12], iRAD

[75], including similar scale, the use of embedded membrane multi-layer structures and the appearance of different flows at top and bottom channels. Therefore, it is possible to make use of kidney-on-a-chip advantages to offer a platform for experimental testing of the next generation iAK devices (as discussed in Fig. 2-8 and 2-9). The advantages of this approach include: (1) Systems which incorporate realistic physical forces, including physiologically relevant levels of fluid pulsatile flow [142], [143], shear stress, cyclic strain and mechanical compression to mimic kidney conditions in vivo [144], [145]; (2) Different membranes, absorptive materials, sensors, micropumps, microvalves and other critical miniature components can be integrated on to these systems for trials [12], [79], [146]; (3) Advanced microfabrication technologies can be used for the smarter fabrication with the better fluidic control and integration of the device. For example, automatic control logic circuits by multilayer lithography and 3D-printed molding [19], [147], [148], SNM membrane fabricated with reactive-ion etching and thermal oxidation [75], [112], 3D printing kidney chip [149], [150]. Some other advances related to implantable kidney studies are shown in Table 2-3.

**Table 2-3. Selected microfluidics and material advances for kidney functional units**

| Characteristics | Details | Example References |
|---|---|---|
| High throughput microfiltration/ separation devices | Use for cell separation, filtration rate reach to several mL/min for a single chip | [151]–[156] |
| Advances in Micropumps | Better performances in terms of high flow rate (>1 mL/min to hundreds mL/min) and simple fabrication | [132], [135], [157]–[159] |
| Integrated designs | Integration of microfluidic system with some electronic devices | [16], [17], [160], [161] |
| Feedback controls sensors | For future monitoring pressure drop and clearance of key ions/minerals | [162]–[164] |
| Microvalves and fluidic logic control | For fundamentals of regulating fluid flow and pressure in the filtration systems | [147], [165], [166] |
| Urea high absorptive materials | E.g., Charcoal, activated carbon, zeolite, two-dimensional titanium carbide (MXene), heterostructured nanoporous particles | [8], [14], [79] |

| | | |
|---|---|---|
| Microfabrication and compatible materials | E.g., 3D printing microfluidics and biomaterials | [167]–[169] |

### 2.6.3 Microfluidics Separation Methods

One of the advances of microfluidics is microscale separation technologies which can be considered here for the task of an artificial kidney, the separation/ secretion of nano and sub-nanosize urea, creatinine and uremic components. As shown in Fig. 2-8, the task can be broken down into some steps which include the first filtration step: separation blood cells, big proteins and other microscale substances from the remaining fluid (e.g. plasma). There are various separation techniques can do this task. Traditional methods for the separation of micro/nanoparticles is based on membranes [170], [171]. This technique can be an ideal to use for sub-nano substances and fluids such as plasma, urea, creatinine, however, is not the best for working with microscale blood cells since the cells will be in a direct contact with membrane and exposed to high pressure and stress which is possibly leading to the damages and loss of blood cells, or might be related to hemolysis (the destruction of red blood cells) or anaemia (not having enough red blood cells in your blood) as seen in hemodialysis. Several other limitations with using membrane for blood cells include clogging and fouling of the cells and big proteins. To overcome these issues, membrane-less microfluidic technologies can be considered as a promising choice for the first filtration step.

The current separation technologies can be classified into two classes: active and passive microfluidic systems. Active separation systems involve external field for cells/ particles separation while passive systems rely on hydrodynamic forces and do not requires any external manipulation.

***Active Separation Techniques***

Active separation techniques offer relatively high microscale particle sorting efficiency and throughput. One of the active popular techniques is fluorescence-activated cell sorting, in which a fluorescence signal emitting from sample cells causes them to be individually recognized at a relatively high speed [172]–[174]. From conventional method using droplet-based switching to eject single cells from a sample stream (via

laser) to modern systems using optical forces, electro-osmotic flow, hydrostatic pressure gradients and parallel microfluidic arrays, the cytometer systems have been micro-sized to proper cells and reached to sorting rate of 100000 cells per second. With the use of laser, this method however, might be invasive to blood cells and some other biological components in blood.

Other choices are dielectrophoreis [175], electrophoresis [176], optical sorting [172], magnetophoresis [177], [178], acoustophoresis [179]. Although there are variety of configurations and advantages, the active microfluidic separation systems mentioned above are non-continuous, relatively costly to fabricate and are probably difficult to miniaturize for portable or implantable purpose.

***Passive Separation Techniques***

Now we look into passive separation techniques which are simpler and less evasive, yet achieving wide ranges of cells/ particle [180], [181]. Deterministic Lateral Displacement (pillar structures or DLD) is a popular microfluidic passive separation technique. The method makes use of arrays of micropillar structures (based on their size, shape, and spacing) integrated into main flow channel to create size-dependent hydrodynamic forces for separation [182], [183]. Continuous sorting of cells based on their sizes, shapes and deformability is achievable if the dimensions and distance of the pillars are carefully controlled [184]. The technique has been used in a wide range of applications with the sizes of cells at tenth of microns and biological components down to 20 nm [185]. The disadvantages of DLD devices for continuous separation including high pressure input required (from 2-8 bar typically) which can damage cells, low concentration input solution allowed and the requirement to change/ wash the part frequently as blockage happened.

Some other passive microfluidic separation includes weir structures [186], crossflow [187], pinched flow fractionation[188], hydrodynamic filtration[189], biomimetic [190] and inertial systems [191]. Importantly, inertial microfluidic devices are able to manipulate cells and particles based on passive flow fields such as hydro-cyclone [153], or curvilinear microchannels (such as spiral channels [192]) where Dean flow playing a role in cell and particle focusing can be a potential first filtration step to minimize

clogging and cell damages for blood filtration required in iAK and pAK. Some recent studies on microfluidic spiral channels shows effective separation efficiency of blood cells and plasma with high throughput (up to 24 mL/min)[152], [156].

### 2.6.4 Microfluidics Valves and Micro-scale Fluidic Control

Regulating the microfluidic flow inside the portable or implantable AK device also requires a mechanism for liquid manipulation since the system is small, simple, as least maintenance as possible.

As a leading liquid-handling approach, microfluidic valves have been designed to connect or isolate liquid-containing microchannels and microchambers upon actuation, through passive [193], electrokinetic [194], pinch [195] and phase-changing [196] methods. Membrane-based microvalves (categorized into normally open [197], [198] (NO) and normally closed [147], [199], [200] (NC) valves) are particularly attractive for functional filtration unit study of this application because they offer simplicity in operation via the deflection of a thin membrane [201]. In addition to their operational simplicity, NC microvalves are becoming increasingly important in sophisticated microfluidic circuits since it offer low operation pressure [166], and can be tailored to a wide range of actuating pressures [142], [202] and switching (ON-OFF) frequencies [148], [203], [204].

Among the NC valve there are normal switch-valves (ON-OFF valves) and diode-valves (check-valves) that having geometrically regulated threshold pressures, enabling the switching action of valve in the fluidic circuit [143], [147]. Although being not popular as switch-valves, the diode-valves can serve to negate backflow and mixing between the solutions in the fluidic system of the AK design.

### 2.6.5 Use of Microfluidics in the Portable Kidney Design

In brief, a microfluidic chip can be used for separation of blood cells from the remaining fluid (e.g. plasma) [152], [205] and/or between nanosized toxic- and non-toxic components [155], [185] as shown in Fig. 2-9A. This part may have potential benefits for use as at least one stage of the filtration process (see Fig. 2-8). Using a pre-

separation step could enable plasma to be directed to the membrane system for extracting toxic substances, significantly reducing the potential for membrane clogging. In a recent study, Fan et al. demonstrated an effective biomolecule cleaning for typical molecules, including urea, creatinine, lysozyme, and β2-microglobulin from simulant liquid and even whole blood, by using a two-layer microfluidic device that integrates a polyamide porous membrane and heterostructured nanoporous particles (see Fig. 2-9B) [79].

In addition, the effectiveness of new components such as micropumps, microvalves, electronic pressure/concentration sensors, new membranes and other absorptive materials can be evaluated for their effectiveness in the larger microfluidic chip as shown in Fig. 2-9C and 2-9D [17], [159]. To develop functional integrated artificial kidney units, some related proposed techniques in implantable electronic devices can guide the development of these integrations, such as elastomer-based stretchable microfluidics [161], neural probe, cardiac pressure/ volume monitoring [162], [206], bladder sensor [163] or other artificial intelligence components for the real-time analysis and feedback response of equipment alarms, filtration parameters, and patient-related data [7] [164]. It should be note that depending on the membrane selection, PDMS-based chips may not be suitable for an artificial kidney unit if applied pressure is too high since it allows a weak bonding between membrane and PDMS slabs. Instead, 3D printing platform [150] is a promising future choice.

The index used to quantify HD and PD treatment adequacy [207], Kt/V, can also be applied as the target metric for scaling up of the NCB microfluidic functional units. In this metric the K represent the clearance performance, a %, t represents the time of operation, in minutes, and V is the volumetric flow rate through the device, mL/min. Since the flow rate of blood coming into the kidneys is ~1000 mL/min, a typical dialysis machine would process about 1/3rd of that (e.g. ~350 mL/min for hemodialysis machine) [208]. However, since hemodialysis is only connected 12-15 hours/ week, so a device which is continuously operating (assuming roughly the same filtration efficiency) could have a much lower average flow rate, something on the order of ~30-40 mL/min. If the device can achieve the same level of clearance in its filtration performance, K (mL/min), but run continuously (i.e., 10X higher t), the potential

advantage of a portable kidney device is that a similar level of filtration capacity can be achieved at considerably lower flow rate. Some reported NCB microfluidic devices, such those with a SNM filter, have been demonstrated to run at ~30mL/min only with arterial-venous pressure differential (without using micropumps) [60], so they are already in the right flow rate range for this approach. The remaining challenges for these, however, are to remove the concentrate (waste) and recycle water back into the body (e.g., achieving a dialysate-free device). A potential solution to this is to use the natural kidney and bladder as much as possible and traditional clinical dialysis as a backup when needed. For scale up of these types of devices, there are several important considerations, such as packing density and the working pressure. If the natural arterial-venous pressure differential is used, then obtaining enough filter area in a small space without exceeding this small pressure limit is a challenge. This pressure limit might be extended, however, by the development of micropumps. In addition, the use of multilayer structures and the development of 3D-printed structured membranes might also enable multi-step filtration as a method to increase permeability and capacity from a limited volume.

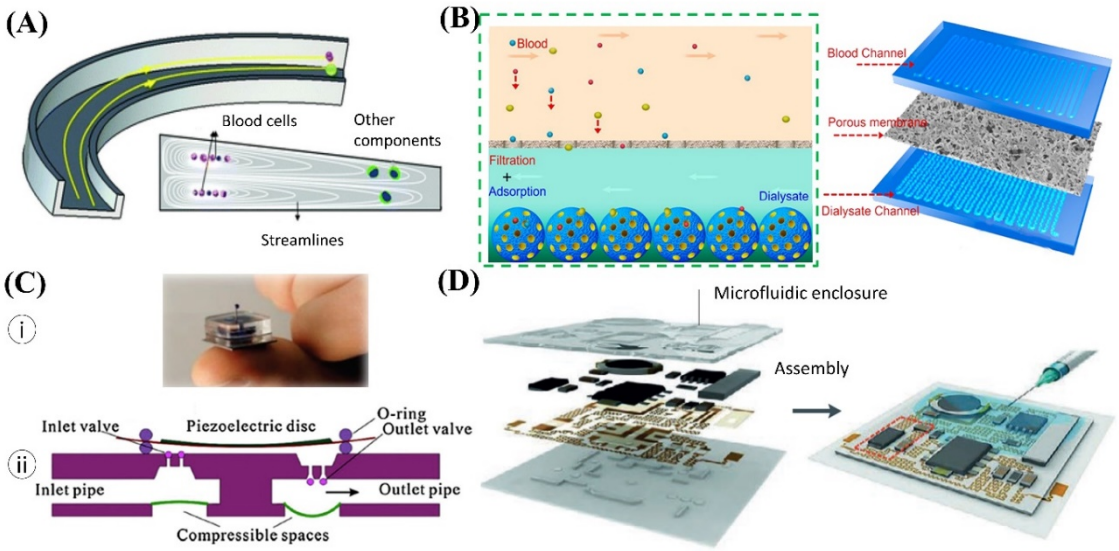


**Figure 2-9. Microfluidic-based integrated devices can be used as functional unit in non-cell-based artificial kidney research.** (A) A typical blood cell separation device [152], [209]. Reprinted from M. E. Warkiani et al., "Slanted spiral microfluidics for the ultra-fast, label-free isolation of circulating tumor cells," Lab Chip, vol. 14, no. 1, pp. 128–137, copyright 2014, Royal Society of Chemistry. (B) A microfluidic device integrated with membrane and active sorbent particles [151]. Reprinted from Fan et al., "Bioinspired microfluidic device by integrating a porous membrane and heterostructured nanoporous particles for biomolecule cleaning" copyright 2019, American Chemical Society. (C) A miropump and mechanical structure of PZT type micropump and operation principles in dispensing mode [159], [210]. Image reprinted

with permission from [210]. (D) Elastomer-based stretchable microfluidics [17]. Reprinted and modified by permission from Springer Nature, X. Hou et al., “Interplay between materials and microfluidics”. Nat. Rev. Mater., vol. 2, no. 5, copyright 2017.

## 2.7 Advances in Membrane Science

Membrane technologies which can be applied for mimicking the glomerulus and the tubular parts of the kidney are also under development. As mentioned above, key challenges for membranes are biocompatibility, anti-fouling and selectivity, in addition to the multitude of challenges in replacing the tubular functions.

### 2.7.1 Membranes Used in Artificial Kidneys

***Hollow Fiber Membrane (used in HD, WAK)***

State-of-the-art high-flux HFM devices typically have a wide pore-size distribution and irregularly shaped pore geometries, making it difficult to achieve the desired hydraulic permeability while maintaining an absolute selectivity barrier [211]. The HFM configuration allows for efficient use of surface area, but gains in membrane density are offset by relatively large pressure drops which lead to a decrease in economical use of the membrane [113]. Additionally, polymer membranes have been shown to have detrimental effects on platelet function [212], increased oxidative stress [213], [214], inflammation [215], and severe biofouling.

Despite these disadvantages, research into HFM can better facilitate the development of NCB iAK devices. By making the membrane thinner, the permeability of dialysis membranes is increased and by improving membrane structure, the membrane area can be reduced, and therefore dialyzers will become smaller [51]. In the conventional dialysis, the inner surface of the fibers is designed to be as fine as possible to keep approximately glomerular size-selectivity as filtering blood, while the outer surface features large pores to reduce filtration resistance and support the membrane structure. For reabsorption of RAD system, however, the filtrate should flow through the lumen and the blood should flow outside the fibers. While this might provide better functionality, large molecules (including blood cells, albumin, and antibodies) are easily trapped in the large pores on the outer fiber surface, resulting in the loss of important serum substances and result in membrane fouling [127].

***Silicon Nanopore Membrane (used in iRAD, WAK)***

In contrast to the wide pore-size distribution and irregularly shaped pore geometries of HFM, MEMS technology allows for the fabrication of membranes with uniform pore size distribution [114], [115]. This fabrication creates extremely precise and tunable geometries with feature sizes on the nanometer scale. Micro-fabricated SNM membranes also enable surface chemistry modification that can limit immunologic reaction and protein fouling, while enhancing selectivity based on electrostatic charge [216]–[218]. The nature of micro-fabrication allows specifically, control of the pore shape within the membrane (e.g. elongated pore shape rather than conventional round pores), leading to even further reductions of hydraulic resistance in the process [219]. Furthermore, MEMS enables device miniaturization not feasible with current polymer hemodialyzers given their inherently large package size and high internal flow resistance.

Biocompatibility studies of silicon-based MEMS substrates indicate that these materials are inert and of low toxicity [220]. As previously reported, the attachment of PEG can significantly reduce protein adsorption and improve biocompatibility of a variety of surfaces [221], [222] and limit membrane fouling by globular proteins, the surfaces of SNM were modified with PEG deposition [223]. The ultrathin SNM has a uniform slit pore with higher hydraulic permeability of about 5nm with less than 1% variability across a 100-mm diameter wafer and allowed the filtration rate up to 110 ml/min using only arterial-venous pressure difference, demonstrated to work for almost 100 hours using anticoagulated blood [76]. With high permeability, this membrane is able to work without the support of external pump.

However, the pioneering research of Fissell and Roy's group on SNM faced difficulties of relatively low permeability and fouling issues. Similar to CB therapy of RAD, they also reported issues of cell distribution, cell attachment, cell viability in SNM [9], [60]. Some other fundamental challenges of glomerulus-like filtration function include improving coating antifouling films [116], enhancing diffusion [76] and reducing platelet stress accumulation [77].

### 2.7.2 Antifouling

Membrane fouling is caused by the adhesion of proteins and other biological matters on the outer surface, inner surface and support layer of the membrane with various fouling mechanisms (e.g. concentration polarization, adsorption, cake layers, gel) [224]. The improvement of membranes used in dialysis is dependent on developments in material and mechanical engineering, which are related to technologies for refining and miniaturization [225]. Advances in water treatment technology [226], [227] and the implanted biosensors [228] can be applied on the development of very low-fouling, even self-cleaning membranes.

Fouling mitigation can be improved with a range of different approaches: modifying feed characteristics, optimizing operational parameters, novel membrane materials and specific flow-disruptors [227], [229]. Several methods have been reported with the potential to reduce or eliminate adhesive fouling by changing the membrane surface chemistry, through either coating or modification during the membrane fabrication process. Examples of coating methods include: a physical coating of water soluble polymers or charged surfactants onto the membrane surface; forming ultrathin films on the membrane; coating hydrophilic polymers on the membrane; grafting and photografting monomers to the membranes and the use of polydopamine to hydrophilize the hydrophobic membrane surface [229]. Modifications during the fabrication process include co-polymerization of hydrophobic and hydrophilic polymers, grafting water-affine groups to membrane surface, adding nanoparticles to membrane matrix [230]–[232]. With silicon membrane, one example of surface modification is the use of thiol groups grafted surface, which has been shown to reduce levels of biofouling and restore fouled surfaces [233].

Effectiveness with respect to both flux and selectivity over time needs further optimization to scale to the timeframe of an iAK, as the anti-foulant would need to survive the same time period as the membrane within the body for viable implementation. An additional recent development is the use of electrolytic etching as a means of reducing fouling, altering the surface of channels to produce a rougher wall for the liquid to interact with. However, further channel design is needed to optimize

viable levels of biofouling with pressure loss and channel design constraints as pressure loss and flux need further improvement [72]. Membrane modification has also been explored by altering cellulose acetate membrane for use in HD, as a blend with sericin. Traditional polymer membranes show issues in HD, degrading relatively quickly in a low pH and with aggressive agents present in blood; the membrane sericin blend has been shown in initial results to demonstrate comparable rejection and flux values with a higher resistance to degradation over time [234]. Polyvinylidene difluoride (PVDF) membranes have also been explored as a novel modified membrane material resistant to fouling when combined with zein without reducing the process flux, maintaining > 95% flux water recovery ratio and could be explored as an option for mitigating biofouling in further work [235]. A number of in-situ monitoring techniques including optical and non-optical probes have been developed so that membrane fouling of iAK devices can be better understood and controlled [236].

### 2.7.3 Biocompatibility

The human complement system is an ever-present factor when considering the biocompatibility of membranes to be used in dialysis. Proteins that can be activated either via the classical or alternative pathway are triggered by certain immunological stimulants, which are long known to be activated by membranes in dialysis [237]. Specifically, patients were found to exhibit elevated C3a antigen levels, later followed by C5a levels towards the end of a typical HD dialysis session [238] indicating the presence of a negative biological response to the membrane. Membrane material was observed early to play an important role in the degree of activation, with an initial observation that cellophanemembrane leading to acute leukopenia within an hour of dialysis [239]. Later work determined effects of membranes in comparison, when cuprophane, cellulose acetate, and polymethylmethacrylate were compared in patients at 1 month, cuprophanhe patients exhibited the highest degree of complement activation [237]. This activation of the human immune response naturally led to membrane selection and development towards greater biocompatibility for improved patient outcomes. Even in recent times, a patient may demonstrate a C3d/C3 ratio increase of up to 70% during a dialysis session, leading to the need for further

improvement in the field [240]. A nationwide study of membrane type used by hemodialysis patients in Japan was conducted with the aim of determining long term effects of each membrane on patient outcomes, and measured mortality rates against the use of common membrane types [241].

**Table 2-4. Membrane materials with corresponding 1-year mortality risk (adjusted for basic factors, dose and nutrients for kidney dialysis patients in Japanese National Dialysis Registry).**

| Membrane Type | Distribution of dialysis type among patients | 1-year Mortality risk (adjusted for basic factors, dose and nutrients). |
|---|---|---|
| CTA | 17.3% | 1.01 |
| EVAL | 1.1% | 1.15 |
| PAN | 1.2% | 1.18 |
| PEPA | 7.5% | 0.97 |
| PES | 12.0% | 0.91 |
| PMMA | 4.9% | 0.86 |
| PS | 56.0% | 1 |

**Data adapted from** [241]**.** Table is reprinted and modified from Abe, M., Hamano, T., Wada, A., Nakai, S., Masakane, I., "Effect of dialyzer membrane materials on survival in chronic hemodialysis patients: Results from the annual survey of the Japanese nationwide dialysis registry, PLoS One 12, p. 1–18." with permission from PLoS.

The negative patient outcomes of complement activation include inflammatory and thrombotic processes, linked to a higher risk of cardiovascular disease as well as fibrosis [242], [243]. Novel ideas for dialysis membranes, include thin-film nanofibrous composite (TFNC) membranes, which comprise of a PVA and a fibrous support layer. The membrane so far demonstrates good hemocompatibility and is thinner than currently utilised counterparts [244]. Membrane modification aimed at improving biocompatibility has also been achieved through altering the length and amount of polyvinylpyrrolidone (PVP) used, to achieve lower fouling and rates of platelet adhesion in continuous RRT [245]. New developments in the field of membrane biocompatibility and size have the potential to offer a realistic pathway to developing viable iAK devices.

### 2.7.4 Channel and Spacer Designs

The design of micro-channels has been generally well studied in the field of biomedical applications, from a wide range of perspectives such as heat transfer and pressure loss. Initially microfluidics was explored with the extensive study and characterization of single phase fluid flow when considering channels of a hydraulic diameter less than 1mm [246]. Additionally, when considering the design of tiny dialysis channels across a membrane surface, the challenge of friction co-efficient needed in calculating pressure drops is solved via the conventional use of Stokes and Poiseuille flow theories, for a flow of single phase [247]. However, the biological complications of capillary sized-flows in membrane channels present new challenges. The mechanical force needed to circulate blood though HD membranes requires a pump, and traditional polymers membranes present a high risk for complications such as thrombosis [111]. In novel challenges, studies need to be conducted on the long-term effects of blood passing through micro-channels and across new membranes – as initial results show the highly challenging nature of reducing fouling while maintaining a viable membrane with respect to bio-compatibility [72]. The use of spacers in membrane design has been highly utilized in water treatment processes, to reduce fouling, pressure drops and promote mass transfer [248], however, in the HD membrane processes the use of spacers to counter these problems is uncharacterized. Implementation of an iAK will be heavily reliant upon spacer design to reduce the high-fouling nature of blood, and as such require further design characterization.

### 2.7.5 Membrane Selection

The selection of the appropriate membrane for an iAK needs to take into account for the fact that the molecular weight cut-off (MWCO) ( e.g. the lowest molecular weight at which 90% is retained by the membrane [249]) and the total throughput must meet strict requirements—requirements which must somehow be maintained over the life of the membrane. Traditional HD membrane demonstrate a MWCO of around 67kDa, placing them in the nanofiltration and ultrafiltration range [250], which is suitable for

keeping blood cells in blood stream and filtering out filtrate (small proteins and organic components, electrolytes and huge amount of water). The implementation of an iAK device will likely require the use of additional membrane processes to further recover water [129], yet remove the urea and creatinine; this will require a membrane in the RO range, as the molecular weight of urea is too similar to the molecular weight of electrolytes/salts to differentiate one from the other (as shown in Fig. 2-8). Keeping blood cells separated from these processes can be helpful to increase input pressure for filtration and reduce stress and filtering effects to natural functions of blood elements. Membrane selection is additionally dependent on the material of a membrane. With traditional dialysis membranes formed through a classical non-solvent induced phase separation process, but currently are limited by a relatively large pore size distribution, leaving room for additional membrane materials [244]. In addition, suitable iAK membranes could be developed in the near-term using a 3D-printed hollow membrane structure which are very similar in geometry/function to the thin-walled fenestrated capillaries of the natural glomerulus [251]. Thus, new bio-mimetic geometries have a lot of potential to be more compact in order to achieve similar filtration capacity in device that is small enough for implantation.

## 2.8 Future Perspectives

Hemodialysis has been used widely, globally but remains as a low treatment quality, discontinuous and is restricted with hospital cost and schedule. Among currently available kidney replacement therapies, the best option is transplantation, but organ donor supply issues are unlikely to improve—particularly not at the rate of increase in demand—going forward.

In under-developing therapies, although stem-cell-based artificial kidneys represent an ideal long-term solution, these are likely to take decades of development due to the limitations of current cell-seeding technology and the various cell-related complications. Alternatively, the developments of non-cell-based wearable (WAK) and micro-scale implantable devices (μAK) to move beyond traditional dialysis treatments are promising choices.

A continuous, dialysate-free, non-cell-based system with micro-size channels (as proposed in some recent works) would be suitable for the system design of implantable devices. However, several challenges remain including low toxic clearance, membrane clogging, miniaturization and compatibility issues. Although, theoretical speaking, components such as micropumps can support the clearance for the membrane while urea adsorbent materials, electronic pressure and concentration microsensors could be integrated into the chip to analyze and solve the challenge of balancing level of water and necessary ions without dialysate, innovative ideas and a consider amount of works needed to be done.

Figure 2-10 shows the historical trend since the first artificial kidney was made successful for clinical use by Kolff in 1945 to current under-research artificial devices and predicted future devices.

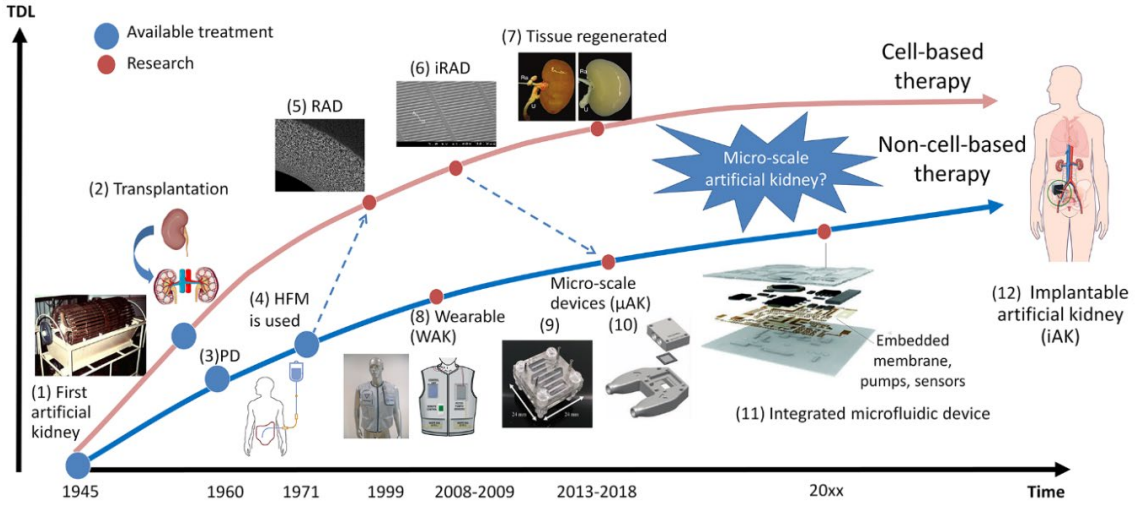


**Figure 2-10. Artificial kidney development timeline.** *y-axis, TDL: technology development level, notice that this is not shown in exact scale of the development since there is mixture of current treatment and under-research therapies. Images reprinted with permission. (1) Photograph of the rotating-drum kidney introduced by Willem Kolff in 1943 [208]; (2) Illustration of kidney transplantation, image's source: https://pixabay.com/; (3) Peritoneal dialysis schematic [252]; (4) and (5) Hollow-fiber membrane (HFM) and kidney cells populated HFM for RAD; (6) SNM membrane in iRAD [219]. Reprinted by permission from IEEE, S. Roy et al., "Silicon nanopore membrane technology for an implantable artificial kidney," Transducers, 15th Int. Conf. Solid-State Sensors, Actuators Microsystems, pp. 755–760, copyright 2009. (7) Cadaveric kidneys for kidney regeneration [11]; (8) Photograph of the wearable artificial kidney (WAK) [123]; (9) Microdialysis implantable system [12]; (10) First implantation of silicon membrane hemofilters [75]; (11) A proposed integrated microfluidic chip for implantable system [161]; (12) A proposed implantable kidney device [60].

## 2.9 Chapter Summary

Based on the review of the literature, we conclude the following three main points: (1) Stem-cell-based tissue regenerated kidneys represent a long-term, complete solution while non-cell-based wearable/portable and implantable devices represent an alternative, near-term choice for research and development; (2) Microfluidic-based integrated devices (with membranes, microspacers, microvalves, small-scale pumps, and electronic microsensors) which employs multi-step filtration mechanism are the promising functional units for the development of implantable artificial kidneys. (3) Absorptive materials, spacers and new membranes can be integrated into the functional unit for their effects in filtration tests. In fact, much of the basic materials, understanding, and groundwork are already available, but additional works are needed to bring together researchers from different fields to demonstrate new designs and devices which can be viable for clinical trial in patients.

There are two primary steps to achieve the aim of the thesis: (1) The first step is to design a non-cell-based mechanism/ system for a multi-step filtration that suits portable and implantable conditions for an artificial kidney. (2) The second step is to experimentally analyze the support of microfluidics, membrane and related advances in developing the system. Chapter 3 (system design and materials and methods) will focus on step (1) and the rest of the Chapters will work on step (2). The next chapter-Chapter 3, introduces a new microscale design, along with the description of some fabrication techniques, materials and the methods used for computational and experimental analysis used in this study.

# Chapter 3

# System Design, Materials and Methods

## Chapter Overview

*The aim of this chapter is to develop and test a possible NCB multi-step filtration system design for the near-term portable artificial kidney. The chapter starts with an explanation of the rationale of the design and its functional unit details. Next, it will move on to the materials and methods used in the experiments and simulations of the study.*

## 3.1 Proposed System Design for a Portable Artificial Kidney

### 3.1.1 New Mechanism Elucidation

As was noted in Chapter 2, a promising near-term solution is the development of a microfluidic-based multi-step filtration unit which integrates membranes, micropumps, microvalves and sensors for functional testing. Figure 3-1 is a description of the proposed NCB system, which uses a multi-step filtration approach, which can be connected in parallel with the natural kidney.

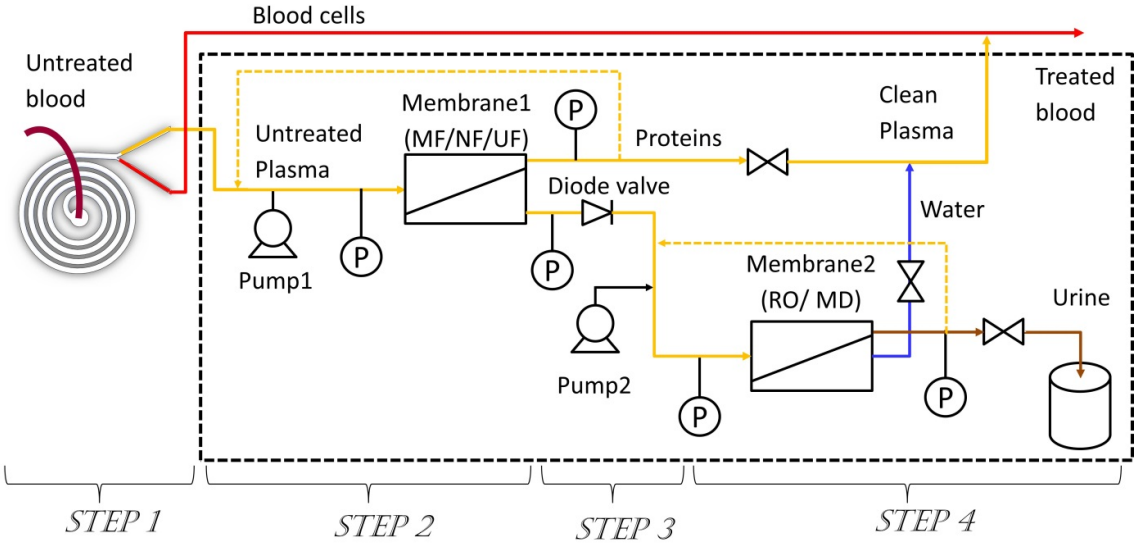


**Figure 3-1. Schematic representation of a portable artificial kidney mechanism based on microfluidics and multi-step filtration.** The dashed box surrounds the scope of this work. P: pressure sensor, RO: reverse osmosis, MD: membrane distillation.

As shown in the Fig 3-1, the proposed filtration system is a dialysate-free system that includes four main Steps: (1) separation of blood cells and large proteins from blood plasma (potentially with a spiral microchannel from UNSW colleagues [152]). The plasma then flows to Step (2), which uses a membrane to filter out the remaining proteins and biological components (i.e., Membrane 1). Next, Step (3) of this design is the Connection step which requires a microvalve and a pump. Lastly, Step (4) uses another membrane (i.e., Membrane 2) to pull clean water back into the blood stream (which eliminates the need for a dialysate input). The present Chapter provides an

overview of this system and subsequent chapters will detail Steps (2)-(4), which are within the scope of this work for this study.

***Step 1***

In Step 1, which is outside the scope of work for this study, untreated blood will be fed into a microfluidic system for the separation of cells from plasma. Although this is a non-trivial step, the feasibility of doing this with microfluidics (e.g. spiral microchannels) has already been proven by another researcher from our group, Dr. Mehdi Rafeie [152], [156]. It should be noted that while this is the envisioned design, there are other possible advanced separation methods for this Step which could also achieve similar results, as have been reviewed in Chapter 2.6.3.

Thus, the assumption for Step 1 is that it will achieve high separation efficiency (near 100 %) at a flow rate of ~24 mL/min (as was demonstrated in the literature [152], [156], [253]). Therefore, Step 1 will pre-filter whole blood continuously to separate large biological components (including red blood cells, white blood cells, platelets and big-size proteins) from plasma. This Step is necessary because it reduces the volume of large components input to the later membrane filtration Steps and it would mitigate cell-related membrane fouling issues. Thus, the starting point of the present work is that only plasma is carried into the proposed filtration system (e.g., the dashed box shown in Figure 3-1). The remainder of this thesis focuses on Steps 2, 3 and 4 as shown within the dashed box in Fig. 3-1.

***Step 2***

As mentioned in the preceding paragraph, the input for Step 2 is untreated plasma. Since Step 1 will use up most of the driving pressure, the untreated plasma must first pass through a pump. After reaching a pressure of 100-300 kPa, the plasma is directed to Membrane 1 for further collection of small and mid-sized proteins (e.g., albumin) and other biological particles (e.g., antibodies and hormones). To concentrate these, the pore size of Membrane 1 should range from a tight microfiltration (MF) to a nanofiltration (NF) [50], [225]. As such, Step 2 essentially mimics the mechanical filtration of the glomerulus.

***Step 3***

The permeate of Membrane 1 from Step 2 goes through a connection Step before being fed into Step 4 (Membrane 2). This connection part includes a one-way microvalve and a pump for controlling the pressure and flow.

***Step 4***

In the last Step of the proposed multi-step filtration system, a different membrane, Membrane 2, is employed to mimic the mechanical filtration and the reabsorption function of the tubular part of the natural kidney.

## 3.2 Design & Fabrication

### 3.2.1 Mimicking the Glomerulus (Membrane 1 – Step 2)

The glomerulus is essentially a very thin-walled ball filled with hollow capillaries (i.e., a densely packed, semi-spherical membrane). Its 3D complexity (as shown in Figure 3-2A) allows a very large membrane area to fit into a small volume. Also, the blood flow path through the sharp turns in microscale capillaries means the flow stays well mixed (e.g., concentration polarization at the membrane surface is limited). Thus, any design seeking to mimic this on the microscale should also include 3D flow and mixing. In this work, rather than producing a membrane with such complex 3D shapes (although this is a design identified for future work), microfluidic channels were designed with zigzag/serpentine shapes and with complex spacers to ensure that the flow experiences an analogous circuitous path through the device and—potentially—enhanced filtration at the microscale.

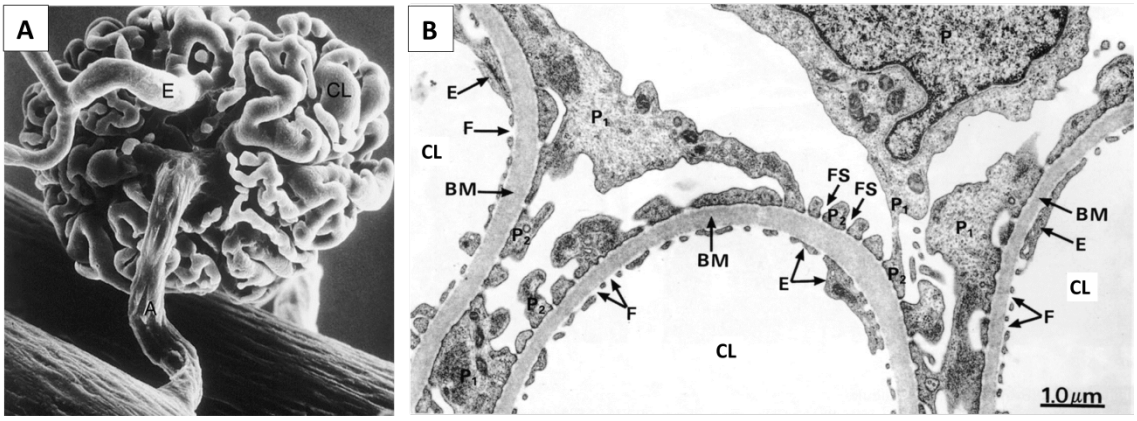


**Figure 3-2. Scanning electron micrographs of a 3D natural glomerulus structure.** (A) Glomerulus's complex capillary loops (CL) and adjacent arteries, A: Afferent, E: Efferent. (Magnification, ×300.) *Courtesy of Waykin Nopanitaya, PhD*. (B) Cross-section of three capillary loops (CL) inside glomerulus, BM: glomerular basement membrane, E: endothelia cell, F: fenestrated area, FS: filtration slits, P: podocyte cell. Reprinted with permission from Creative Commons via license: CC BY-NC-ND 3.0 [30].

As mentioned in Chapter 1, the glomerulus has a total membrane area of ~ 0.136 $m^2$ and can process a 550 mL/min input flow rate. Thus, the aim of this Step is to design and test a functional unit which can eventually reach similar levels (e.g., up to 242 LMH). As a basic membrane filtration unit, the model that was experimentally tested for Membrane 1 was a channel covered with a flat-sheet membrane [12]. As such, the following sections will provide details about the channel design, spacer design, and membrane selection (i.e., Sections 3.2.2, 3.2.3, and 3.2.4). The full results of performance testing with this design will be reported in Chapter 4.

## 3.2.2 Initial Photolithography-based Fabrication

### *Fabrication of master mold: photomask*

Microfluidic channels can be produced to provide similar dimensions to the capillaries found in the glomerulus. In addition, with advances in microfabrication methods, structures such as serpentines, herringbones, and other pressure-gradient patterns can easily be produced. At first, a selection of channel designs was designed using AutoCAD 2016 software (Autodesk Inventor, California, US). The CAD drawings (Fig. 3-3) were

then transferred to photomask (by JD Photo Data, UK) which are then used for the photolithography process for fabricating these 'kidney-chip' channels.

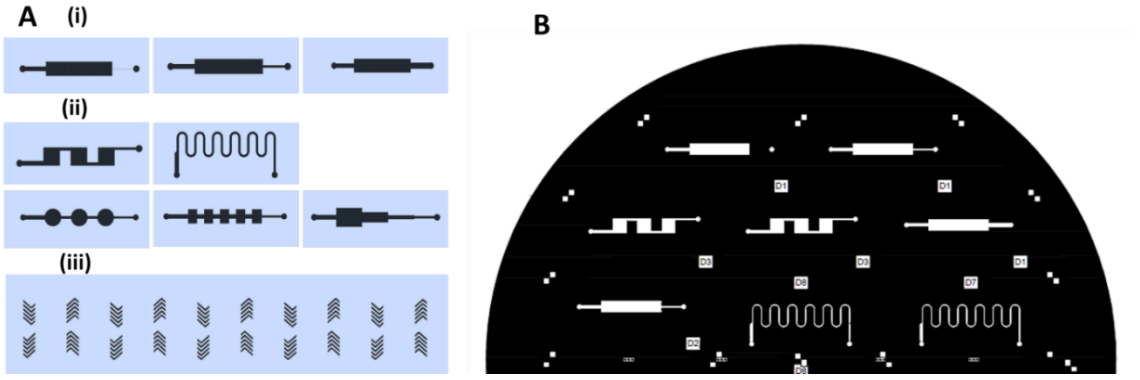


**Figure 3-3.Mold design in photolithography method.** (A) Simple CAD drawings of flow patterns, (i) outlet size changes, (ii) X-Y flow patterns and pressure gradient patterns, (iii) X-Y-Z flow using herringbone and serpentine patterns; (B) Half of a photomask (for photolithography-based fabrication).

## *Microfabrication Process*

For fabricating a complex microchannel (e.g., having features inside the channel), a multilayer photolithography process is traditionally required. As shown in the Fig. 3-4, the fabricated photomasks were designed as separated channel layers for multiple UV exposer processes to create patterns on photoresist-coated substrates.

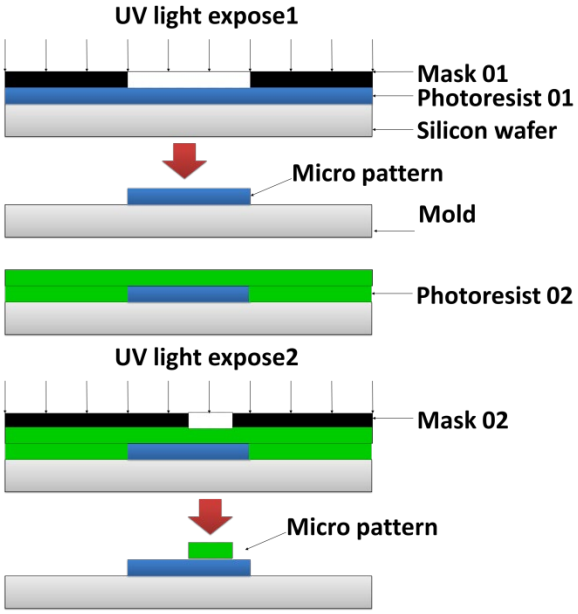


**Figure 3-4. Multi-layer photolithography fabrication principle.**

The whole process was conducted in a clean room as depicted in the Fig. 3-5A, followed by the fabricated mold shown in the Fig. 3-5B. A few of the SU-8 photoresist series (including SU-8 2015, SU-8 2050, SU-8 2075, MicroChem) were selected, depending on the target layer heights and spin-coated on to a 4-inch silicon substrate (University Wafer) before being baked at the specified temperature and time. Each of the substrates was then inserted, together with a designed photomask, into a Mask Aligner machine MA6 (SUSS MicroTec SE) for the multilayer photolithography process. After UV exposer (to crosslink the photoresist into the desired patterns) under photomask's guide, the substrate then underwent post exposer baking and a development process which uses chemicals to remove non-crosslinked resins. Finally, the substrate was hard-baked and cooled for the final product.

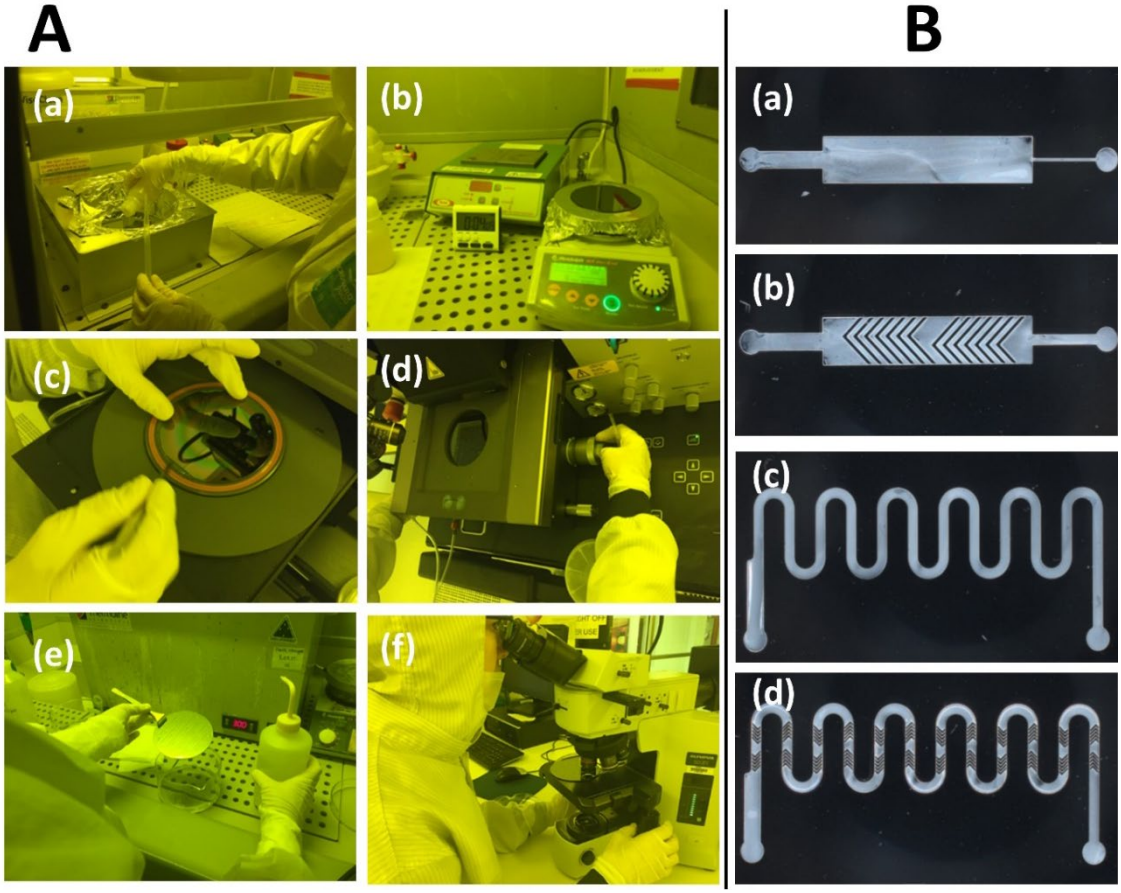


**Figure 3-5. Multi-layer photolithography mold fabrication.** (A) Photographs of the clean-room process: (a) Spin-coating photoresist on substrate, (b) Baking photoresist on substrate, (c) Inserting photomask and substrate on the Mask Aligner UV machine, (d) UV expose setup and run, (e) Chemical-based development process, (f) Quality check; (B) Microscopy images of the SU-8 mold products: (a) Plain channel, (b) Plain channel with herringbone, (c) Serpentine channel, (d) Serpentine herringbone channel.

After the molds were fabricated, they were checked for roughness (Fig 3-7 A (i)) and underwent a silanization process to modify the wettability of the printed model. This was followed by soft lithography replication of the designs using PDMS, as is shown in Fig. 3-6.

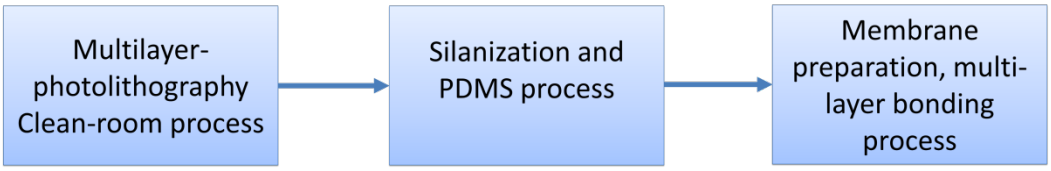


**Figure 3-6. Microchannel fabrication process overview.**

The silanization step is important for this application because it covers the surface of silicon substrate with organofunctional alkoxysilane molecules, which makes the substrate hydrophobic. To achieve a thin and uniform silane layer, the mould was placed in a vacuum chamber as shown in Figure 3-7A (ii). Fig 3-7 A (iii) (iv) (v) (vi) shows the processes of making the PDMS soft-lithography layer (ratio curing agent: base as 1:10), cutting the membrane, making PDMS glue (PDMS: toluene as 1:2 v/v), and the final PDMS bonding respectively.

For initial testing the Membrane 1 module made from this fabrication method, a common lab-used polyethylene terephthalate (PET) membrane sheet (cut from 4.67 $cm^2$, thickness 10 µm) with with 0.4 µm pore size (from Transwell) was used. Fig 3-7B show images of the assembled Membrane 1 design.

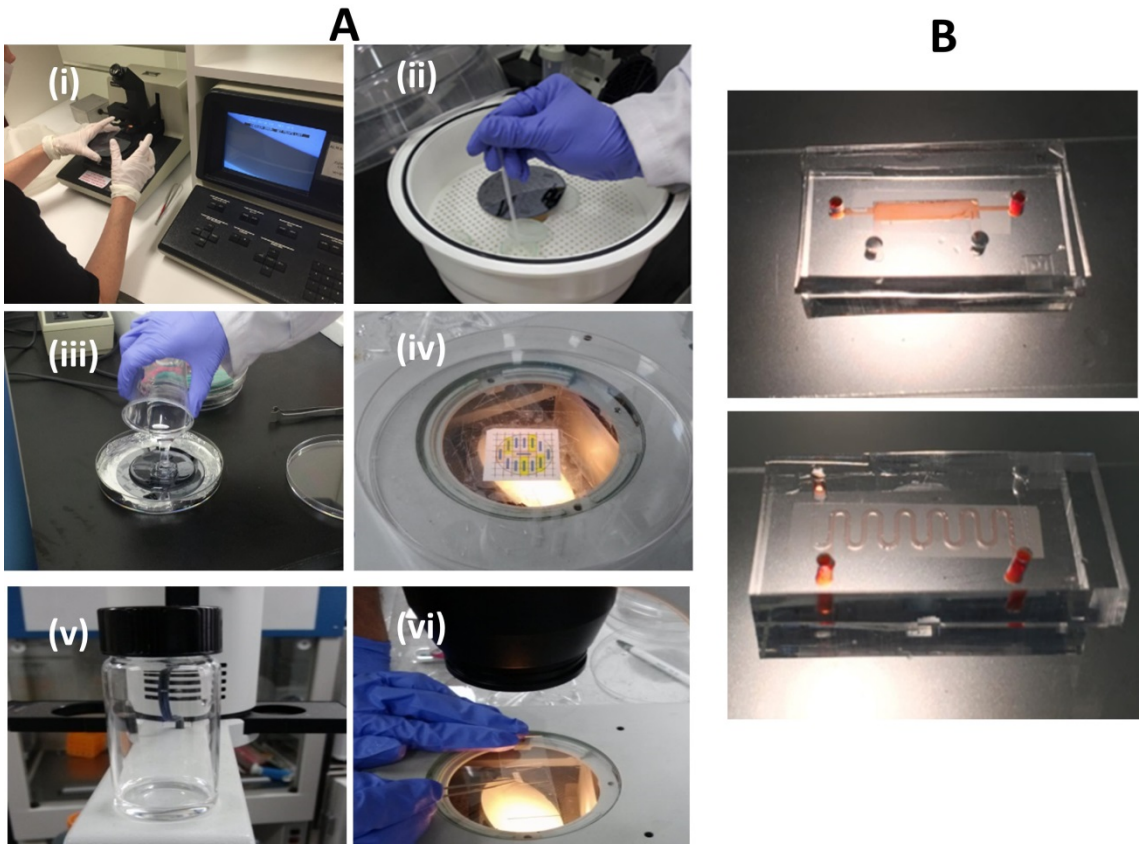


**Figure 3-7. Multi-layer photolithography device mold fabrication.** (A) Silanization and PDMS casting process, (i) Mold Checking with Pattern Waviness, (ii) Silanization, (iii) PDMS casting, (iv) Membrane cutting, (v) Toluene-PDMS glue preparation, (vi) Multi-layer PDMS and membrane bonding; (B) Samples of plain and serpentine-shape photolithography-based membrane devices.

### *Initial Test*

An initial experimental setup using a simple syringe pump (Cole-Parmer, model #74905 series) and an inverted microscope (Olympus, model IX73) was established to evaluate the input flowrate and the separation capacity as shown in Fig. 3-8A. In these initial tests, the device was tested for its ability to separate red food color particles (~500 nm) from a base fluid of clean water as shown in Fig. 3-8B.

However, the devices faced serious leaking and bubble-generation problems. More importantly, the permeate fluxes were recorded were <10 µL/min with allowed input pressure just around 35kPa, experimentally.

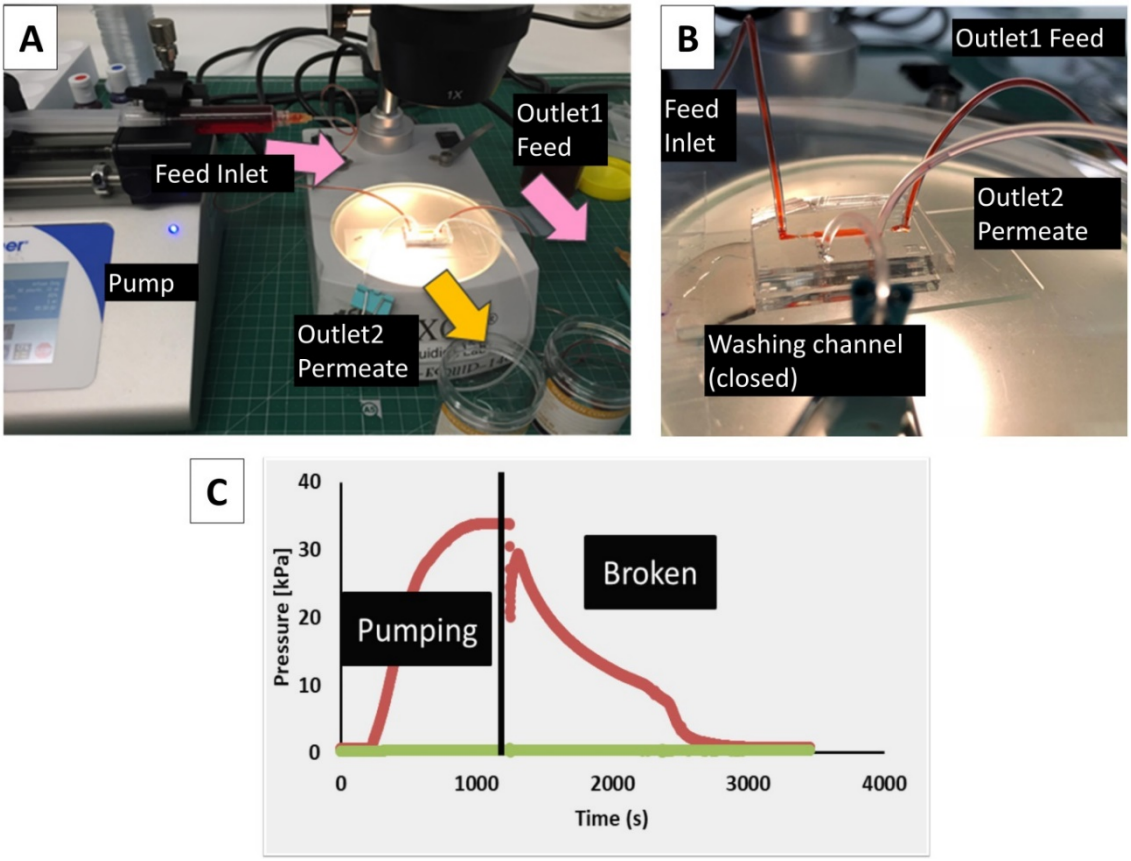


**Figure 3-8. Multi-layer photolithography–based device setup.** (A) Experiment setup, (B) Initial experiment with food color sample, (C) Device input pressure limit test.

### *Leaks and Bubbles*

With the initial photolithography-based fabrication method, the inlet pressure applied to the device was not able to exceed 40 kPa, as is shown in Fig. 3-8C. When the input pressure to feed channel is higher than this value, the bonding between the membrane and PDMS layers burst, as shown in Fig 3-9A. Also, a significant difficulty was found with bubbles constantly being generated inside the permeate channel, as shown in Fig. 3-9B.

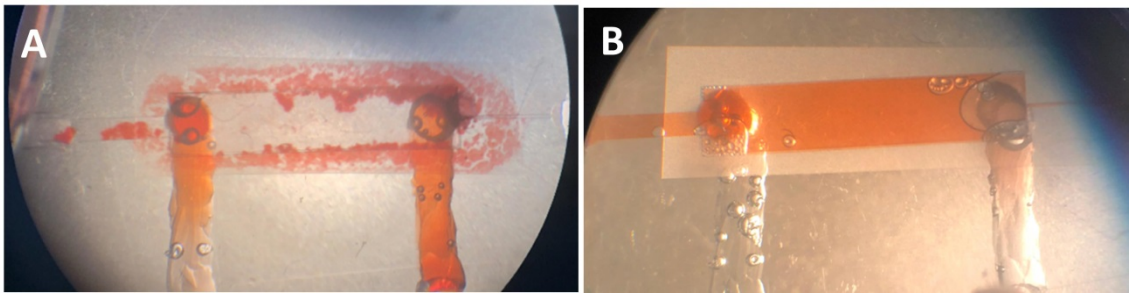


**Figure 3-9. Multi-layer photolithography-based device issues** (A) device leaking and (B) bubble generated issues.

Although the bubble generation issue can be reduced by degassing the system thoroughly before the experiment, the leaking issue made it difficult to achieve similar levels of glomerular filtration. As a result, the fabrication technique of *multi-layer photolithography* was deemed *not* suitable for the aims of this research.

### 3.2.3 3D Printing-based Fabrication

Due to the failure of the multilayer photolithography-based fabrication approach, 3D printing was considered next, as an alternative (and potentially better) way to build functional chips for filtration testing. The advantages of 3D printing include: (1) More choices for the designs and the range of geometries to mimic the glomerulus or tubular structures, (2) Designs which allow mechanical fastening for higher input pressure and flowrates, (3) Rapid prototyping for design modification. The next section will outline the Membrane 1's testing platform/module designs (i.e., serpentine and herringbone spacer-filled channels) which were fabricated with this 3D printing approach.

#### *3D-Printed Spacers*

Spacers are commonly used in large-scale membrane systems to manage fluid flow, reducing concentration-polarization, and enhance filtration efficiency and throughput [248]. As can be seen in Fig. 3-10, as fluid flows around a conventional spacer (annotated in yellow), the flow changes direction by a characteristic angle (the angle between the crossing filament) along a zigzag path in the Z-direction (annotated with blue arrows). At the macro-scale, this creates turbulence and mixing [254], but in the present study—which is low Reynolds number, laminar flow—turbulence promotion may not be a viable enhancement mechanism for filtration.

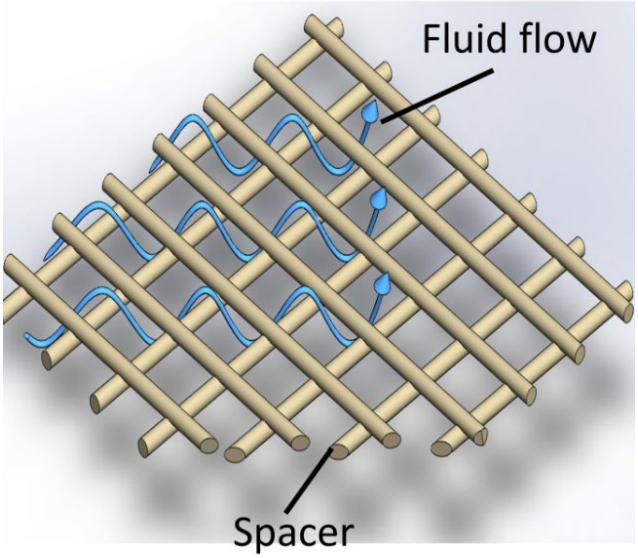


**Figure 3-10. Conventional spacer fluid flow streamlines (Fluid flow behavior with spacers)**

However, by using different 3D spacers it may also be possible to enhance filtration in at the microscale. By integrating microspacers into a feed channel filtration unit, the overall design more closely mimics the glomerulus' fluid management compared to conventional hollow fiber membrane (HFM) units in hemodialysis.

### *3D Geometry Capability*

By using 3D printing, more complex channel designs can be freely developed. Micromixer features, such as herringbones can be stacked, and incorporated into the feed channel designs of membrane testing modules as shown in Fig. 3-11A. Further, more complex structures, such as a gyroid (an infinitely connected triply periodic minimal surface), can also be fabricated to induce a complex flow mixing mechanism [255]. Fig. 3-11B and C show the CAD designs of a 3D gyroid structure to be incorporated into the flow channels.

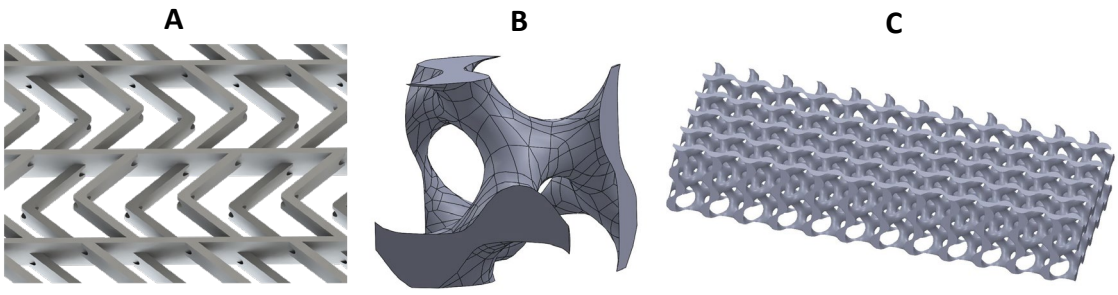


A herringbone stack | Single gyroid | An array of microscale gyroid

**Figure 3-11. 3D printing structural design capability.** (A) A herringbone stack, (B) A Single gyroid Structure, (C) An array of microscale gyroid

The details effects of 3D-printed microspacer in filtration units will be discussed further in Chapter 4.

### *3D Printing Process/Protocol*

The spacers and the filtration unit models were designed using SolidWorks 2017 and subsequently 3D-printed with a ProJet® 3500 HD Max or ProJet® MJP 5600 3D printers (3D systems, SC, USA). These 3D printers use multi-jet manufacturing (MJM) technology and have a minimum printing resolution of 12µm. Visijet M3 Crystal/ VisiJet CR-CL 200 material was used in the printer along with wax as a support material for overhanging features. After printing, the models were heated in an oven to a temperature of around 60 °C to melt the supporting wax. This step was followed by sonication in a vegetable oil bath at 60 °C for ~2 hours to remove any residual support wax. Afterwards, residual oil was removed in a secondary sonication process in a water bath (for 30 mins). These steps are illustrated in Fig. 3-12.

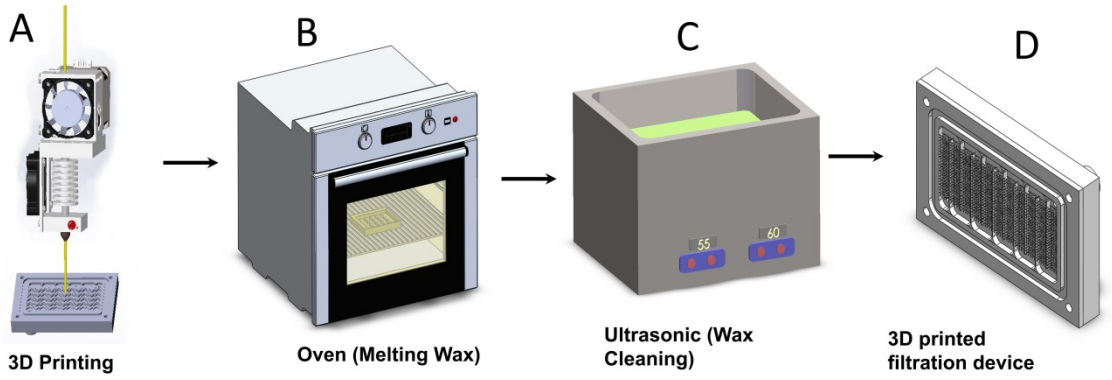


**Figure 3-12: Fabrication process for a filtration unit (with 3D printing).** (i) 3D-printing integrated spacer microfiltration unit, (ii) Melting wax in the oven, (iii) Cleaning wax in an ultrasonic oil bath and water bath, (iv) 3D printed filtration device (feed part).

### *3D Printing Quality Check and Roughness Measurement*

The fabrication quality and deviation of these produced 3D-printed spacers were checked via image analysis from an inverted microscope (e.g., a Zeiss Axiocam 512 color) and Image J software (available from U. S. National Institutes of Health [256]).

Additionally, the surface roughness was measured using a laser scan microscope (e.g., a Keyence VK-X200 series). Details are shown in Figure below:

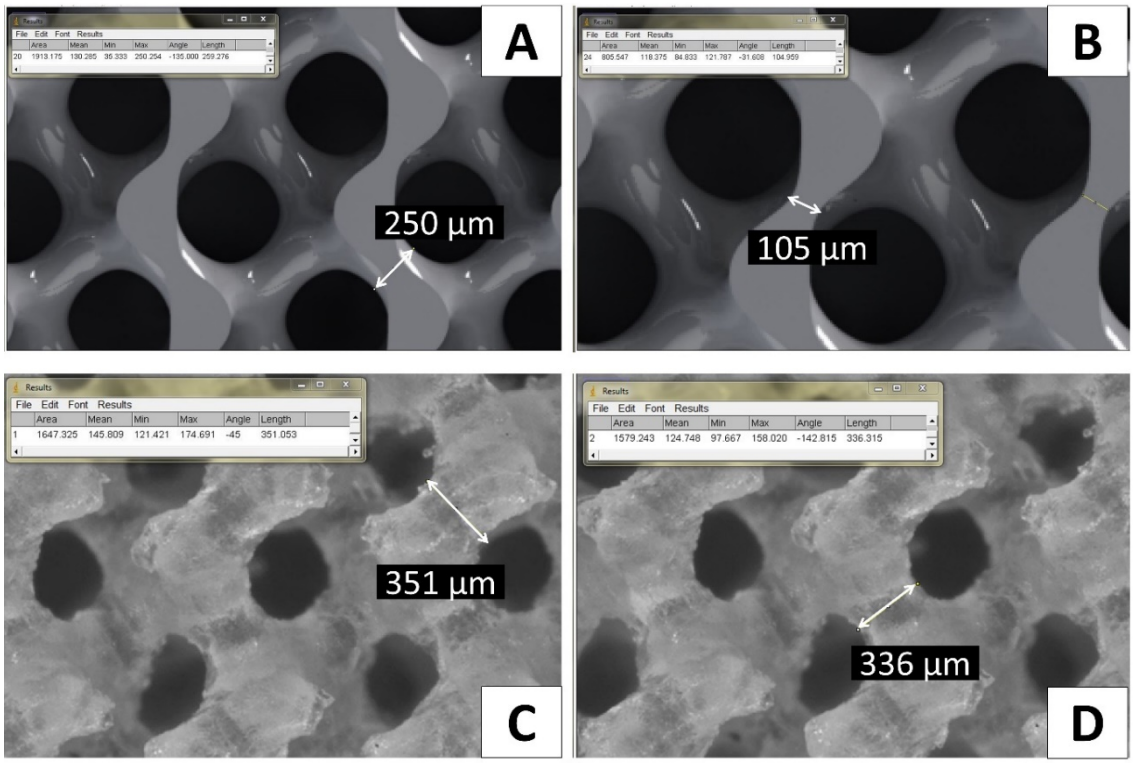


**Figure 3-13. Fabrication deviation measurements between design and actual microscopic images by Image J.** (A) and (B) the measurements on CAD designs, (C) and (D) the measurements on 3D-printed spacers.

The roughness of 3D printed parts (e.g., spacers) was also monitored by spot checking the roughness of the spacer's surface using a laser scan microscope (Keyence VK-X200 series), with some characteristic results shown in Fig. 3-13). The average roughness is shown in the Table below.

**Table 3-1. Spacer geometry roughness measurements**

| Spacer type | Average Roughness $R_a$ (µm) | Sample amount | Location |
|---|---|---|---|
| Plain | 10 | 3 | Arbitrary |
| HB1x | 22 | 3 | Arbitrary |
| HB2x | 30 | 3 | Arbitrary |
| Gyroid | 16 | 3 | Arbitrary |

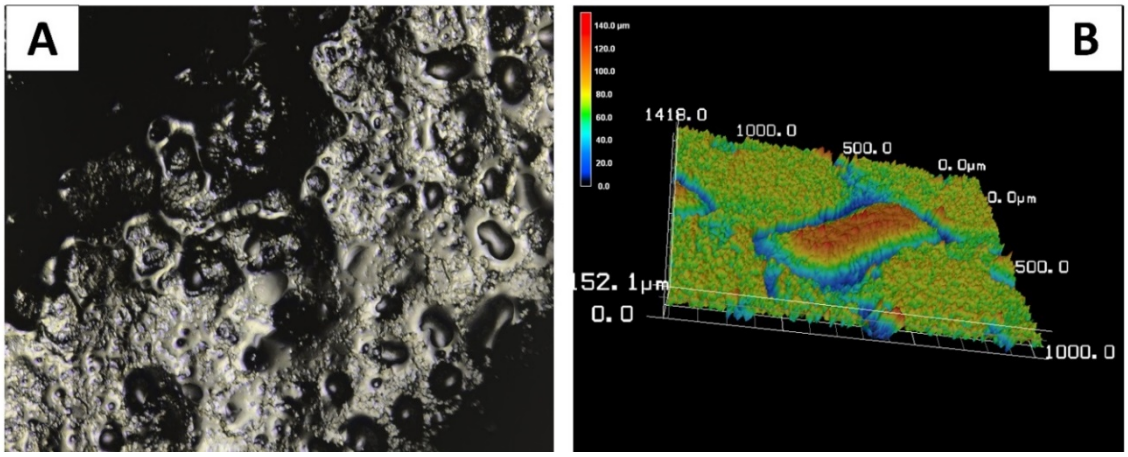


**Figure 3-14. Surface roughness measurement of 3D printed spacers.** (A) Surface roughness microscopic image of a herringbone spacer, (B) 3D display surface roughness measurement of a gyroid spacer.

### *3D-printed Channel Design Samples*

The results of the fabrication process are shown in the Fig. 3.13 below. It can be seen that the designs have rough surface with the quality check results presented above. Each design has holes for screws and a gasket to get high bonding pressure. The effects of spacer-integration into microchannels for glomerulus-like filtration will be analyzed in detail in Chapter 4.

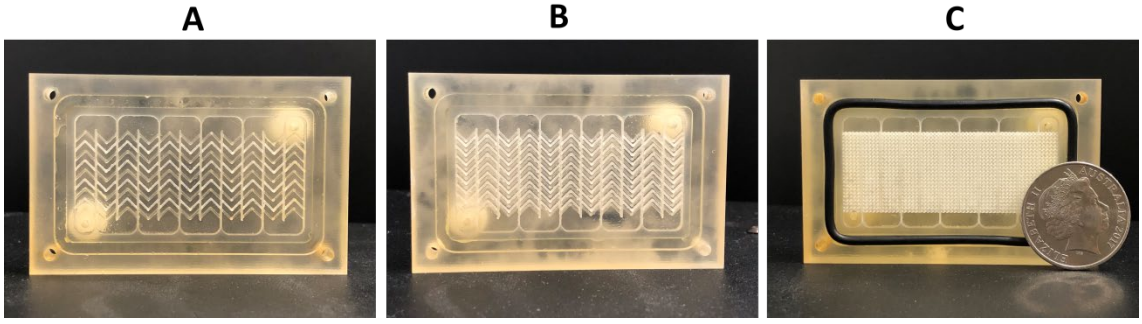


**Figure 3-15: Samples of 3D spacer-filled feed channel designs of filtration units.** (A) Herringbone (HB1x), (B) Double herringbone (HB2x), (C) Gyroid.

## 3.2.4 Membrane 1 Selection

For Membrane 1 and the spacer development test, a membrane with a filtration area of 3 cm × 5.8 cm (e.g. a flat PVDF membrane from Durapore®, with an average pore size of 200 nm, thickness: 125 µm) was utilized as the middle layer of the spacer-integrated microfluidic filtration (SMF) unit. Note that this membrane was only selected for proving the effect of spacer-integration in the narrow channel, and for a

higher permeate flowrate collection; it cannot retain any small-size proteins. For the pAK system, Membrane 1 should be further considered with the much smaller pore-sire (e. g., from 68 kDa to just several kDa).

As this is a lab-scale research device, hollow fiber membrane (HFM) [257] and other types of commercial channel design such as spiral wounded modules [258] were not considered. Flat-sheet membranes fit best with the designs mentioned above and ensure the most simplified system for experimentation. The membrane selection also neglected other materials which were assumed to be pre-filtered out from Step 1 (e.g., cells and large proteins) and the biocompatibility of this membrane was also neglected.

### 3.2.5 Mimicking the Tubules (Membrane 2 – Step 4)

Similar to Membrane 1, the functional testing unit for Membrane 2 was a simple flat-sheet membrane. Again, this fits with the form factor of the 3D printed designs mentioned above.

The main criteria for selecting Membrane 2 come from trying to match the flow rates and separation ability required for the application. That is, the tubule part of the kidney receives 120 mL/min of filtered plasma and mainly needs to remove urea, creatinine and other toxic uremic substances, while returning 119 mL/ min water and other necessary substances back to the blood stream. This means Membrane 2's structure should be less complex compared to Membrane 1 design, although the use of channel designs and spacers is still useful for its potential filtration enhancement. Details about membrane 2 study and performance testing are discussed in Chapter 6.

### 3.2.6 Membrane 2 Selection

As discussed in Chapter 2, the tubular of the nephron is responsible for the reabsorption of proteins, hormones, electrolytes and most of the water. In our design, a reverse osmosis (RO) or a membrane distillation (MD) membrane is used to mimic the critical function of the tubular part: reabsorbing water (from glomerular filtrate) which accounts for ~99% of the reabsorbed fluid volume.

For the RO testing purposes, since salt has similar molecular weight to urea, membrane was selected for testing based on its salt rejection rate. Thus, a Toray flat-sheet polyamide-TFC RO membrane (UTC-73HA, Sterlitech) which can achieve a NaCl Rejection rate 98.7-99.6% was selected for the functional unit test for Membrane 2. A filtration area of 4 cm × 10 cm (0.004 $m^2$) was cut from a flat-sheet 457 mm × 457 mm for each module. Since the test investigates the effect of the design and the working conditions on selectivity and filtration efficiency, the biocompatibility of this membrane was neglected.

For the MD testing purposes, tubular microporous membranes are needed and Polypropylene (PP) membranes (ACCURL® PP S6/2, a porosity of 70%, mean pore radius of 0.2 µm, and the membrane thickness of 0.45 mm) were chosen for the hollow-fiber membrane module. Details on this selection will be explained in Chapter 6.2.2.

### 3.2.7 Geometric Design Criteria

Other design criteria for functional testing platform/ filtration models of Membrane 1 and 2 are summarized in the Table 3-2 below:

**Table 3-2. Ideal design criteria for Membrane 1 and Membrane 2**

| Design Criteria | Membrane 1 (glomerulus) | Membrane 2 (tubule) |
|---|---|---|
| Model types | Flat-sheet | Flat-sheet |
| Size | <120-230 $cm^3$ | <120-230 cm3 |
| Filtration area | 0.136 $m^2$ | - |
| Channel width | ≥20 µm | - |
| Spacer use | yes | yes |
| Target selectivity | 2-68 kDa. | < 50 Da |
| Membrane type testing | MF/UF/ NF | RO/ MD |
| Input Pressure | 7.3 kPa to ~200 kPa | 200 to ~800 kPa (RO), >50 kPa (MD) |
| Working Flowrate | 550 mL/min | 120 mL/min |
| References | [30][12] | [30], [259], [260] |

The designs for the two membrane modules are platform for testing and chosen as flat-sheet membrane module for the simplicity. About size, in the ideal case, it should be as small as natural kidney in volume or capillary in channel width but having as much as filtration area and condensed as it is in glomerulus. Membrane types were chosen depending on purpose of tests and followed by the corresponded input pressure condition. The working flowrates were set based on the glomerulus and tubular plasma and glomerular filtrate level, respectively.

### 3.2.8 Other Fabrication Aspects

The fabrication cost depends on materials, printing time, energy, and labor cost. Considering only the consumables, the Visijet M3 Crystal material used in the printer along with wax support (e.g., less than 100 mL) had a cost of less than 30 USD for a microspacer-integrated filtration unit presented herein. For a single filtration unit, depending on complexity of the microspacer design, the printing time was about 2-4 hours, which gives some indication of the fixed cost of using the printer as compared to its service life (i.e., in the range about 5-7 years).

With the design and fabrication methods described in this part, the main parts Membrane 1 and Membrane 2's filtration testing modules were made. As discussed in the Chapter 3.1, the remained Connection part (i.e., microvalves) will be needed (e.g., to regulate the pressure in the connection parts) for the proposed filtration system. How the diode-like type of microvalve was made, its operation and further detailed analysis of the valving system will be mentioned in Chapter 5.

## 3.3 Test Solution Preparation

Four main types of solutions were tested in this study, including: water, a plasma mimicking solution (PMS), a blood mimicking solution (BMS), and a uremic mimicking solution (UMS). The following sections will discuss how these were synthesized.

***Plasma mimicking solution (PMS) and nanoparticles (Membrane 1's feed)***

To mimic a plasma filtration process (such as serum or protein separation), we also employed a plasma mimicking solution (PMS) in this study by using MACs (Magnetic-activated cell sorting) buffer solution containing low-density polystyrene particles ($\rho = 1.04$ g/cm$^2$) of around 50nm in diameter at a concentration of 0.2% v/v to mimic large protein in blood plasma. The MACs buffer solution was prepared with 0.5% bovine serum albumin (BSA) (Miltenyi Biotec, Germany) to provide a similar level of protein (albumin) that is in plasma. The BSA also helps prevent the nonspecific adhesion of the particles to the tubing and spacer's microstructures.

To evaluate filtration selectivity, the polystyrene size and concentration in the feed and permeate solution were tracked using *nanoparticle tracking analysis* (with a NanoSight LM14). Further details regarding this measurement are presented below in the Chapter 3.3.1.

***Blood mimicking solution (BMS) (Membrane 1's feed reference)***

As described in Fig. 3-1, the assumption of the system is Step 1 (a membrane-less microfluidic separation) taking out the blood cells from plasma, thus, reducing the burden for the following membrane filtration steps. However, this blood mimicking solution was made to be the reference case to the filtration performance test with PMS solution (in this case, blood is pumped directly into Membrane 1 without using pre-filtration step: Step 1). The blood mimicking solution (BMS) was simply prepared by blending glycerol (30%) and xanthan gum (0.025 wt.%) in water [261]. To prepare this solution, a xanthan gum powder was sprinkled into glycerol first and then mixed for 20 minutes before adding water to get a homogeneous solution. Xanthan gum was used because it mimics the non-Newtonian characteristic of whole blood (without the cells), matching its density and viscosity and partly reflect the real fouling behavior.

***Uremic Mimicking Solution (UMS) (Membrane 2's feed)***

Since this is Membrane 1's post filtration (filtrate) and Membrane 2's feed (input) solution, the uremic mimicking solution (UMS) includes water, electrolytes, a small concentration of small-size proteins, and importantly, key uremic substances that pass through Membrane 1, including urea, and salts. Since creatinine (116 Da) has molecular weight bigger than urea, it is not mixed in this UMS solution. To investigate the filtration performance of the RO/ MD membrane with different input concentration, several solutions were prepared for the UMS. The synthesis process involved mixing urea powder (U5378, Sigma-Aldrich) with DI water, and then blending this mixture with BSA protein (Miltenyi Biotec) and, if required, sodium chloride (NaCl) (Sigma-Aldrich, USA). The concentrations of urea, protein, and salts were selected based on data from a healthy individual (as baseline reference) and an end-stage kidney failure urea level and several salt concentration levels (as the filtration variables) [262], [263]. The concentrations used for the uremic solutions are listed in Table 3-3.

**Table 3-3. Design criteria for the UMS**

| Types | Uremic mimicking solution | Urea concentration | Salt concentration | Protein concentration |
|---|---|---|---|---|
| **Reference solution** | Urea + Water (a healthy standard reference) | 3.7mmol/L (or 10.4 mg/dL) | 135-145 mEq/L (or 783-841 mg/dL) | 0 |
| **Reference solution** | Urea + Water (Kidney Failure Patient level) | 8-50 mmol/ L (or 48-300 mg/dL) | 135-145 mEq/L (or 783-841 mg/dL) | 0 |
| **Model feed 1** | Urea + Water | 50 mmol/ L (or 3 $g.L^{-1}$ ) | 0 | 0 |
| **Model feed 2** | Urea + Water + NaCl | 50 mmol/ L (or 3 $g.L^{-1}$ ) | 0-140 mEq/L (or 0, 1, 3, 8 g. $L^{-1}$) | 0 |
| **Model feed 3** | Urea + Water + BSA+ NaCl | 50 mmol/ L (or 3 $g.L^{-1}$ ) | 0-140 mEq/L (or 0, 1, 3, 8 g. $L^{-1}$) | 0.45 % v/v |

***Permeability comparison between solutions***

DI (deionized) water was used for permeability testing while the BMS and PMS solutions were used to estimate the filtration efficiency in biological mimicking sample demonstrations (e.g., in Chapter 4 and 6 below). Fig. 3-16B shows the difference in

permeability between different solution tests. The highest permeability was achieved with water (as expected) followed by PMS and BMS, which indicates fouling might occur during these tests. This result also reflects the importance of viscosity and Newtonian/non-Newtonian fluid dynamics in the membrane filtration units. Figure 3-16, depicts characteristic results of the different solutions using gyroid channel and Membrane 1 (PVDF) at a constant flow rate of 90 mL/min.

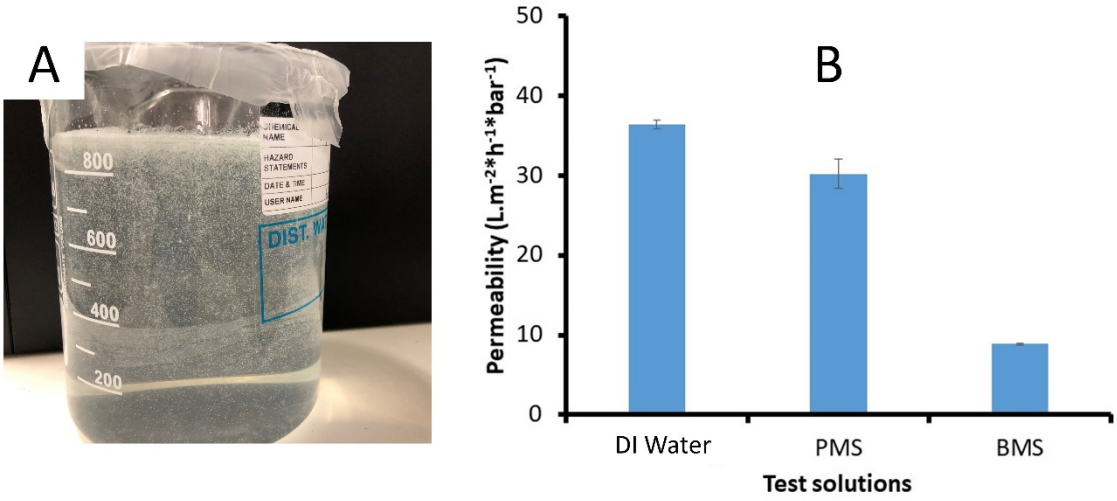


**Figure 3-16. Solution preparation and permeability.** (A) A sample of the blood mimicking solution used in these tests and (B) Membrane 1's permeability results based on solutions.

### 3.3.1 Nanoparticle Concentration and Size Measurement

In order to monitor the size distribution and concentration of permeate solution, we used a microscope equipped with a particle tracking analysis system (e.g., a NanoSight LM14). This instrument takes sequential images of the particles floating in suspension to calculate the particle size based on deviations from Brownian motion (see Fig. 3-17A). To conduct this test, small samples (1-2 mL) of the permeate flow were collected at regular time intervals and compared to the particle concentration and particle size in the feed flow. As shown in Fig. 3-17B, the intensity of different particle sizes was captured. The results were collected from all measurements and shown in the Fig. 4-9 in Chapter 4.

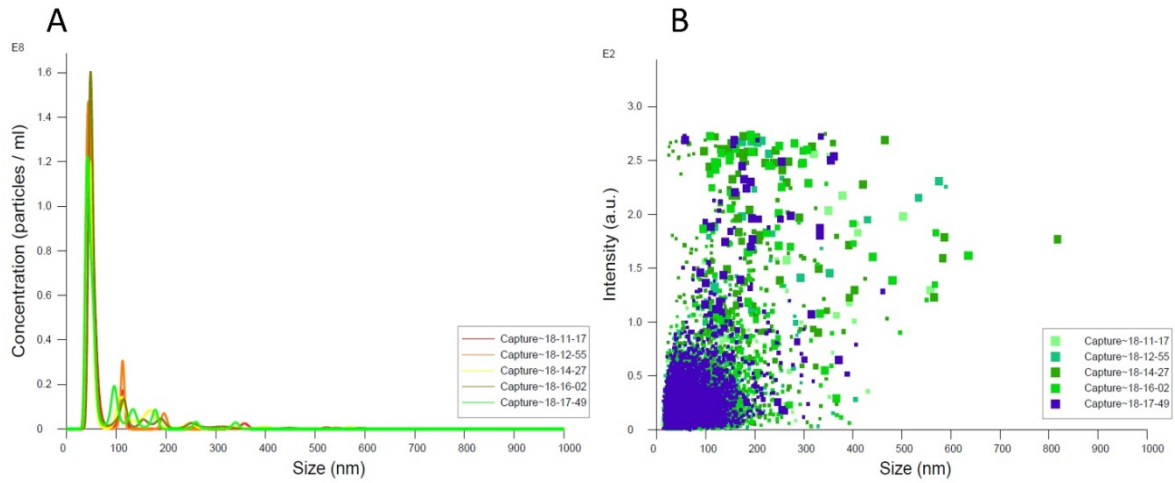


**Figure 3-17. Nanoparticle size and concentration measurement.** (A) Nanoparticle size and concentration, (B) Laser intensity captured with different size of particles

## 3.4 Experimental Setup

With testing platform/ modules had been designed and fabricated, solution and other components had been prepared, the next step was to build the simplest setup for filtration performance tests.

### 3.4.1 Principal System Diagram for a Single-Step Membrane Filtration

The Step 2 and 4 in the proposed system (see Fig. 3-1) involved in the single-step membrane filtrations. The principal setup for each of the filtration step follows a simple diagram as shown as in Figure 3-15.

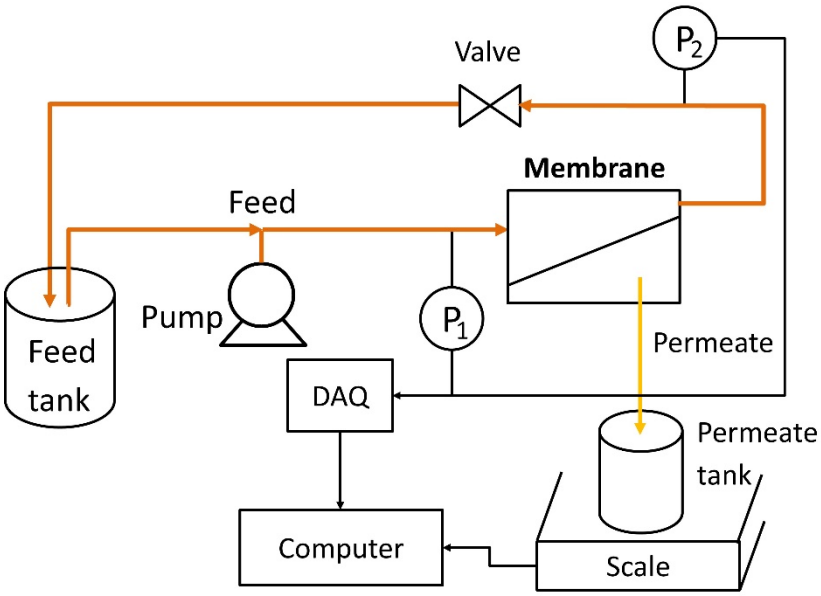


**Figure 3-18. General principal experimental setup for Step 2 and 4**

For each of a typical single-step filtration test, membrane filtration module was connected to a fluidic circuit including feed (inlet) pump, feed and permeate tanks, valve and pressure measurement system (see Fig. 3-18). The pump (e.g., peristaltic, diaphragm) and valves were placed in the fluidic circuit to regulate pressure and flowrate in the system. Depending on the requirement of the inlet pressure and flow, different type of connections and sensors were needed. The pressure was measured at the inlet and the outlet of the membrane housing and was monitored by a data acquisition system (e.g., a National Instruments), connected to a computer running LabVIEW software. The permeate was also measured continuously and recorded through scale software setup in computer. Details for experimental diagram of each test of Step 2 (Membrane 1) and Step 4 (Membrane 2) is presented in the following Chapters 4 and Chapter 6.

### 3.4.2 Membrane 1 Testing

#### 3.4.2.1 Experimental setup

The Membrane 1's experiment setup is shown generally as in Fig. 3-19 and more detail in Fig. 4-3 (Chapter 4), using a peristaltic pump (Thermoline Scientific, WT600-1F, pump

head KZ25, tubing size #35), pressure sensors (OMEGA, Model PX309-050G, with a 0-3.4 bar range), a data acquisition (DAQ) (NI USB-9174) which was connected with a computer, device filtration unit (and its holders/clamps), solution container (beaker), and an electronic balance (to monitor flowrate). The LabVIEW software was used to monitor and record the results of all tests. Measured data were shown on the screen and saved continuously in the computer.

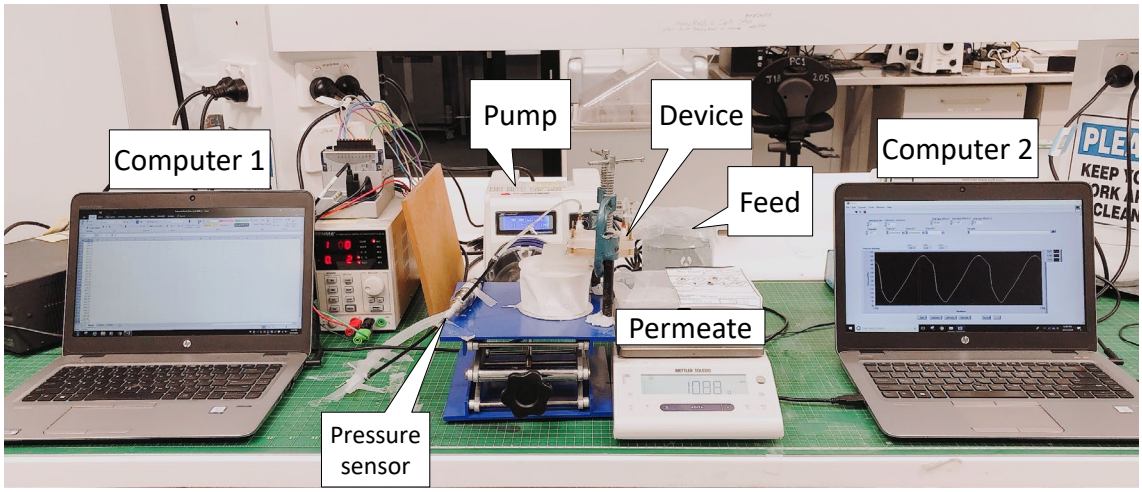


**Figure 3-19. Experimental setup of Membrane 1 filtration test.** The setup includes a peristatic pump, feed and permeate tanks, filtration module, support devices, power supply, a scale connected to computer (1) for auto permeate recoding, and a DAQ for pressure sensors connected to computer (2) for pressure measurement. A barrier (in orange) is used to prevent water splashing into electrical devices.

### 3.4.2.2 Pressure Connections

It should be noted that since Membrane 1 works with pressure lower than 3 bar, plastic tubes and connectors were found to be sufficient to make the connections for the pump, inlet, outlets, and plastic T-connectors for sensors (see Fig. 3-20).

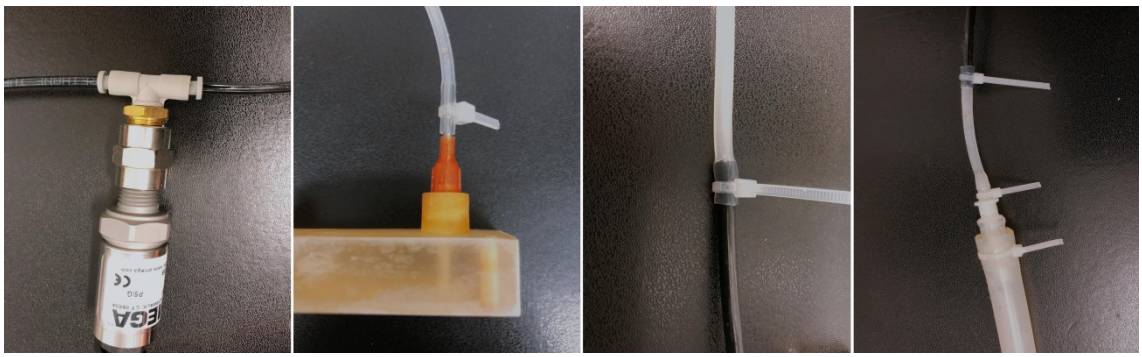

**Figure 3-20. Connections used in Membrane 1 setup**

### 3.4.3 Membrane 2 Testing (RO Membrane module)

#### 3.4.3.1 Experimental Setup

Similar to the Membrane 1 setup, the experiment setup for Membrane 2 also includes a portable electric diaphragm pump (STARFLO FL-200, with maximum pressure of 200 psi at a flow rate of 10 L/min), sensors (OMEGA, Model PX309-150G5V and PX309-100G5V, with maximum 10 bar and 7 bar), valves, a solution container, a balance, and the membrane filtration unit. However, since Membrane 2 with RO membrane requires higher operating pressure, the pump and connections were designed to be more robust. The sensors and the filtration unit were also designed around the higher operating pressure.

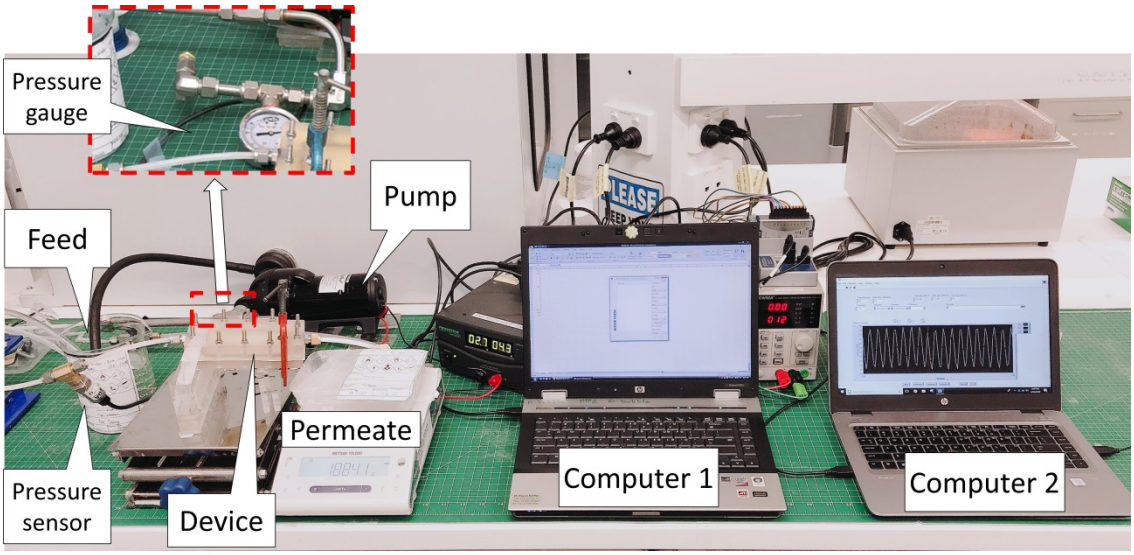


**Figure 3-21. Experimental setup of Membrane 2 filtration with RO membrane module test.** The setup includes a diaphragm pump, 2 power supplies (for pump and for sensors), an additional pressure gauge for safety control, and all other equipment for auto permeate recoding and pressure measurements.

#### 3.4.3.2 Pressure Connections

As mentioned above, Membrane 2 for RO membrane setup is required to work under higher pressures (up to 8 bars), requiring metal connectors with threaded inlets and outlets and an O-ring, as are shown in Fig. 3-22.

**Figure 3-22. Connections used in Membrane 2 setup**

In the case Membrane 2 uses membrane distillation (MD) configurations, the feed side contains low pressure (typically, less than 3 bar [260], [264]). Thus, it is not necessary to have this kind of connectors in the system setup. The experimental setup for MD is described more in details in Chapter 6.2.2.

### 3.4.4 Whole System Setup

The whole system for experimental testing essentially puts the set-up from Membrane 1 and Membrane 2 in series, with the permeate from Membrane 1 (Step 2) going through a Connection part (Step 3) using a one-way microvalve and a pump before being fed into the Membrane 2 (Step 4). In the limited timeframe of this thesis, the connection part was not optimized for continuous integration. Instead, an intermediary permeate tank (filled by the outlet from Membrane 1) was used as the feed inlet for Membrane 2.

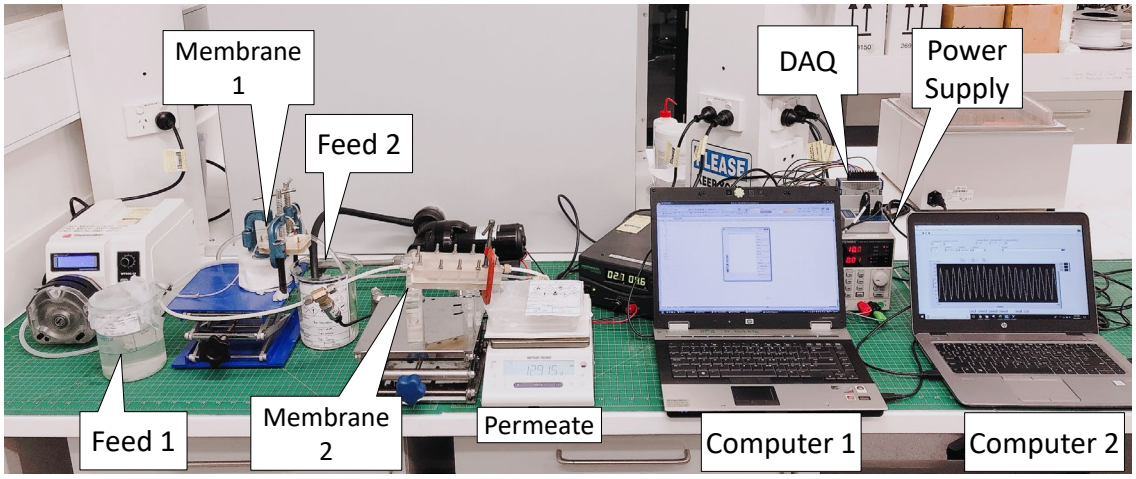


**Figure 3-23. Experimental setup of the whole proposed filtration system.** The setup includes two pumps (for membrane 1 and 2), feed and permeate tanks, membrane 1 and 2 filtration devices, supports, 2 power supplies (for pump and for sensors) and DAQs for pressure sensors, a pressure gauge for safety control, a scale connected to computer (1) for auto permeate recoding; an addition computer (2) for pressure measurements. This setup is for the case Membrane 2 using RO system.

## 3.5 Numerical Calculations

### 3.5.1 Flux and Pressure Analysis

Flux and pressure values are key parameters for the evaluation of filtration efficiency as well as other filtration factors such as effects of utilizing different spacers and channel designs. In this study, measured values of the flow rates, pressure drop, elapsed time, and geometry were used to calculate the flux (J) and permeability ($L_P$) (which is flux/transmembrane pressure) through the membrane with the following equations [12], [248]:

$$J = \frac{V_F}{A \times T_F} \tag{3-1}$$

$$L_P = \frac{V_F}{A \times T_F \times TMP} \tag{3-2}$$

where $V_F$ is the measured volume of the permeate (L), $T_F$ is the filtration time (hour), A is the area of the membrane ($m^2$) and *TMP* is transmembrane pressure (bar). This final term, TMP, can be further broken down to its constituent pressures by using the following equation [12]:

$$TMP = \frac{P_I + P_O}{2} - P_M - \Delta\pi \tag{3-3}$$

where $P_I$ and $P_O$ are the measured feed inlet and outlet pressures, $P_M$ is the permeate side pressure, and Δπ is the osmotic pressure caused by the concentration difference across the membrane [12] (It should be noted that all pressures are reported in Bar in this study for consistency). In our experiment, some of these pressures can be neglected since they are small compared to $P_I$ and $P_O$. Thus, it was assumed that $P_M$~0, $\Delta\pi$~0, which makes *TMP* simplify down to:

$$TMP = \frac{P_I + P_O}{2} \tag{3-4}$$

Further, since permeate pressure was considered to be 0, the pressure drop ($\Delta P$) in the system can also be simplified to:

$$\Delta P = P_I - P_O \tag{3-5}$$

### 3.5.2 Pressure Drop in Membrane 1

In addition to measuring the flux through the membrane under various operational conditions, a key aspect of this work was to identify the net benefit of adding in design features, such as 3D-printed microspacers (as mentioned above). This must account for the additional pressure drop created by the spacers. Since the experimental rig used in this work includes pumps, tubing, and a valve, measure the pressure drop over the actual device is not straight-forward. The fluidic circuit of the ultrafiltration system is represented by diagrams A and B below:

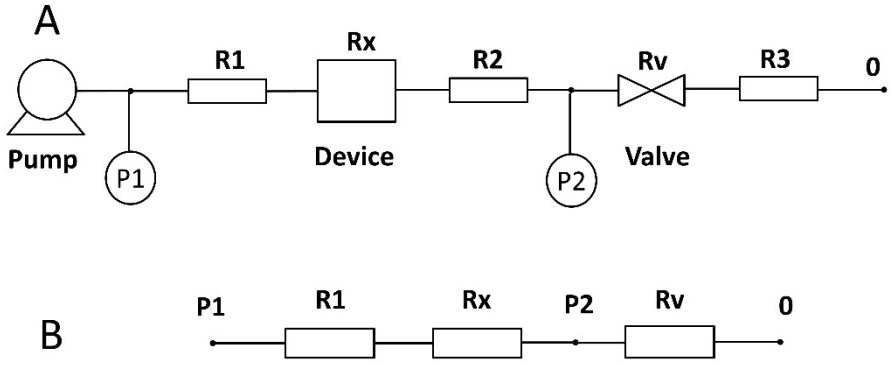


**Figure 3-24. A schematic diagram of pressure drop calculation** (A) Schematic diagram of the experimental set-up of a single filtration unit, (B) Simplified schematic diagram of the Membrane 1's experimental set-up.

In this figure, the circles labelled $P_1$ and $P_2$ represent the pressure sensors. The rectangles labelled $R_1$, $R_2$, $R_3$ are the fluidic resistances of the connection tubes and the

other shapes labelled *Rx* and *Rv* represent the pressure drop of the device (e.g., the value we want to measure) and the pressure drop of the valve.

The pressure drop in the circular cross-section connection tubes can be calculated by a simple theoretical equation (which was implemented in a MATLAB code), which depends on the flow rate and the geometry and using the nominal dimensions listed in Table 3-4 below:

$$\Delta P_1 = Q.R = Q.\frac{8\mu L}{\pi r^2} \tag{3-6}$$

**Table 3-4. Dimensions of the tubing using in the experimental test**

| Channel | Diameter (mm) | Length (cm) |
|---|---|---|
| R1 | 0.9 | 50 |
| | 2.5 | 13 |
| R2 | 2 | 13 |
| | 2.5 | 7 |
| R3 | 2 | 6 |

The pressure drop calculation for the tubing can be simplified as shown in Fig. 3-24B. According to Kirchhoff's law (applied based on the hydraulic-electrical analogy), it is possible to add up the channel resistances since they are in series, which can be written as:

$$\begin{cases} P_1 = \Delta P_1 + \Delta P_x + \Delta P_v \\ P_2 = \Delta P_v \end{cases} \tag{3-7}$$

Therefore, we have:

$$P_1 - P_2 = \Delta P_1 + \Delta P_x$$

$$\text{Or, } \Delta P_x = \Delta P - \Delta P_1 \tag{3-8}$$

That is, the measured total pressure drop ($\Delta P$) (obtained by pressure sensors) contains the pressure drops of the surrounding tubing ($\Delta P_1$), which must be subtracted off to gain the experimental pressure drop on the device ($\Delta P_x$).

### *Pressure Measurement*

As mentioned above the experimental pressures were monitored with sensors and a data acquisition system connected to the LabVIEW software. As shown in Fig. 3-25A(i), the inlet and outlet pressures, depicted with blue and orange lines, respectively, were

obtained with a large number of measurement points (every 3 ms). The zoomed in pressure profile shows the fluctuation of pumping pressure. These wavy curves of pressure profiles are an expected result as using the peristatic pump (see Fig. 3-25A(ii)). In addition, as shown in Fig. 3-25B, the pressure drop had some initial variation, but leveled out after 200 minutes. Thus, for all tests, only the results achieved after 300 minutes were used for the analysis.

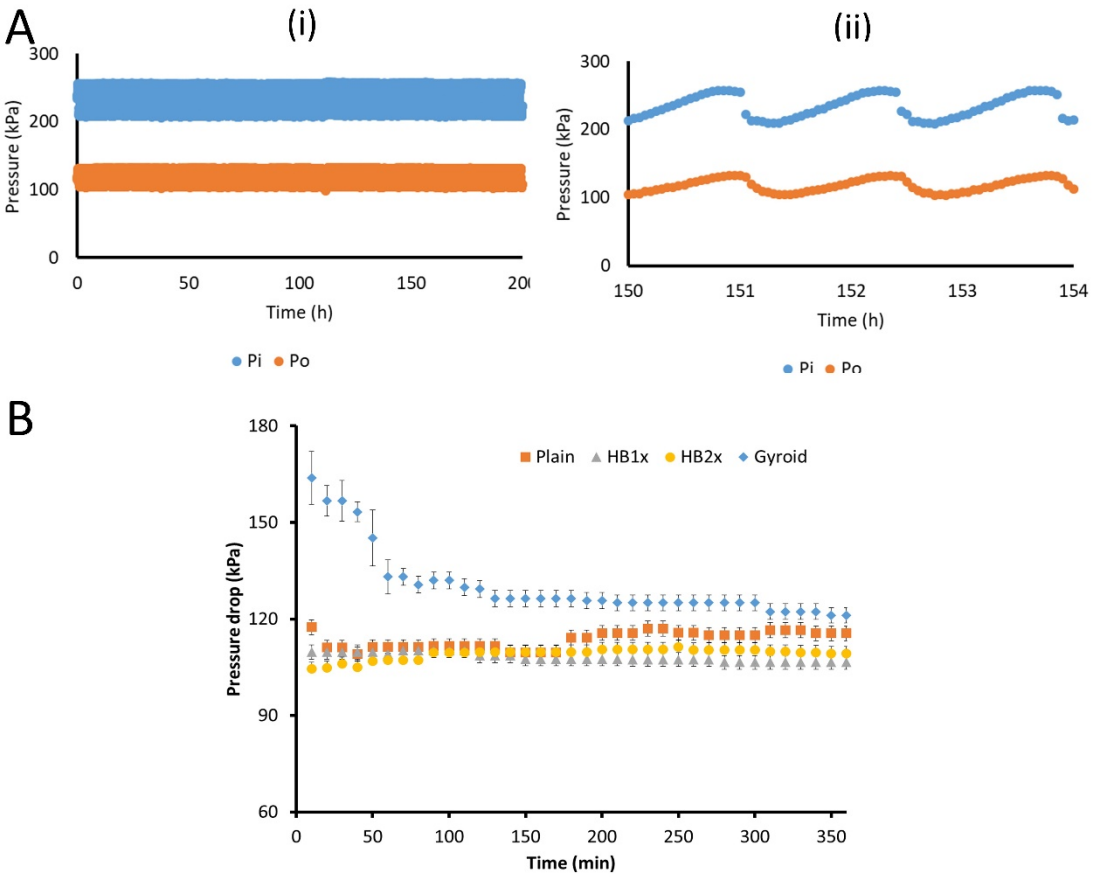


**Figure 3-25. Pressure measurement method. (A)** (i) Inlet (blue) and outlet (orange) pressures, (ii) Inlet and outlet pressure zoomed in profiles; (B) Pressure drop monitor in devices using DI water at flowrate 90 mL/min.

### 3.5.3 Estimation of Concentration Polarization

As mentioned above, concentration polarization is another important parameter to consider for its effect on filtration performance (e.g., a factor which might be mitigated by adding microspacers). According to previous work [265], [266], concentration polarization was reduced with a higher level of wall shear stress on the membrane surface. Theoretically, large molecular particles can be preferentially transported away

from the membrane surface by the shear-induced diffusion while the small molecular substances were transported away by both shear-induced diffusion and by Brownian diffusion [265]. Therefore, the relationship between flux enhancement and concentration polarization can be roughly estimated based on established models.

In these tests, the plasma mimicking solution has a similar viscosity to raw river water (which includes humic substances and small colloids, μ~ 1.2 mPa. s) [265]. Brian et al. established and validated a model using a similar solution to PMS to estimate membrane concentration polarization reduction (e.g., of a similar micropore PVDF membrane to Membrane 1 test) based on the membrane wall shear stress. The relationship between mass transfer coefficient (*k*) with an increasing shear rate was calculated by [265]:

$$k = 2 \times 10^{-7} \gamma^{1.5} \tag{3-9}$$

where ($\gamma$, $s^{-1}$) is the shear rate at the membrane surface.

The next step in this model is to calculated the concentration polarization modulus (*CP*), according to [266]:

$$CP = \frac{C_m - C_p}{C_b - C_p} = \exp\left(\frac{J}{k}\right) \tag{3-10}$$

where $C_m$, $C_b$ are the concentration at the membrane surface and in the bulk solution on the feed side, and $C_p$ is the concentration in the permeate solution.

Pulling these together, the relationship between concentration polarization and shear stress ($\tau = \gamma\mu$, where μ is the viscosity of test fluid (Pa. s)) can be estimated by:

$$CP = \exp\left(\frac{J}{2\times10^{-7}\left(\frac{\tau}{\mu}\right)^{1.5}}\right) \tag{3-11}$$

# 3.6 Membrane Quality Checks in Experiment

## 3.6.1 Membrane Checks

Another key aspect of any membrane filtration study is to investigate any damage done to the membrane during testing. In the present study, the membrane was pulled out of the device and imaged after every 6 hours of testing. This allowed the periodic monitoring of the quality of the membrane by visual inspection and by microscope check (if needed). By managing the clamping forces and the cleanliness of inlet solutions and the spacer designs, little damage was observed to the membrane

throughout the test. The main issues observed (see Fig. 3-26) were related to the clamping, where a good seal with the microchannel was designed to avoid leaking. A smooth, cleaned feed and permeate spacers and channel is also important to keep the membrane at a low damage level.

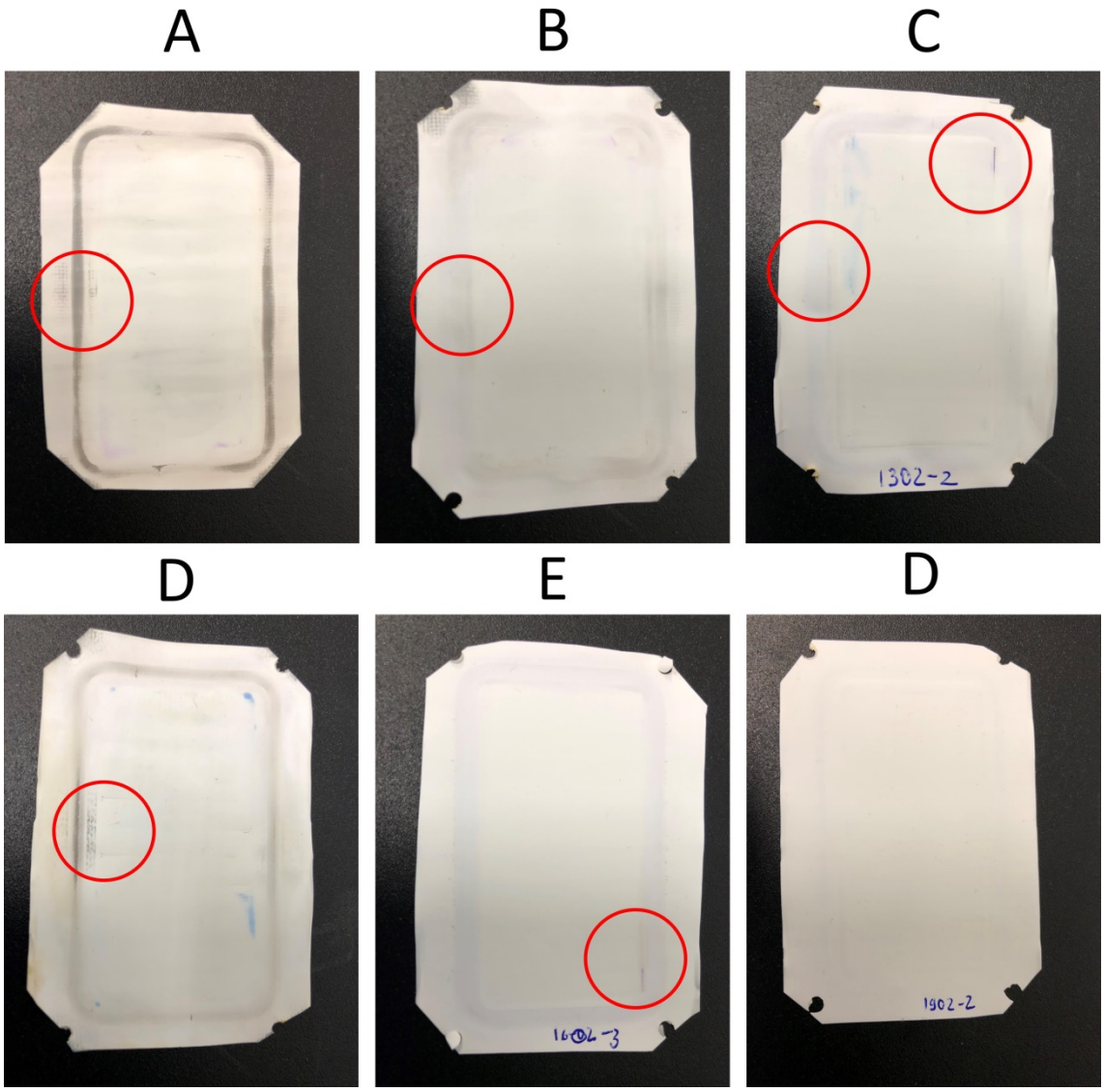


**Figure 3-26. Membrane damage monitoring.** (A) Serious clamping damage. The dark outer squares correspond to the O-ring area, (B) Light clamping damage, (C) Permeate spacer damage with spacer's marks on membrane, (D) Mixed damage type with clamping damage and serious feed spacer's marks on membrane, (E) Light damage due to permeate spacer's edge, (F) a considerable no-damage spacer. The spacers are captured after 6 hours running test.

Surface wettability of the membrane is another important parameter that should be investigated since it can influence flux and fouling resistance of the tested membranes [267]–[269]. Penetration of the feed solution into the membrane pores occurs if the

transmembrane hydrostatic pressure surpasses the liquid entry pressure (LEP) of the pores. Pore wetting leads to either permeate flux reduction (partial pore wetting) or permeate increase with its quality deterioration (full wetting) [269], [270]. When membrane is fully wetted, much higher permeate flux is observed [269], that can fool the result of testing the effect of filtration enhancement methods (e.g. using microspacers).

The LEP of a solution (sometimes incorrectly called “wetting pressure”) is defined based on the Young-Laplace equation (Young, 1807), as [271]:

$$\Delta P = -\frac{2B\gamma_L \cos\theta}{r_{max}} \quad (3\text{-}12)$$

where $B$ is a pore geometry coefficient, $\gamma_L$ is the liquid surface tension, $\vartheta$ is the contact angle (CA) measured on the liquid side, where the liquid-vapor interface meets the membrane surface and $r_{max}$ is the maximum pore size of the membrane.

To study the membrane wettability, the contact angles of the membranes were measured by a contact angle measuring system (e.g., an Attention Theta from Biolin Scientific). Experimental results on membrane wettability of Membrane 1 are shown and discussed in Chapter 4.

## 3.7 CFD Simulation

Computational fluid dynamics was used in this work, but some assumptions are needed including: the flow was assumed to be an incompressible Newtonian liquid; the Navier–Stokes and continuity equations was assumed that it can be applied with the sub-millimeter scale and the results of the CFD simulations in a single channel can represent what happens in the larger filtration unit (a combination of a number of single channels, see 3.7.2 for more details).

### 3.7.1 Governing Equations of Fluid Flow in Microscale Filtration.

The main feature of a microfluidic device is that it has at least one dimension on the microscale. This significantly increases surface area to volume ratio of the fluid environment and the small hydraulic diameter means that these devices are typically in laminar flow, where surface tension and capillary effects dominate. Additionally,

because of their flow areas, even very small suspended particles in a solution can cause partial or complete blockage of the system [272]. The microscale is still much larger than the mean free path of fluid molecules, so continuum simulations should be able to achieve accurate results. As such, in this study the flow was assumed to be an incompressible Newtonian liquid which can be described by the Navier–Stokes and continuity equations as shown in (3-13), and (3-14), respectively,

$$\rho\left(\frac{\partial u}{\partial t} + (u \cdot \nabla)u\right) = f - \nabla p + \mu\nabla^2 u \tag{3-13}$$

$$\nabla \cdot u = 0 \tag{3-14}$$

where $u$ is the velocity vector, $f$ the body force, $\rho$ the density of the fluid, $p$ the pressure, $t$ the time, and $\mu$ the dynamic viscosity of the fluid. The basic phenomenon of mixing was assumed to be described by the convection–diffusion equation [272]:

$$\frac{\partial c}{\partial t} + (u \cdot \nabla)c = D\nabla^2 c \tag{3-15}$$

where c is the species concentration and D is the diffusion coefficient.

### 3.7.2 CFD Modelling Assumptions

#### 3.7.2.1 Model of the Whole Device (feed-side)

The channel designs were built in the CAD program Solidworks 2017 (Dassault Systèmes) with the microspacers integrated in the feed channel as single components. The membrane was located on top of the spacer-integrated channels. The fluid domains for CFD were then subtracted from the CAD designs. Initially, the CFD models were processed with the whole device design (which included 11 similar channel components, flowing in series). The CFD model's membrane surface was considered the bottom wall of the fluid domains. The initial results for the whole filtration device used in Chapter 4 are captured in the Fig. 3-27 below (for the case of herringbone HB1x channel design):

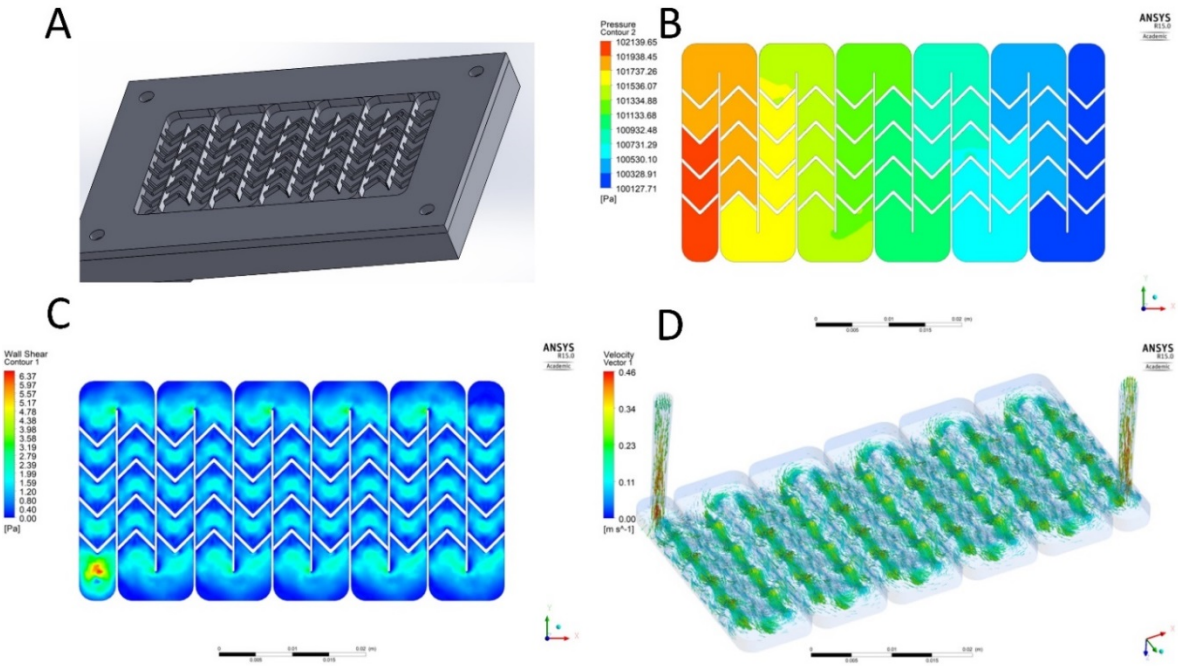


**Figure 3-27. CFD models for whole channel.** (A) CAD design of spacer-integrated microfiltration unit (feed side), (B) Pressure drop along the whole channel, (C) Wall shear stress on membrane surface, (D) 3D velocity profile.

However, due to the complexity of the spacer designs and the microscale details of the spacer-integrated channels, especially the gyroid (as shown in Fig. 3-10B and C), the number of elements required for a good mesh (generated and checked in ICEM CFD 19.1) can go much more than 20 million as estimated through trials. Therefore, it was decided to simplify complex CFD model into single channel fluidic component of each design as can be seen in Fig. 3-28 below.

### 3.7.2.2 Model of the Single Channel (Feed-side)

Fluidic domains (after being extracted from the spacer-integrated feed-side of the filtration unit) were cut into single channels to be the input geometries for CFD using Autodesk Netfabb Premium 2019, as shown in Fig. 3-28.

The meshes were developed (using ICEM CFD 19.1) up to 3 million elements (for a single gyroid channel). The CFD models then were matched with experimental flow rate condition with considering the pressure drop value. CFD cases were running in ANSYS (Ansys, Inc.) using high-performance computers. Each case took around 60-120 minutes to run, using a high-performance computing (HPC) cluster with 8 x 2.6 GHz

Intel(R) Xeon(R) E5-2670 v2 processors, 30GB memory. Details about CFD results including 3D velocity, shear stress on the membrane surface and grid convergence in the present of microspacers are discussed in Chapter 4.

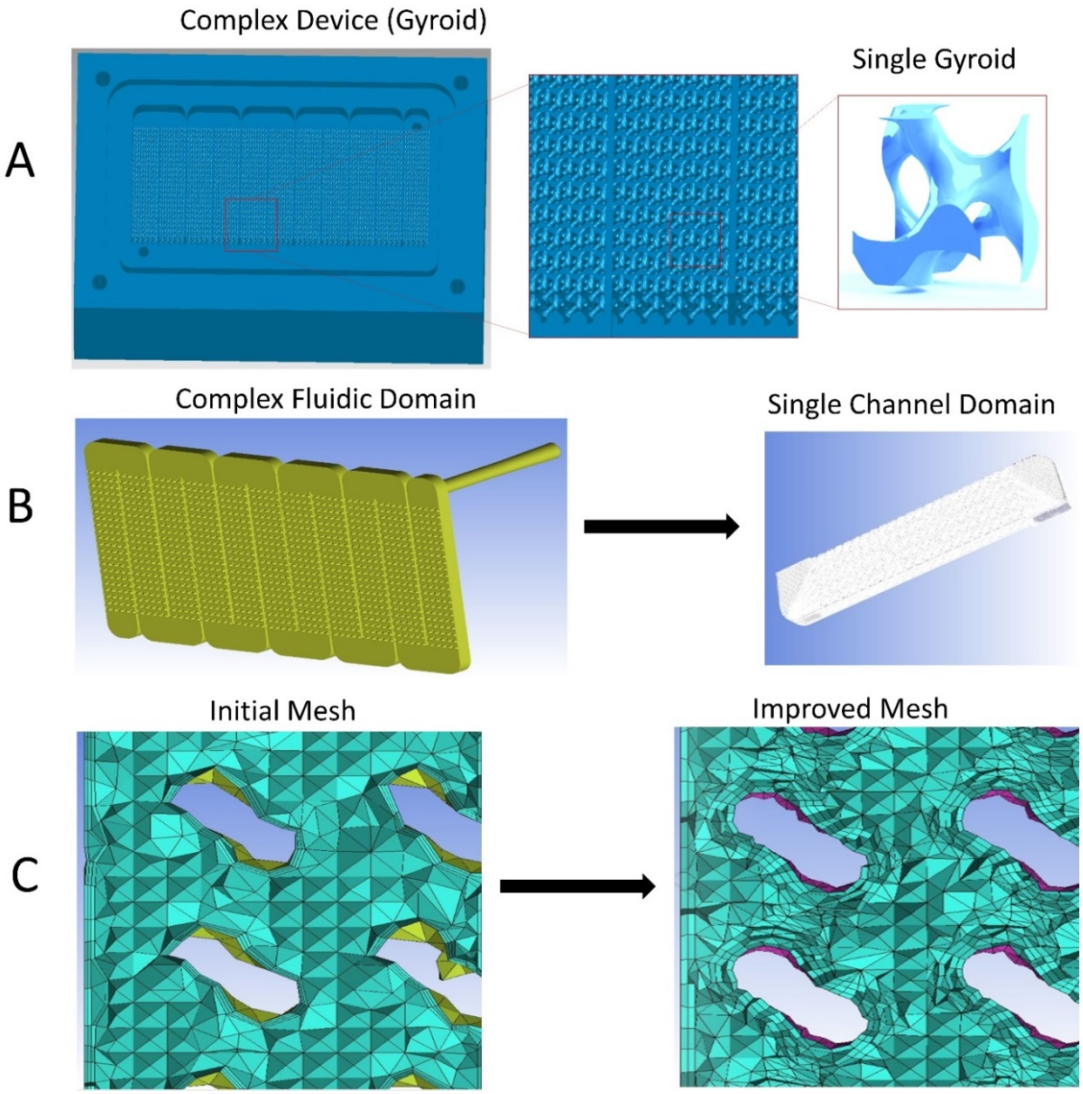


**Figure 3-28. CFD models using single channels.** (A) CAD design of gyroid spacer and its integration into feed channel in a microfiltration unit, (B) Making a single channel model from 11-repetitive-channel CAD design, (C) Mesh development in a single channel model.

### 3.7.3 Mesh Independence Study

A mesh independence study was conducted to confirm the mesh quality provides the required accuracy.

As shown in Fig. 3-29, the number of elements over $3 \times 10^5$ is enough for the study. In our manuscript, ~$5 \times 10^5$ elements were used for the HB1x spacer which is certainly

enough elements for a good mesh. The mesh-independent number of elements for selected for the different spacers designs is shown in Table 3-5:

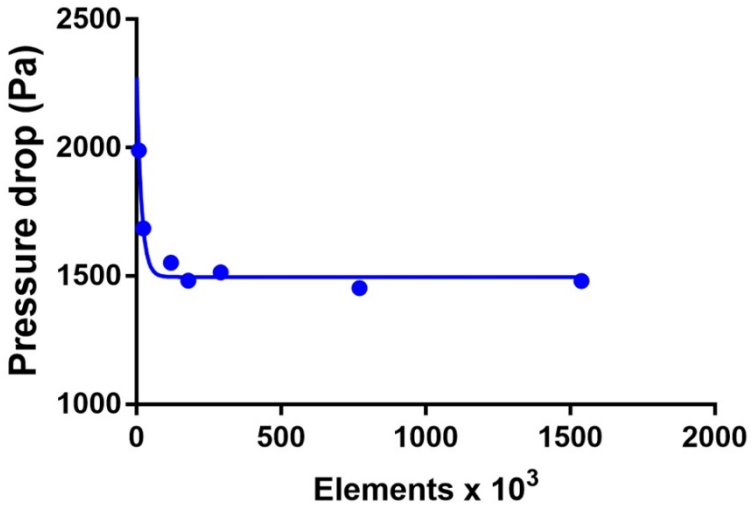


**Figure 3-29. Mesh independence study (for the HB1x spacer).**

**Table 3-5. Number of elements used**

| Spacer types | Elements |
|---|---|
| Plain | 198668 |
| HB1x | 467073 |
| HB2x | 1379679 |
| Gyroid | 2544879 |

### 3.7.4 Iterative Convergence Study

An iterative convergence study was conducted to confirm specified level of residual error provided an appropriate level of accuracy. The parameters of interest were monitored including wall shear stress on membrane surface and pressure drop in the channels. Figures 3-30A and 3-30B demonstrate that 300 iterations of equation solution are enough to gain stable values for wall shear stress and pressure drop (data for gyroid), within 1.15 % and 1.33% difference, respectively. In addition, as shown in Fig. 3-30C, upon further simulation, the number of iterations needed to achieve the smallest residuals error of continuity condition, and x, y and z velocity was determined at around 1000.

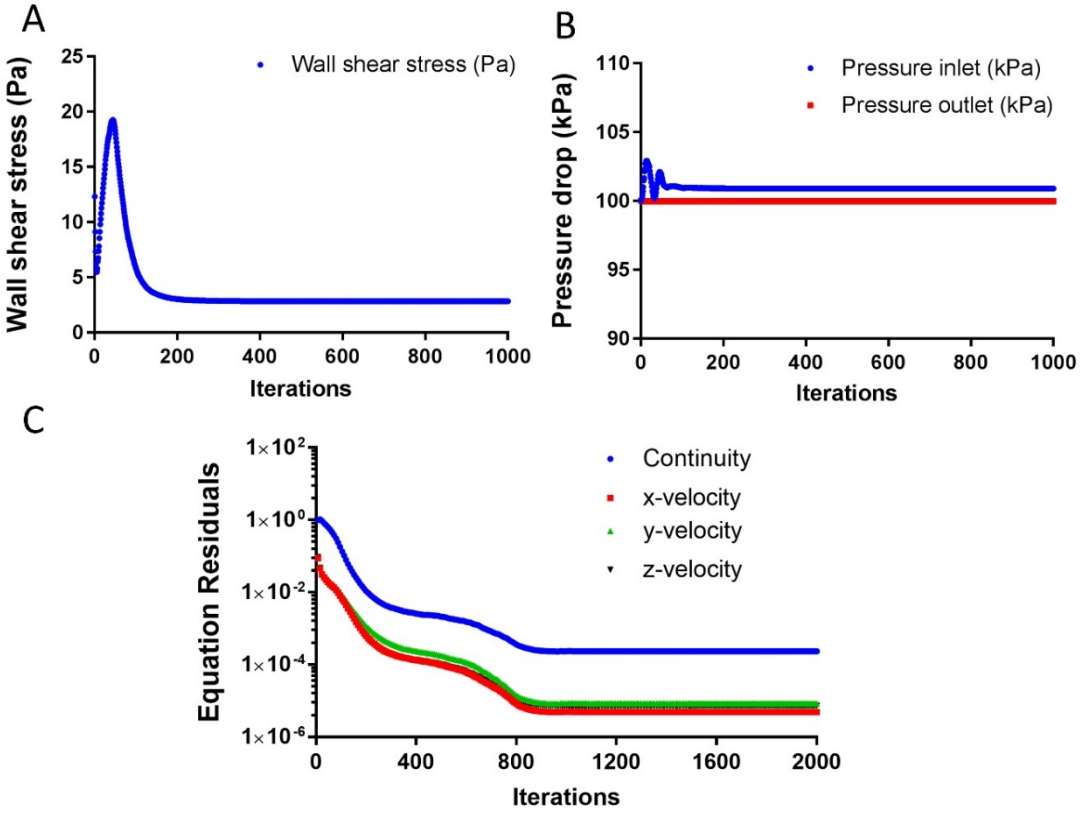


**Figure 3-30. Iterative Convergence Study** (Data with Gyroid spacer, single channel, total elements is ~ 2.5 million). (A) Wall shear stress convergence study, (B) Pressure drop, (C) Continuity, and x, y and z velocities

## 3.8 Chapter Summary

This Chapter discussed the system designs approach and the fabrication methods, materials, and experimental and simulation methods for each step of the proposed filtration system. The further improvements are needed overall for 3D printing quality, materials and membrane selections, etc. For example, later study on human plasma needs to adjust more carefully the membrane selection depending on the amount of biological components inside the fluid (e.g. Membrane 2's feed has no blood cells and protein concentration compared to the amounts in Membrane 1's feed).

In the following chapters, detailed analysis and results will be presented. In particular, Chapter 4 will present the full experimental analysis of how the Membrane 1 designs perform as the first Step of a portable, artificial hemofiltration system.

# Chapter 4

# Membrane 1: A Study on Effect of Spacer in Microscale Hemofiltration

## Chapter Overview

*Despite their ubiquitous use in large-scale filtration processes, the benefits – if any - of adding spacers on microscale filtration units remain unknown. At larger scales, spacers improve performance by directing the flow and inducing turbulent mixing. However, at low Reynolds numbers, it becomes increasingly difficult to initiate mixing because viscous forces dominate over inertial forces. In general membrane filtration applications, concentration polarization and membrane fouling can severely limit filtration efficiency, and even a small amount of fluid mixing presents the potential to mitigate these issues. In this study, three complex 3D-printed microspacer designs (with feature sizes in the range of 100~400 µm) were incorporated into narrow channels, to determine their enhancement effects for artificial kidney filtration applications.*

*This study is a bridge between current non-spacer hemodialysis filtration and future 3D glomerulus-like membranes. The focus is on analyzing how fluid flow acts inside a complex 3D structure which mimics the flow structure in a glomerulus. The results suggest the possible advantages of the development of 3D printed membranes for future artificial kidneys.*

*Note: The content in this chapter has been published with the journal, Separation and Purification Technology;* ***Dang, B.V.****; Charlton, A.J.; Li, Q.; Kim, Y.C.; Taylor, R.A.; Le-Clech,*

*P.; Barber, T., 'Can 3D-printed spacers improve filtration at the microscale?', Separation and Purification Technology, 256, 117776 - 117776 (2020). http://dx.doi.org/10.1016/j.seppur.2020.117776.*

## 4.1 Introduction

Traditional microfluidics devices are 2D in nature due to the manufacturing techniques available. However, recent processes (such as 3D printing) are enabling new capabilities in microfluidic applications, by providing a pathway for the manufacture of complex, 3D geometries. Thus, 3D-printed structures can potentially allow microfluidic devices to incorporate 3D physical forces, such as shear stress, mixing, and complex liquid manipulation. These forces might also be utilized to benefit organ-on-a-chip platforms [273], [274], digital logic circuits [143], [275], [276], electro-assisted microchips [277], [278], multiplexed biosensing devices [19], and other complex on-chip architectures [17], [80], [272], [279] and can provide beneficial effects for microfluidic-based filtration applications such as serum separation [280] or protein separation [130], [281]. With respect to the present study, 3D-printed structures may allow for more fluid interaction with membranes, for a microfluidic-based portable artificial kidney devices [13], [75], [76], [282].

In a general microfluidic-based filtration unit, a membrane is incorporated in the middle layer of a multi-layer structure with top and/or bottom microfluidic channels. Micro-scale filtration devices, however, have seen little research and development uptake, due to their relatively low throughput, permeate flowrate (or flux), and filtration efficiency [283]. As a recent example, To et al.[12] reported a multi-layered microdialysis system which had a permeate flow rate of ~0.2 $mL.h^{-1}$ (over 5 hours) and filtration coefficient less than 70 $mL/ m^2$. h.mmHg. Similarly, Sakuta et al. [128] utilized a microfluidic system that allows only 2.1 $mL.h^{-1}$ input flowrate for 35$mm^2$ while using a 12-14 kDa molecular cut-off hemodialysis membrane. In another example, a nanoporous membrane device developed by Fan et al. [79] was also reported to have an input flowrate of just around 8 $mL.h^{-1}$. At these low flow rates, two major underlying factors can conspire to limit the performance of membrane filtration: concentration polarization and fouling. Concentration polarization occurs when the fluid near the membrane has a significantly higher concentration than the bulk fluid. In the extreme, concentration polarization can completely shut off the flux through the membrane [284]. Membrane fouling occurs when particles adhere to the membrane, increasing the resistance to flow through the membrane.

In the case of a microfluidic-based filtration device, the lack of mixing in the laminar flow regime amplifies these problems. As such, several researchers have reported progressively lower flux, solute permeability, and detrimental changes in selectivity over time with microfluidic membrane filtration designs [12], [21], [128]. In addition, on this small scale, microfluidic systems are particularly sensitive to particle deposition and blockage due to their small channel size [272]. Unlike macro-scale filtration units, it is challenging to create mixing through increasing the flow rate, due to the fact that PDMS-based micro-scale filtration units have a fixed allowable strength owing to the bonding between the device (PDMS) layers. If this pressure limit is exceeded, a microfluidic device may leak or burst (as can be seen in a failed initial experiment in Fig. 3-9 in Chapter 3).

On the macro-scale, membrane systems usually employ spacers to improve flux and filtration efficiency [248], [285]. A feed spacer, or netting, provides better fluid management at the membrane surface [254] because it controls concentration polarization and flux and influences energy input [286]. Feed-side spacers are often used in flat-sheet modules and are essential in spiral-wound designs [287], [288] because they define the height of the feed channel while promoting mass transfer.

The benefits of the spacer are not free—there is a trade-off between flux improvement and energy input. Spacers increase the pressure drop of the design, which raises pumping power and the structural requirements of the system. Thus, *optimally* designed feed spacer geometries can help to reduce fouling and increase filtration efficiency without an excessive increase to the system pressure drop or its capital and operational costs [248], [289]. As an example, research has shown that by using spacers in reverse osmosis systems for purifying brackish water, the permeate flux can be improved by up to 23% at the expense of only slightly higher pumping energy, 5–7% [290], for a benefit to cost percentage ratio of ~4.

In recent years, additive manufacturing (i.e., 3D-printing) technology has emerged as a rapid and cost-effective method for fabricating complex components, including spacers for macro-scale membrane systems [251], [291]–[293]. Several 3D-printed feed spacer geometries have been demonstrated, including herringbones, ladders, helical structures [294], [295], twisted tapes, filaments and multi-layer designs [296].

Although resolution and quality of 3D printed parts remains an issue, the spacers, which are designed to better control 3D flow field, have been reported to show at least as good performance as commercially manufactured spacers (which are typically 2D) [297]. Numerical simulations have shown that the mass transfer enhancement of 3D-printed spacers (for spiral wound membrane modules) can overcome their conventional 2D counterparts due to the increased wall shear perpendicular to the bulk flow and streamwise vortices [298]–[300].

While some of these designs have been implemented in narrow channels (i.e., sub-millimetre) [301], [302], no reports have examined how microscale spacers effect fluid mixing and fluid management. At the micro-scale [272], the Reynold number is small ($Re < 800$) and complex 3D-spacers may not be enough to disturb the viscous laminar flow to create recirculation/advection zones. Further, since microfluidic systems have pressure limitations, it is unclear if added back pressure can result in potential flux enhancement beyond the leak/burst pressure of a microfluidic device.

To systematically investigate these questions, three different 3D-printed microspacers within Membrane 1's microfluidic-based filtration system were designed, fabricated, tested, and simulated. As such, the relative benefit of these designs in terms of their potential was experimentally examined for improvement on fluid management, flux, fouling and other parameters (shear stress on membrane, selectivity and pressure loss) with respect to Membrane 1's filtration. The designs under consideration were two herringbone structures (of different feature sizes) and a triply period minimal surface (i.e., a gyroid). These designs were chosen because they have been used in passive microfluidic mixers [303], [304] and/or as spacers in macro-scale filtration devices [255], [305]–[307]. Since their geometry is to be very small to match the narrow channels scale, advanced 3D-printing, with a resolution of 12.5 µm, was employed. Further, the spacer's ability to filter blood mimicking solution (BMS) and a plasma mimicking solution (PMS) [78], [261], [308] has been tested and proved by flux performances. Since the input solution for Membrane 1 filtration is mainly plasma solution, BMS solution is considered as a reference for studying filtration performance of PMS solution here. By conducting tests with these fluids, the extent of biofouling caused by protein adsorption was also analyzed. Thus, a selectivity test was also

conducted with the use of nanoparticles at 50-100nm to mimic a protein separation process.

In brief, the aims of these tests in this chapter are to: (1) Examine the capability of 3D-printing and integrating microspacers into microfluidic-based filtration (SMF) (or Membrane 1) units; (2) Understand the effect of such spacers and determine the trade-off between the flux enhancement and energy input at the microscale; (3) Test their biological feasibility for kidney filtration application (e.g., filtration efficiency and fouling reduction with BMS/PMS).

## 4.2 Theory

### 4.2.1 Membrane Fouling of Biological Sample at the Micro-scale

Membrane fouling is a complex process and not well understood for general flow cells or in SMF units [272]. Although fouling is influenced by the surface physico-chemical characteristics of the membrane (e.g. hydrophobic-hydrophilic properties, microstructure and morphology of the surface), much of the performance degradation over time can be attributed to factors which are influenced by fluid flow (e.g. concentration polarization, cell and protein adsorption, and a few other key factors) [309], [310]. Concentration polarization occurs when a higher concentration of ions, particles, cells, or proteins accumulate near the membrane surface. Concentration polarization generally leads to higher fouling rates because of the increased deposition rate on or inside the membrane.

Membrane fouling in biofiltration processes (such as hemofiltration) can be attributed—in large part—to protein adsorption on the membrane surface [281]. The adsorption of proteins on artificial surfaces represents the initial step in a sequence of events (e.g. coagulation activation) which can naturally result in blood clot formation [310]. If the artificial surface is a membrane, even a small amount of protein adsorption can increase osmotic pressure and add hydraulic resistance to the flow [309]. On the scale of the proposed microfluidic-based filtration system, concentration polarization and fouling can eventually clog the channels [272].

### 4.2.2 Fluid Flow Behavior in Spacer-integrated Filtration Units

In large scale filtration units, as can be seen in Fig. 3-11, a conventional spacer module directs a portion of the flow to change direction, thereby inducing mixing (see the Chapter 3.2.3 for more details). This action effectively reduces concentration polarization and membrane fouling. The chapter is an investigation of whether these - or analogous - effects are still possible and beneficial at the micro-scale?

The design of a plain non-spacer channel (A) versus a filled-spacer in microfluidic channels (B, C) is depicted in Fig. 4-1 below.

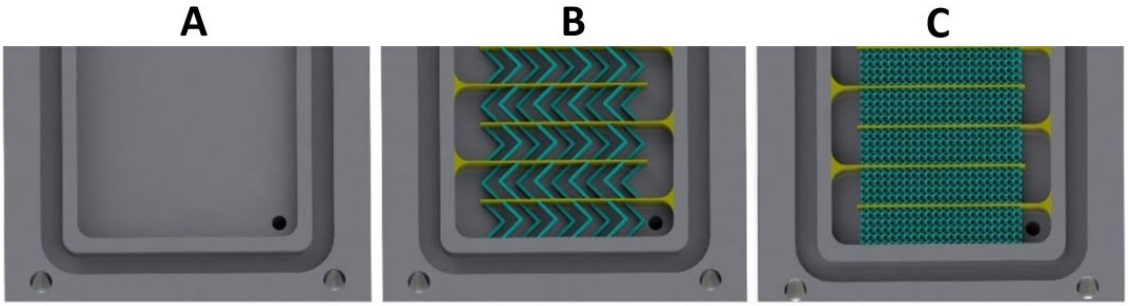


**Figure 4-1: Spacer in microfluidic channels.** (A) Non-spacer channel, (B) Herringbone-filled channel and (C) Gyroid-filled channel.

Figure 4-2 below shows the proposed designs and corresponding predictions of fluid flow directions in the narrow channels with and without using a spacer. On one hand, since the Reynold number is low (< 800 in the plain channel and even lower in the spacer-integrated designs), it is unlikely that much fluid mixing will occur. However, on the other hand, since the flow will be forced to have more turns, especially with the Z-direction-component (towards the membrane and perpendicular to the axis of flow), there should be more fluid interaction with the membrane. Thus, as the 3D printed microspacers will create a more complex 3D flow, it is hypothesized that a net benefit may still be possible.

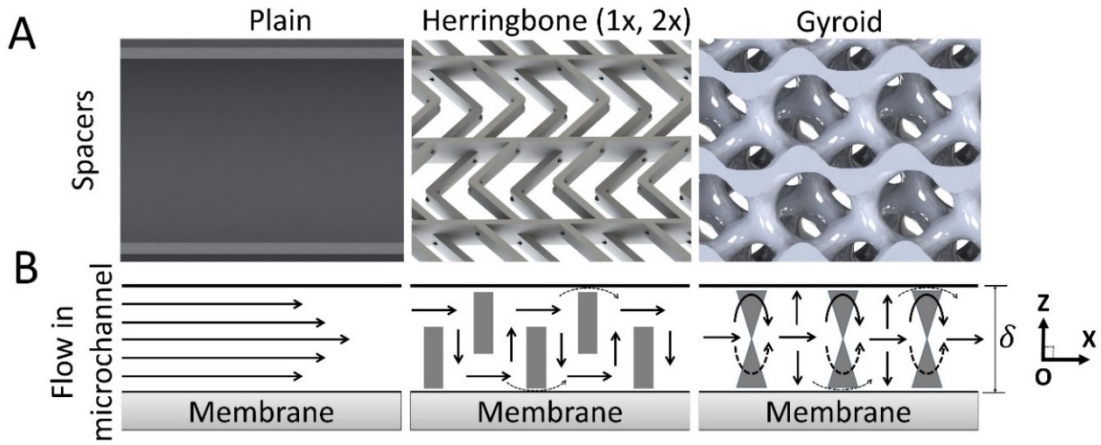


**Figure 4-2: The concept of using of microspacers in microfluidic-based filtration.** (A) Spacer CAD designs including plain, herringbones and gyroid, (B) Prediction of microspacer's effects in laminar flow management.

## 4.3 Methods

### 4.3.1 Experimental Setup

As discussed in detail in Chapter 3.2 and 3.5, to test the effect of spacers, a simple three-layer structure microfiltration unit was used for our experiments (see Fig. 4-3A(i)). The flow units include a feed flow inlet (top) and permeate (bottom) and concentrate (top) outlets and a flat-sheet membrane (PVDF) is used to separate the two outlet flows. As mentioned above, 3D-printed spacer designs were investigated in this study and compared to a plain channel. Two herringbones (denoted 'HB1x' and 'HB2x', with a feature size of ~400 µm and interval spaces of ~1200 and 400 µm, respectively) and a gyroid structure (denoted 'gyroid', with minimum feature of ~100 µm) were integrated into the narrow serpentine-shape feed-side channel ($W_C$=5mm, $H_C$= 2mm, $L_C$=30mm) via 3D-printing, as three spacer-channel components. An O-ring was incorporated into the designed arrays to prevent leaking in the filtration process.

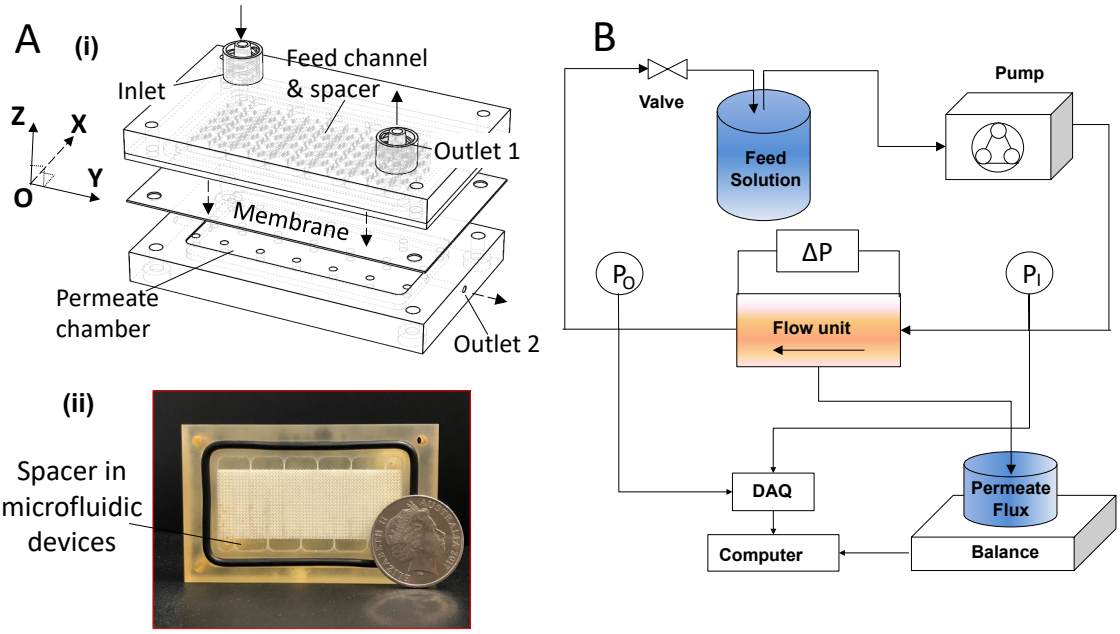


**Figure 4-3: Details Membrane 1 device setup.** (A) (i) 3D structure of a micro-scale filtration unit, (ii) Spacer_integrated microfluidic filtration unit (SMF); (B) Details of the experimental setup.

As shown in Fig. 4-3A(i), a membrane with a filtration area of 3 cm × 5.8 cm (e.g., a flat PVDF membrane from Durapore®, with an average pore size of 0.22 µm) was utilized as the middle layer of the SMF unit. The SMF unit consists of the top layer (the spacer-integrated narrow feed channel) and the bottom layer (permeate chamber). Fig 4-3A(ii) shows the image of the 3D-printed top layer alone with the spacer integrated into microfluidic channels. As shown in Fig. 4-3B, a peristaltic pump (Thermoline Scientific, WT600-1F, pump head KZ25, tubing size #35) was used to circulate the feed solution through the filtration unit. The inlet and outlet pressures, $P_I$ and $P_O$, respectively, were measured by two pressure gauge sensors (OMEGA, Model PX309-050G, with a 0-3.4 bar range, connected to a National Instruments NI USB-9174 Digital I/O device and LabVIEW software). The permeate flux was measured by weighing the permeate-side outlet liquid with an electronic balance (Ohaus PA2102C, with a resolution of 0.01mg). A permeability test was done for 10 hours, with mass measurements every 30 minutes, to check the operational permeability of the membrane. To prepare for fouling tests, new membranes were put in the device while running with water at TMP 1 bar for 30 minutes and left for about 8 hours overnight. The filtration performance (also, fouling propensity) tests were then conducted for each design in which the designs were

exposed to 6 and/or 30 hours of flow with permeate weights recorded at 10-minute intervals.

### 4.3.2 Simulation

To demonstrate the fluid flow behavior occurs as suggested in Fig4.2B, a simulation on ANSYS Fluent 19.1 was carried out with these geometries, under the same pressure and flow conditions used in the PMS solution experiment. The computational fluid dynamics (CFD) models of the devices were simplified from the original designs with the repetitive serpentine shapes of 11 channels, by using a single channel unit cut from the designs. As shown in detail in Fig. 4-10 below, the CFD results for shear stress on the membrane surface and 3D velocity inside spacer-integrated models were compared. Details about simulation governing equations, assumptions and methods are in Chapter 3.7.

## 4.4 Results and Discussion

The performance of the microspacer designs was determined through four experimental studies: (1) A permeability test using deionized water; (2) A flux and pressure drop test with different flowrates using the PMS solution; (3) Filtration performance experiments with both the BMS and PMS solutions; and (4) A selectivity test using nanoparticles in the PMS solution. All of these tests were completed with all three spacer designs and compared to the plain channel as a reference (under the same operational conditions).

### 4.4.1 Characterization of the 3D-print Microspacers

Figure 4-4 shows the fabrication accuracy in the 3D-printed products using the multi-jet printer, compared to the CAD design references. In each case, the printed spacers' size is slightly larger than specified in the design. Fig 4-4A shows the CAD models of each spacer along with the microscope images of the 3D-printed spacers. With features at around 100µm or lower, there is a clear difference between the printed device and its

3D design, which reflects the fact that the 3D printing resolution is not as high as stated by the manufacturer (e.g, 16 µm minimum layer thickness for ProJet® 3500 HD Max). Fig. 4-4A(ii) shows the discrepancies of the 3D-printed features when compared to the designs (Fig. 4-4A(i)) for the gyroid microspacer. The bigger feature than design of 3D-printed microspacer, the smaller voidage/free space for water to travel through it. This will lead to higher-than-expected fluidic resistance and a higher pressure drop than the theoretical value. The average surface roughness of the 3D-printed spacers is in the range Ra (5-30 µm) (details are shown in Fig. 3-14), which may also cause some protein adhesion to the spacers.

As shown in Fig. 4-4B(i), the deviations of 3.7% and 8.3% were observed for the HB1x, HB2x, respectively. These measurements were conducted using top-view microscope images (see Fig. 4-4B(ii)). With the gyroid design, the complexity and the size of the features resulted in a much higher deviation, up to 39.1%. With the rapid development of printing resolution [292], [311], however, it is likely that it will soon be possible to print geometries at this scale with much higher accuracy.

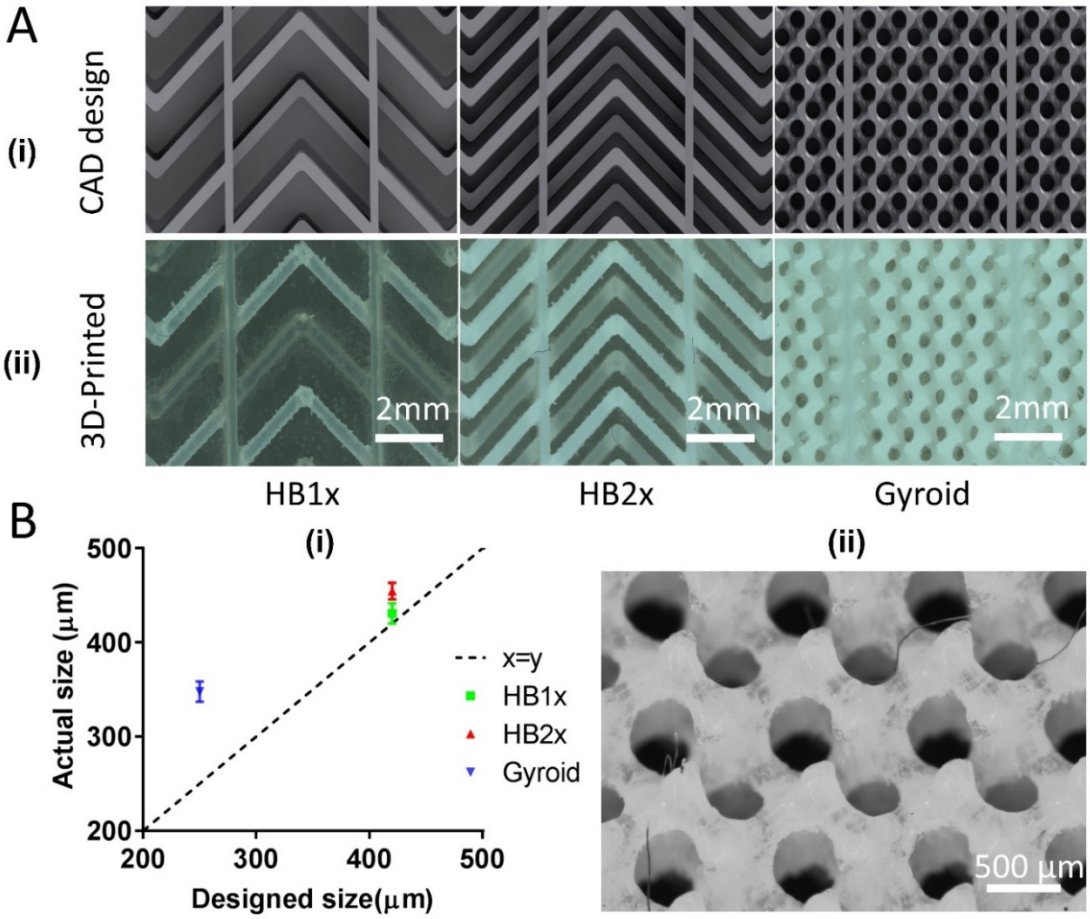


**Figure 4-4: 3D printed spacer fabrication accuracy.** (A) (i) CAD design and (ii) actual 3D-printed spacers; (B) (i) Deviation of actual 3D-printed spacers compared to designed sizes, (ii) 3D-printed gyroid structure under the microscope.

### 4.4.2 Flux Enhancement vs Energy Input

In order to understand the trade-off of adding 3D printed microspacers into narrow channels of the Membrane 1 filtration part, flux and pressure drop versus flow rate measurements were carried out for all the spacers. The feed side pressure drop represents the hydraulic resistance to flow and a parameter to be minimized in the design. As shown in the left Y-axis of Fig. 4-5, the pressure drop was found to be nearly a linear function of average flow rates. That is, as the feed flow rate increases, the corresponding pressure drop increases. For an average flowrate commonly used in the hemofiltration applications [12], [76], i.e. Q=100 mL.min$^{-1}$, the plain channel was found to have a pressure drop equal to 53.6 kPa. For the microspacers, the pressure drop values at this flow rate increased to 58.6, 59.4 and 66.9 kPa for the HB1x, HB2x and gyroid designs, respectively.

In comparison, the permeate flux represents the vertical flow or filtration capacity. As can be seen in the right Y-axis of Fig. 4-5, at the same flow rate Q=100 mL.min$^{-1}$, the plain channel achieved lowest permeate flux at about 14.4 Lm$^{-2}$.h$^{-1}$. This was enhanced considerably by the spacer-integrated designs to 29.6, 33.3 and 37.1 Lm$^{-2}$.h$^{-1}$ for the HB1x, HB2x and gyroid, respectively.

As expected, there is a clear trade-off between flux improvement and flow resistance. For the gyroid, the pressure drop exhibited a ~23% increase compared to the plain channel, followed by HB2x and HB1x units with ~10% and ~6% increase, respectively. Importantly, the benefit to the cost percentage ratio, which is the % enhancement in the flux divided by the % increase in the pressure drop, was 8.5, 7 and 4 for HB1x, HB2x and gyroid with PMS solution, respectively. This demonstrates the intrinsic limitation of spacer integration into the channel: the more complex spacer used, the greater the cost of the energy input. However, as long as the pressure drop is well-below the leak or burst pressure of the device, this increase can be considered as an incremental increase in the pumping power requirements for operation (which are typically negligible). In the designs presented here, the optimal range for operation of input flowrate for the gyroid spacer should be in the range of 110-120 mL.min$^{-1}$ (as highlighted by the blue region in Fig. 4-5).

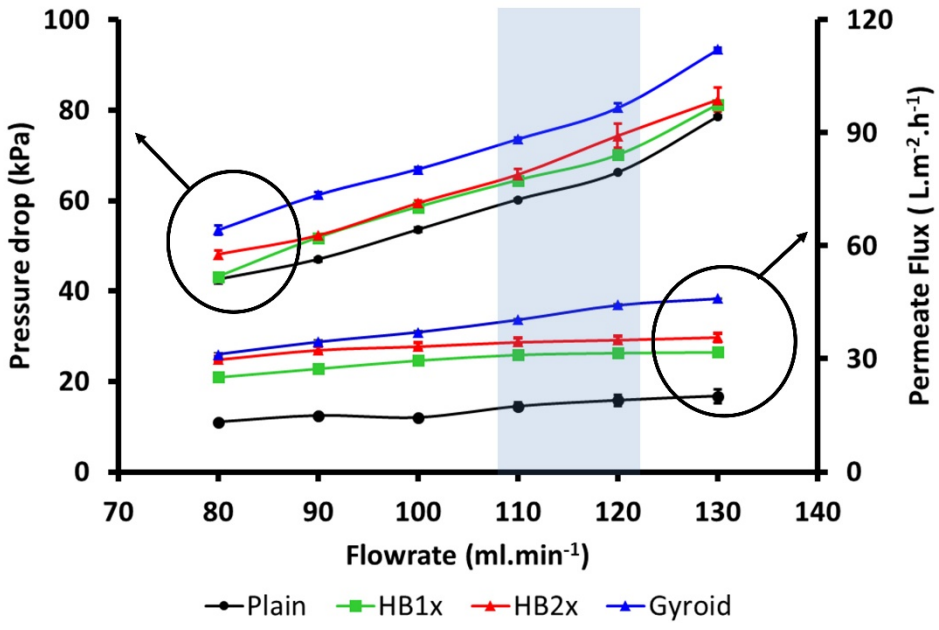

**Figure 4-5: Flux enhancement vs optimal energy input range of spacer designs.** Pressure drop (above lines, shown on the left y-axis) vs Permeate flux (bottom lines, shown on the secondary y-axis on the right) vs different flowrates in the spacer-based microfiltration units and the plain channel. Flux is measured every 10 minutes when a steady sate of the filtration process is achieved. Pressure drop is averaged within the measurement intervals. PMS solution is used in the feed channel.

This experimental trend of pressure drop generally agrees with theoretical results for plain and herringbone designs. The gyroid design, however, had an experimental pressure drop slightly higher than its theoretical predicted value. The increase in experimental fluidic resistance of the gyroid design can be explained by the printing error (39% deviation), as shown in Fig. 4-4B(i)).

## Pressure drop comparison (experiment vs simulation)

After the experimental pressure drop data was obtained it was compared to the simulated results. Because CFD simulations were conducted on single channels, the theoretical pressure drop on the device ($\Delta P'_x$) (which includes 11 repetitive channels) was calculated as 11 times of the pressure drop in each single channel models (see Chapter 3.8.2).

To have an apples-to-apples comparison showing sensors' measured values, both ($\Delta P_x$) and ($\Delta P'_x$) were then added with the pressure drop in the tubes ($\Delta P_1$).

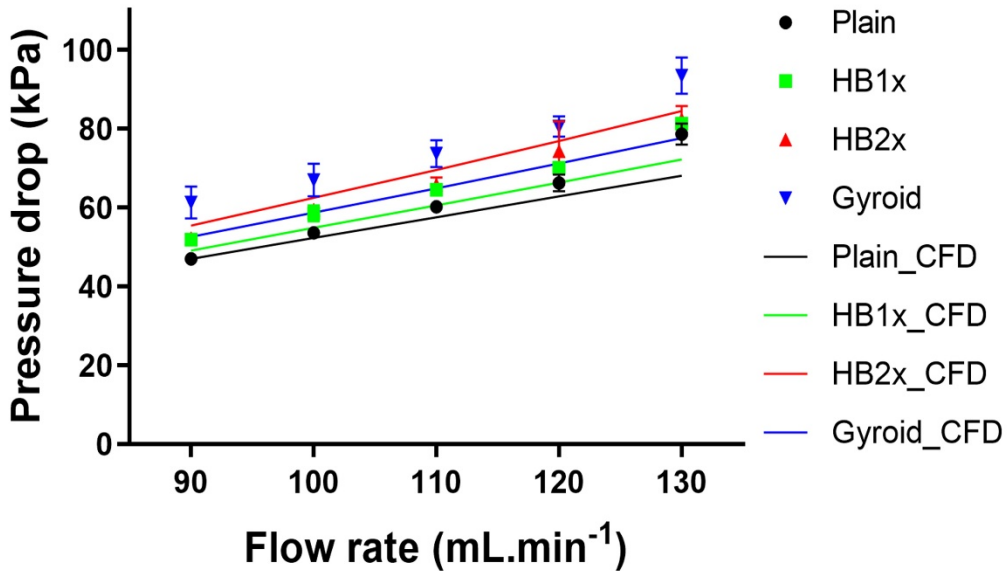


**Figure 4-6. Experimental pressure drop in comparison to theoretical pressure drop**

Figure 4-6 shows that experimental trend of pressure drop generally agrees with the CFD results for plain and herringbone channels, although with a slight under-prediction likely due to the surface roughness of the spacer (ranging from 10 - 30 μm). In the solutions used in this study, it is likely that rough spacers lead to protein adhesion and a slight increase in fluid resistance. For the gyroid design, there is a larger mismatch between the experimental and numerical results (12-17%). This increase stems from the printing error (39.1% deviation as observed above), which meant the actual printed geometry was much larger than the simulated design (and particularly for the smallest feature sizes (around 100 μm), leaving less hollow space for fluid to move, increasing resistance. This was demonstrated in Fig. 4-4B(i).

### 4.4.3 Biological Application Feasibility

The next tests in our study utilized blood & plasma mimicking solutions (BMS and PMS) to demonstrate possible use of microspacers in membrane modules for the artificial kidney application, especially in Membrane 1 (mimicking glomerulus). The BMS solution is used as a reference for the target of filtering PMS solution in Membrane 1 system as described in Fig. 3-1 (Chapter 3). The initial test length was chosen as 6 hours because in the literature, the typical spacer flux test varies from 2 hours to 40 hours, depending on the intended application [305], [307], [312]–[314]. And an extended test for 30 hours for the main solution PMS (feed solution of Membrane 1) was also conducted to confirm the performance of microspacers in the iAK filtration device over time. The main aim is to determine the relative performance between the proposed spacers and a plain channel.

#### 4.4.3.1 Filtration Performance Test with Blood Mimicking Solution

The results of the tests with the BMS solution are shown in Fig. 4-7A(i). It can be seen that the feed spacer with the gyroid structure produced the highest overall flux, followed by the two herringbone spacers when compared to the plain channel. The percentage of flux enhancement is plotted in Fig. 4-7A(ii). It was found that the flux recovery is approximately 81.4% for gyroid, followed by 61.6% for HB2x and 52.7% for HB1x. The data indicates that microspacer integration in narrow channels significantly

improves the filtration performance and the gyroid spacer appears to be the most effective; one of the likely reasons is the high mixing effect of this spacer contributing to fluid management in all X, Y, Z directions (See Fig. 4-2). This more complex fluid management might eliminate the small remaining low flow, dead zones inside the filtration unit and should increase shear stress near the membrane surface to minimize protein adhesion, thus, reducing fouling and increasing filtration efficiency.

The BMS solution used has some factors leading to this fouling, such as glycerol and xanthan gum. Figure 4-7A(i) shows that the gyroid design yielded the best result, with a 25.3% reduction in biofouling compared to a plain channel, followed by the HB1x and HB2x spacers with 17.3% and 15.9% reductions, respectively.

#### 4.4.3.2 Filtration Performance Test with Plasma Mimicking Solution

Fig. 4-7B shows the permeate flux as a function of time using the plasma mimicking solution (PMS) for all spacer designs in 6 hours. The trends for all spacer designs are similar when compared with a constant transmembrane pressure (TMP) applied and, with the flux decreases with time (Fig. 4-7B (i)). The highest permeate flux produced was obtained for the gyroid structure with an average flux of 32.1 $L.m^{-2}.h^{-1}$, followed by the HB2x and HB1x designs, and the plain channel with 28.2, 25.1 and 16.6 $L.m^{-2}.h^{-1}$, respectively. Compared to the plain channel, the permeate flux enhancement using the PMS solution for HB1x, HB2x and gyroid was found to be 51.1 %, 69.9% and 93.4%, respectively (Fig. 4-7B (ii)).

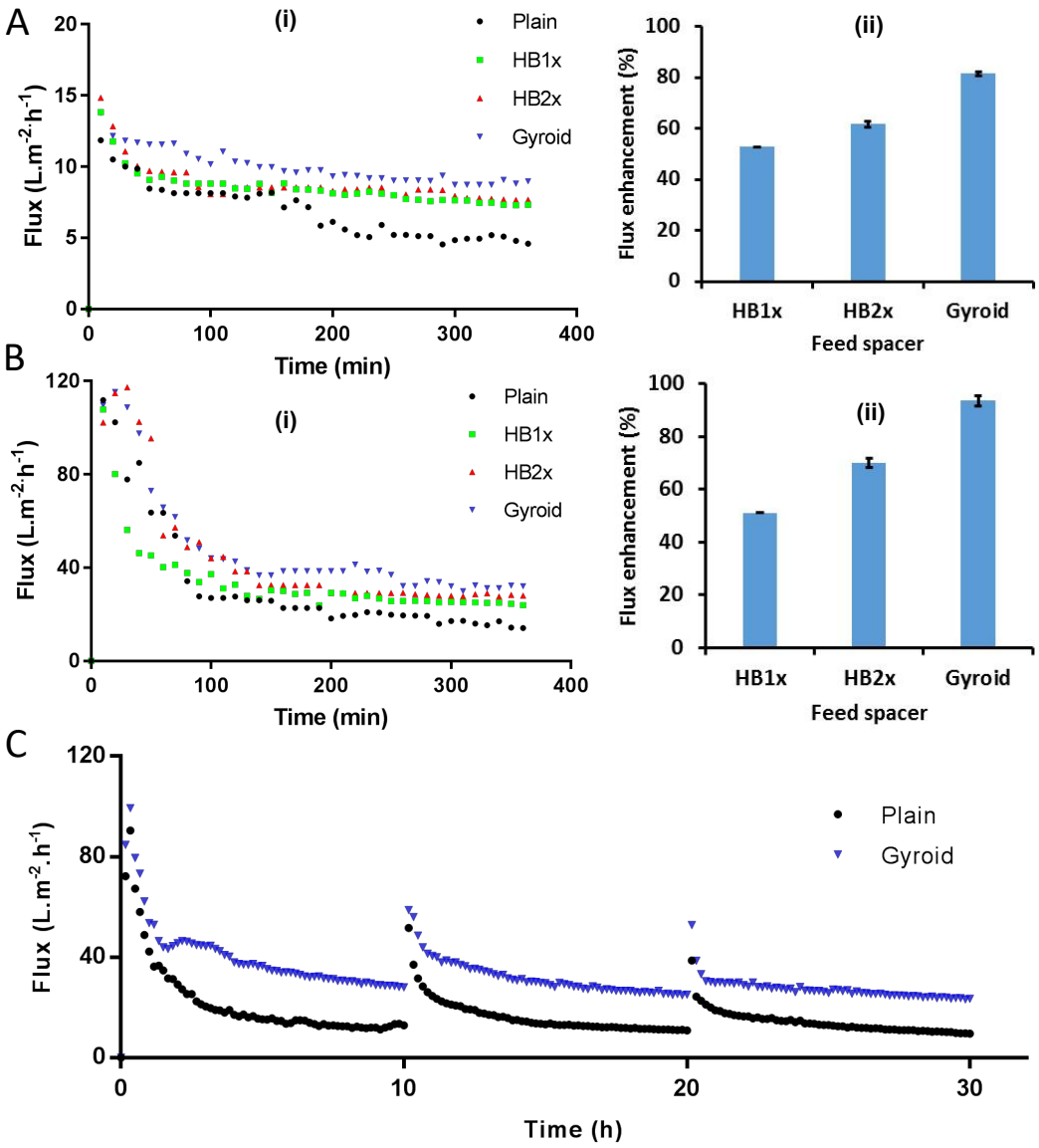


**Figure 4-7. Filtration performance test of the spacer designs with blood and plasma mimicking solutions.** (A) Test with BMS solution. (i) Permeate flux as a function of time and (ii) flux enhancement (compared with plain channel); (B) Test with PMS solution. (i) Permeate flux as a function of time and (ii) flux enhancement (as compared to a plain channel); (C) Extended 30-hour test (with the PMS solution) for the plain channel (no spacer) and the gyroid (the best performing microspacer). All of these tests were conducted under constant transmembrane pressure (i.e., a TMP=1 bar), a constant feed flowrate of 90 mL.min-1, and the permeate was measured every 10 minutes.90 mL/min. Permeate was measured every 10 mins.

An extended test (for 30 hours) was also conducted to confirm that the relative performance difference between the plain channel (no spacer) and the gyroid microspacer maintained over time. This will assure how long the Membrane 1 part of the proposed portable artificial kidney device can work sustainably without the need to replace its membrane. To do this, the tests were performed 10 hours per day for 3

consecutive days for these two designs using the PMS solution. At the end of each day, the PMS solution was withdrawn, and deionized water was run through device for a brief (30 minutes) rinse before leaving the membrane filtration submerged in water overnight. At the start of the next day, the test was resumed with the PMS solution. The results depicted in Fig. 4-7C indicate a constant relative flux enhancement in the performance of the gyroid microspacer is still present after 30 hours. In particular, over the last three hours of the test, the gyroid achieved a 129.4 % flux gain compared to non-spacer channel [e.g., 24.1 ($L.m^{-2}.h^{-1}$) versus 10.5 ($L.m^{-2}.h^{-1}$) for the plain channel]. The higher values of flux at the beginning of each day represent the performance recovery of membrane after the relaxation time [315].

Overall, for the mimicking solutions, the following points can be made: (1) The flux achieved by the target solution PMS is lower than the permeability flux with DI water but higher than the reference whole-blood mimicking solution (BMS); (2) Flux enhancement is also higher using PMS solution compared to BMS solution. However, relative to water and the BMS tests, for the PMS the gyroid has less of an improvement over the other structures. This result is reasonable since it shows that the lower viscosity fluid without the presence of xanthan gum PMS (~1.2 mPa. s), compared to BMS (~2.65 mPa. s), has less fouling.

While there is less potential for fouling reduction, the spacer designs can still reduce the concentration polarization compared to the plain channel.

#### 4.4.3.3 Wettability Effects on Flux Performance

Surface wettability of the membrane is another important parameter that can be investigated, since it can influence flux and fouling resistance of the tested membranes [267]–[269]. To test this for our designs, the water contact angles (CA) of the PVDF membranes were measured in three conditions: clean/new membrane, water-exposed membrane (e.g., after 30 minutes run at a TMP of 1 bar, and leaving exposed to pure water for 8 hours overnight, followed by a quick dry with lab airflow), and a PMS-exposed membrane (e.g., after a 30-hour test using PMS solution, followed by quick drying with lab airflow). The results of these tests are presented in Fig. 4-8A and B.

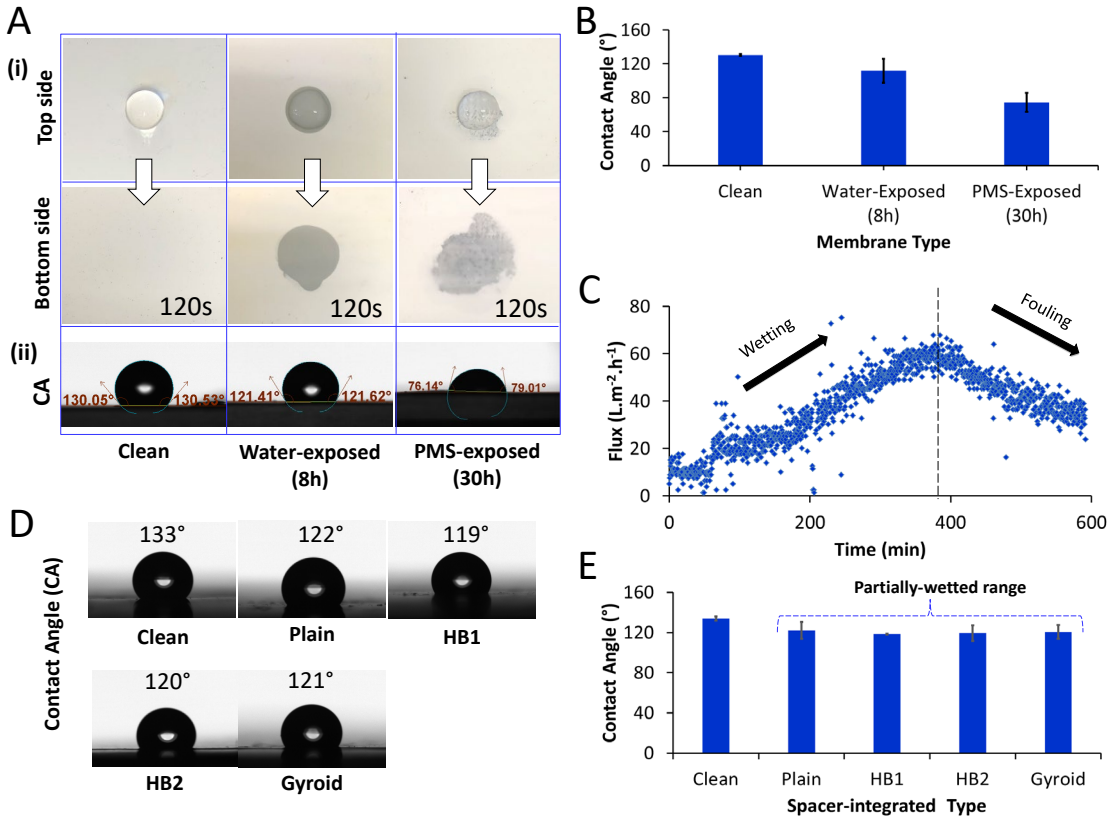


**Figure 4-8. Membrane wettability study.** (A) (i) Images of water droplets on the top (above) and reverse (below) surfaces of 3 types of the membranes: Clean/ new, Water-exposed membrane (running 30 mins at TMP 1 bar and leaving about 8h overnight), and PMS-exposed membrane (after 30h test using PMS solution), (ii) Contact angle measurement of the membrane types above, (B) Corresponded contact angle values of part A, (C) An illustration of getting wetted process with PMS solution, TMP=1 bar, feed flowrate 90 mL.min$^{-1}$ (D) Contact angle images of membranes after running with different spacer designs for 6h using PMS solution, (D) CA values in part C.

Figure 4-8 shows that the clean membrane was resistant to a water droplet over the test time. For the water-exposed and PMS-exposed membranes, it took ~2 mins for the water droplets to soak through the membrane, which reveals the increased wettability of the membranes during operation. The other side of the membranes, labelled as the 'bottom-side' images, reveal the different wetting characters with symmetric wetting for the wetted membrane and an asymmetric wetting for the PMS-exposed one.

As can be seen in Fig. 4-8B, the PMS-exposed membrane has the lowest contact angle value at around 70° to less than 90° compared to water-exposed and clean membranes. This may be the result of the membrane getting wetted further after the longer testing time. However, despite higher wettability, the membrane also becomes fouled after 30 hours filtering with PMS solution, which has BSA protein. Possibly, as a

result of fouling, the pores can be partially blocked and therefore the recorded fluxes are still reducing.

Figure 4-8C show that the flux increases initially due to increased wetting but then drops off as fouling occurs. This additional demonstration test showed that the recorded flux climbed up to a peak value and then went down after that point. This test was conducted with a new/clean membrane and using PMS solution at transmembrane pressure at 1 bar; permeate weight was recorded every 30 seconds.

Figure 4-8D and E show the result of contact angles of membranes after 6 hours of filtering using different integrated-microspacer channels (Plain, HB1, HB2 and Gyroid). The result reveals that despite the use of different spacers, all membranes have lower contact angles after testing, going from ~130° to a range from 115 to 122° (see Fig. 4-8D). This means that—as might be reasonably expected—the spacers do not measurably affect the wettability of membrane.

#### 4.4.3.4 Selectivity Test with Nanoparticles in Plasma Mimicking Solution

Membrane selectivity depends mainly on the membrane pore size. However, there can be a slight difference in filtration results due to the additional effects of spacers. A selectivity test was carried to confirm to what extent the nanoparticles, which are 50nm diameter size representing large-size protein molecules in hemofiltration solutions, can be separated from the fluid using different spacers.

Fig. 4-9 shows how the concentration of nanoparticles changes in both the feed and permeate sides of the membrane. As a result of using the same membrane (same pore size), the result shows a similar trend of permeate concentration between the designs while the feed channel became more concentrated. The general downtrend also suggests there can be a fouling layer created on the membrane surfaces that prevent particles from being filtered to the permeate side.

However, there were differences in the permeate concentration between spacers over time. After 6 hours of testing, the gyroid, HB2x and HB1x maintained a higher concentration of particles on the permeate side with $5.68 \times 10^8$, $4.02 \times 10^8$, and $4.50 \times 10^8$, respectively, compared to $1.82 \times 10^8$ particles.mL$^{-1}$ of the plain channel. HB1x-spacer microfiltration unit ended up with a higher permeate concentration observed than HB2x and was very close to the gyroid spacer. However, the overall trendline

plotted logarithmically shows that the HB2x and gyroid still have better selectivity than HB1x if the test is carried out for a longer period of time. Interestingly, the gyroid design showed the low concentration of nanoparticles in the permeate solution after the first 2 hours, but after 6 hours of the test, it was found to achieve the highest concentration of particles in the permeate compared to the other spacer designs as shown in Fig. 4-9. This is possible because the complex structure of the gyroid causes the albumins and particles to be initially attached to the gyroid structure's surface. Possibly, with the advantage of the hypothesized mixing effects (see Fig. 4-2), the gyroid unit still produces the best filtering function trend for the nanoparticle solution.

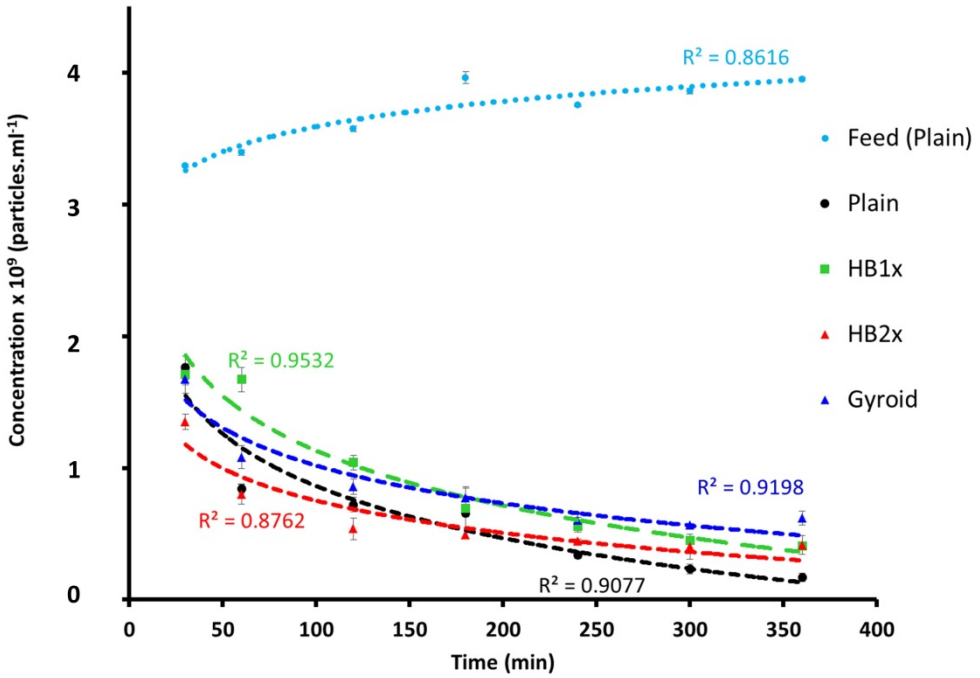


**Figure 4-9. Selectivity test with PMS solution.** Feed and permeate particle concentration, t=6 hours. Tests were conducted under constant transmembrane pressure, TMP=1bar, feed flowrate 90 mL.min$^{-1}$.

### 4.4.4 CFD Results and Discussions

To illustrate the fundamental hydrodynamics occurring, numerical simulations were utilized. Methods for the simulation is presented in detail in Chapter 3.7.

Over the range of velocity inlets from 0.15-0.217 m.s$^{-1}$ (as was done in the experiments), the CFD pressure drop results for the target solution PMS (viscosity μ~1.2 mPa. s) agree with the experiments for plain, HB1x and HB2x (at about 40-80

kPa) and only a slightly increase in practical pressure drop in gyroid design due to the fabrication error (Fig. 4-4).

CFD results revealed the ability to create complex 3D flows in the laminar domain, by using microspacers. As can be seen in Fig. 4-10A, the flow is essentially straight pathlines with the plain design, whereas the fluid moves vertically in the z-direction (the direction perpendicular to the membrane surface) in the herringbone spacer integrated channels. With the gyroid spacer design, 3D flow is created. In the hollow space of gyroid design, part of the flow moves irregularly around in all X-, Y-, Z-directions. This 3D flow and hydrodynamic mixing enhancement are the reasons for better shear stress on the membrane surface (see Fig. 4-10B) using gyroid and herringbone spacers, which enhance filtration.

Concentration polarization in NF and MF membranes can be reduced by increasing the shear rate [265]. Here, the CFD results with PMS solution in our study demonstrated that spacers have a significant effect in increasing the wall shear stress on the membrane surface, therefore, reducing concentration polarization and increasing flux. As shown in Fig. 4-10B(i), the gyroid design has the highest shear stress on its membrane surface, followed by HB2x with 32% lower shear stress, HB1x with 59% lower shear stress and plain channel with 70% lower shear stress than that of gyroid design. Fig. 4-10B(ii) illustrates how the shear stress is applied on the membrane surfaces for each channel of the spacer designs.

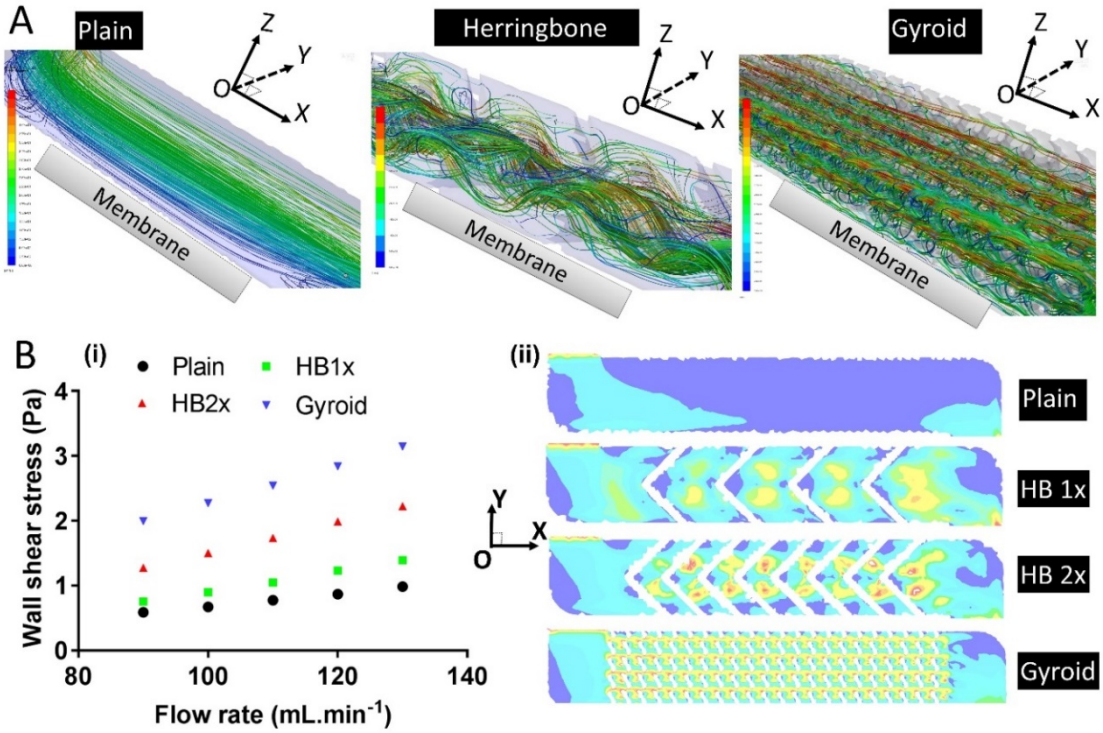


**Figure 4-10. Shear stress on the membrane surface and 3D velocity in the presence of various spacers.** (A) 3D velocity pathlines on different spacer-integrated channels; (B) (i) Wall shear stress magnitude on membrane surface, (ii) Shear stress on the membrane surface of different spacer-integrated channels

## Concentration Polarization Discussion

With higher membrane shear stress, lower concentration polarization occurs in the fluid domain. This explains the flux enhancement of the gyroid, and herringbone spacers compared to the plain channel when using PMS solutions as shown in Fig. 4-7B &C. Based on the previous model, the level of concentration polarization reduction in comparison in comparison with the flux enhancement was estimated. As discussed in Chapter 3.5.3, The *CP* equation (3-11) was plotted against the experimental flux enhancement results, and is shown in Figure 4-11 below:

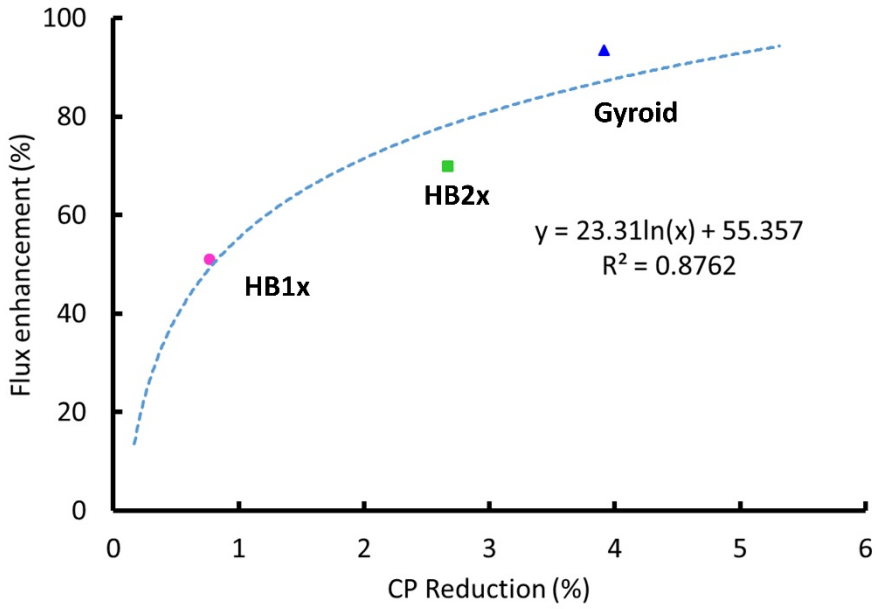


**Figure 4-11. Percentage of flux enhancement vs concentration polarization reduction.**

As shown in Fig. 4-11, a small change in concentration polarization can lead to a big change in flux enhancement. This trend shows that with about only 1-3% CP reduction, the gyroid surpassed other spacer designs by 20-40% in flux enhancement. The logarithmic trend also revealed the ability to improve the spacer design even more in the future to get greater CP reduction and further enhance flux.

However, due to the differences in membrane type, solution, size and a shorter range of shear rate, the established model was used here only to show the trend and to understand more about the relations between shear stress, CP reduction and flux enhancement. It should be noted that this estimation should only be used as an indicator to understand how the flux can be increased by the reduction of concentration polarization while using the microspacers. Many other factors can play a role, so an area for future work is to develop a more detailed model which accounts for the size of filtration unit, the membrane type, and the solution.

### 4.4.5 Future Work

Due to the complexity of the gyroid spacer with minimum features of ~100µm, the current 3D printing process provides a deviation of up to 39% (Fig. 4-4B). With the rapid development of 3D printing, it should be possible to manufacture these small

sized microspacers at scale for small-format filtration systems (e.g., artificial kidneys, serum, and protein separators). In addition, larger-scale printing areas are also now available (e.g the ProJet® MJP 5600 which has 518 x 381 x 299 mm (x, y, z) and ProX 950 has 1500 × 750 × 500 mm print dimensions), opening the potential of microspacers for spiral-wound modules and other applications which require large area, thin spacers (e.g., to fit into their membrane-membrane gaps). For this project, a relatively small printer was used, (i.e., a ProJet® 3500 HD Max from 3D systems) which can only accommodate a 298 × 185 × 203 mm (x, y, z) print volume with a minimum 16 µm layer thickness.

Platelets play an important role in surface fouling of biological samples filtration. In this thesis's proposed system, platelets were assumed to have been removed in Step 1 (a microfluidic separation, which is potentially clog free [152], [316]). However, if there is any platelet remains, they will be rejected completely when entering Membrane 1 (nanoporous, ideally, around 68 kDa or lower molecular weight cut-off (MWCO) and it cannot reach Membrane 2 of Step 3 (See Fig. 3-1). It is possible that the spacer surface could foul, leading to clogging. Further work is required to mitigate this, if it becomes an issue. This could be done by checking the 3D-printed spacer's quality (via image analysis from an inverted microscope, e.g., a Zeiss Axiocam 512 color) and surface roughness measurements (using a laser scan microscope, e.g., one of the Keyence VK-X200 series) before and after filtration (similar to the methods presented in Chapter 3.2). And further study on fouling characteristics including fouling layer scanning electron microscope images and fouling thickness of different biological solutions should also be measured.

Also, further tests on spacer and device materials and their biocompatibility are required to conduct extremely carefully. In addition to flux-energy input trade-off study, economic analysis can be further studied based on energy cost which is proportional to the product of pressure drop and feed flow rate.[248]

## 4.5 Outcomes

In this Chapter, microspacers were investigated for their effect on filtration efficiency, in narrow channels of the Membrane 1 compartment of the proposed portable kidney

system. These unique designs, including two herringbone geometries and a gyroid structure, were 3D printed, tested, and simulated to determine if concentration polarization and flux could be improved relative to a reference plain channel with the same form factor under the same operating conditions. The hydrodynamic performance in terms of feed channel pressure drop and filtration efficiency, and the biological application feasibility of the microspacers were evaluated and compared.

These points are concluded: (1) Three microspacers (with size from 100-400 μm) were successfully integrated into channels and produced using 3D printing technology. However, the high deviation (up to 39%) with small features at around 100 μm remained as the limitation of our current 3D printing; (2) Despite the sacrifice of increasing pumping power, adding microspacers into narrow-channel flows significantly enhanced filtration with the net benefit (of flux enhancement) relative to the cost (the increase of pressure drop) for all spacer designs. Under different flowrates (80-130 $mL.min^{-1}$) and solutions used (i.e., BMS and PMS solutions), the microspacers designs boosted permeate flux. Experiments and simulations found that the gyroid design achieved the highest membrane flux enhancement (i.e., 81 and 93% above a plain channel for blood mimicking and plasma mimicking solution tests, respectively). This was significantly better than the enhancement by herringbone designs. All of the spacers added back-pressure, with gyroid incurring a 23% higher pressure drop than the plain channel, which was considered as an acceptable performance trade-off; (3) CFD results agree with the experimental results and showed that by using microspacers, 3D flow and mixing were presented in the microspacer-integrated channels. This fluid management eliminates the small remaining low flow and dead zones inside the filtration unit and may also aid in diffusing shear stress to minimize protein and particle adhesion on the membrane, thus reducing concentration polarization and fouling.

Based on these results, it can be concluded that the spacer-based 3D printed system showcased in this study has shown excellent potential for one-step fabrication as a filtration unit for flux enhancement (e.g., Membrane 1 and Membrane 2 units). Although the effect of geometry on membrane wetting and fouling require further study, further studied, the results suggest the potential use of microspacers and the

possible advantages of the development of 3D printed membranes 3D-printed structured membranes (e.g., in a gyroid structure) for future artificial kidneys.

# Chapter 5

# Microfluidic Diode Valve for the Connection Part of the Proposed System

## Chapter Overview

*This Chapter describes the investigation of the Connection part (Step 3, as shown in Fig. 3-1, Chapter 3) of the proposed system, which includes the valve and the pump. Since there is a higher pressure on the downstream side, the valve must be a special one-way valve. However, microfluidic diode valves are not well-established in the literature. The characteristics of general microvalves are analyzed and additive manufacturing techniques for fabrication and prototype testing of a proposed one-way, microfluidic diode or check valve are described. This Chapter also includes an additional analysis of multi-valve control, and evaluation of the feasibility of using microfluidic diode valves for microscale liquid handling applications in the proposed system.*

*Note: The general microvalve characterization and applied valving system of this Chapter were previously published in ACS Sensors;* ***Dang, B. V.,*** *Hassanzadeh-barforoushi, A., Syed, M., Yang, D., Kim, S., Taylor, R.A., Liu, G., Liu, G., Barber, T., 'Microfluidic actuation via 3D-printed molds towards multiplex biosensing of cell apoptosis', ACS Sens. 4, 8, 2181–2189 (2019).*
*https://doi.org/10.1021/acssensors.9b01057.*

*The microscale diode-valve's structure and operation were based on the author's collaborative works during his Master's course, published in Sensors & Actuators: B. Chemical; Kim, G.,* ***Dang, B. V.****, Kim, S.-J., 'Stepwise waveform generator for autonomous microfluidic control', Sensors Actuators B. Chem. 266 614–619 (2018). https://doi.org/10.1016/j.snb.2018.03.160.*

## 5.1 Introduction

### 5.1.1 Microfluidic Valve for Liquid-handling

In the last decade, a critical enhancement in the usability and capabilities of microfluidic technologies has been achieved—in part—through the development of standardized, scalable, and versatile control systems [17], [147], [304]. Many miniaturized devices and integrated systems can now allow high-throughput and sophisticated fluid flow control [165], [201], [317]. Recent influential examples include biomimetic models [318], [319], biomolecular analysis [320], [321], drug discovery [322]–[324], and single cell analysis [325], [326]. At the core of each of these systems is an advanced liquid-handling mechanism, such as mixing [327], [328], pumping [329], oscillating [276], and flow control via magnetic [330], acoustic [331] or droplet manipulation methods [332], [333]. The key factor that leads to successful operation of these microfluidic-based devices is the ability to precisely deliver liquids on demand. This Chapter is a consideration of the method of liquid handling that is suitable for connecting Membrane 1 (Step 2) and Membrane 2 (Step 4) for the proposed portable artificial kidney system (see Fig. 3-1 of Chapter 3).

As a leading liquid-handling approach, microfluidic valves can be designed to connect or isolate liquid-containing microchannels and microchambers upon actuation. Microvalves can be categorized into normally open (NO) [197], [198] and normally closed (NC) valves [147], [199], [200] (See Chapter 2.6.4 for nore details). And NC microvalves can be further sub-classified into normal valves (switch-valves) and microfluidic diode valves (MDV) (also called microfluidic diode or check-valves) [147]. In these valve-based microfluidic circuitries, the switching action of the valve helps to open/shut off flow, which is enabled by geometrically regulated threshold pressures. Because of the low threshold pressure of NC valves, microfluidic diode valves can open with low inlet pressure, but at the same time, resist high pressure from the outlet side of valve, rejecting any backflow and diffusion in its closed state [143], [147]. Thus, this type of valve represents an ideal candidate for the connection part in the proposed system. Specifically, a microfluidic diode valve is needed between the permeate side of Membrane 1 and the high-pressure level generated by Pump 2.

### 5.1.2 3D Printing: An Emerging Microvalve Fabrication Method

Although microvalves provide operational simplicity and control (as mentioned above), their fabrication has historically been complex, time-consuming, and costly. That is, the requisite 3D geometry and relatively small scale has made microvalve-based systems hard to fabricate, often requiring a complex multi-layer photolithography process. In the conventional process, two or more photomasks and photoresist layers are required along with a highly experienced-based alignment procedure between UV-exposure/chemical development steps in a clean room environment [143]. A simple-to-fabricate method would enable much wider adoption of microfluidic handling systems for countless chemical and biomedical device applications.

During the last few years, 3D printing has emerged as a rapid and cost-effective tool for fabricating microfluidic systems with increasing resolution and quality [153], [334], [335]. With respect to the fabrication of microvalve-based devices, one-step fabrication of the whole valving system has been recently reported [336], [337]. For example, Folch's group fabricated, via stereolithography (SL), a microvalve entirely from WaterShed plastic with a membrane thickness of 115 µm [336]. A later design from the Folch group used a 3D-printed Quake-style valve based on poly(ethylene diacrylate) (PEG-DA-258) with a thinner, 10-25µm-thick, membrane to simplify the valve's architecture and piping for large-scale arrays [338]. In these designs, however, the range of the valve's operating pressures and actuation frequencies were limited by the elasticity of the printing materials. For instance, at least 10 psi (~70 kPa) is needed to cause enough deflection in a PEG-DA-258 membrane (Young's modulus, E ~ 130 MPa; valve size, A ~ 1mm$^2$; membrane thickness, $T_M$ ~ 25 µm) for a perfect seal [338]. In another attempt, Nordin's group reported a new procedure incorporating a modified resin for printing durable microvalves with $T_M$ of ~50 µm for a valve with a 1.08 mm diameter using a digital light processing-stereolithographic (DLP-SLA) 3D printer [337]. However, this valve also required relatively high control pressure (4-12 psi) and draining of the PEG-DA-258 precursor after printing proved to be a challenge. The valve also shows poor microscopic observability and requires 3D piping in connecting integrated valve arrays.

In a different approach, 3D printers were recently utilized to create master molds that can be used for soft lithography using PDMS. 3D printed molds have been used for fabrication of NO valves and making rapid prototyping of complex channels, possible in hours [339]–[341]. However, 3D printing for fabricating NC microvalves has not yet been reported. Due to the zero distance of membrane-to-valve-seat in the initial state, current methods of direct 3D-printing, which require removal of supporting material, are not able to print this type of microvalve. In addition, most of the previous microfluidic systems were introduced with only one of the sequential [342], [343] or parallel [329], [344] fluidic manipulations and yet demand sophisticated computer control and complex peripheral equipment [345], [346]. Centrifugal microfluidic systems have been introduced with the capability of performing sequential and parallel assays; however, they do not offer the operational flexibility provided by valve-based systems and their fabrication is relied on the complex lithographic processes [347], [348].

In this chapter, the use of 3D-printed molds is presented for fabricating NC valves as a new way for fabricating microfluidic diodes and more complex circuitries, especially those suitable for the portable kidney application. With this method, the complications associated with either photolithography or one-step 3D-printing of the whole valving system will be eliminated, expectedly. The NC valves fabricated with this method use PDMS membranes and therefore can be operated at significantly lower operating pressures (e.g., < 5 kPa as compared to 25-220 kPa reported in previous 3D-printed valve studies) [336], [337], [341]. Based on the characterization of a single normal NC valving unit, a simple way to manipulate fluid routing in a system of valves is expected to be designed and built via 3D printing.

This chapter describes: (1) The development and testing of a new 3D-printed-moldfabrication method capable of making a single NC-valve and a NC-valve-integrated multiplexed microfluidic-logic chip; The demonstration of the performance of the NC-valve in both sequential and parallel fluidic controlling logics; (2) The use of this knowledge of normal NC-valve valve to fabricate, test and analyze microfluidic diode valves (MDVs) for the application of portable kidney device.

## 5.2 Theory

### 5.2.1 Normally Closed (NC) Valve's Operation

A normally closed (NC) valve is a three-layer polydimethylsiloxane (PDMS) microfluidic device which follows the initial membrane valve designs proposed by Grover et al [199]. As shown in Fig. 5-1, the 3D-printed NC elastomeric valve consists of a top channel (top, blue color) with a protrusion interrupting the microchannel flow, a bottom chamber (bottom, light blue color), and a thin membranous middle layer (red). The valve provides a variable resistance to the fluidic stream [349]. The inlet and outlet regions of the NC valve are located in the valve's top layer. Valve actuation is achieved through a square chamber located in the bottom layer. The flexible PDMS membrane in between can deflect into the chamber to allow the flow from source to drain region in the interrupted channel. In a fluidic circuit, a normally closed (NC) elastomeric valve corresponds to an electronic transistor which has three regions, so-called the source, gate, and drain (See Fig. 5-1).

The elastomeric valve is closed in a normal state and open when the subtraction of the source pressure ($P_S$) and the gate pressure ($P_G$) is greater than a certain value which defined as the opening threshold pressure ($P_{thO}$). The opening threshold pressure, or $P_{thO}$, is critical, for valve characterization and for the operation of any microvalving circuits. This is an intrinsic parameter defined by the valve's design, material and membrane characteristics (see Fig. 5-1).

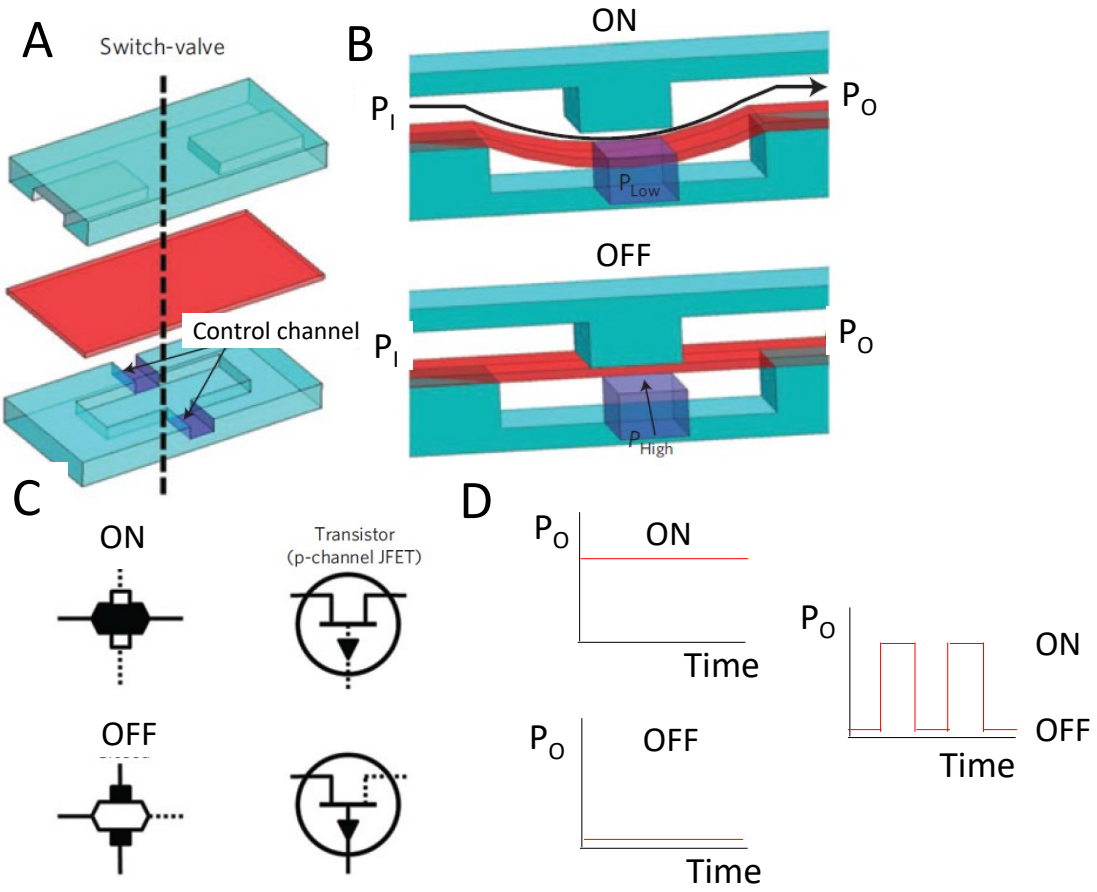


**Figure 5-1. Elastomeric components of a general normally-closed (NC) microfluidic valve (switch-valve).** (A) A three-layer composite of the general NC microvalve. (B) Cross-section schematic of the general NC microvalve in both the open and closed state based on different control pressure (low and high), (C) The p-channel JFET transistor shown as analogous electronic components to the general switch-valve, (D) Outlet's pressure profile when valve opened and closed. Image at (A), (B), (C) adapted and reprinted by permission from Springer Nature, Mosadegh, B., Kuo, CH., Tung, YC. et al. "Integrated elastomeric components for autonomous regulation of sequential and oscillatory flow switching in microfluidic devices", Nature Phys 6, 433–437 (2010), copyright 2010 [147].

### 5.2.2 Microfluidic Diode (Check-valve) Operation

Like standard NC microvalves, microfluidic diode valves (MDVs) have an elastic membrane in the middle layer. In the proposed MDV, a 3-layer PDMS diaphragm-based device design was selected. The main difference of the MDV design is that it has a through-hole in the membrane layer on the source or drain side to connect one side of the interrupted microchannel to the top layer with the chamber on the bottom layer (gate). As shown in Fig. 5-2, the through-hole effectively creates a diode-like function that allows unidirectional fluidic motion and negates backflow and diffusion in the

valve's close state. When liquid moves in the forward direction at the top channel of the diode (cross-section A-A' in Fig. 5-2), the membrane of the diode moves downwards, and the liquid can thus move along the top channel. However, if the liquid moves in the reverse direction, it pushes up the membrane and thus prevents reverse liquid motion.

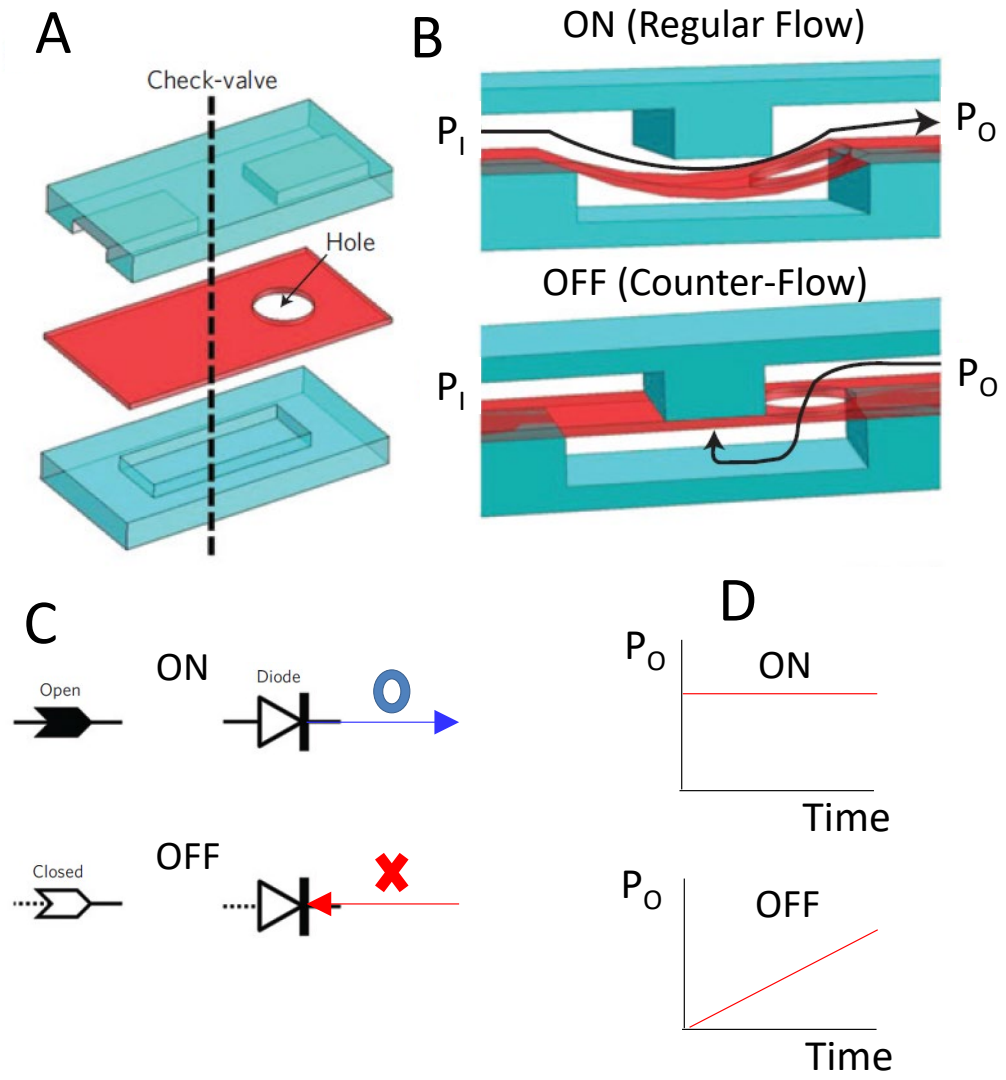


**Figure 5-2. Elastomeric components of a microfluidic diode valve (check valve).**(A) A three-layer composite of the diode valve. (B) Cross-section schematic of the diode valve in the open and closed states using regular flow (inlet to outlet direction) and counter-flow (outlet to inlet direction), (C) The diode shown as analogous electronic components to the microfluidic diode valve, (D) Outlet's pressure profile when valve opened and closed. Image at (A), (B), (C) adapted and reprinted by permission from Springer Nature, Mosadegh, B., Kuo, CH., Tung, YC. et al. "Integrated elastomeric components for autonomous regulation of sequential and oscillatory flow switching in microfluidic devices", Nature Phys 6, 433–437 (2010) [147].

## 5.3 Methods

### 5.3.1 Numerical Calculations

It is possible to use the electrical network analogy (equating pressure to voltage, flow rate to current, fluidic resistance to electrical resistance) to calculate the steady state operation of the microvalves proposed above. This general calculation can be used for all NC valves (including MDV valve) when flow in the forward direction from inlet to outlet. In normally closed valves analyzed in this Chapter, the default state is 'off' and no flow goes through it because of the adhesion force between the membrane and the valve-seat as shown in cross-section A-A' of valve (Fig. 5-1). By elastic deformation of the membrane, the valve will open when the difference between the inlet pressure ($P_I$) and the control pressure ($P_C$) is greater than the opening threshold pressure ($P_{thO}$):

$$P_I - P_C > P_{thO} \tag{5-1}$$

In contrast, when $P_C$ is relatively high enough to overcome closed threshold pressure ($P_{thC}$) [142], it pushes the valve's thin membrane upward. This motion closes the valve as the membrane tightly contacts the valve-seat in the top layer.

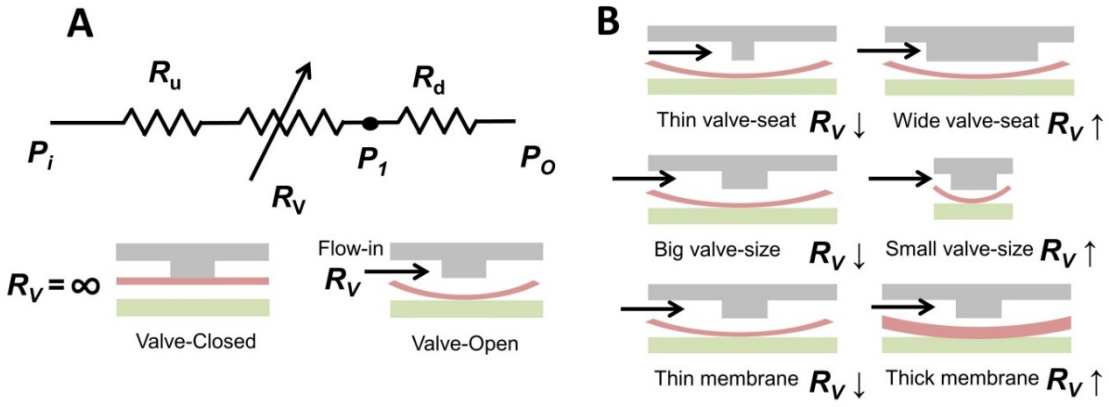


**Figure 5-3. Principle of operation analysis.** (A) Schematic of equivalent electronic channel for a single valve, (B) Schematic of the prediction of valve resistance change according to the changes of valve-seat sizes, valve sizes and membrane thicknesses.

As shown in Fig. 5-3, the fluidic resistance in the system comes from microfluidic channels, connected to both the upstream and downstream sides of the valve. Figure 5-3A provides an equivalent circuit diagram, which define how the pressure nodes ($P$) interact with the microfluidic valve's resistance ($R_v$), the fluidic resistances: upstream ($R_u$) and downstream ($R_d$) of the valve. The constant fluidic channel resistances (for

rectangular cross-section channel) such as $R_u$ and $R_d$ can, in turn, be calculated by the following equation [148]:

$$R = \frac{12\mu l}{wh^3\left\{1-\frac{192}{\pi^5}.\frac{h}{w}\left(tanh\frac{\pi w}{2h}+\frac{1}{3^5}.tanh\frac{3\pi w}{2h}+....\right)\right\}} \quad (5\text{-}2)$$

where $w$, $h$ and $l$ are width, height and length of channels, respectively, μ is the dynamic viscosity of water. The fluidic variable resistance of a single valve ($R_v$) can be obtained by using the network model of fluidic resistors [202]:

$$R_v = \frac{P_I - P_1}{P_1 - P_O} R_d - R_u \quad (5\text{-}3)$$

where $P_I$, $P_O$, $P_1$ are inlet, outlet and the pressure at position 1 ($P_1$ in Fig. 5-3A), respectively. $R_V$ is shown to approach infinity as $P_1 \sim P_O$, or in valve's closed state. The values of flow rate were obtained by the Poiseuille's formula:

$$Q = \frac{P_I - P_O}{R_V + R_u + R_d} \quad (5\text{-}4)$$

The opening threshold pressure, or $P_{thO}$, is crucial for valve characterization and for the operation of any microvalving circuits. This intrinsic parameter refers to the minimum value of the subtraction ($P_I - P_C$) between the inlet pressure ($P_I$) and the control pressure ($P_C$) that leads the valve turning from closed to open state.

From the closed to open state, the membrane's deflection, $y$, of the valve with equivalent hydraulic radius, $r$, working under a certain input pressure, $P_I$, can be determined as a first approximation from Eqn. (5-5). This equation allows us to predict the maximum deflection $y_{max}$ at the center of the membrane with a given Young's modulus $E$, Poisson's ratio $v$, and thickness, $T_M$ [336]:

$$\frac{P_I\, r^4}{E{T_M}^4} = \frac{5.33}{1-\vartheta^2}\frac{y}{T_M} + \frac{2.6}{1-\vartheta^2}\left(\frac{y}{T_M}\right)^3 \quad (5\text{-}5)$$

### 5.3.2 Microvalve Design Considerations

As discussed above, a normally-closed MDV was selected to put between Membrane 1 (Step 2) and Membrane 2 (Step 4). The following sections describe how this type of microvalve was designed, fabricated and tested. The key step in designing a valve-based microfluidic system is the determination of the geometry of the valve and its membrane. To do this, a parametric study was performed by solving for the valve's deflection under three different geometrical parameters of valve size ($S_V$), valve-seat size ($W_S$), and membrane thickness ($T_M$), as presented in Table 5-1.

**Table 5-1. Geometric dimensions of the 3D-printed valves**

| Valve size- $S_V$ ($mm^2$) | Valve-seat size- $W_S$ (µm) | Membrane thickness- $T_M$ (µm) |
|---|---|---|
| 1×1 | 300 | 30 |
| 2×2 | 600 | 70 |
| 4×4 | 900 | 110 |

Next, the materials must be selected. From a comparison of several potential membrane (diaphragm) materials, PDMS (E ~ 2 MPa, ν = 0.50) was selected because of its elasticity compared to other direct-printing materials reported recently, such as WaterShed (E = 2700 MPa, $v$ = 0.30) from [336]. Eqn. (5-5) predicts that a PDMS membrane of a hydraulic radius $r$ = 2.26 mm (equivalent radius of a squared valve 4mm×4mm) deflects at its center by $y$ = 722µm at $P_I$ = 3 kPa. Thus, all the valves were designed with a control channel depth of 1.8mm (more than 2 folds of 722 µm) to make sure the valve can be fully opened, with relevant radius $r$ ranges from 0.5 to 2.26 mm. As can be seen in Fig. 5-10 (below), decreasing the control pressure, $P_C$, and the membrane thickness, $T_M$, along with increasing the valve size, $S_V$, would yield an even higher membrane deflection.

### 5.3.3 Finite Element Analysis

A finite element analysis of the membrane deflection was performed using the COMSOL Multiphysics (MP) software [166]. Structural mechanics physics was used to define the geometry of the valve-seat and the membrane. The assembly was then

connected by defining contact pairs and meshed with free tetrahedral mesh. The optimum mesh size was selected based on a grid convergence study with max = 80 µm and min = 10 µm and the average number of mesh of 50,000 elements. The boundary condition for the pressure at the inlet was chosen to be $P_I$ = 3 kPa and the control pressures were chosen according to the experimental conditions. A free boundary condition was set at the drain. The computation for each simulation was completed in ~1 hour using a personal computer with Intel Core i5-560M processor.

### 5.3.4 3D-printed Molding Method

As shown in Fig. 5-4, a 3D-printed molding process was used for the fabrication of the normally-closed (NC) membrane microvalving system. This was chosen because it was capable of achieving a resolution as small as 100 µm without a requirement for a cleanroom and it would enable less complex manual sample handling protocols. It would also require less overall fabrication time than photolithography methods [199], while keeping the high flexibility advantage of a PDMS membrane in the valve structure.

As such, single valve-top and valve-bottom layers were 3D-printed as shown in Fig. 5-4. For the valves' mold design, the top layer's mold contains the geometry of microchannels for sample delivery separated in the middle with a groove representing the valve seat and a guiding circle for alignment of the top and bottom layers. The bottom layer's mold is a protrusion defining the corresponding valve size and the fluidic resistance towards an actuation port (see Fig. 5-4A(i)). Next, the PDMS pre-polymer was casted on the molds to create the top and bottom PDMS layers. Subsequently, the PDMS slabs are bonded together with a thin PDMS membrane as a middle layer (Fig. 5-4A(ii)). The final product has separate channels for the main fluid and the secondary control fluid/ gas (control channel) (as shown in Fig. 5-4A(iii)).

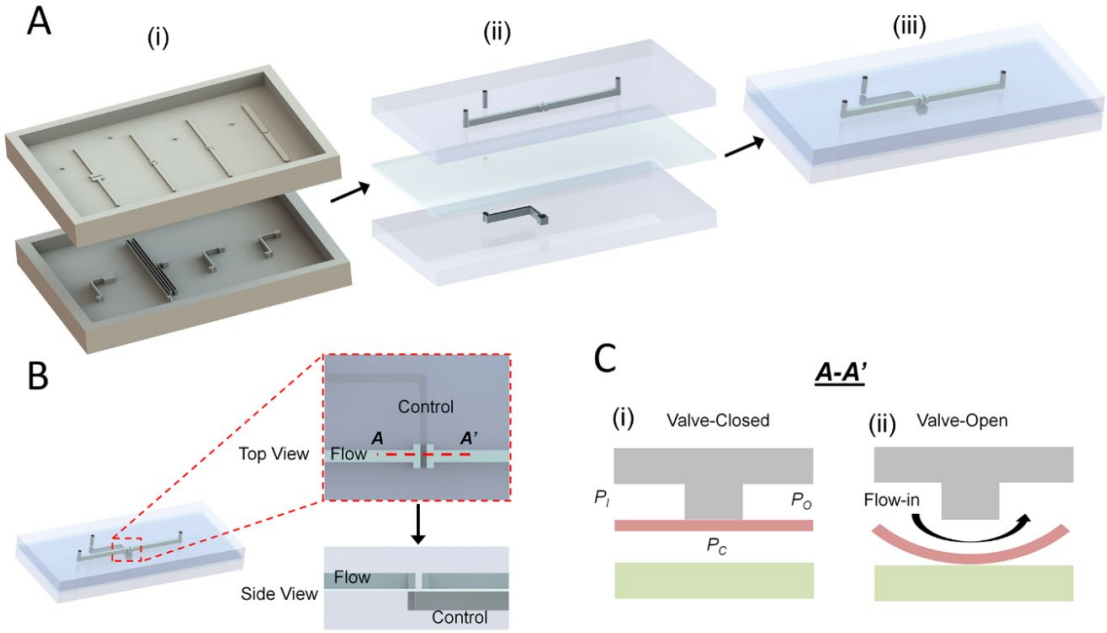


**Figure 5-4. Schematic illustration of fabricating single microvalve via 3D-printed molds.** (A) (i) Individual molds were 3D-printed for the valve top and bottom layers; (ii) Soft lithography on 3D-printed molds and casted PDMS layers; a thin PDMS membrane was fabricated using spin coater at a certain speed; (iii) Schematic of the assembled normally-closed microfluidic actuation unit. (B) Top view and Side view of the valve. (C) Cross-sectional view demonstrating the valve operation mechanism.

### 5.3.5 Valve Fabrication Procedure

The CAD models of the molds for both the top and bottom layers were designed using SolidWorks 2017 and 3D-printed with a ProJet® 3500 HD Max (from 3D systems). A Visijet M3 Crystal material was chosen due to its plastic durability and stability. To remove the supporting wax, the printed models were placed in an oven at 60°C temperature until the wax liquefied (see Fig 5-5A). The parts were then wiped away and washed thoroughly with bleach to remove any remnants. This multi-jet manufacturing (MJM) 3D printer has a printing resolution of 750×750×1600 dpi and 16µm per layer. Based on this resolution, channels and valves with sizes as small as 100 µm were successfully and reliably fabricated.

The 3D printed molds then were silanized (using vaporized trichloro IJ1H,1H,2H,2H-perfluorooctyl silane, purchased from Sigma Aldrich) in a vacuum chamber over night to render the surface hydrophobic, for easier release of cured PDMS. The PDMS (i.e.

Sylgard 184 Silicone Elastomer Kit, Dow Corning) was prepared by mixing a standard 10:1 ratio of the base and the curing agent and degassed, in a vacuum chamber for 1 hour. The mixture was then poured onto the 3D printed top and bottom layer molds. The PDMS is cured at the room temperature for 24 hours and peeled off the molds. The fluidic access holes for inlet and outlets were punched using a 1.5mm puncher on PDMS layers. These fabrication steps are illustrated in Fig. 5-5A.

In addition to the top and bottom layers, a thin PDMS layer with 30, 70, and 110 µm thicknesses was prepared by spin-coating PDMS on silanized glass and baking in oven at 120°C for 20 minutes, to serve as a membrane between these layers. For bonding, all three layers were placed inside an oxygen plasma cleaner (PDC-002, Harrick Plasma, Ossining, NY) while the valve-seat and the chambers was temporarily covered by PDMS stamps. Finally, the valve-seat covering was removed, and layers were irreversibly bonded together to obtain the final arrangement of the actuation unit as shown in Fig. 5-4A(ii) with the bonded layers were checked under the microscope for alignment. The final products are shown in Fig. 5-4A(iii) and Fig. 5-5B(i) for the actuation unit and in Fig. 5-5B(ii) for the multiplex microfluidic chip, a system of different valves.

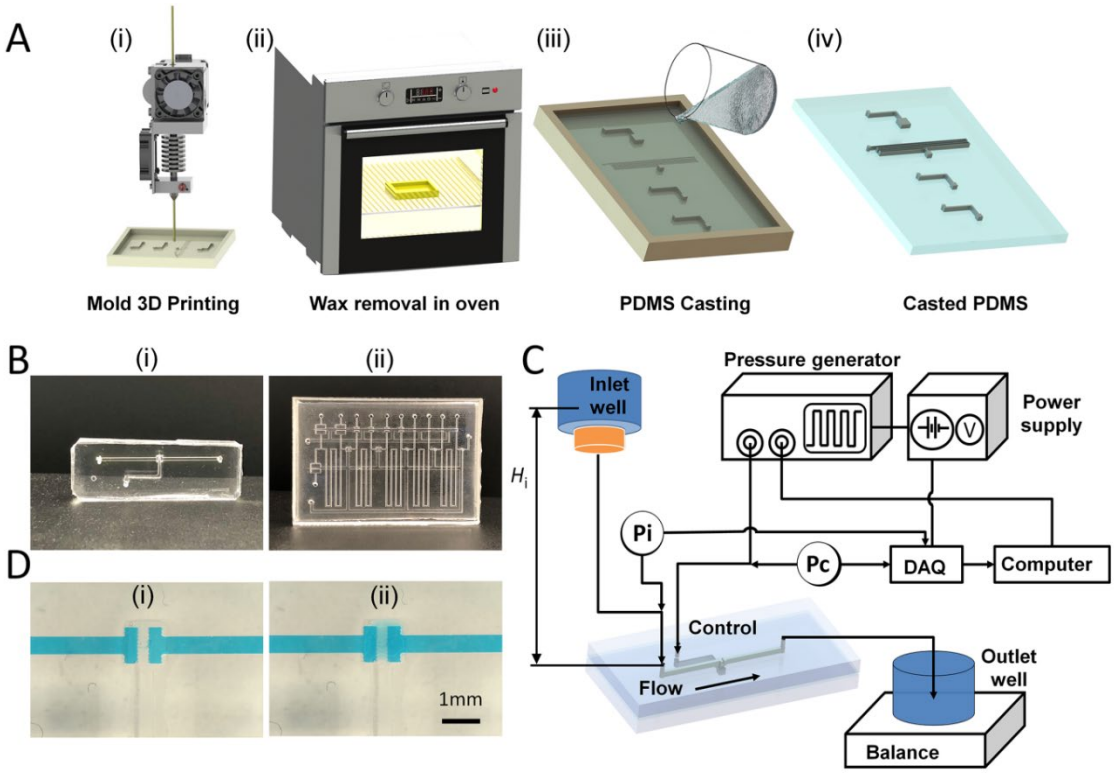

**Figure 5-5. 3D printing process and experiment set up.** (A) Fabrication steps for the valving system using 3D-printed molds. (B) Image showing the single valve as well as a multiplexed biosensing device made of PDMS from 3D-printed molds. (C) Schematic of the experimental setup. (D) Microscopic pictures of valve closing and opening states.

### 5.3.6 Fluidic Circuit Setup

As shown in Fig. 5-5C, the valve control channels were connected to the microfluidic pressure & vacuum pump (AF1-dual, Elveflow, Paris, France), to achieve pressure ranging from -700 mBar to 1 Bar. Actual controlling pressure is measured by disposable pressure transducers (range 0-36 kPa, Utah Medical Products Inc, Utah, USA) which were controlled by a National Instruments NI USB-9174 Digital I/O device connected to a power supply at constant voltage 10V. The LabVIEW software package (from National Instruments) was used to handle the measurement endpoints.

For the single-valve characterization, the inlet of the top layer was supplied by hydrostatic pressure of an inlet well held at a certain height $h_1$ while the outlet is connected to an outlet-well at the zero-surface. To show opening and closing states, the inlet of the flow channel is connected to a bottle containing blue food coloring dye (as shown in Fig 5-5D). The flow rate was measured by weighing the outlet liquid by an electronic balance. All the readings from the balance were recorded at an interval of 3 minutes.

In the next test, Rhodamine B was used as the working fluid to measure the change in the valve's opening ratio with the applied $P_C$. For this test, images were taken using an Olympus IX73 fluorescent inverted microscope with ImageJ software (NIH, Bethesda, USA) used for post-processing.

## 5.4 General NC Microvalve Characterization

Despite the presence of reports in literature on the fluidic characterization of NC valves, none of them have presented the characteristics of NC valves made out of 3D

printed molds and with the size and resolution offered by 3D printing technology [340]. In order to systematically design a 3D-printed valve for our current fluidic circuit, it is crucial to evaluate a single NC valve's performance under different control pressures ($P_C$), different valve sizes, valve-seat sizes and membrane thicknesses. Below is a finite element analysis of the valve's fluidic operation, followed by experimental results for geometrical variations of $S_V$, $W_S$, and $T_M$ (as shown in Table 5-1 above).

### 5.4.1 Numerical Simulation Results

As shown in Fig. 5-3B, wider valve-seat size ($W_S$), smaller valve size ($S_V$), and the thicker membrane ($T_M$) all result in higher values for the valve resistance ($R_V$). Higher resistance, consequently, leads to a lower flow rate through the valving system according to Eqn. (5-4). In general, the effect of the $R_V$ change to the behavior of the fluidic system depends on the ratio between $R_V$ and the network of upstream and downstream resistances and the applied pressures according to Eqn. (5-3).

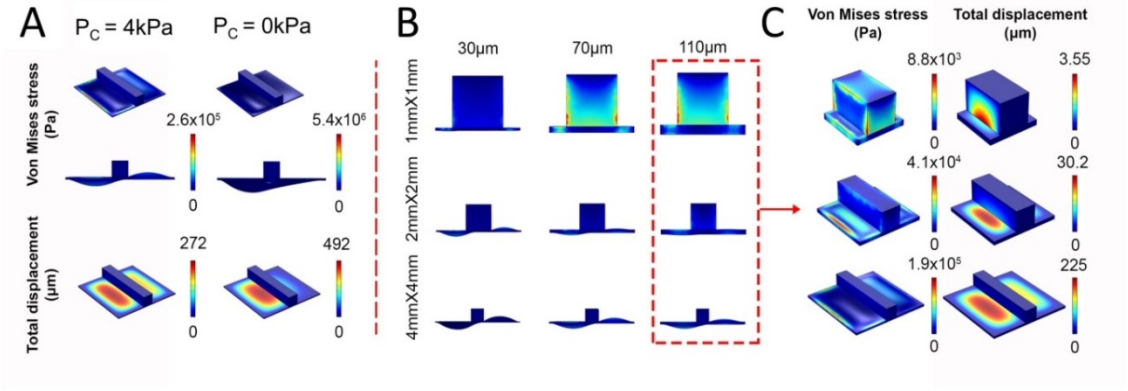


**Figure 5-6. Computational simulation analysis to confirm prediction about valve's behaviors.** (A) Different control pressures was used $P_C$ = 4kPa and $P_C$= 0 kPa, (B) Different membrane thicknesses was used including 30µm, 70µm, 110µm, (C) Simulation result with different valve-seat sizes: 900 µm, 600 µm, 300 µm (from top to bottom).

A series of numerical simulations were performed to further understand the valve behavior through modeling under different operating pressures and geometries. Fig. 5-6A presents the membrane deflection of a 4 mm × 4 mm valve with $T_M$ = 30 µm under constant inlet pressure of $P_I$ = 3 kPa and two different control pressures of $P_C$ = 0 kPa and $P_C$ = 1.4 kPa. At higher control pressures ($P_I$ = 1.4 kPa), the membrane deflects downwards on the inlet side and upwards on the drain side, due to the existing

pressure differences between valve sections. When the control pressure decreases ($P_C$ = 0 kPa), the inlet pressure overcomes the control pressure on the drain side, leading to larger membrane deflection. Consequently, the valve will be opened more and the flow rate through the valve increases. Looking into Fig. 5-6A, it can also be seen that when the control pressure decreases, the valve experiences much higher stress and this stress is more uniform across the geometry of the valve. This knowledge is important in selecting the membrane's material. For the PDMS membrane used in this study, the ultimate tensile strength is between 3.51-7.65 MPa [350]. The stress distribution of Fig. 5-6A confirms that the pressure distribution on the membrane is within the allowable PDMS tensile stress range (less than 5.4 MPa).

Fig. 5-6B demonstrates membrane deflection in valves with three valve sizes of 1 mm × 1 mm, 2 mm × 2 mm, and 4 mm × 4 mm and three membrane thicknesses of 30 µm, 70 µm and 110 µm under the same operating condition of $P_I$ =3 kPa and $P_C$ =1.4 kPa. The results of numerical simulations show that bigger valves are bent easier under the same valve operating pressures. A smaller valve with a thicker membrane (1mm×1mm valve with 110 µm membrane) has the least deflection the studied cases.

Fig. 5-6C shows an isometric view of the stress distribution and total displacement on the membrane as well as the valve-seat area. As can be seen, when the valve size increases, the stress distribution transfers from the valve-seat to the surface of the membrane, which leads to increased membrane deflection on both sides of the valve-seat. The enhanced deflection of the membrane on the drain side leads to higher flow rates as the control pressure decreases.

### 5.4.2 Experimental Geometric Characterization

To investigate the experimental flow rate through the valve, the inlet pressure was kept at $P_I$=3 kPa while the control pressure $P_C$ was decreased, changing the valve's state from fully closed to the fully opened condition (Fig. 5-7A(i)). As can be seen, when valve-seat size is small (e.g., when $W_S$=300 µm or 600 µm), the valves are opened earlier at a similar control pressure ($P_C$~2 kPa). Only with a bigger valve-seat size (e.g., $W_S$=900 µm), the valve is closed more tightly and a further reduction in control pressure ($P_C$=1.7 kPa) is required to open the valve. When $P_C$ is reduced to a certain

value ($P_C$ ~0.5 kPa) the valve is in the “fully open” state and all valves show equal values for the flow rate.

Fig. 5-7A(ii) demonstrates the effect of valve size on flow rate of a 3D-pinted single valve. Interestingly, the opening pressure $P_{thO}$ shows a significant segregation between valve sizes. The biggest valve size (4 mm×4 mm) opens first when $P_C$ is decreased to ~2.5 kPa ($P_I$-$P_C$= 3-2.5= 0.5 kPa), whereas, the smallest valve (1 mm×1 mm) remains in the closed state until $P_C$ is reduced to just about 1 kPa ($P_I$-$P_C$ =3-1= 2 kPa). Indeed, the small valve allows most of the movable membrane area to be in contact with the valve-seat, leaving no extra space for the flow to pass through. Finally, when the valve is fully open ($P_C$ = -1.5 kPa), the smaller valve shows lower flow rates due to its higher valve resistance ($R_v$) (See Eqn. 5-3).

Furthermore, figure 5-7A(iii) shows the variation of flow rate with different membrane thicknesses. Valves of different thickness are in the fully closed condition at the similar control pressure ($P_C$~3 kPa). Once the $P_C$ decreases down to a critical value (~1 kPa), the membrane suddenly deflects. Notably, a sudden jump-up of the flow rate with the thicker membrane due was observed, which corresponds to the sudden decrease of $R_v$, expediting the valve’s fully open state.

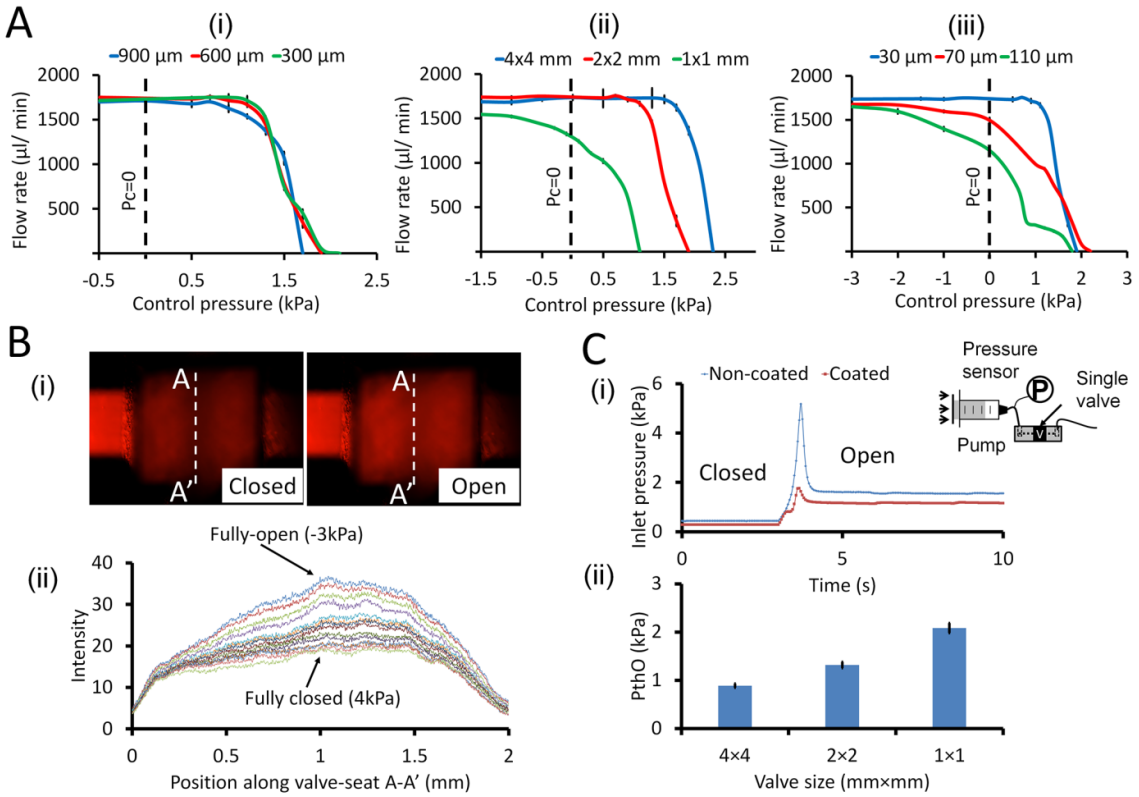


**Figure 5-7. 3D printed valving unit characterization.** (A) Variation of flow rate through the NC valving unit with control pressure under different valve geometries: (i) Valve-seat sizes ($W_S$) of 300, 600, and 900 µm, valve size ($S_V$)=2mm×2mm and membrane thickness $T_M$=30 µm; (ii) Valve sizes of 1×1, 2×2, 4×4 (mm × mm), when $W_S$=600 µm and $T_M$=30µm; (iii) Membrane thicknesses of 30, 70, and 110 µm when $S_V$=2mm×2mm and $W_S$=600 µm (n=3 for each experiment). The dash line shows the control pressure $P_C$=0 relative to atmospheric pressure. (B) Variation of opening fraction of the valve unit with different control pressure: $P_C$ are 4 and -3 kPa for closing and opening states: (i) Experimental microscopic picture of valve in open and closed states; (ii) Corresponded intensity value. (C) Variation of $P_{thO}$ with coating and non-coating cell culture media conditions, (i) Setup for $P_{thO}$ test and inlet pressure value, (ii) $P_{thO}$ for different valve sizes (4×4, 2×2, 1×1 (mm × mm)). All tests are with $W_S$=600 µm, $S_V$= 2mm×2mm (except C (ii)), and $T_M$=30 µm.

### 5.4.3 Opening Fraction

The opening fraction, which is proportional to the distance between the membrane and the valve-seat, is important since it determines the range of control pressure and ensures accurate fabrication. This factor was evaluated based on the fluorescent intensity of Rhodamine B when the solution passed through the valve at different control pressures (Fig. 5-7B(i)). Constant pressure was imposed at the top channel of a NC valve ($S_V$=2mm×2mm, $W_S$= 600µm, $T_M$=30µm) by keeping the fluorescent solution at a constant height of 30cm. As shown in Fig. 3B(ii), the fluorescent intensity increases proportionally with control pressure from the minimum value of 18.8 (a.u.) at $P_C$=4 kPa

to the maximum value of 37 (a.u.) at $P_C$=-3 kPa corresponding to valve at fully closed and fully open states respectively. This is in accordance with the calculation of the valve maximum deflection calculated with Eqn. (5-5).

### *Opening Threshold Pressure ($P_{thO}$)*

Lower $P_{thO}$ reduces the valve's pressure input which consequently leads to easy control and less energy input required for its operation. This factor is a critical issue when designing complex microfluidic automation systems with several single valves. To assess the valve's opening threshold pressure ($P_{thO}$), the single valve's inlet ($S_V$=2 mm×2 mm, $W_S$= 600 µm, $T_M$=30 µm) was connected to a syringe pump on the top-layer when the valve was maintained at the closed state (see Fig. 5-7C(i)). The fluid was pumped continuously into the inlet until the valve opens. The value of $P_{thO}$ was calculated based on the Eqn. (5-1). As shown in Fig. 5-7C(i), a sudden decrease in inlet pressure was observed in a single valve as it opens. In order to reduce $P_{thO}$, a strategy was adopted in which the cell culture medium (DMEM, Sigma Aldrich, USA) was used for coating the inner space of the valve on the top layer for 24 hours. The result shows a significant reduction in the inlet pressure needed for opening the valve and measurement of $P_{thO}$ for different valve sizes confirmed that the smallest valve (1 mm×1 mm) has the biggest $P_{thO}$ (see Fig. 5-7C(ii)).

## 5.5 Microfluidic Diode Valve Characterization

### 5.5.1 Device Whole Size and Through-holes Location

As explained in Chapter 5.2.2, the only difference in the structure of microfluidic diode valve (MDV) is it has a through-hole in the membrane layer on either the source or drain side to connect fluid flow from the top layer with the chamber on the bottom layer. Therefore, between Fig 5-4A(ii) and 5-4A(iii) in the valve's fabrication process, there is a step for punching the through-holes on the membrane layer before plasma bonding. Figure 5-8 represents the characterization of punched holes location on membrane and whole size of the microfluidic diodes.

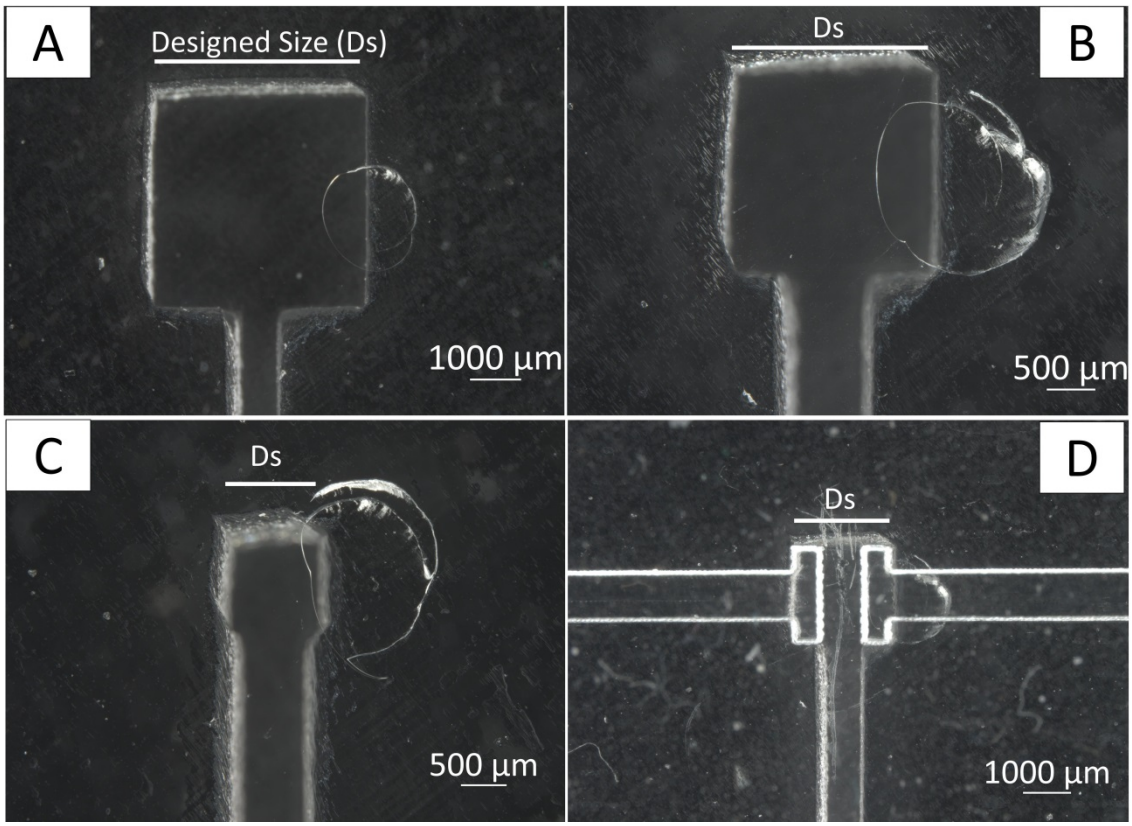


**Figure 5-8. Microfluidic diode valve whole size and through-hole location on PDMS membrane.** (A) (B) and (C): Bottom chamber and membrane for valve size 4mm×4 mm, 2mm×2 mm and 1mm×1 mm, respectively, (D) Whole bonded diode valve (valve size 2mmx2 mm).

From the microscopic images captured, the bottom chamber and whole valve were produced correctly in size by 3D printed molds with only less than 5% error in terms of the design specs (see Fig. 5-8). Through-holes which were created by manual punching at the same size of 1.5 mm in diameter shows acceptable location observed.

### 5.5.2 Microfluidic Diode Valve Pressure Characterization

The maximum pressure that a microfluidic diode can resist on the drain side is considered and measured using the setup shown in Fig. 5-9. The schematic of experimental setup including a syringe pump, a MDV valve and a pressure measurement system with a pressure sensor, a data acquisition and a computer was demonstrated in Fig. 5-9A. The syringe pump was connected to the outlet of the valve.

Since the MDV valve allows only one way of flow from the inlet to outlet, the test shows the maximum pressure at which the valve can withstand.

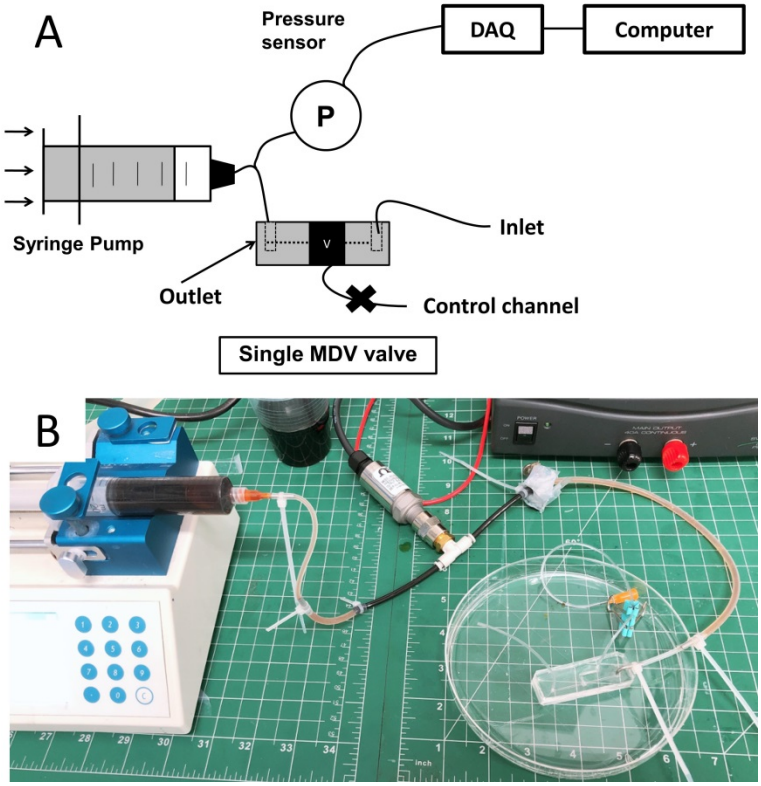


**Figure 5-9. Experimental setup for pressure tolerance test (maximum diode pressure test) of single microfluidic diode valve (MDV).** (A) Schematic of the test setup, (B) Experimental image of diode valve pressure test setup.

The study on controlling of general NC Microvalve places a profound background for an effective controlling of MDVs. Several important results from the above study include: (1) The valve open and closed states can be controlled by adjusting opening threshold pressure ($P_{tho}$), (2) $P_{tho}$ can be adjusted by valve's dimension parameters and coating materials; allowing effective liquid controlling in a system of valves. These results are the guidance to design microfluidic diode valves for the connection part (Step3) of the proposed portable artificial kidney system. As can be seen in Chapter 4, although feed pressure of a typical Membrane 1 unit is at about 2 Bar, permeate chamber of Membrane 1 which (is connected to Membrane 2) own a very low pressure (several kPa, estimated). Therefore, the MDV valve is expected to work well as located in the

system fluidic circuit since it can operate at a low pressure of filtrate (only 1-3 kPa) and able to resist much higher pressure ($P_{max}$) from the other side.

Fig. 5-10A represents the detail of (i) flow direction throughout the MDV valve and (ii) counter direction flow of the valve. In the first case, flow is from inlet to outlet (I→O) and the second case from outlet to inlet (O→I). The real image of the microvalve maximum pressure test set up is shown at Fig.5-10B. Flow is introduced from the outlet side of the valve; even if the inlet is opened, flow cannot go throughout from outlet to inlet due to the diode characteristic of the valve. The set of experiments was conducted to characterize the unidirectional flow controlling characteristics of the MDV valve.

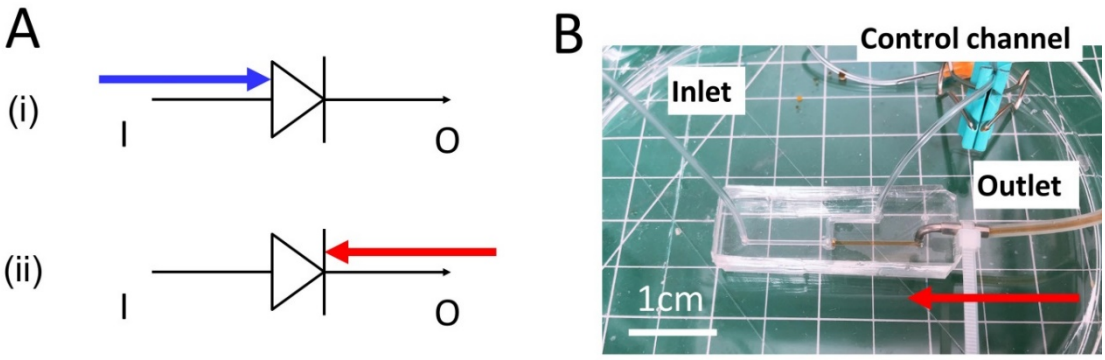


**Figure 5-10. Microfluidic diode valve (MDV) schematics.** (A) Schematic of MDV valve with two cases, (i) regular-flow direction from inlet to outlet, (ii) counter-flow direction from outlet to inlet, (B) An actual single MDV valve with counter-flow. Fluid is introduced from outlet; control channel is closed; inlet is opened. The valve behaves like a diode, stopping flow.

### *Opening Pressure and Diode Pressure*

The results of the experiment using the setup represented in Fig. 5-9 and Fig 5-10 are shown in Figure 5-11 below. With unidirectional flow from the valve's inlet to outlet, the MDV valve was operated first as a standard NC microvalve. As per its design, the valve opened when inlet pressure reaches a peak value, as shown in the chart (~ 2 kPa) in Fig. 5-11A. The peak pressure shows the opening threshold pressure, which is an intrinsic parameter depending on valve size, valve seat size, membrane thickness and coating material (as discussed In Chapter 5.4). After the peak, the pressure reduced to a constant level of pumping pressure.

In contrast, when the pump is connected from outlet side, the MDV valve behaves totally differently from a standard NC valve. In this case, the liquid moves to the through hole on the membrane area down to bottom chamber of valve and pushing the membrane up towards valve-seat; the counter-flow from outlet to inlet is completely stopped. The pressure builds up in the bottom chamber of the valve until the device leaked/ burst. The maximum pressure that the MDVs can handle represents the safety level for pumping pressure that can be used for Pump 2 for Membrane 2. This pressure can be called "*maximum diode pressure*" (MDP). Fig 5-11B shows the diode pressure of the valve 2mm ×2 mm at the flow rate of 0.2mL.min$^{-1}$.

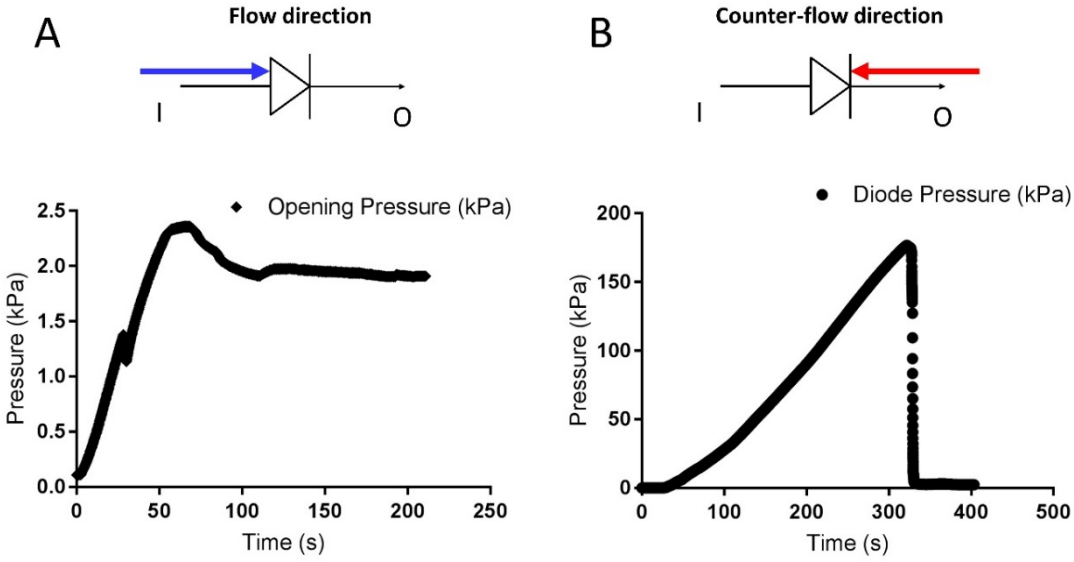


**Figure 5-11. Experimental data of diode pressure.** (A) Opening pressure (when flow is introducing from inlet towards outlet), (B) Diode pressure (when flow is introducing from outlet of microfluidic diode valve), valve size 2mm×2 mm and flowrate 0.2mL.min$^{-1}$.

The results of Fig. 5-11B are quite promising for the portable kidney application since the MDP pressure can reach above 180 kPa or ~ 2 Bar which is the typical starting point for a reverse osmosis membrane (RO) to have permeate. However, further discussion about the working condition of the diode valve in the proposed system will be presented in the following sections.

### 5.5.3 Diode Valve Pressure for the Proposed System

This section will be a discussion about the working condition of the MDV valve and the improvement of valve design and fabrication to meet the required maximum diode

valve pressure. Considering the MDV valve and its position in the proposed system (see Fig. 5-12A), the inlet of the valve is connected to permeate side of Membrane 1 which is at low pressure (e.g. 5 kPa). This pressure value depends on Membrane 1's feed condition and pore size, despite the fact that it is connected to the atmosphere in the experiment. With this input pressure and the possible negative pressure from pump 2, the valve should be opened normally ($P_{thO}$ depends on the fabrication and is typically at around 2-4 kPa as shown in Fig. 5-11). When counter-flow appears, it tends to move from the Pump 2 side towards the valve when the MDV valve is closed. Since the high pressure generated from the pump is connected to Membrane 2 side, this pressure will not fully be applied to the outlet side of the MDV valve. The valve is located in this position just to make sure there is no backpressure from pump affecting membrane 1 filtration. However, if there is an accidental situation when all the pressure generated from the pump is applied on the outlet of the MDV, the valve could be burst.

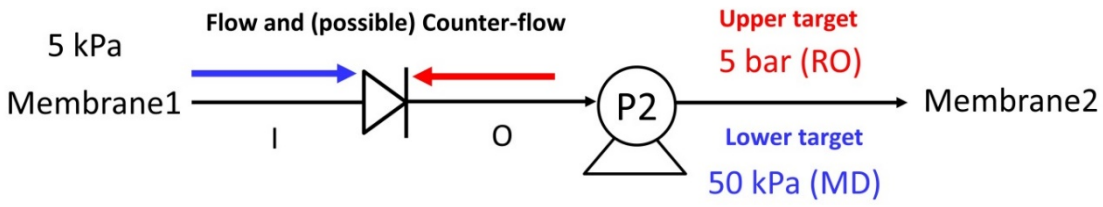


**Figure 5-12. Schematic of microfluidic diode valve in the proposed system with estimated flow and pressure working condition.** Target pressures are set following the choices of Membrane 2's filtration (5 bar for RO filtration in red fonts and 50 kPa for MD filtration in blue fonts).

If an RO membrane is used for the Membrane 2, the necessary pressure for running an RO membrane with reasonable flux is typically from 2-8 Bar [351], [352] for low-density fluid such as fresh and plasma. An average MDP pressure of 5 Bar is set as the target for the improvement in maximum diode valve pressure of the diode valve.

If a MD membrane is used for Membrane 2, this type of membrane only requires a minimal driving pressure on the feed side to carry permeate from Membrane 1 to Membrane 2 [353]. An average MDP pressure of 50 kPa (estimated based on the channel fluidic resistance and expected flow rate) is set as the lower-target for the maximum diode valve pressure of the diode valve. This pressure has already being

achieved, according to Fig. 5-11. This type of membrane filtration, however, requires the input (feed) solution of Membrane 2 being heated up to about 60°C, and a vacuum pump may be needed in the permeate side of the membrane. Further discussion on the feasibility of the method is discussed in the next Chapter (Chapter 6).

Fig. 5-11B shows the current value of MDP pressure with 3D-printed diode valve (2mm ×2 mm) is approximately 2 Bar. If membrane 2 is a RO membrane, a much higher MDP pressure (target of 5bar) is needed to make sure the system is safer when having the diode valve. Therefore, a series of tests have been conducted to reach a higher MDP pressure.

### *Diode Pressures by Valve's Sizes*

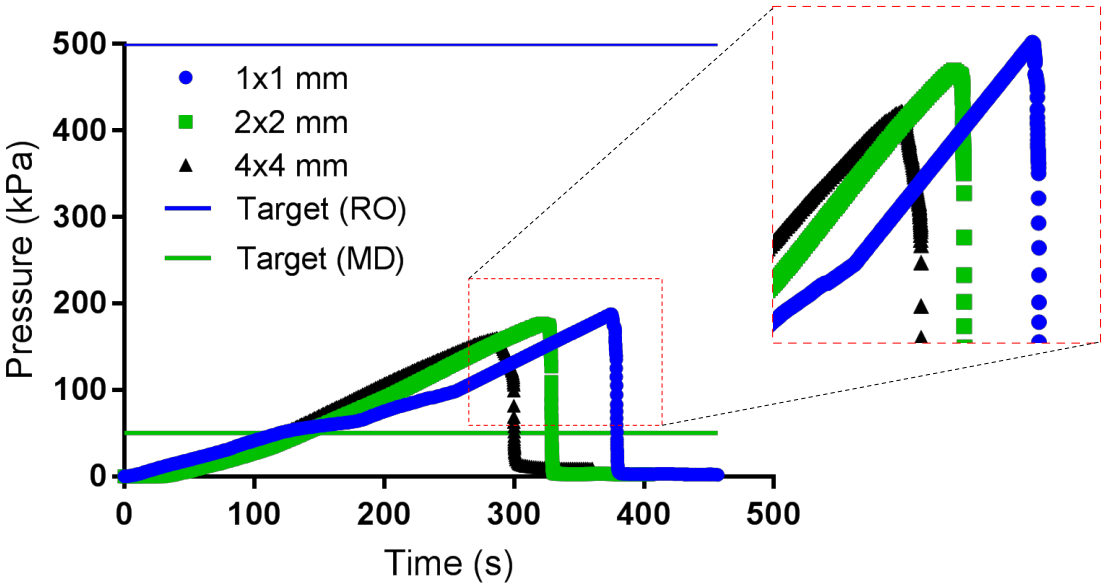


**Figure 5-13. Maximum diode pressure test with different valve sizes.** The valves includes 1×1, 2×2, 4mm×4 mm sizes, and run at the flowrate of 0.2mL.min$^{-1}$.

Fig. 5-13 reveals the low level of diode maximum pressure gain in by utilizing different valve sizes. Although the valve 1mm ×1 mm shows MDP pressure improved 6% and 19% compared to the bigger microvalves 2mm ×2 mm and 4mm ×4 mm, respectively. The improvement of this method of changing the valve's size is marginal. Although the MDP pressure has surpassed the target of pressure tolerance for using MD membrane, it is still far from the pressure target for RO membrane.

### *Diode Pressures and 3D-printed PDMS Device's Burst Pressure*

One of the reasons for devices burst at low pressure is the bonding PDMS-PDMS strength. For the current device, the MDP pressure of the 3D-printed microvalve is restrained by the device's burst pressure.

A simple experiment was conducted to clarify if this burst limitation value is different from MDP pressure. The target is to compare the maximum tolerance pressure between the following two cases: (1) A configuration where the device's outlet is connected to the pump ; (2) The device's inlet is connected to the pump (flow direction from inlet to outlet) and the outlet is closed, manually. Two devices (2mm ×2 mm) with the same parameters were used for the test using the same input flowrate condition.

As shown in Fig. 5-14, the diode pressure (blue) and the burst pressure (green annotation) are at the same level of about 2 Bar with current 3D-printed PDMS device (2mm ×2 mm, running at 0.2 $mL.min^{-1}$). With faster input flowrate (e.g., 0.5 mL/min), the burst pressure of the device is not much different as when it is with lower input flow rate and the device was broken earlier, as shown in the black data line in the Fig. 5-14.

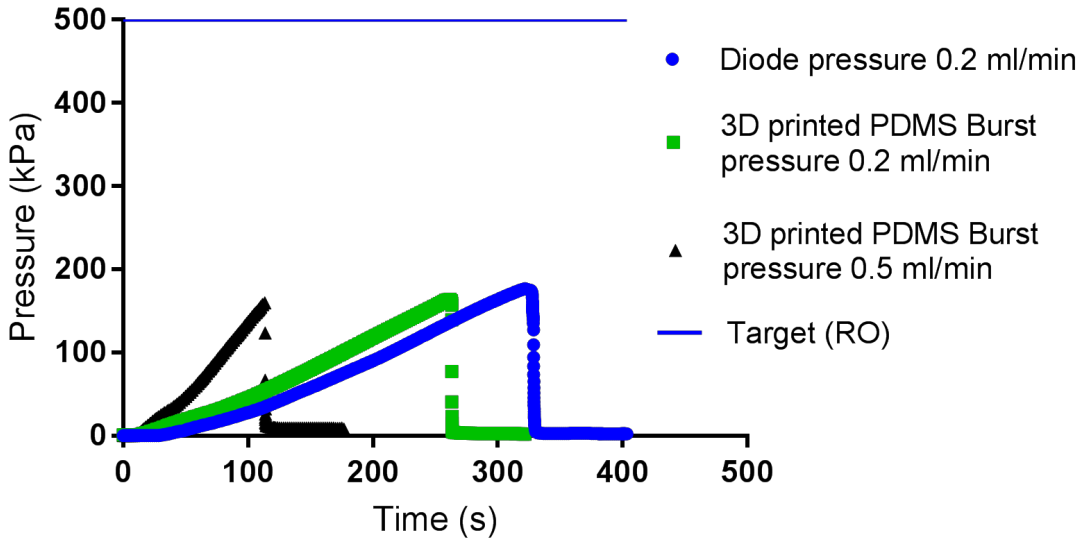

**Figure 5-14. Diode pressure and PMDS-PDMS burst pressure.** Counter-flow from outlet to inlet is used to accumulate diode pressure until device burst; regular flow from the inlet to outlet is used to accumulate pressure until the 2 devices burst with flowrate 0.2mL.min$^{-1}$ and 0.5mL.min$^{-1}$. Three devices are at same valve size (2mm ×2 mm) and parameters.

## *Diode Pressures by Surface Roughness*

With the limited current 3D printed quality, the surface roughness of 3D printed molds and their corresponded PDMS layer may have affected its PDMS-PDMS bonding strength. As shown in Fig. 5-15A, by refining the 3D printed mold's surface, lowering these surface roughness (e.g. from Ra=30 µm to Ra=4 µm), the MDP pressure improved significantly from around 2 Bar to roughly 4 Bar. This value is still under the target for RO membrane pressure but far surpassed the target for MD membrane use. This promising potential improvement in the diode pressure of the microfluidic diode valve came from the use of a CNC grinder for smoothing the 3D-printed mold before casting PDMS. Fig. 5-15B reveals 3D surface roughness measurement values and surface quality in the two cases.

Briefly, with a smoother surface roughness of 3D-printed mold, the casted PDMS surface quality is better, followed by a stronger oxygen plasma-assisted PDMS–PDMS bonding. This is a critical understanding to improve the diode pressure.

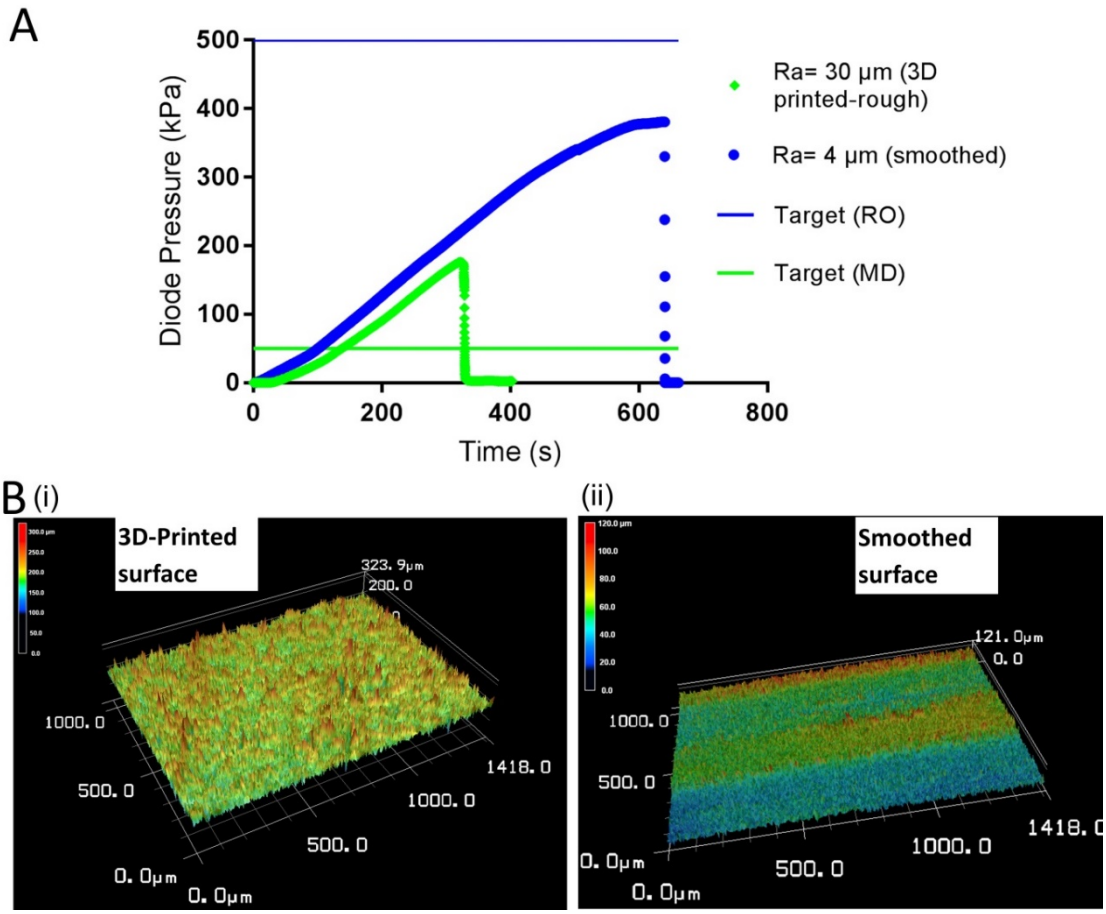


**Figure 5-15. Maximum diode pressure test with different 3D-printed mold roughness** (A) Diode pressure of different surface roughness molds by time, (B) Surface roughness measurement of 3D-printed mold's surface and smoothed surface roughness, (valve size 2mm ×2 mm). The flowrate was at 0.2mL.min$^{-1}$.

### 5.5.4 Diode Valve Discussions and Future Works

Although the MDV valve has the potential to reach higher maximum diode pressure with a smoother mold surface; leaking can still happen before bursting of the device. As shown in Figure 5-16, the causes of leakages in the experiment may be from connection issues (e.g., loose punched holes, loose inlet tips) and the burst happens when the pressure is higher than the bonding strength between PDMS slabs. Leakages made the diode pressure could not be far bigger than 4 Bar in the repeated experiments. For these issues, more precise inlet/outlet punches, using Teflon tape in connections, and achieving higher 3D printing surface quality may prevent leakages temporarily. However, if higher working pressure is required, a new method and material for making the diode valve should be further developed.

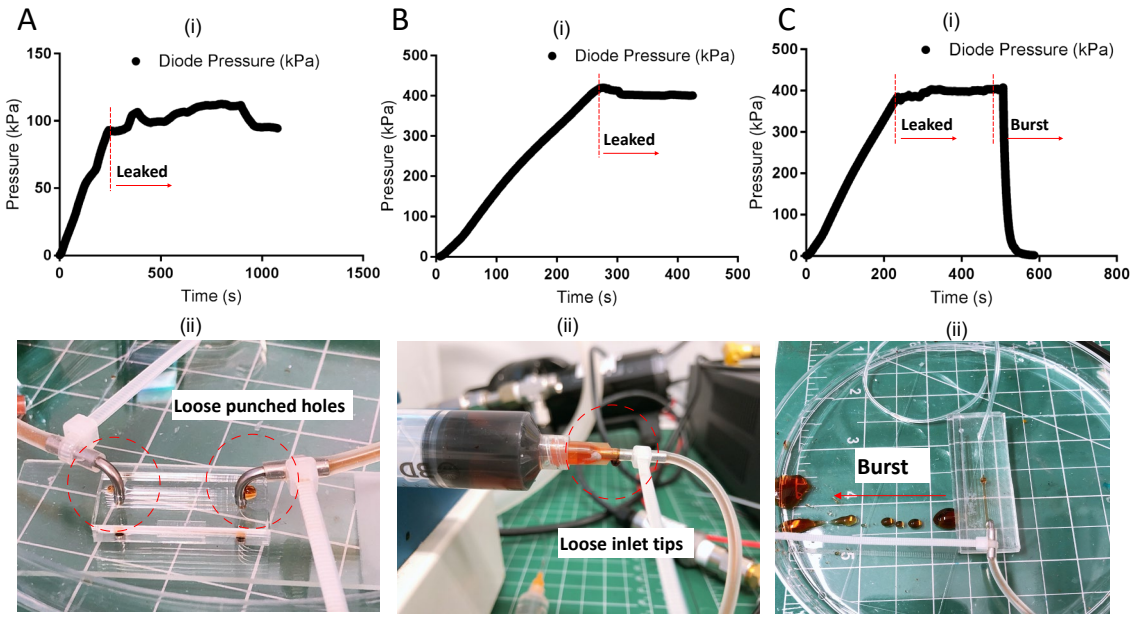


**Figure 5-16. Leakages in testing maximum diode pressures.** The vale 2mm ×2 mm, was run at the pumping flowrate 0.2mL.min$^{-1}$. (A) A leak at the connection area as using loose punch holes, (B) A leakage happens at plastic connections with pump, (C) Burst happens when accumulated diode pressure goes over PDMS-PDMS bonding pressure of the 3D-printed valve.

As proven from the above experiments, the current MDV valve can resist only up to roughly 4 Bar (when there is a counter-flow applying to valve's outlet). Since the bonding area is less than 10 mm radius, bigger bonding area should be tested for strengthening PDMS bond. To consider a further improvement, this figure 5-17 below explains clearer on pressure regulation in the system.

As shown in Fig. 5-17, the diode pressure which is monitored by pressure sensor $P_4$ can be affected by the work of the Pump 2, the amount of recycling flowrate and the permeate pressure of Membrane 1. When using MD for Membrane 2, $P_4$ is low (e.g. ~50 kPa), a current diode valve can tolerate safely with this pressure. When using RO for Membrane 2, because in a portable device, the device should work in as small as possible pressure; a target for running Pump 2 to under 5 Bar is set by the author. With an input pressure ranging from 2-5 Bar, a reasonable flux can be achieved. Part of this pressure can be applied to the diode valve, depending on the recycle rate; thus, for the safety of the system, it is a requirement to develop a diode valve with a higher pressure

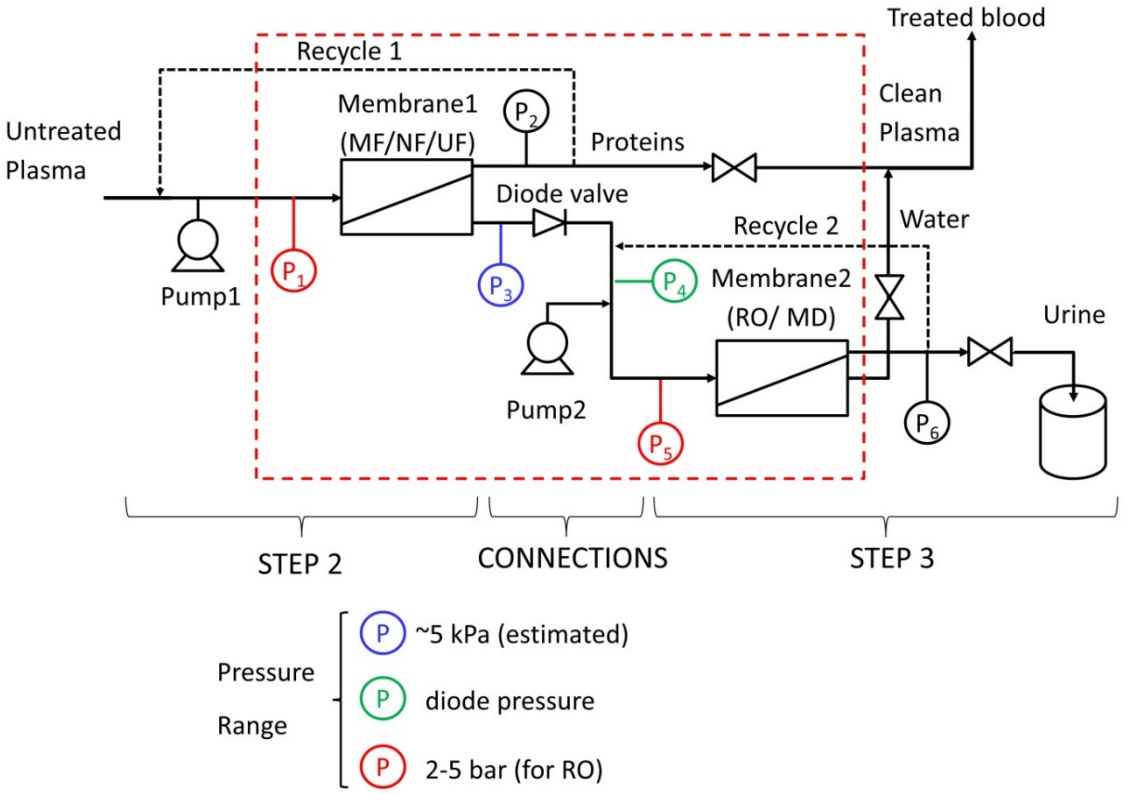


**Figure 5-17. A schematic of a microfluidic diode valve in the proposed portable artificial kidney system.** The schematic also presents pressure distribution around the inlet and outlet of the valve.

tolerance MDP (e.g., at 5 Bar). With a rapid 3D printing resolution up-gradation, the burst pressure can be increased, which mean maximum diode pressure will be released from device pressure's limitation. Future methods such as using a series of MDV valves (sequential or parallel) or developing the valves with more advanced pressure-tolerate materials may provide higher MDP pressure.

The one-way microfluidic diode valve used in the proposed pAK system has an inlet connected to the output (filtrate) of Membrane 1 and has its outlet connected to Pump 2 and Membrane 2, so the inlet and outlet flow rates should match. The current normally-closed diode valve was observed to work well with the experimental input flow rate condition (0- 3 mL/min) and it potentially allows a much wider range of flow rates (i.e., 0-170 mL/min, estimated below). There is also the potential to re-design, or replace, this valve with other types to handle higher filtrate flow rates in Membrane 1 (maximum 120 mL/min) due to the following reasons:

(1) The actual filtrate flow rate of Membrane 1 in a fully-developed pAK system can be lower than the natural glomerular filtration rate of 120 mL/min to achieve the similar toxic clearance level of hemodialysis. Indeed, as explained in Chapter 2.6.5, since hemodialysis is only connected 12-15 hours/ week, the proposed continuously operating pAK device would have a much lower average flow rate, assuming at a roughly similar filtration efficiency it would run at ~30-40 mL/min [3]. For instance, if the device can achieve the same or higher level of urea and creatinine clearance in its filtration performance (See the comparison in Chapter 6.5), K (mL/min), but run continuously (i.e., 10X higher time t), a similar level of filtration capacity can be achieved at considerably lower flow rate.

(2) Based on Chapter 4.4, with the current membrane type and membrane area used, the experimental filtrate flow of the Membrane 1 (the flow rates the valve must handle) is only 0- 3 mL/min. Meanwhile, according to Fig. 5-7A (Chapter 5.4.2) with only a 3 kPa input pressure, the valve has a flow rate of 1.7 mL/min. However, the valve can handle an input pressure up to 4 bar according to Chapter 5.5.3, indicating the valve could handle at least 100X the tested flow rate (i.e., around 170 mL/min). When PC (the control pressure) decreases, the inlet pressure PI overcomes PC at a certain value equal or higher than the opening threshold pressure (PthO), leading to a membrane deflection and opening the valve. The values of flow rate were obtained by Poiseuille's formula:

$$Q = \frac{P_I - P_O}{R_V + R_u + R_d} \tag{5-4}$$

Zooming in to the valve's flow rate test in Fig. 5-7A (Chapter 5.4.2), the valve's flow rate is similar for the different valve sizes of (2 mm×2 mm) and (4 mm×4 mm), which means that the flow rate has been constrained by the upstream and downstream resistances. Thus, if the valve is redesigned with larger upstream/downstream channels and bigger valve sizes, the membrane will deflect even more, enabling considerably higher flow rate through the valve.

(3) Alternatively, another type of one-way valve could also be employed to the purpose of pAK system, if it is compact/ small and easy to operate. For example,

ball/ spring [354], and diaphragm check valves [355] have all been used with HPLC pumps and/or with other experimental instruments and medical devices [356]–[358].

## 5.6 System Valve Characterization: A Control Analysis

As discussed from the above part, maximum diode pressure (MDP) cannot be increased if the 3D-printed PDMS device's burst pressure (which is depending on the PDMS-PDMS bonding strength) is not improved. With this bonding strength limit, a system of valves for increasing MDP pressure will not work. Specifically, if a valve is burst due to over-pressurizing, the valve system (with sequential or series of PDMS valves) will also burst. However, if the bonding strength limitation (burst pressure) is overcome with higher 3D printing resolution (smoother 3D-printed mold surface) or more advanced pressure-tolerate materials, we can use the system of valves. This use can increase MDP pressure and/or allow mixing the primary fluid (e.g., permeate solution) with other different fluids (for measurement or detection of filtration that a portable kidney device may need).

In this section, a system of different valves was designed and fabricated to elucidate a further understanding of microvalve control. This is helpful for the future development of the future small-scale portable device where more complex permeate liquid handling (mixing, measurement or detection) is required. The dependence of the opening threshold pressure on the valve size (Fig. 5-7A(ii) and Fig. 5-7C) in Chapter 5.4.2 can be used as a guide for the design of a more complex sequential or multiplexed system which allows sequential control of series of valves.

Here, a novel design which enables multiplexed control of different liquid samples by incorporating microvalves via 3D-printed molds was demonstrated. The device integrates 3 types of valve sizes which have been characterized above: 1×1, 2×2 and 4×4 mm with $P_{thO}$ ranges from ~1 to ~2.3 kPa (Fig. 5-18B). As shown in Fig. 5-18A, the sequential device consists of 5 main channels (with inlets and outlets shown in green, purple, yellow, pink and red, and named A, B, C, D, E, respectively). These channels are

equipped with valves of different sizes integrated at their inlets and outlets which allow the channels to be filled with 5 different solutions or chemicals. The other channel (Channel X in blue color) is specifically designed for the purpose of filling the sample solution (e.g., the permeate from Membrane 1) and can run through all 5 counterpart channels. For a simple demonstration of the valve system's capability, the 6 food color wells are kept initially at a constant height and connected to the inlets of 5 channels and channel X in the device, respectively. Connections to the air pumps are connected to dual pressure & vacuum pumps 1 and 2. Application of positive and negative pressures (by the dual pumps) to these channels enables controlling the valves opening and closing modes and subsequently leads to filling each channel with the color samples on demand.

Figure 5-18C demonstrates the process by which solutions A, B, C, D, E are sequentially injected into the channels. The pumps were adjusted by considering the $P_{thO}$ of the valves (see Fig. 5-18B). Initially, the valves connected to channel X were closed by applying $P_C$=4 kPa via pump 1. Next, the air channel controlling the 5 main channels was activated. In the first step, valve 4×4 was opened by applying $P_C$ =2.3 kPa via pump 2, which let solution A to flow through and fill channel 1 (see Fig. 5-18C(i)). As shown in Fig. 5-18C(ii), when $P_C$ is decreased to 2.1 kPa, channels 2 and 3 were filled with B and C due to the opening of valve 2×2. In the next step, by adjusting $P_C$ to 1.6 kPa, valve 1×1 opens, leading to the release of samples D and E into channels 4 and 5 (see Fig. 5-18C(iii)). Finally, pressure was applied to close all the valves connected to the 5 sample channels while pump 1 was released to open the remaining valves and letting sample solution X (shown in blue) running through the device (see Fig. 5-18C(iv) and (v)). The sample solution X, therefore, is able to run through all 5 main channel compartments and react with the samples in each of those channels. Using this approach, sequential logic controls (X+A, X+A+B, ..., X+A+B+C+D+E) can be obtained.

In another way, if X was inserted from inlets of individual channels A, B, C, D, E after coating time, the parallel logics (X+A, X+B, ..., X+E) can be achieved along with the sequential opening of valves connected to these channels. Similar parallel results can also be achieved if we use additional channels connect to original channel X to the

outlets of each individual channel A, B, C, ..., E with suitable pre-defined hydraulic resistances.

Having the capability of opening all of the valves on demand due to their different control pressures, it is possible to: (1) Selectively allow detection fluids/ permeate samples to run through pre-defined channels instead of allowing all channels at the same time, (2) Apply different opening time for different channels, (3) Achieve different combination of the primary sample/ permeate solution X with additional solutions A, B, C, D using only a single air-control line. The capability of using a single air-control line eliminates the need for several solenoid valves and DAQ controllers in a more complex system incorporating a much higher number of valves.

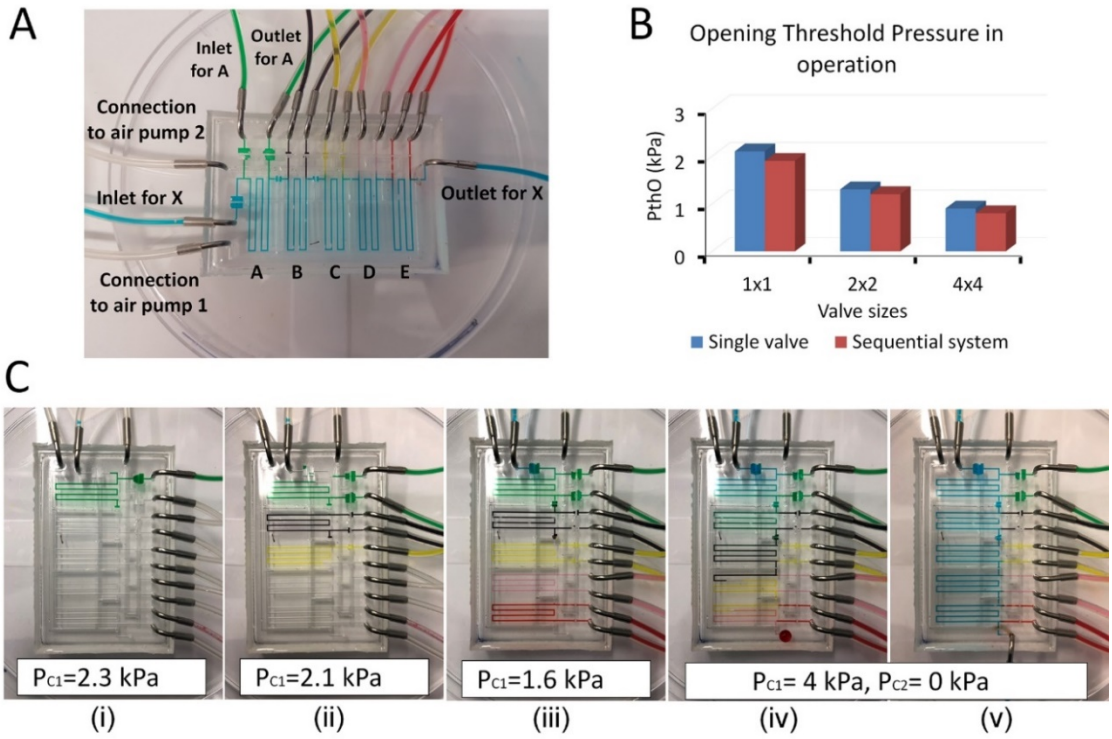


**Figure 5-18. Proof-of-concept of a 3D-printed sequential valving system for multiplexed fluidic control using food colors.** (A) Schematic of device in final coating process. (B) Opening threshold pressure of the valves operated as single valve and in the sequential device. (C) Operation of the sequential valving system: 5 main channels are first filled sequentially with A, B, C, D, E solutions (shown in green, violet and yellow, pink and red, respectively) before the X solution (in blue) runs through all channels. The operation is due to the different control pressures introduced by the pumps.

One limitation of the device is the $P_{tho}$ is affected by valve size due to 3D printing resolution and the limited range of valve size's difference, which consequently affects

the packing density of the portable device. Nevertheless, the different $P_{tho}$ can also be achieved by controlling coating material as presented in Fig. 5-7C. The printing resolution limitation is shared by most of the existing commercial 3D printers and the development of improved 3D printing materials and technologies [359], [360] can lead to a more compact portable system.

In brief, this system device is to make for further understanding of valving system control. Further discussion of when and how the valve system can support the development of the complex integration of mixing part (for the detection/ measurement of ions or specific component) to the portable device for kidney filtration application remains as future works.

## 5.7 Chapter Outcomes

This Chapter describes the analysis of a general normally-closed (NC) microvalves and one-way microfluidic diode valves (MDV) and the system of valves for portable kidney applications. New 3D-printed fabrication methods were presented to quickly and reliably produce these microvalves. As such, this work represents a pioneering work to design, fabricate, and test NC 3D-printed MDV valves using a full geometrical characterization and operational analysis.

Firstly, the experiments on the general NC valve revealed the correlation of the factors (valve sizes, valve-seat size, membrane thickness, coating materials) with a critical parameter: opening threshold pressure. Thus, it allows an effective switching control of the valves' open and closed states. A NC-valve-integrated microfluidic-logic system which can perform both sequential and parallel fluidic controlling logics was fabricated and tested. The valving system study proved the potential ability to use the valves in the portable kidney device system where the integration of complex permeate liquid handling (mixing, measurement or detection) is required.

Based on the characterization of the general NC valving unit, microfluidic diode valves were successfully fabricated and analyzed. The results showed that the valve successfully performed a diode-like function that allows unidirectional fluidic motion and negates backflow in the valve's close state. Maximum diode pressure could reach up to 4 Bar (about 80% of the target pressure for using RO membrane filtration (2-5

Bar) and surpass the pressure requirement for running an MD membrane (50 kPa). Further study showed that the diode valve's tolerance pressure could be improved through a higher resolution of 3D printing and improving 3D-printed surface roughness. Future works will be on using the larger boding area or more suitable material for improving maximum diode pressure and the development of a series of valves which allows mixing (for detection/ measurement) of filtration fluids. These findings are promising for applying these types of valves in fluid handling in the proposed small-scale portable kidney system.

# Chapter 6

# Membrane 2: Reverse Osmosis and Membrane Distillation for the Portable Kidney System

## Chapter Overview

*This aim of this Chapter is to explore Membrane 2 (Step 4 of the proposed multi-step filtration system, as shown in Fig. 3-1, Chapter 3) which mimics the critical tubule's filtration functions: urea removal and water reabsorption. As mentioned in previous chapters, the main reason for this Step is to eliminate the need for a dialysate input. Since urea has an extremely high affinity to water* [361]*, a key experimental measurement in this chapter is urea removal efficiency. Two approaches will be explored: reverse osmosis or membrane distillation, both of have been proven in the literature for water recovery but their ability to remove urea under-studied.*

## 6.1 Introduction

As outlined in Chapter 2, non-cell-based wearable/portable devices represent a promising, perhaps near-term alternative, to the ambitious research and development challenges of cell-based artificial kidneys. In Chapter 3, a proposed portable artificial kidney (pAK) system using a pre-filtration separation device and multi-step membrane filtration was proposed (See Fig. 3-1). As presented in Chapters 4 and 5, improvements in filtration efficiency (e.g., by using microspacers or, potentially, by 3D-printed membrane structures) integrated with microscale components (e.g., microvalves, micropumps or sensors) can result in a miniaturized system. A major barrier to portability for conventional dialysis machines is that they require a dialysate system. A dialysate system would require a large volume liquid to be carried with the system and it needs a to be frequently changed. This significantly increases the total system weight and reducing the portability.

The removal of urea, the primary waste product of the metabolism process, is another major challenge for the realization of the proposed pAK system. Given these two challenges, this chapter explores two filtration mechanisms (reverse osmosis and membrane distillation) to study the feasibility of a dialysate-free system capable of removing urea.

### 6.1.1 Urea Removal and Multi-step Filtration Mechanism

As was discussed in Fig. 2-6 (Chapter 2), non-cell-based (NCB) mechanisms: hemodialysis and its miniaturized version (WAK) are one-stage filtration systems, typically using hollow-fiber membranes. In contrast, the cell-based RAD, iRAD devices, and the bioengineered kidney utilise a two-stage mechanism (filtration and reabsorption) which mimics the natural kidney. However, these solutions face the complexities of taking on the metabolic functions of the kidney will also be catering to living cells, which adds many more challenges (see Fig. 2-6). In this thesis, the NCB multi-step filtration system (including Membrane 1 and Membrane 2) is proposed to have potential to bridge between the two cases [see Fig. 2-6 A and B (Chapter 2)] [13], [129].

The target filtration for the proposed system is the removal is nano-size components including urea (60 Da), creatinine (113 Da) and uremic components (~500 Da) from water, as shown in Fig. 2-8 (Chapter 2). Unfortunately, the sizes of these waste components fall between good components which need to stay in the bloodstream (such as water and salt). This makes a single-step dialysate-free ultrafiltration unit, unsuitable. So, the choice of using multi-step filtration supports the target filtration removal and Membrane 2 plays the crucial role in this work. In addition, continuously reclaiming the water reclaim water without taking urea, creatine, and other uremic compounds with it has not yet been demonstrated for the system. It should be noted that if urea (60 Da) can be removed by Membrane 2, the following toxic substances such as creatinine (113 Da), uremic acids (several hundred Daltons) will also be removed.

### 6.1.2 Urea Characteristics

Urea is made during metabolism, when proteins are broken down in the liver and via the deamination of amino acids (the monomers that make up proteins) under the secretion of enzymes. Urea is toxic, so it must be removed at kidneys through the bladder in the form of urine [362]. As mentioned above, may be difficult to separate urea from water/ filtered plasma in Membrane 2. This is due to the following: (1) Like water, the urea molecule is polarizable and has no charge in suspension [361]; (2) urea is neither a strong base nor a strong acid; (3) it is neither very nucleophilic nor electrophilic [363]; and (4) Like water, urea has a low molecular weight, (5) it can form hydrogen bridges and, therefore, has a high affinity to water, and (6) because of its non-reactiveness, only a few substances can attack urea in the presence of water and only under extreme conditions [363], [364].

The above list essentially leaves us with only one viable, but relatively difficult, option: membrane-based filtration. The good news is that, apart from dialysis, there have been a few commonly used membrane-based technologies that can separate low-molecular-weight molecules (e.g., salt) from water-based solutions. For comparison, the physical properties of water, urea and sodium chloride are shown in Table 6-1.

**Table 6-1. Basic physical properties of filtration molecules**

| Properties | Water | Urea | Salt (common) |
|---|---|---|---|
| Molecular weight | $H_2O$ | $CH_4N_2O$ | NaCl |
| Molecular weight | 18.01 | 60.06 | 58.44 |
| Density | 0.998 g/cm$^3$ (20°C) | 1.32 g/cm$^3$ | 2.17 g/cm$^3$ |
| Appearance | Clear liquid | Transparent in solution | Transparent in solution |
| Melting point | 0.0 °C | 132-135 °C | 801 °C |
| Equilibrium vapor pressure | 6.27 kPa (37 °C) | <0.01 kPa (20 °C) | 0.133 kPa (865 °C) |
| Boiling point | 100 °C | 332.48°C (estimate) | 1465 °C (2,669 °F; 1,738 K) |

It should also be noted that Urea also has a low melting point and boiling point compared to sodium chloride, but the parameters are still higher than water. This can enable thermal-driven membrane separation process (i.e., membrane distillation).

### 6.1.3 Reverse Osmosis

Since the molecular weight of urea (60 Da) is very similar to sodium chloride (a common salt with a molecular weight of 58.5 Da), membranes used in salt removal processes (desalination) have potential for use for urea removal, though efficiency can be lower (since urea is an uncharged molecule) [365]. Thus, reverse osmosis membranes which are commonly used in the desalination industry [259], [366], [367], have the potential for urea removal.

Reverse osmosis (RO) is named for a water purification process that uses a partially permeable membrane to reject particles from passing through a membrane relative to "pure" water. In this process, a high enough pressure must be applied on the feed channel to overcome osmotic pressure, an intrinsic property that is driven by chemical concentration differences of the solvent. To date, RO is the leading technology for *desalination* installations all over the world [259].

During the RO process, the ions (or unwanted molecules and particles) are retained on the feed side of the membrane and the pure water/ solvent can pass through to the other side. Although ion diffusion does occur, RO membranes can reject a high

percentage of nano-size substances and monovalent ions, while other membranes, including nanofiltration (NF), ultrafiltration (UF), and microfiltration (MF), are designed to remove larger size particles. As shown in Fig. 6-1, UF and NF membranes are categorized by the molecular weight cut off (MWCO) barrier of the membrane, where the membrane will retain at least 90% of the solute in solution [259]. The general MWCO ranges for UF and NF are 2000–500,000 Da and 250–2000 Da, respectively. MF is usually characterized by a nominal pore size (0.05 µm–10 µm) or by the membrane's rejection (90% rejection of a specific particle size in µm).

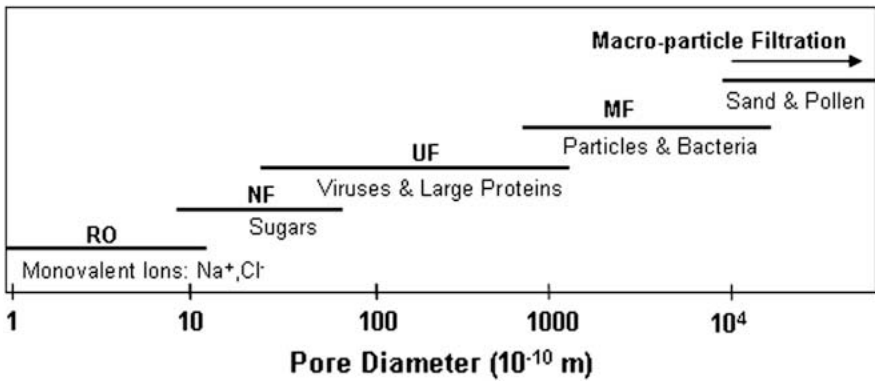


**Figure 6-1. The nominal pore diameter range of some commercially available membranes** [368]**.**

In a typical membrane process where the fluid is forced through the membrane by an applied hydraulic pressure, filtration also depends upon the membrane porosity (and the thickness of the membrane). At the same time, the fluid flux through the membrane occurs due to diffusion. Therefore, the transport is determined by pore flow and diffusion and can be described as follows [369]:

$$N_{Ax} = \frac{\rho_A k}{\mu}\frac{dp}{dx} - D_{AB}\frac{dp_A}{dx} \quad (6\text{-}1)$$

where $N_{Ax}$ is the mass flux of A in the x-direction (perpendicular to the membrane surface), $\rho_A$ is the mass density of A, $k$ is the permeability, $\mu$ is the viscosity, $dp/dx$ is the pressure gradient in the x-direction, and $D_{AB}$ is the diffusion coefficient for the diffusion of A in the membrane B.

For the membranes with larger pore-size (e.g., MF and UF), diffusion is negligible compared to the pore flow (the convection factor). Solvent transport through smaller pore-size membranes (e.g. NF) occurs through a combination of convective flow and

diffusion [370], [371], and is primarily controlled by diffusion [372]. For RO membranes, however, transport is controlled by diffusion since no open channels exist for pore flow. Based upon this fact, RO transport has been named “solution-diffusion” [373]–[375]. In this mechanism, the water concentration gradient (water-membrane) across the membrane causes the water molecules to diffuse down to the permeate side of the membrane. The water molecule then desorbs from the membrane and becomes part of the bulk permeate [373], [374].

Although a large amount of work has been done on reverse osmosis (RO) membranes, the majority of it has been directed towards water treatment and desalination applications [376]. There is limited information available on the use in artificial kidneys and the rejection of urea by RO membranes. However, RO membranes have been tested for urea removal over the last 40 years ago in connection with two applications: regeneration of water for a miniature artificial kidney [364], [365] and water reclamation from urine during prolonged space flight [351], [377]. Specifically, in one report by Kraus et al. [365], the urea-rejecting properties of a few aromatic polyamide membranes had shown to regenerate dialysate water in a peritoneal dialysis-based artificial kidney. Good urea rejection of 92-96 % and filtration rates of 80-180 $L.m^{-2}$ per day from an aqueous urea solution (1000 ppm NaCl + 5000 ppm urea) were achieved at the pressure input of about 51 Bar.

The main advantages of RO filtration are that it requires a simple setup and ensures the removal of most of waste metabolites (e.g. >99% of proteins, >95% of salts , and ~70-96% of urea with polyamide membranes [129], [365], [378], [379]). The disadvantage of RO, however, is the requirement of high driving pressure (minimum 2 Bar, typically) which can damage cells and biological components in the bloodstream. Because of this pressure requirement, in some previous studies [361], [365], RO is not used directly in the filtration of blood or plasma but only in filtering the substitute solutions (e.g. dialysate) to reclaim clean water. Similarly, in this thesis (See Fig. 3-1 in Chapter 3 and Fig. 6-2 below), no cells or proteins are input into Membrane 2. Thus, pressure requirements of an RO membrane can be used directly to reclaim water from the protein-filtered plasma. In addition, the recent development of microfluidic

technologies [21], materials [8], [79], 3D printing [380] and advances in RO membrane research [259], [376], can be pulled together for a miniaturized RO membrane system.

A more specified schematic description of the proposed multi-step PAK system with Membrane 2 (using RO/ MD membrane) is given in Fig. 6-2.

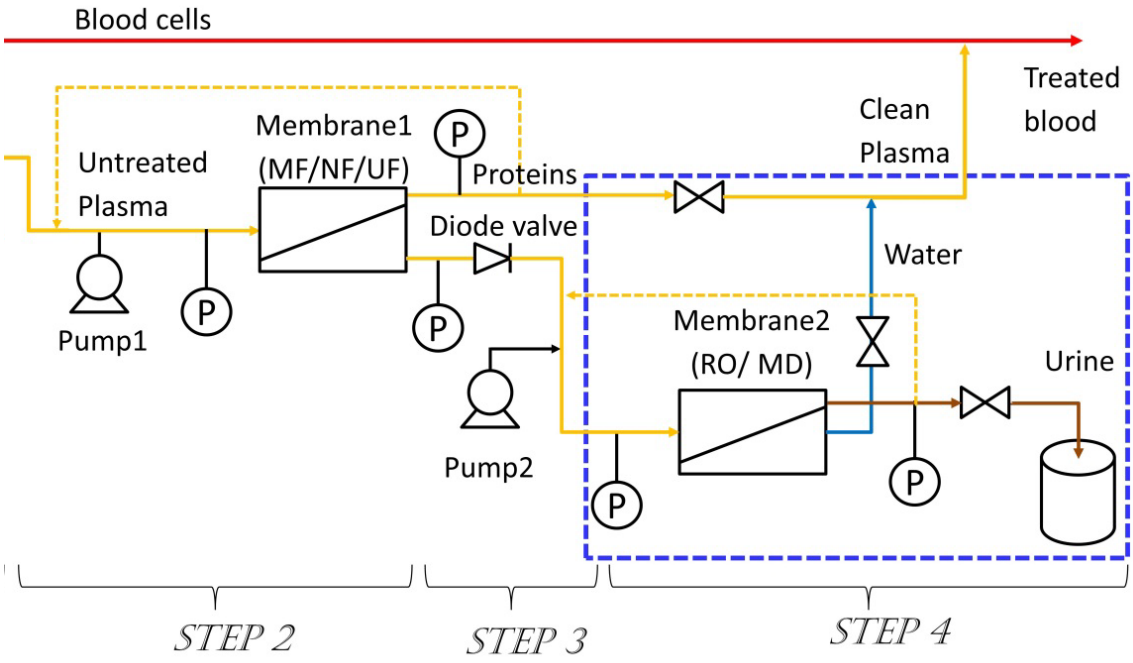


**Figure 6-2. Schematic representation of the Step 2 to Step 4 in the proposed portable artificial kidney (pAK) mechanism.** The light blue dash box (containing Membrane 2, Step 4) is the focus of this Chapter.

It should be also noted that RO rejects salt. But it is extremely important to maintain the salt concentration level in blood stream while using an artificial kidney system. Thus, the development of clever selective membranes and the use of supplement solutions (e.g., saline which has been using in dialysis [12], [381]), dietary supplements or additional tablets for patients that can compensate salt losses in the proposed system is necessary.

### 6.1.4 Membrane Distillation

Although Reverse Osmosis (RO) is the most widely developed commercial desalination technology, a thermally-driven membrane distillation (MD) process may also achieve the same objective of removing low- molecular weight molecules [353], [382], [383].

MD has been studied for a variety of applications including wastewater treatment [384] and the concentration of fruit juices, radioactive solutions [385], acids, dyes and valuable salt and minerals [386]–[388]. Recent interest in MD systems has focused on the filtration of high salinity feeds (using thermal energy), where RO and other technologies are not suitable [389]–[391]. MD has a higher salt rejection rate in comparison with RO in high salinity fluids [392] because it is not limited by the osmotic pressure. This is useful because human blood plasma has a high salinity of sodium, in the range of 137 to 142 $mEq.L^{-1}$ (about 8 $g.L^{-1}$).

In the MD process, the feed side is a hot-temperature solution (e.g. 50-80°C) and permeate side is cooled directly or indirectly (typically at about 35°C or lower) [393]. Pure water and volatile compounds are able to evaporate at the interfacial surface of the membrane on the hot feed side, diffuse through the microporous membrane structure, then condense and are extracted at the cold permeate side [393]. The driving force of the vapor movement is a partial vapor pressure difference commonly triggered by the temperature difference. The membrane used in this process is a hydrophobic microporous membrane which presents a barrier for the liquid phase, allowing the only the vapor phase (i.e., water vapor) to pass through the membrane's pores. As can be seen in Fig. 6-2 below and Fig. 3-1 (Chapter 3), the feed for Membrane 2 is already a cell-free and protein-filtered after Step 1 (Cell separation) and Step 2 (Membrane 1 filtration, typically 68 kDa pore-size). This solution can be used as the feed for Membrane 2 and the concentrate can be discharged to bladder/ waste after filtration.

Depending on target filtration and MD configuration, the liquid entry pressure (wetting pressure), membrane thickness, and porosity and tortuosity should be considered. Hydrophobic (non-wetting) microporous membranes are used in the MD process. These membranes are typically made from polytetrafluoroethylene (PTFE), polypropylene (PP), Polyethylene (PE) or polyvinylidene fluoride (PVDF), sometimes incorporating coatings [264]. The mean pore size for these membranes are typically around 0.2-0.5 (µm) and their permeability varies over the range of 10-200 $L.m^2.h^{-1}.Bar^{-1}$) [260], [394].

## What Happens to Urea at Elevated Temperature?

For MD membrane filtration to work, a hot-temperature (e.g., 50-80°C) will be applied to the feed solution. A potential concern is that the elevated temperature may cause chemical reactions to change the urea characteristics/ level in the permeate. The following hydrolysis reaction is possible [395], [396]:

$$NH_2CONH_2 + H_2O \Leftrightarrow 2NH_3 + CO_2 \quad (6\text{-}2)$$

Wherein urea gets converted to ammonia and carbon dioxide. The process goes through an intermediate step, where ammonium carbamate is created:

$$NH_2CONH_2(l) + H_2O(l) \Leftrightarrow H_2NCOO^- + {NH_4}^+ \quad (6\text{-}3)$$

Then, the ammonium and carbamate ions react, resulting in carbon dioxide and ammonia gases:

$$H_2NCOO^- + {NH_4}^+ \Leftrightarrow CO_2(g) + 2NH_3(g) \quad (6\text{-}4)$$

It has been revealed that temperature plays a significant role in this hydrolysis process [397]. Under a normal industrial processing conditions, with steam at 380 °C and 2.45 MPa [398], urea is hydrolyzed to ammonium carbamate and the carbamate is decomposed to ammonia and carbon dioxide. The intermediate reaction (shown as Eq. 6-3) is a slow and exothermic process, whereas the reaction shown in Eq. 6-4 is a fast and endothermic. Thus, the reaction rate of Eq. 6-3 controls the rate of the overall thermal hydrolysis process. Generally, this thermal hydrolysis rate is influenced by the temperature of the solution, the pressure, and the concentration of urea, with temperature being the controlling factor. Besides improved reaction kinetics, the higher temperature improves the breakdown of the by-products to ammonia.

According to some previous works, only at a low-enough pressure and a high temperature (>120 °C), the breakdown of the by-products to ammonia happens, thus, it is able to complete the hydrolysis process [398]–[400]. In MD filtration process, however, the water temperature for the feed solution was heated up to less than 80 °C (353.15 K). Therefore, typically, over this range of temperature, sufficient energy will not be available to overcome the activation energy for the reaction (6-4). The urea water (feed) solution at this temperature range is considered as a weak electrolyte

solutions [397] according to (6-3); urea (and salts) molecules are present in the 'hot' feed but they are non-volatile [397]–[399]. Therefore, at the MD working temperature range (45 - 80 °C), only water would evaporate and pass through the MD membrane system.

In brief, the aim of this Chapter is to clarify the feasibility of the two approaches: reverse osmosis and membrane distillation for Membrane 2 compartment of the proposed pAK system, by: (1) Building up the RO and MD systems for testing these filtration technologies, (2) Analyzing permeate flux and energy input of each technique, (3) Analyzing salt and urea rejection rates, (4) Discussing about challenges and solutions, and comparing these techniques with conventional dialysis.

## 6.2 Materials and Methods

### 6.2.1 Reverse Osmosis (RO) Materials and System Setup

A Toray flat-sheet polyamide-TFC RO membrane (UTC-73HA, Sterlitech) with a filtration area of 4 cm × 10 cm (0.004 $m^2$) and salt rejection level of 98.7-99% was utilized as the middle layer of the RO filtration unit. The fabrication process for the RO filtration module was presented in Chapter 3, Fig. 3-12. Based on the result of Chapter 4, a gyroid 3D-printed spacer design (which has highest filtration efficiency) was integrated in the top channel.

Like Membrane 1's configuration, a simple three-layer structure was used for the flat-sheet unit for the RO experiments. The assembly of the feed inlet (top) and permeate (bottom) parts and the selected RO membrane (middle) is displayed in Fig. 6-3A(ii). The feed flows from inlet through the device to concentrate outlets (top), letting the permeate go through the membrane, where it can be collected at the permeate outlet (bottom).

Fig. 6-3B shows a full experimental setup for a RO test with Membrane 2. A high-pressure portable electric diaphragm pump (STARFLO FL-200, capable of a maximum pressure of 13.8 Bar at a flow rate of 10 L/min) was used to circulate the feed solution through the filtration unit. The feed operating pressure is set in the range of 5-10 Bars by adjusting the valve and pump controller. The inlet and outlet pressures on the feed

channel, $P_I$ and $P_O$, respectively, were measured by two pressure gauge sensors (OMEGA, Model PX309-150G5V and PX309-100G5V, with maximum 10 Bar and 7 Bar, respectively, connected to a National Instruments NI USB-9174 Digital I/O device and LabVIEW software). A simple code was developed to handle the continuous pressure measurements. The permeate flux was measured automatically by weighing the permeate-side outlet liquid. This job was done by connecting the electronic balance (Mettler Toledo New Classic ML3002 balance, with a resolution of 0.01 mg) through PC-direct operation via RS232 serial port. Mass measurements were recorded every 30 seconds to check the operational permeability of membrane and permeate flux of the filtration process.

To prepare for the filtration tests, new membranes were put into the device for running with water at TMP 1 Bar for 30 min and leaving for 8 hours overnight. The filtration performance tests were then conducted and the permeate weight was recorded at 30 second intervals.

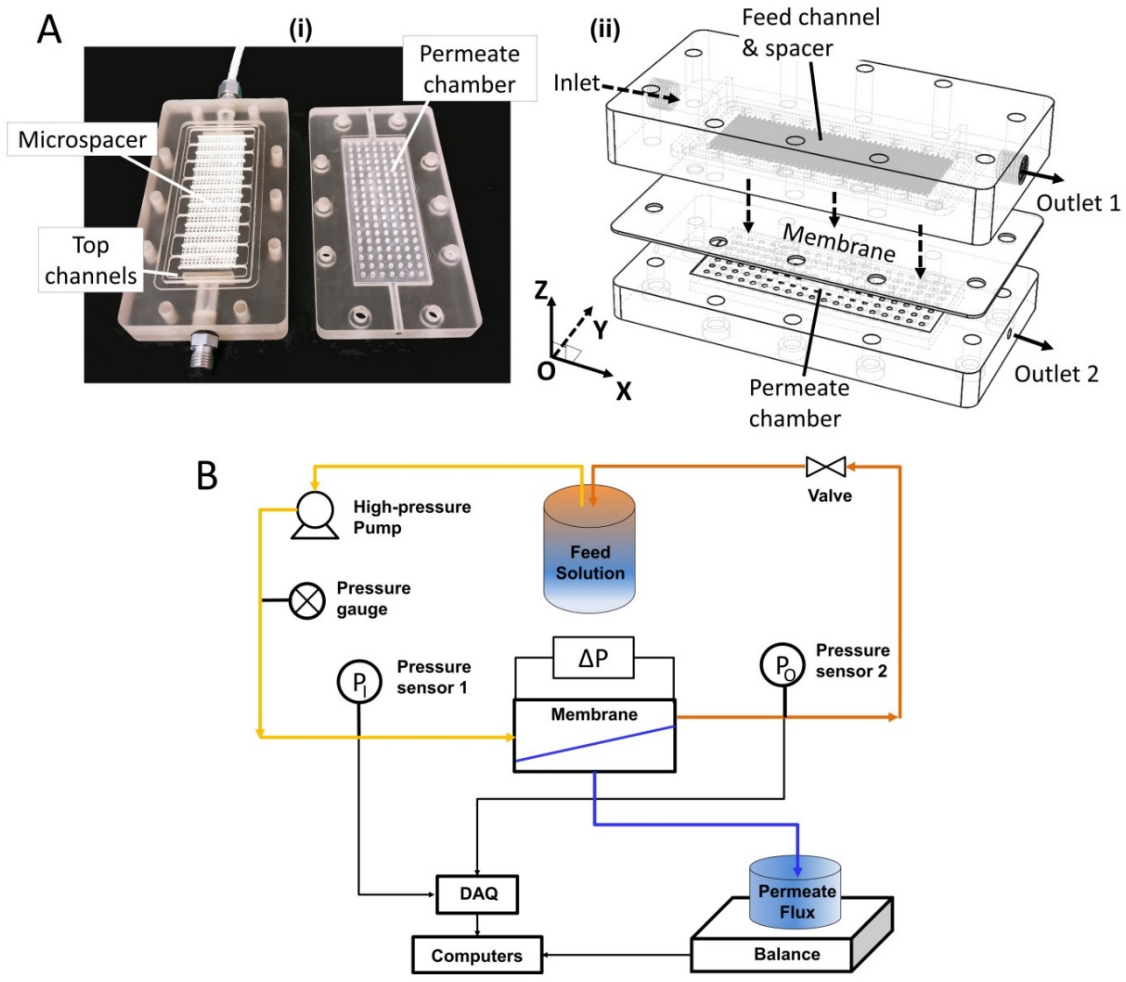

**Figure 6-3. Membrane 2 performance test using Reverse Osmosis technique.** (A) (i) 3D printing products (ii) Flat-sheet filtration module, (B) Experimental setup. The setup includes a diaphragm pump, feed and permeate tanks, a filtration module, power supplies, an additional pressure gauge for safety control, and devices for permeate recoding, and pressure measurements.

***Numerical Analysis***

Mass transport through RO membranes can be calculated as follows [259], [369], [372]:

$$N_A = L(TMP - \Delta\pi) \tag{6-5}$$

where $N_A$ is water flux through the membrane, L is the permeability coefficient, $TMP$ is the transmembrane pressure, and $\Delta\pi$ is the osmotic pressure difference between the feed and the permeate membrane surface.

For a thermodynamically ideal solution, osmotic pressure can be calculated based on ion concentration (e.g., salt) and the solution temperature as follows [259], [401]:

$$\pi = CRT \tag{6-6}$$

where C is the ion concentration (mol/L), R is the ideal gas constant (0.08206 L atm/mol K), and T is the operating temperature (K).

The flux through Membrane 2 was calculated from measured values of the flow rates, elapsed time, and geometry based on flow through the membrane and equation (3-1) (in Chapter 3) [12], [248]:

$$J_{M2} = \frac{V_F}{A \times T_F} \tag{6-7}$$

where $V_F$ is the measured volume of the permeate (L), $T_F$ is the filtration time (hour), A is the area of the membrane ($m^2$).

Membrane salt/urea rejection (R) is a measure of overall membrane system performance and is given by the equation (3-5) (in Chapter 3) (for membrane with crossflow operation) [402]:

$$R = (1 - \frac{C_{permeate}}{C_{feed}}) \times 100\% \tag{6-8}$$

Normally, RO membranes achieve a salt (NaCl) rejection rate of 98–99.8% [402] (while NF membranes exhibit rejection values greater than 90% for multivalent ions and between 60 and 70% for monovalent ions) [403], [404]. Urea rejection can be related,

but will generally be at a slightly lower rate compared to the salt rejection of RO membrane [365].

### 6.2.2 Membrane Distillation (MD) Materials and System Setup

Since the MD permeate is in vapour state, the nanopore-size of membrane and the high-pressure input of RO system are not necessary in a MD configuration. Instead, the membrane can be microporous and hydrophobic. For this work, hollow-fibre membranes (HFM) were used in this test for higher packing density [405], [406]. To enhance the flux further, a vacuum-based MD system (VMD) was used in these experiments and due to its availability in the lab.

As shown in Fig. 6-4A, the VMD unit consists of 20 pieces of hollow-fibre (HFM) Polypropylene (PP) membranes (ACCURL® PP S6/2, a porosity of 70%, a mean pore radius of 0.2 $\mu m$, a tortuosity of 2, and a membrane thickness of 0.45 mm), each of which has an outer diameter of 2.7 mm with an active length of 100 mm, providing a membrane area of 0.016 $m^2$ per module. The HFM membranes were potted by epoxy in an array housed by an acrylic tube shell (40 mm in diameter). The design also contains PVC end caps and vacuum port (Type: KF25). The liquid feed flow in/out is on the shell side of the MD module and the water vapor can be 'pulled' out from the lumen side of the HFM membranes through the vacuum port. To prevent leakage from the feed and permeate side of the module, nitrile O-rings are inserted between all mating surfaces/joints (e.g. between feed tube, shell flanges, PVC end caps, potting tubes) (Fig. 6-4Bii)[391].

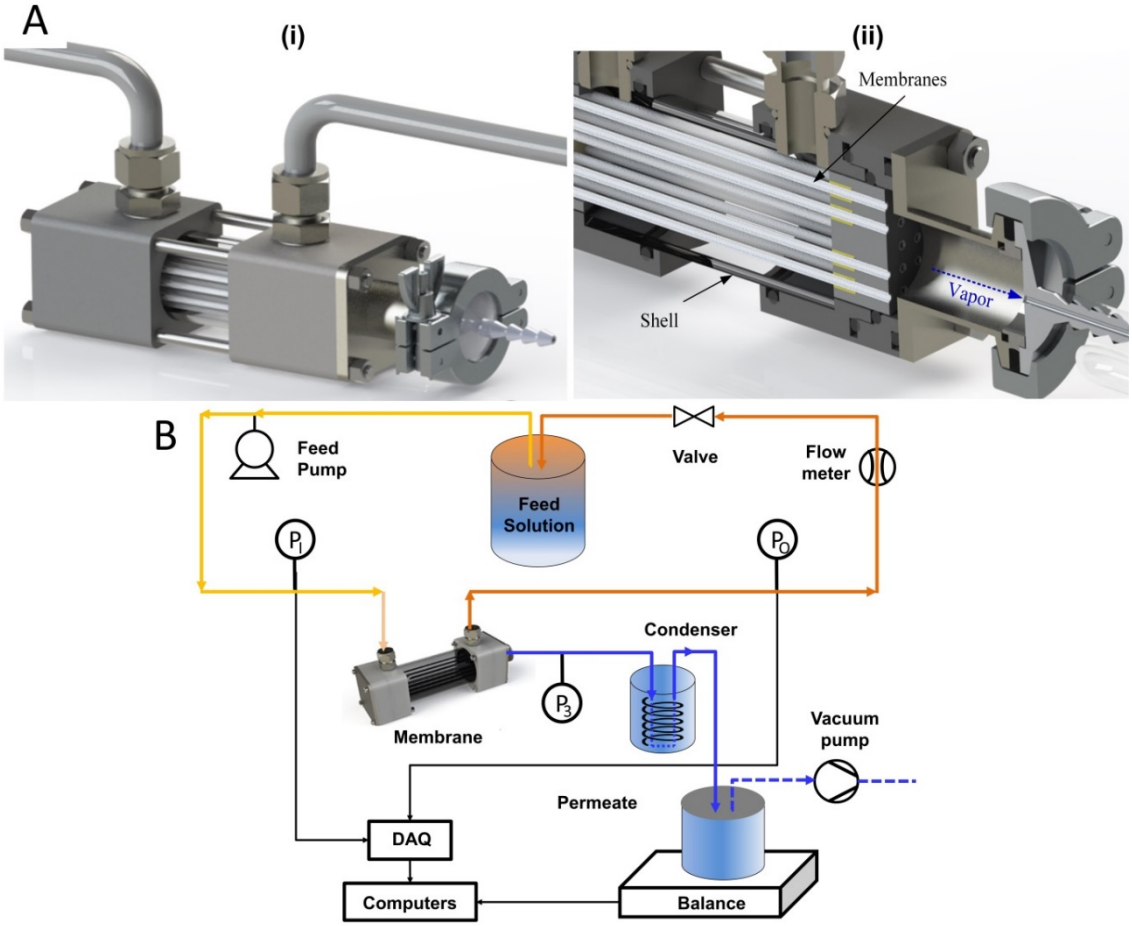


**Figure 6-4. Membrane 2 performance test using Membrane Distillation technique.** (A) The hollow fiber vacuum membrane distillation (VMD) module design: (i) 3d view of module, (ii) Cross section view of the module; (B) Experimental setup. The setup includes small-size diaphragm and vacuum pumps, feed and permeate tanks, a condenser, filtration module and a DAQ for pressure sensors, a scale, computers.

### *MD Module and Experimental Setup*

The test rig (Fig. 6-4B) consists of a water bath (Model: Julabo ED), one VMD module, 1 set of vacuum tanks and vacuum pump, and a water condenser consisting of a coil submerged in cold water. The feed solution was heated up and maintained at a temperature in the range of 45-70 °C before being pump into the shell/feed side of VMD module. The filtration process was then started by opening the vacuum pump which triggers permeate from feed to permeate collection chamber (vacuum pressure was set at the range 5-10 kPa). RTDs (4 wires, PT100) were used to test the temperatures of the inlet/outlet of feed, and pressure transmitters (CB1020/CE1010, LABOM) were used to measure the vacuum pressures of permeate sides. Temperature

and pressure measurements were recorded using a data acquisition system (c-Daq-9174, National Instruments). One DC water pump (4.5-12 V) was used to pump the feed solution through the system, while the feed temperatures were controlled by the water bath settings. Permeate vapor produced from module was directed into the coil condenser. Finally, the condensate was collected in the permeate tanks, while the vacuum pressure was adjusted by pressure regulator valves.

***Numerical Analysis***

The permeate flux, *J* [*kg m$^{-2}$ s$^{-1}$*], from the VMD module can be calculated by Eq. (6-9) [407]:

$$J = 0.018K_w \cdot \nabla P = 0.018 \cdot K_w \cdot \left(P_f^{Sat} - P_v\right) \quad (6\text{-}9)$$

Where $P_f^{Sat}$ is the vapor pressure at the feed side of the membrane interface, $P_v$ is the vacuum pressure on the permeate side of the membrane; 0.018 *[kg/mol]* is the molecular weight of water, and $K_w$ denotes the vapor permeability of this Polypropylene membrane obtained by the previous experimental study [407]. The saturated water vapor pressure of a solution can be calculated by the Antoine coefficients ($a_A$, $b_A$ *and* $c_A$), which are given in Table 6-2 [407]. Alternatively, the permeate flux (mass transfer through the membrane) can also be obtained by Darcy's law and the Knudsen flow model [408].

The (latent) heat transfer rate *[W]* of the MD (water evaporating) in the HFM MD module ($\dot{Q}_{ev}$) can be calculated as [409]:

$$\dot{Q}_{ev} = \dot{m}_{ev} \cdot h_{fg} \quad (6\text{-}10)$$

where $h_{fg}$ is the enthalpy of evaporation with phase change from fluid to gas/ vapor *[kJ/kg]* (value is given in Table 6-2), while the permeate mass flow rate ($\dot{m}_{ev}$) *[kg/s]* can be calculated by Eq. (6-11), where the heat transfer area (membrane area), $A_{mem}$, is 0.016 m$^2$ per module.

$$\dot{m}_{ev} = J \cdot A_{mem} \quad (6\text{-}11)$$

The heat transfer coefficient (HTC) from feed to the membrane, $h_{\text{f-mem}}$, can be obtained from a correlation developed by Mengual et. al, which has been experimentally validated for Re ranging from 250-2,500 in a shell-and-tube HFM membrane module [410].

$$Nu = \frac{h_{f-mem} L_c}{k_l} = 0.206(Re \cdot \cos\theta)^{0.63} Pr^{0.36} \quad (6\text{-}12)$$

Where *Pr* and $k_l$ are the Prandtl number and thermal conductivity of feed solution. The outer diameter of the membrane $d_{mem}$ can be used as the characteristic length $L_c$. θ is yaw angle of the membrane module, θ is chosen as 87° in this case of more parallel flow than cross flow [410].

The Reynolds number is defined based on maximum crossflow velocity as below:

$$Re = \frac{\rho_l \cdot V_f \cdot L_c}{\mu_l} \quad (6\text{-}13)$$

Where $\rho_l$ *and* $\mu_l$ represent the density and dynamic viscosity of feed solution (shown in Table 6-2), and the velocity across the HFM membrane ($V_f$) can be calculated by considering the mean shell side velocity, membrane transverse pitch between fiber centers, $S_{mem}$, and membrane diameter, $d_{mem}$ [411].

The heat transfer rate transferred from feed to feed-membrane interface in the module can be expressed as:

$$\dot{Q}_{f-mem} = h_{f-mem} A_{mem} \left(T_{\text{f,ave}} - T_{\text{mem,ave}}\right) \quad (1\text{-}14)$$

According to conservation of energy during the heat transfer process:

$$\dot{Q}_{ev} = \dot{Q}_{f-mem} \quad (6\text{-}15)$$

Solving the nonlinear equations was done with the Solver function in Excel or via Matlab algorithm by using an iterative procedure. Thus, given the operating conditions (e.g., feed inlet temperature, salt concentration, feed mass flow rate and permeate vacuum pressure), it is possible to determine the membrane surface temperature ($T_{mem}$) and permeate vapor flux (*J*).

**Table 6-2. Parameters assumed in the performance analysis** [391]**.**

| Symbol | Value | Unit | Symbol | Value | Unit |
|---|---|---|---|---|---|
| $D_{mem}$ | 2.7 | mm | $K_w$ | $7.53 \times 10^{-6}$ | Mol $m^2$ $s^{-1}$ $Pa^{-1}$ |
| $A_b$ | 0.014 | $m^2$ | $A_{mem}$ | 0.016 | $m^2$ |
| $a_A$ | 10.2 | - | $Pr$ | 1.85-3.55 | - |
| $b_A$ | 1730.6 | - | $k_l$ | 0.65-0.67 | W $m^{-1}$ $K^{-1}$ |
| $c_A$ | -39.7 | - | $\rho_l$ | 994.0 | Kg $m^{-3}$ |
| $c_p$ | 4190.0 | J $Kg^{-1}$ $K^{-1}$ | $\rho_v$ | 0.05 | Kg $m^{-3}$ |
| $G$ | 9.8 | m $s^{-2}$ | $\mu_l$ | 0.0003-0.00072 | Kg $m^{-1}$ $s^{-1}$ |
| $h_{fg}$ | 2300-2400 | kJ $kg^{-1}$ | $P_v$ | 5000-40000 | Pa |
| $h^*_{fg}$ | 2350-2450 | kJ $kg^{-1}$ | $S_b$ | 15 | mm |
| $H_b$ | 32.0 | mm | $S_{mem}$ | 6.5 | mm |
| $v_l$ | $0.3\text{-}1.0 \times 10^{-6}$ | $m^2$ $s^{-1}$ | $h_{gf}$ | 2257 | kJ $kg^{-1}$ |

### 6.2.3 Energy Calculation

#### *RO energy consumption*

The hydraulic pumping power ($Q_{RO}$) *[kW]* can be calculated based on the equation [412]:

$$Q_{RO} = \frac{Q \cdot \Delta P}{60000} \tag{6-16}$$

where $Q$ is the flow rate *[L/min]* and ΔP is differential pressure across the pump (kPa).

#### *MD energy consumption*

The heating energy ($Q_H$) *[W]* for MD feed can be obtained as below [413]:

$$Q_H = Q_f \cdot C_{p-f} \cdot (T_{f-in} - T_{f-out}) \tag{6-17}$$

where $Q_f$ is the feed flow rate (kg/s); $C_{p\text{-}f}$ is the feed specific heat (J/(kg. K)), $T_{f\text{-}in}$ the feed temperature at the module inlet (K); $T_{f\text{-}out}$ the feed temperature at the module outlet (K).

The cooling energy ($Q_C$) *[W]* for the permeate include latent heat ($Q_{C\text{-}L}$) for water condensing (phase change from gas to fluid) and the sensible heat ($Q_{C\text{-}S}$) for vapor temperature drop.

$$Q_C = Q_{C-L} + Q_{C-S} \tag{6-18}$$

The (latent) heat transfer rate *[W]* of the MD module ($\dot{Q}_{C-L}$) can be calculated as [61]:

$$\dot{Q}_{C-L} = \dot{m}_{ev} \cdot h_{gf} \quad (6\text{-}19)$$

where $h_{gf}$ is the enthalpy of condensation with phase change from gas/ vapor to fluid *[kJ/kg]* (value is given in Table 6-2) [414], while the permeate mass flow rate ($\dot{m}_{ev}$) *[kg/s]* can be calculated by Eq. (6-11). Thus, the (latent) heat transfer rate:

$$\dot{Q}_{C-L} = h_{gf} \cdot J \cdot A_{mem} \quad (6\text{-}20)$$

Sensible heat transfer of the MD module ($Q_{C-S}$) can be calculated as [413]:

$$Q_{C-S} = Q_p \cdot C_{p-p} \cdot (T_v - T_p) \quad (6\text{-}21)$$

Where $Q_p$ is the feed flow rate (kg/s); $C_{p\text{-}p}$ is the permeate specific heat (J/(kg K)), $T_v$ is the saturated vapor temperature, $T_p$ is the condensed permeate temperature. For this test, a 7.5-10 kPa vacuum pressure was used, therefore, $T_v$ is about 44°C [415].

Energy needed for inlet pump and vacuum pump ($Q_{MD\text{-}p}$) can be also calculated following equation (6-16).

Energy consumption (total) can be calculated as:

$$Q_{MD} = (Q_h + Q_C + Q_{MD-p})/GOR \quad (6\text{-}22)$$

Where GOR is gained output ratio which typically, range from 1 to 5 depending on the heat recovery efficiency (i.e., the heat associated with water vapour) [416], [417].

### 6.2.4 Solution Testing Preparation

A uremic plasma mimicking solution (UMS) which contains plasma mimicking solution, and urea was used in these Membrane 2 experiments using different concentrations of salt (0, 1, 3, 8 $g.L^{-1}$, respectively) and a constant urea concentration of 3 $g.L^{-1}$ or 50mmol/ L (similar to blood-urea-nitrogen (BUN) level at ~140 mg/dL). This urea concentration was selected because it is considered as the highest level present in patients with end-stage kidney failure [262], [263]. Detailed information about solution preparation is described in detail at Chapter 3.3.

### 6.2.5 Measurement and Characterization

#### 6.2.5.1 Pump control, flowrate and pressure drop measurement (RO membrane system)

As seen in Fig 6-3 above, a high-pressure diaphragm pump was used for supplying inlet pressure for the RO filtration module. The feed operating pressure was set in the range of 2-10 Bars by adjusting the valve and the voltage of the DC power supplier. With the inlet pressure supplied to the RO membrane module, a certain value of feed flowrate was generated. Figure 6-5A and B show the linear relationships between the supplied voltage to the input pressure and between the feed flow rates and the input pressure. As can be seen in Fig. 6-5B, flowrate depends on the applied pressure but is almost independent from salt concentration. This is because the permeate flowrate is much smaller than the feed flowrate, therefore, a slight change of permeate flowrate (due to elevated osmotic pressure) will not make a significant difference in the feed flowrate.

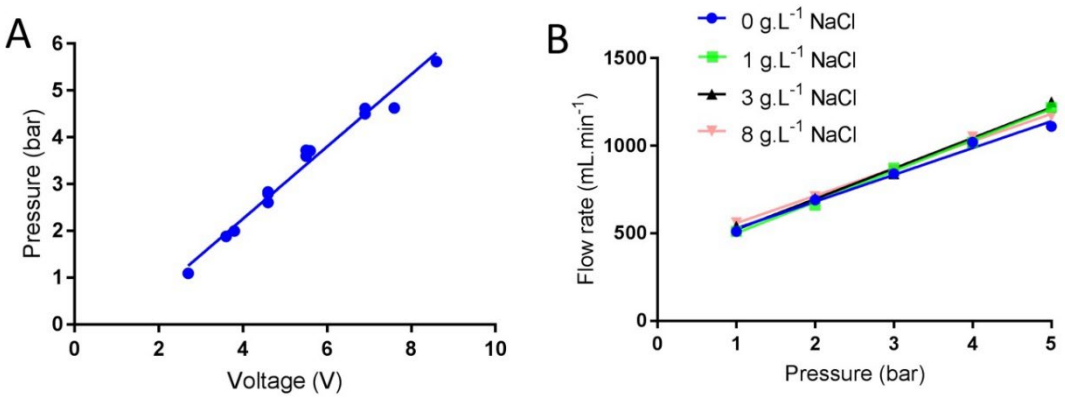


**Figure 6-5. Pump control, flowrate and pressure drop measurements (RO membrane system).** (A) Voltage control value and corresponded feed pressure, (B) Pressure and flowrate relation.

#### 6.2.5.2 Permeate and Flux Measurements

To measure flux, the mass of the permeate was recorded periodically using an electronic balance with its auto record function as described in the details of RO

system setup above. In Fig. 6-6A, the recorded permeate data is plotted as a function of time. The permeate data was then used to calculate the flux according to equation (6-7), and the result is presented in Fig. 6-6B.

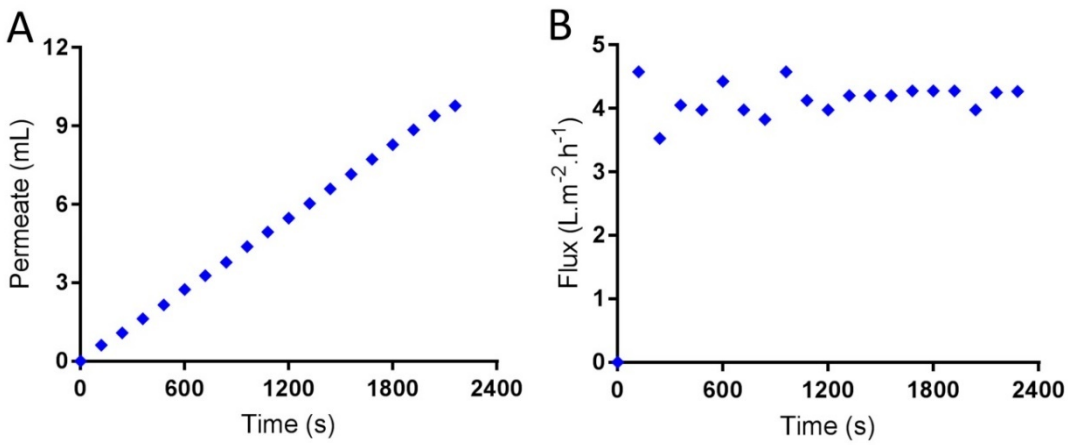


**Figure 6-6. Permeate and Flux measurements over time.** The test was done at a feed pressure of 3 Bar and a flow rate of 840 mL/min. (A) Permeate flux, (B) Flux level.

***Permeability Check (RO system)***

Water permeability was checked to examine whether the RO system works (without leaking and other issues) and whether the manufacture's flux/ permeability was correct. Fig. 6-7A shows the linear relation between the amount of permeate collected per hour by varying the pressure of feed using deionized water. Based on the weighed permeate value, permeability was calculated accordingly, following the equation (3-1). As shown in Fig. 6-7B, water permeability for the used RO membrane is at around 2.5 ($L.m^{-2}.h^{-1}$ $Bar^{-1}$), which is reasonable as compared to the manufacture's water permeability specification ($7.8L.m^{-2}.h^{-1}$ $Bar^{-1}$) for the polyamide-TFC RO membrane [418].

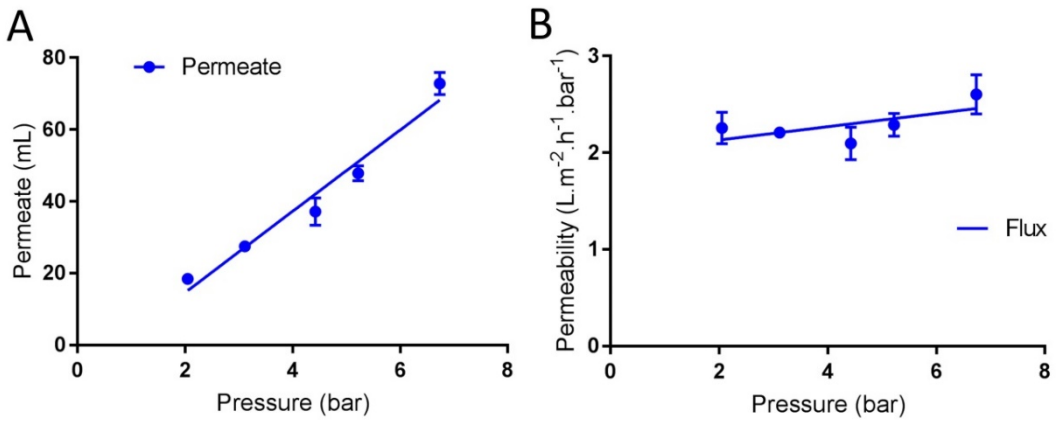


**Figure 6-7. Membrane permeability test,** (A) Permeate measurement with different feed pressures; (B) Corresponded permeability.

### 6.2.5.3 Salt concentration (Conductivity measurements)

The salt concentration of the feed and the permeate solutions were estimated via conductivity measurements. Conductivity was measured using a Conductivity Probe (i.e., a K 0.1 from Atlas Scientific LLC) which can measure with ±2% uncertainty over the conductivity range of 0.07 − 50,000 µS/cm.

The conductivity measurement system was placed next to the experimental system as can be seen in the red-dash box in Fig. 6-8A. Samples were collected and prepared (at the same desired volume of 30 mL) from filtration including feed and permeate solutions of different test conditions (See Fig. 6-8B). The measurement was conducted by inserting the probe into the sample test tube, as shown in Fig. 6-8C. The values were then saved into an iPad which was connected to the conductivity meter via Bluetooth. The data was then analyzed together with the filtration dataset.

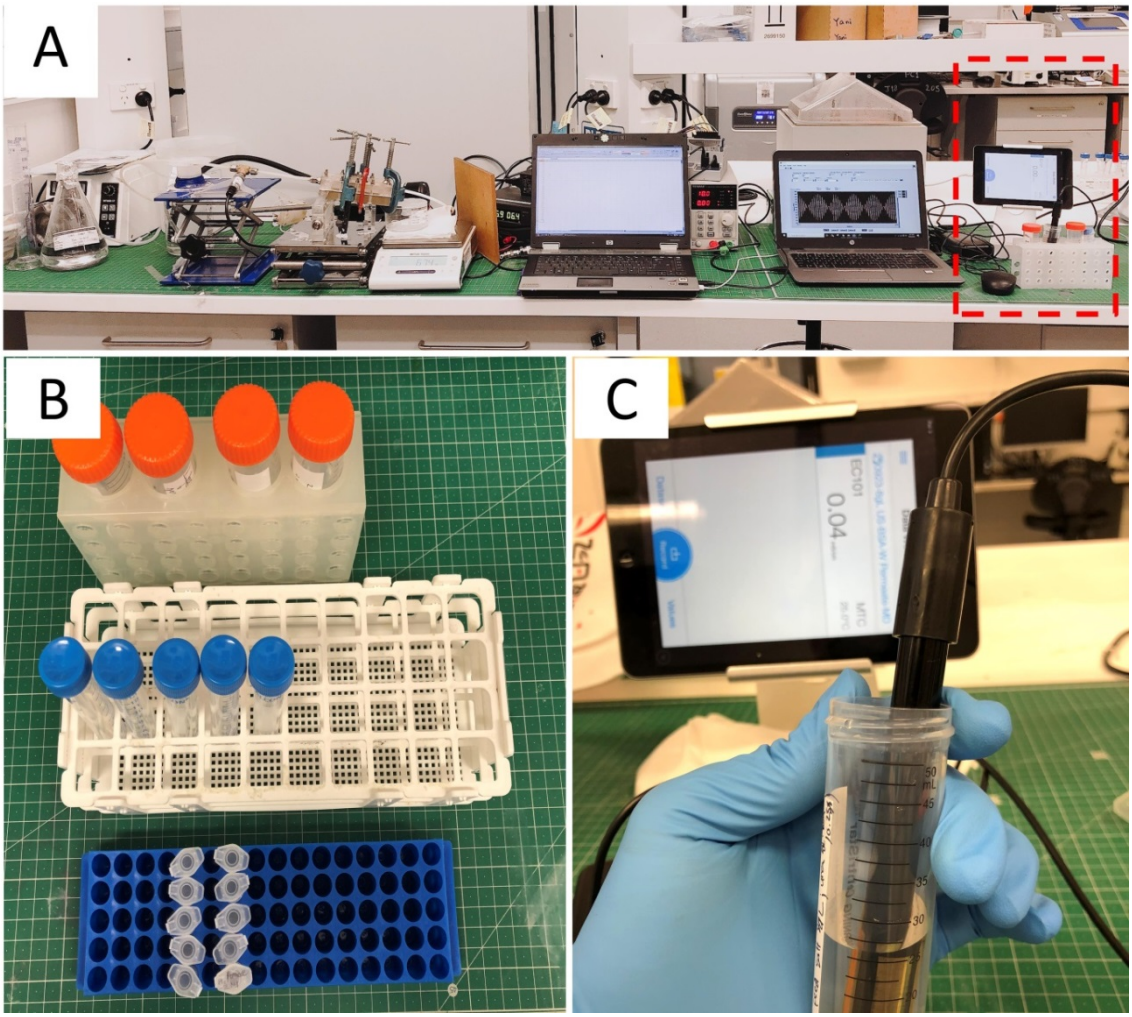


**Figure 6-8. Salt concentration (electrical conductivity) measurements.** (A) Position of conductivity meter in the system; (B) A set of filtration feed and permeate samples; (C) Conductivity measurement.

From the measured conductivity value, the concentration can be estimated. The calibration curve for defining salt concentration from conductivity value is made by simple calculation measurements with samples of salt-resolved solution with concentration: 0, 1000, 2000, 3000, 4000, 5000, 10000 ppm, respectively. The calibration curve is reported in the Fig. 6-9 below:

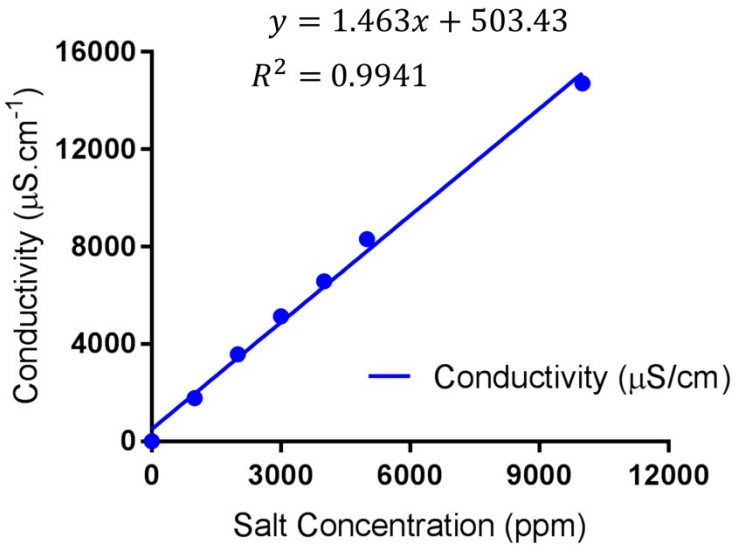


**Figure 6-9. Conductivity calibration curve**

### 6.2.5.4 Urea concentration measurement

To measure urea concentration, a urea assay kit was used. Firstly, filtration samples were collected as shown in Fig. 6-8B. Next, samples were diluted with buffers and mixed the chemicals and enzymes of the urea assay kit MAK006-1KT (Sigma-Aldrich), following the standard protocol (below). As shown in Fig. 6-10A, the samples were then pipetted into a standard clear 96-well plate (Fig. 6-10B). Lastly, after mixing and incubation, the samples were mounted into a SpectraMax iD5 microplate reader (Molecular Devices) for absorbance measurements at a wavelength of 570nm.

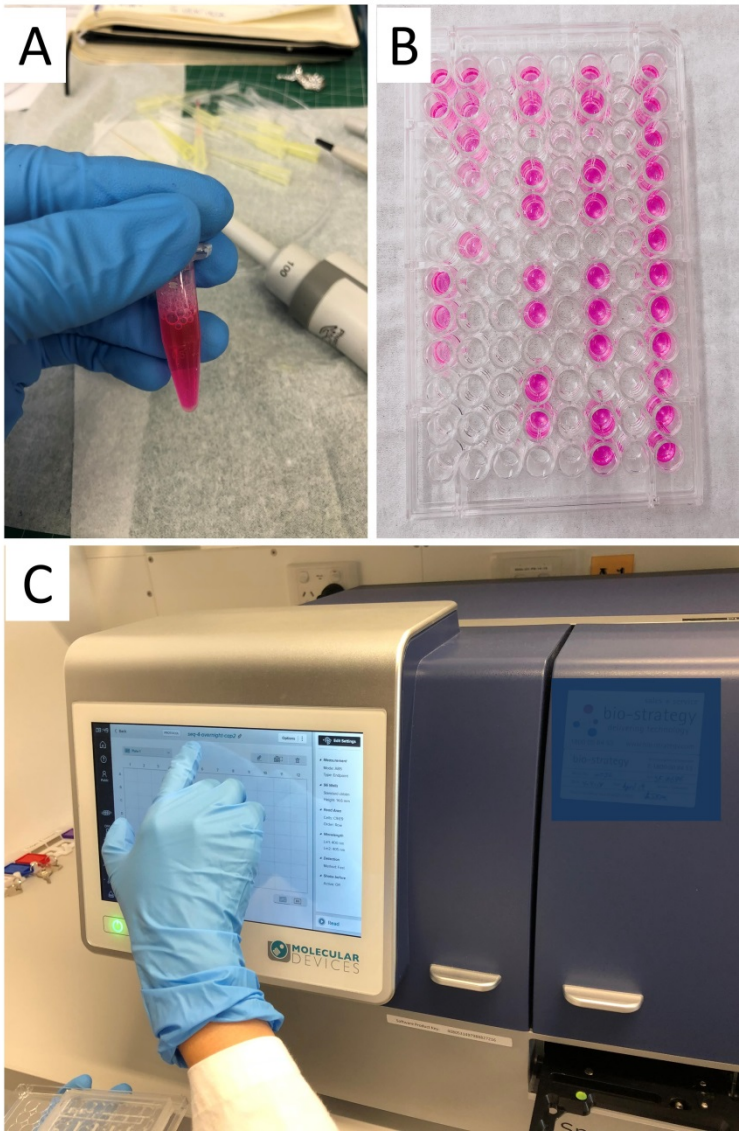


**Figure 6-10. Urea concentration measurement.** (A) Sample preparation/mixing according to protocol using pipettes; (B) An image of 96-well plate with a ready-sample set, (C) Image of the microplate reader machine for the absorbance measurement process.

Figure 6-10C presents process steps for carrying out the absorbance measurement with the microplate reader. The absorbance data were then recorded and used to calculate the corresponded urea concentration based on a standard calibration curve (given by the kit's manufacturer). The details of the calibration curve and the standard protocol for urea measurement are as follows:

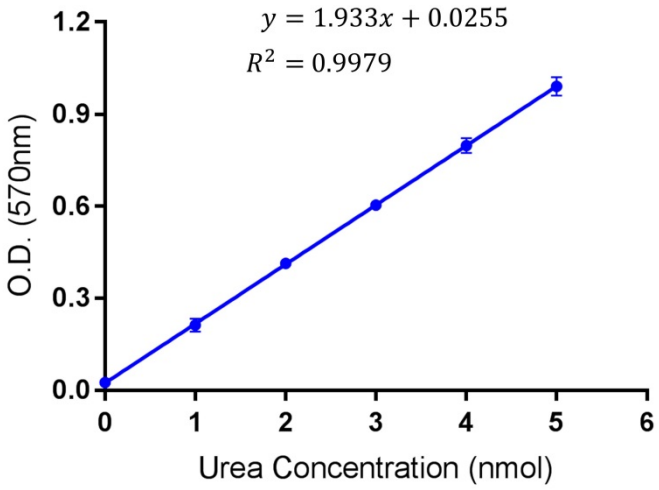


**Figure 6-11. Urea absorbance-concentration standard curve.**

***Urea Detection Protocol Specifics:***

A frozen urea detection kit was thawed to room temperature to melt the solution prior to use. The kit's buffers and enzymes were briefly centrifuged before opening. The first stage of the process was to verify the kit's performance using the standard urea concentration-absorbance curve from the manufacturer, and a range of concentrations of urea from urea powder (at 0.5, 1, 2, 3, 4, 5, 10 $g.L^{-1}$). Samples were then diluted with the urea assay buffer, according to the kit's technical directions, to get a 50 µL solution in each well in the 96-well plate. The blank (background sample) and standards reaction mix were also created according to guidelines. The reaction mix includes urea assay buffer, peroxidase substrate, enzyme mix, developer and converting enzymes. Subsequently, 50 µL of the appropriate reaction mix was added to each of the wells, which brings the total volume increased to 100 µL/ each well.

After preparation, samples were mixed well and incubated for 1 hour at a temperature of 37°C before doing the absorbance measurement using the SpectraMax iD5 microplate reader.

The microplate reader was set at a 570 nm absorbance wavelength and data was recorded for each well. The quantitative values of the absorbance of the urea-containing solutions were defined after subtraction of background reading. Note that these values can be affected by the pipetting process (e.g., uncertainty in the volume),

the dilution process (e.g., uncertainty in the initial concentration), the existence of bubbles in the fluid, and any variations in time and temperature.

Based on the absorbance values of the standard solutions, a concentration-absorbance curve was estimated to confirm the standard curve linear trend. Then, the concentration value of urea in permeate and feed samples from the experiment were found according to urea absorbance-concentration standard curve as shown in Fig. 6-11.

#### 6.2.5.5 Urea concentration estimation from salt concentration (RO & MD systems)

When a urea assay kit or other possible measurement methods (such as High-Performance Liquid Chromatography (HPLC), Total organic carbon (TOC) or Nuclear Magnetic Resonance (NMR) spectroscopy) are not available, urea concentration can be estimated based on conductivity (salt concentration measurement). Since urea has a similar molecular weight to salt, a membrane should reject a corresponding amount of salt as urea [361], [365]. Thus, based on historical measurements of salt and urea rejection ratios reported in literature for the specific type of membrane, urea concentration can be estimated via the conductivity measurements. The detailed estimation of urea concentration for RO will be presented in the following result of the RO filtration test.

For the MD membrane, at the feed to the temperature up to 70°C in this test, as proven in 6.1.4, chemical reactions for the urea hydrolysis process are not completed due to insufficient energy. Therefore, conductivity (and the corresponded salt concentration) of the permeate may relate well with the actual urea concentration in the solution. As the result, the urea rejection rate via MD would be similar to the salt rejection rate (>99%).

## 6.3 Results for the Reverse Osmosis

This section will present and compare the results for the filtration operation of Membrane 2 using RO and MD membrane systems.

### 6.3.1 Permeate Flux

Since RO membranes possess a small dense nanopore, flux is limited, and it requires a relatively high feed (input) pressure to achieve a reasonable flux. In order to understand the trade-off of feed pressure and flux, experiments were conducted.

As can be seen in Fig. 6-12A, the flux was found to be nearly a linear function of feed pressure (with all different salt concentrations). The results indicate that the permeate flux mainly depends on the operating pressure. A permeate flux of 1-4.5 $L.m^{-2}.h^{-1}$ can be achieved with feed pressure from 2 to 4 Bars for treating feedwater with salinity levels of 3 $g.L^{-1}$.

Also, the permeate flux was found to be higher with lower salt concentration in the feed. The flux was recorded to typically be around 1.77 $L.m^{-2}.h^{-1}$ with a salt concentration of 8 $g.L^{-1}$. However, it achieved the highest level at around 10.04 $L.m^{-2}.h^{-1}$ at zero-concentration of salt (4.5 times higher than the feed with salt concentration of 8 $g.L^{-1}$ at the same 5 Bar input pressure).

With human blood plasma, the salt concentration is about 8 $g.L^{-1}$ (or 140 $mEq.L^{-1}$) which can significantly limit the flux of the RO system due to the high osmosis pressure. As an example, the mimicking urea-containing plasma mimicking solution, UMS, showed the lowest level of flux with just about 1.4 $L.m^{-2}.h^{-1}$ at 4 Bar and 2.5 $L.m^{-2}.h^{-1}$ at 5 Bar. As expected, there is a clear trade-off between flux and the input pressure. By raising feed (input) pressure, it is possible to increase the permeate flux. In fact, with a salt concentration of 0-8 $g.L^{-1}$, an input pressure above 4 Bar is needed to obtain a measurable amount of flux in all cases.

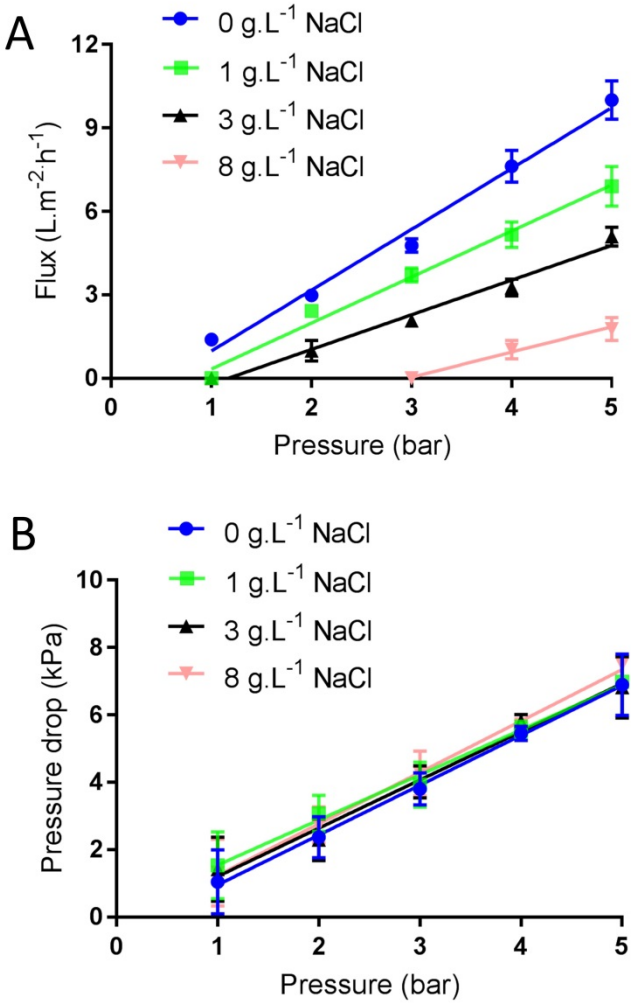


**Figure 6-12. Experimental permeate flux and pressures in RO test.** (A) Flux and input pressures with different salt concentrations, (B) Feed pressure and pressure drop. The test was done at a feed flow rate of 510-1250 mL/min (depending on feed pressure).

Fig. 6-12B shows the pressure drop values according to the input pressure. It can be seen that there is a linear relationship between pressure drop and input pressure. Also, when salt concentration is higher in the feed, it has a negligible effect on pressure drop. This is noticeably different from permeate flux results which is significantly affected by salt feed concentration.

For a feed containing BSA, as can be seen in Fig. 6-13, the permeate flux of Membrane 2 (using RO) is shown to have a linear relationship with the feed pressure. Also, having the microspacer and a lower level of BSA in the feed solution yielded a higher measured permeate flux. At the same feed pressure (P=5 Bar), the 0.2% v/v BSA feed and without spacer module achieved the lowest permeate flux at about 3.5 $L.m^{-2}.h^{-1}$,

whereas, the 0% BSA feed with spacer-integrated module reached the highest permeate flux at roughly 7 $L.m^{-2}.h^{-1}$. This two-fold enhancement showed a clear effect of having microspacer integrated in the module, which confirms the result in Chapter 4. Also, at the same condition of using the spacer and the same salt concentration and feed pressure, the presence of BSA reduced flux. For example, at the same 4 Bar feed pressure, having BSA resulted in a decrease of flux from 5.5 $L.m^{-2}.h^{-1}$ to around 3.6 $L.m^{-2}.h^{-1}$ (see the blue and black dots in Fig. 6-13). In the envisioned application, the input feed of Membrane 2 (which is the permeate of Membrane 1) should have no protein remaining. However, if there is some residual protein, it will reduce the flux in the RO system.

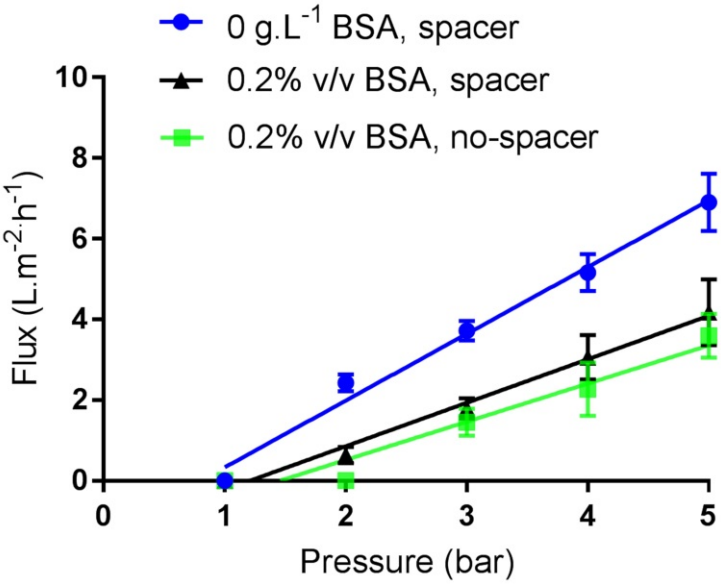


**Figure 6-13. Flux and input pressures with and without spacer and protein (BSA) in the solution.** The test was conducted with the same amount of salt of 1 g. $L^{-1}$, at a feed flow rate of 510-1250 mL/min (depending on feed pressure).

### 6.3.2 Salt Rejection of the RO Membrane

Salt rejection was also measured and calculated to confirm the ability of the system to reject salt, which can be an indication to estimate roughly the urea rejection rate [365]. It should be noted again that it is assumed that the salt losses can be compensate by the use of supplement injection solutions (e.g., saline which has been using in dialysis [12], [381]) or additional tablets/ diets for patients.

Permeate conductivity test shown that the averaged conductivity of 0, 233 and 1853 µs/cm was obtained from DI water, the permeate, and the feed solutions, respectively. From these values, salt concentrations were calculated according to the conductivity calibration curve in Fig.6-9.

Fig. 6-14A shows the salt concentration of the feed and the permeate solutions at different pressures, from 1 to 5 Bar. As shown in the chart, the feed concentration is reasonably stable at the input level of nearly 1000 ppm (1 $g.L^{-1}$), whereas the permeate was reduced from around 232 ppm to about 131 ppm as the input pressure increased from 1 to 5 Bar. The salt rejection rates were calculated following the equation (6-8) mentioned in 6.2.1. As shown in Fig. 6-14B, the rate achieved its peak of 85.8% at a 5 Bar feed pressure.

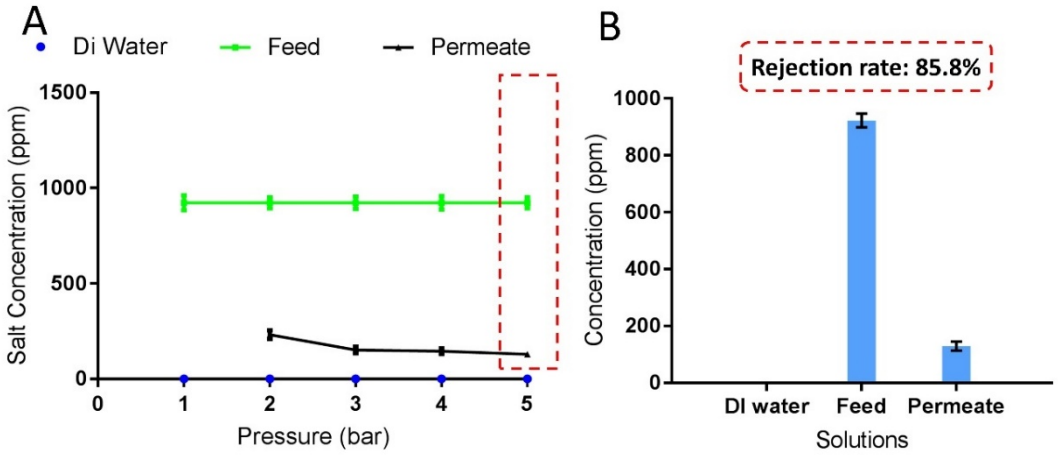


**Figure 6-14. Salt feed and permeate concentrations in the RO membrane system.**

This is an interesting result since it explains why we need to run an RO system at a high pressure for a reasonable flux and rejection rate. For example, in this case, the highest flux and the highest rejection rate (the lowest salt level in the permeate solution) can be achieved only at the highest input pressure of 5 Bar. This is because the salt rejection rate was impacted by both water transportation and salt diffusion through the membrane, as shown in Fig. 6-15.

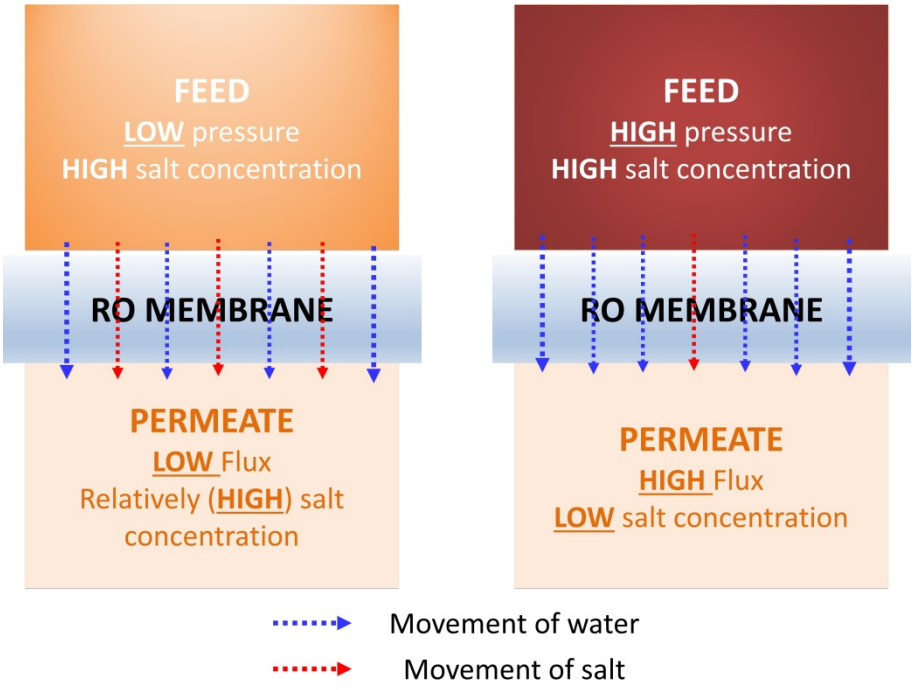


**Figure 6-15. Salt feed and permeate concentrations in the RO membrane system.**

When the feed (input) pressure is greater than the osmotic pressure of the solution, water transport across an RO membrane occurs in three separate steps: Step #1, water is absorbed onto the membrane surface; Step #2, water diffusion occurs through the thickness of the membrane; and Step #3, desorption occurs from the permeate surface of the membrane [373]–[375]. Within this process, as shown in Fig. 6-15, when the feed pressure is low, the flowrate of permeate is low, but the movement of salt (by diffusion) is relatively high. This leads to a relatively high salt concentration in the permeate, which means the rejection rate is lower when the feed pressure is low. Whereas with a high applied feed pressure, a much higher water permeate flowrate is recorded, so the salt diffusion is relatively small. That is, less salt can be seen in permeate flowrate, making the salt rejection rate higher.

### 6.3.3 Urea Rejection of the RO Membrane

***Estimation of Urea Rejection based on Salt Rejection***

Urea rejection can be estimated through salt concentration. Kraus et al. [365] reported a urea rejection rate averaged at 88% (up to 96%) (according to Table 2 of the reference [365]) with highly urea-rejecting aromatic polyamide RO membranes. At the same

time, these membranes were reported to have a 97.5% average salt rejection level at same feed pressure (around 50 Bar). Meanwhile, McKinney et al. [378] also reported a urea rejection of 92% with the salt rejection rate of 99% with the same type of membrane (at ~ 41 Bar feed pressure). Recent technologies allow RO membrane to run at lower feed pressure (e.g. 2-15 Bar) and to perform similar/ improved level of salt and urea rejection [363], [367], [419]. Since the experiment setup in this chapter also used a polyamide RO membrane, using these above references may allow us to roughly estimate level of urea rejection if salt rejection rate is measured. Fig. 6-16 shows the salt and urea rejection rate for several polyamide RO membranes in the literature.

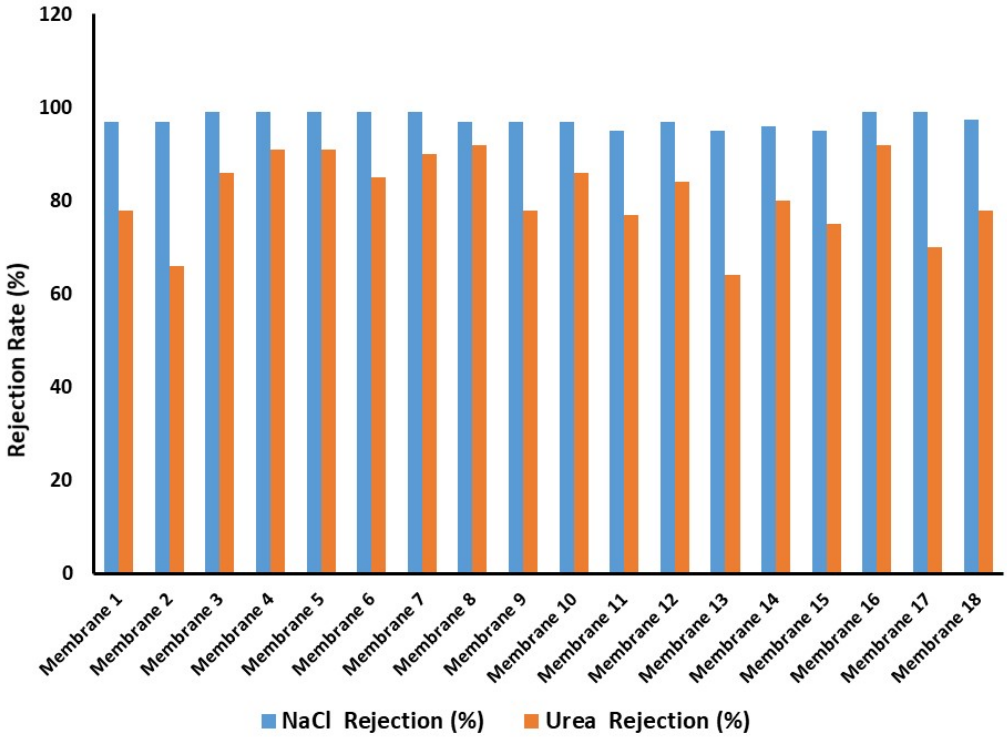


**Figure 6-16. Salt and urea rejection correlation of the polyamide RO membranes in the literature** (See detailed information in the table in the Appendix B)**.**

Thus, as a rough correlation, a polyamide RO membrane which can reject roughly 98.25% of salt will reject about 90% of urea on average. However, with a much lower pressure, both the salt rejection rate and the urea rejection rate can be lower. In fact, as can be seen in Fig. 6-14 above, the salt rejection is 85.8% at 5 Bar feed pressure. Assuming a proportional relationship, the urea rejection rate will be 76%, as estimated at 5 Bar feed pressure.

## 6.4 Results for Membrane Distillation

### 6.4.1 Flux and Energy Input (Feed Temperature)

In this experiment, after heating up the feed solution (Uremic plasma mimicking solution (UMS), a urea concentration of 3 $g.L^{-1}$ and a salt of concentration 10 $g.L^{-1}$) to a temperature from 45-70°C, the temperature was maintained, and the solution was pumped into the VMD module. The vacuum pump was started and permeate flux could be measured (See Fig. 6-3).

As shown in the Fig. 6-17A, the permeate flux is proportional to the feed temperature. As the feed temperature increased from 45 to 70°C, the permeate flux rose from just above 1 $L.m^{-2}.h^{-1}$ to over 10 $L.m^{-2}.h^{-1}$. At 70°C, the permeate flux of the MD system is at its peak (of about 10.8 $L.m^{-2}.h^{-1}$), more than 4 times higher than the permeate flux achieved by the RO system using even higher level of salt in the plasma mimicking solution. For the RO system the permeate flux was 2.2 $L.m^{-2}.h^{-1}$ at 5 Bar with same area unit of membrane, salt concentration 8 $g.L^{-1}$. The theoretical model was validated by comparing numerically and experimentally obtained permeate flux over different operation conditions with deionized water and a UMS solution (with a salt concentration of 10 $g.L^{-1}$). As can be seen in the Fig. 6-17A, the experimental results show good agreement with the numerical analysis results (method discussed in 6.2.2), although no flux was recorded at 50 °C and lower, and slight differences can be recognized from 53 to 70°C.

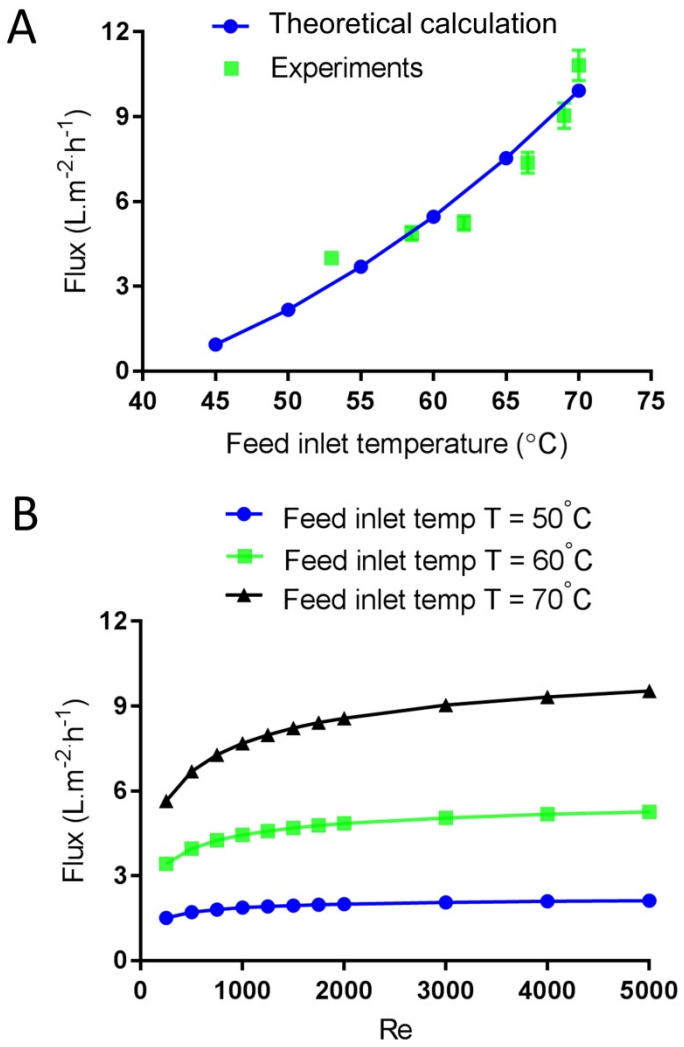


**Figure 6-17. Experimental vs simulated permeate flux results in MD tests.** The results are at different feed temperature and feed flow rate: (A) Validation under Pv= 7.5 kPa, feed flow Re~1000 (1.2 L/min), and salt concentration of 10 g.L$^{-1}$, (B) at crossflow Re of 20-4,000 (0.02-4 L/min), vacuum pressure of 7.5 KPa, and salt concentration of 10 g.L$^{-1}$.

Fig. 6-17B shows the theoretical permeate flux results at different feed temperatures (50°C, 60°C, 70°C) and feed flow rates (at crossflow Re of 20-4,000 or 0.02-4 L/min). At a 50°C feed temperature, the flux was the lowest at about 1.5 L.m$^{-2}$.h$^{-1}$ at a Reynold number of Re=250. This value increased slowly until it reached a flux level of about 2 L.m$^{-2}$.h$^{-1}$ at Re=2000, where it plateaued. At the highest flow rate, at Re=5000, the flux was 2.12 L.m$^{-2}$.h$^{-1}$. By comparison, at 70°C feed temperature, the permeate flux started at about 5.6 L.m$^{-2}$.h$^{-1}$ at Re=250 and then increased considerably, reaching 8.6 L.m$^{-2}$.h$^{-1}$ at Re=2000. The permeate flux, in this case, reached its highest recorded value of 9.5 L.m$^{-2}$.h$^{-1}$ at Re=5000. This reveals that a feed flow rate of ~1.2–2 L/min (Re = 1000–

2000) provides a preferred feed flow range, whereas any further increase of flow rate will only provide a limited flux enhancement.

### 6.4.2 Salt Rejection of the MD Membrane

Salt rejection was also measured for the MD membrane system. This result also can be an indication of urea rejection, as mentioned above. An electrical conductivity probe (as mentioned above) was used for DI water, permeate and feed solutions, respectively. According to the conductivity calibration curve in Fig.6-9, the salt concentration of feed and permeate and deionized water solutions are given in Fig. 6-18A. The sensor detected zero salt in the DI water (as expected) and a very low (negligible) level of salt in permeate solution of MD module (22 ppm) in comparison to a high level of salt in feed (7,858 ppm or about 8 g/L), which results in the salt rejection rate of 99.7% for MD system.

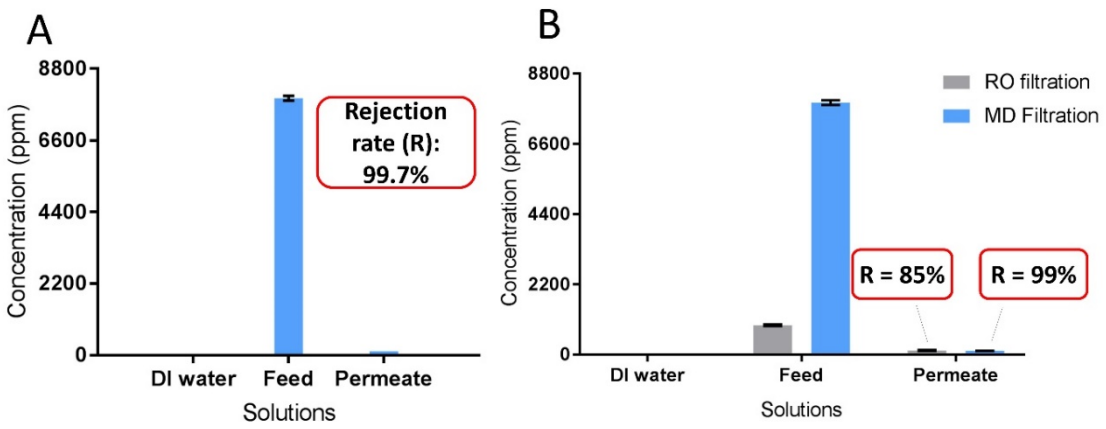


**Figure 6-18. Salt feed and permeate concentration.**

Fig 6-18B compares salt concentration of DI water, feed and permeate between RO and MD system. As can be seen from the chart, even with much higher feed concentration (8 g/L compared to 1 g/L of RO system. 8 g/L is also the level of salt in human plasma), MD filtration achieved a slightly lower level of salt in permeate solution. This led to the much higher salt rejection rate by the MD membrane module (99%) compared to RO membrane module (85%). This can be due to the higher rate of permeate flux and/or because of the MD mechanism that only allows evaporated water to pass through the membrane.

### 6.4.3 Urea Rejection of the MD Membrane

***Estimation of Urea Rejection based on Salt Rejection***

In this study, the MD membrane system runs at 45-70°C (343.15 K). At this range of temperature, there is not sufficient energy to complete the urea hydrolysis process. Thus, it was assumed that no evaporation/ volatilization of urea during the MD operation. And therefore, as explained in Chapter 6.2.8, the urea concentration in the permeate of MD system also can be estimated based on salt concentration (or conductivity) measurement, without a need for a direct measurement of urea concentration. As the result of salt rejection in Chapter 6.4.3, salt rejection rate is above 99%, which indicates the similar urea rejection rate of over 99%.

## 6.5 Discussion

### 6.5.1 RO and MD Comparison

A summary of the experimental results for both the RO membrane and MD membrane are presented in Table 6-3. As can be seen in the Table, with the same salt concentration and same input flowrate, the permeate flux was higher with MD compared to the RO option. For instance, for the same membrane area, the equivalent permeate flux of the RO membrane system (feed input pressure at 5 bar, feed solution at 25-37 °C) can be estimated as 1.77 $L.m^{-2}.h^{-1}$, which is about only 18% of the amount of flux achieved by MD membrane (7.5 kPa vacuum pressure, and feed solution at 70 °C). While the MD method requires much lower input pressure compared to RO (less than 10 kPa compared to at least several Bar), it requires the feed solution to be at a temperature of 50-70 °C. Interestingly, Interestingly, the MD membrane had a higher salt and urea rejection rate than the RO membrane: 99% vs 85% for salt and 99% vs 76% for for the estimated urea rejection rate.

**Table 6-3. RO and MD parameters in comparison**

| Parameters | RO Membrane | MD Membrane |
|---|---|---|
| Salt Concentration in Feed | 8 $g.L^{-1}$ | 8 $g.L^{-1}$ |
| Input Flow Rate | 0.5- 1.2 L. $min^{-1}$ ($18000\ L.m^{-2}.h^{-1}$) | 0.5- 1.2 L. $min^{-1}$ ($4500\ L.m^{-2}.h^{-1}$) |
| Input Pressure | 5 Bar (at feed side) | 7.5 kPa (at permeate side) |
| Feed Temperature | 25-37 °C | 50-70 °C |
| Membrane Area | 0.004 $m^2$ | 0.016 $m^2$ |
| Permeate Flux | $1.77\ L.m^{-2}.h^{-1}$ | $10.04\ L.m^{-2}.h^{-1}$ |
| Salt Rejection | 85% | 99% |
| Urea Rejection | 76% | 99% |
| Energy Consumption (not including the heat recovery) | 5.65 Wh/L (typically, 3-10 $kWh/m^3$ of permeate water) | 442 Wh/L (typically, 200-700 $kWh/m^3$ of permeate water) |
| Battery, weight, and operating time | 10x AA battery, 230g, can allow ~19h run time | 10x AA battery, 230g, can allow ~15 min run time |

Although the MD proved its potential, it it has a much higher energy consumption than the RO process. The energy calculations were conducted with the following equations (6-16) for RO and, (6-17) and (6-18) for MD under the following conditions: the RO feed was run at 1.2 L/min at 5 Bar; the MD feed was run at 0.3 L/min (by relative membrane area), being heated from 20°C initially to 70°C, and the permeate was cooled down to 37°C.

As shown in the Table 6-3, the energy consumption for the RO process is estimated at about 5.65 Wh/ L or $kWh/m^3$ permeate water. Meanwhile, the MD process requires 442 Wh/ L or $kWh/m^3$ permeate water which is ~75 times higher energy consumption compared to RO. The results are in typical ranges, RO costs 3-10 $kWh/m^3$ permeate water [420], [421] and MD costs about 200-700 $kWh/m^3$ [394], [422], depending on level of heat recovery (single- or multi-effect/ multi-stage process).

For the estimation of the battery requirement, a regular AA size lithium, rechargeable battery with the capacity of 3Ah at 3.7V (SONY), and weight about 23g had been considered. 10 of them could make 30Ah at 3.7V or, 108Wh. If a series of 10 AA batteries is used, it can supply energy for Membrane 2 part alone to run 19 hours with

RO and only ~15 mins with MD, with assumption of the water reabsorption rate is at 1 L/h (15% of natural tubule absorption).

Therefore, to be useful in the kidney portable system, the MD module needs to be further developed with consideration of using new heating and cooling solutions, utilizing heat recovery of the permeate vapor heat, choosing smaller vacuum pumps. These issues can be considered as an area for future work, which is discussing in more detail in 6.5.3.

### 6.5.2 Comparison to Hemodialysis (HD) and the Natural Kidney

The general overview of RO and MD systems in comparison to hemodialysis (HD) and the natural kidney is presented in the Table 6-4 below. Since dialysis removes urea simply by diffusion, the challenges with the proposed mechanisms will be on how effective it is in urea rejection and in claiming clean water back into the bloodstream.

***Advantages***

As shown in the Table, the proposed RO and MD systems mimic the natural kidney better than hemodialysis with two subsequent stages: filtration and absorption versus single-step diffusion (through hollow-fiber membrane) of conventional dialysis. Due to high pressure-driven and temperature-driven mechanisms, these methods also allowed high urea rejection rate, up to 99% (with MD system) which can be considered as higher than conventional hemodialysis (HD). The water reabsorption rate (per unit membrane area) also favored the RO and MD systems compared to HD process (zero reabsorption) with experimental data of 7.08 and 10.04 $L.m^{-2}.h^{-1}$ for RO and MD system, which accounts for 13 and 19% of the reabsorption rate of natural kidney (Note that RO and MD use 10 times higher input flow rate). The ability to miniaturize the system is also a potentially significant advantage of RO and MD systems compared to conventional HD which relies on a large dialysate system.

**Table 6-4. An overview of the proposed RO and MD systems in comparison to hemodialysis and natural kidney's tubule.**

| Parameters | Natural Kidney | Hemodialysis (HD) | RO System (test) | MD System (test) |
|---|---|---|---|---|
| Filtration Structure | 2 stages: glomerulus (filtration) and tubules (reabsorption) | 1 stage: UF (HFM) (diffusion) | 2 stages: UF (filtration), RO (reabsorption) | 2 stages: UF (filtration), MD (reabsorption) |
| Urea Rejection Rate | High (diffusion, transport of enzymes) | Low (diffusion) | 76% | 99% |
| Input Flowrate (Tubule Part) | 120 mL. $min^{-1}$ | 300-500 mL. $min^{-1}$ | 500- 1200 mL. $min^{-1}$ | 500 - 1200 mL. $min^{-1}$ |
| (Water) Reabsorption Rate | ~52.5 $L.m^{-2}.h^{-1}$ (~119 mL. $min^{-1}$) | 0 | 7.08 $L.m^{-2}.h^{-1}$ | 10.04 $L.m^{-2}.h^{-1}$ |
| Membrane Area | ~0.136 $m^2$ (glomerulus) | 1 $m^2$ | 0.016 $m^2$ | 0.016 $m^2$ |
| Input Pressure | ~7.3 kPa | ~50 kPa | 5 Bar | 7.5 kPa |
| Feed Solution Temperature | 37 °C | 37 °C | 25-37 °C | 50-70 °C |
| System Size | Small (120-230$cm^3$) | Big (~several $m^3$) | Able to miniaturize | Able to miniaturize |
| References | [30], [31] | [50], [283] | [365] | [391] |

***Disadvantages***

The RO system, however, requires a high input flowrate (up to 1.2 L. $min^{-1}$) in the experiment compared to hemodialysis (i.e., around 300-500 mL. $min^{-1}$) due to the work of high-pressure pump. This issue can be fixed by using modern high-pressure pumps (which can create high pressure without the need for high input flowrate) [423]. RO and MD systems also require either high input pressure (RO needs about 5 Bar) or high feed (input) temperature (MD needs about 50-70 °C) to get a reasonable reabsorption rate. The high pressure and heat conditions are acceptable for multi-step filtration strategy since the cells, proteins and bio-components has been rejected completely after Membrane 1's ultrafiltration. In addition, as can be seen in the Fig. 6-2, and Fig. 3-1 (Chapter 3)-the system diagrams, the feed solution of Membrane 2 will be discarded to bladder/ waste after reabsorption and any recycling process.

With the lowest membrane area and system size, and still achieving highest reabsorption rate (per membrane area), it shows clearly how extraordinary and

superior the natural kidney is, compared to all the artificial kidney replacement methods.

**Table 6-5. Design of enlarged module relative to the lab-scale module.**

| **Parameters** | **Natural Tubules** | **RO System (test)** | **MD System (test)** | **Scale Factor 30X for RO)** | **Scale Factor 6X for MD)** |
|---|---|---|---|---|---|
| Input Flowrate (Tubule Part) | 120 mL. $min^{-1}$ | 1200 mL. $min^{-1}$ | 500 - 1200 mL. $min^{-1}$ | 1200 mL. $min^{-1}$ | 500 - 1200 mL. $min^{-1}$ |
| (Water) Reabsorption Rate | ~52.5 $L.m^{-2}.h^{-1}$ (~119 mL. $min^{-1}$) | 1.77 $L.m^{-2}.h^{-1}$ | 10.04 $L.m^{-2}.h^{-1}$ | 52.5 $L.m^{-2}.h^{-1}$ | 52.5 $L.m^{-2}.h^{-1}$ |
| Required membrane area | - | 0.004 $m^2$ | 0.016 $m^2$ | 0.119 $m^2$ | 0.084 $m^2$ |
| Number of membranes | - | 1 | 1 | 30 | 6 |
| Estimated Energy for 8h run | - | 45.2 Wh | 3.53 kWh | 1.36 kWh | 21.1 kWh |
| Estimated Battery Weight for 8h run | - | 96 g | 7.5 Kg | 2.9 Kg | 45.1 Kg |
| Estimated Module Size (x scale factor) | - | 0.1 $m^3$ | 0.2 $m^3$ | 3 $m^3$ | 1.2 $m^3$ |
| **Miniaturization Factor** (assumed portable weight: 5 kg and size: 0.5 $m^2$) | **Small (120-230$cm^3$)** | **1** | **1** | **6 (size)** | **9 (weight)** |
| References | [30], [31] | [365] | [391] | - | - |

The Table 6-5 presents the estimated performance of the reabsorption-based scale-up modules (i.e., 30X for RO and 6X for MD) and the determination for Miniaturization factor for a portable device (assumed a possible portable device's weight is 5 kg and size is 0.5 $m^2$). As can be seen in the Table, to get to the natural kidney tubules reabsorption level, the corresponded membrane area and the required energy for RO and MD needed to increase by factor of 30X and 6X, respectively. This leads to the expanding in weight and size of the device. With the assumption of the current module sizes for RO and MD are 0.1 $m^2$ and 0.2 $m^2$ respectively, the Miniaturization Factor for RO is 6 times reduction in size and for MD is 9 times reduction in weight after the scaling up. It should be noted that for the RO system to be miniaturized, the optimum/ multilayer stack design [12], [424] of assuming 30-membrane layers can be used and

not necessarily requires multi-times module space. For the MD system miniaturization, however, the change in system weight depends on the heat (energy) recovery efficiency (discussed in Chapter 6.5.3) and the development of battery storage technologies. The future challenges of this remain, since the reductions related to the development/ miniaturization of fabrication method, micropumps, battery size and weight (see Appendix A).

### 6.5.3 Improvement Tasks and Future Works

#### *Urea Rejection Rate Experimental Measurement*

The urea rejection rate also can be measured with a urea assay kit as discussed in the methodology part (Chapter 6.3.4.4). Although substantial effort was put into using a urea assay kit, the results were not reliable due to the kit's quality; the process was time-consuming to conduct for every operational test. In details, initial measurements have been conducted twice; the urea concentration results for RO and MD filtration tests with errors compared to the standard curves of manufacture are reported in the Appendix B of this thesis. Therefore, salt concentration was used as a proxy in in Chapter 6.3.3. However, further experiments should be taken to confirm the actual measured values of urea concentration. Some other methods e.g., HPLC, TOC or NMR can also be considered to use for this task.

#### *Reabsorption Rate of Membrane 2*

In comparison to the natural tubule's reabsorption rate at around ~52.5 $L.m^{-2}.\ h^{-1}$ (for the input flowrate of glomerulus filtrate at only ~120 $mL.min^{-1}$), the experimental results of Membrane 2 using RO and MD showed that water reabsorption rate by these artificial methods are just 7.08 and 10.04 $L.m^{-2}.h^{-1}$, respectively (for the input flowrate of Membrane 2 at ~1.2 $L.min^{-1}$). That means the real recovery of post-filtration water back to blood stream is currently only around 1-2% compared to the natural kidney. This low water recovery/ reabsorption level exposed the need to recycle feed solution of Membrane 2 to get more clean water return to the blood circulation. To able to extract urea and reabsorb more clean water (e.g., up to about 50% of the feed), it is roughly estimated that the feed must be recycled at least 15 times for the scaled-up

membrane systems. However, this is just a rough estimation, it may require even much more recycling times with the RO system because the more filtrate/ water being filtered and returned to blood stream, the saltier the feed solution of Membrane 2 is. Thus, as the experimental result shows in Fig. 6-12, the increase of salt concentration makes significant lower water flux and requires much higher input pressure incase RO membrane is used. Some other membrane techniques such as forward osmosis (FO) membrane can also be investigated for solving the water reabsorption challenge of Membrane 2. For example, Dou et al. [419], [425] has recycled the spent dialysate using the dialysis concentrate as the draw solution. The work achieved up to the water recovery of approximately 64%.

### *Improved Reabsorption via Urea Adsorptive and Bio-cleaning Materials*

In a recent paper, Fan et al. demonstrated an effective biomolecule cleaning for some targeted molecules, including urea, creatinine, lysozyme, and β2-microglobulin from whole blood and simulant liquid [79]. As shown in Fig. 2-9B Chapter 2, this method uses a heterostructured nanoporous poly(acrylic acid)−poly(styrene divinylbenzene) particles in the dialysate (bottom) channel for reabsorption urea and other substances in the blood (top) channel using a two-layer microfluidic device that integrates polyamide porous membrane. This method can be applied for the Membrane 2 design by attaching these hetero-structured nanoporous particles on to the feed/ permeate channel of Membrane 2 for an even higher urea rejection rate of the RO/ MD system. Similarly, charcoal, two-dimensional titanium carbide (MXene) and other urea adsorptive materials can be also investigated for these further potential improvements [8], [14], [79].

### *Improved Reabsorption of Other Important Substances*

It is true that only two critical materials (*urea and water*) were covered in this chapter using the RO/ MD filtration methods. Although these represent the ‘big ticket’ materials, and the system produced an improvement in urea rejection rate and water reabsorption compared to traditional traditional one-step filtration hemodialysis (as

shown in the Table 6-4), the other materials $Na^+$, $K^+$, $Cl^-$; $Ca^{2+}$, $HCO_3^-$ and $PO_4^{2-}$; glucose, and amino acids were not studied in this work.

In the worst case of 0% reabsorption of these materials, the proposed system can still be viable with patient supplements, dietary or additional tablets for patients that can compensate the component losses (mentioned in Chapter 6.1.4). Besides, the development of clever selective membranes with controlled transmembrane ion transports [426], [427], the addition of supplement solutions – monitored with sensors – into the system circulation (e.g., saline), and the future work on using absorptive and biomaterials for improving functions of Membrane 2 (noted above) can be tested on to solve the problem.

### *Miniaturization*

As mentioned above, conventional HD relies on the large dialysate system, but for RO and MD systems, smaller/ portable pumps are the most important improvement needed to make the system portable. The development of a smaller, high-pressure pump is especially important for the pressure-driven filtration mechanism such as RO system. Some recent pump types have already reached the requirement; for example, high performance liquid chromatography (HPLC) pumps (e.g. piston, syringe pumps) used in HPLC system are small size (around 1-2 kg, currently) but they can provide super high pressure (up to one thousand Bars) at low flow rates (several $mL.min^{-1}$) [428]–[430]. Depending on the target for pressure and flowrate, a lower pressure and higher flowrate pump, therefore, can be developed specifically for the pAK application. The miniaturization of vacuum pumps [431]–[433] is also important for MD process. Taylor et al. [433] has report a miniaturized diaphragm vacuum pump by multi-material polyjet 3D-printing that allow estimated 200 kPa maximum stress and can deliver mass flow rates as high as 200 mL/min at 71 kPa. With the fast improvement in this field and the development of other pumping methods (e.g. magnetostrictive pump [423]), the opportunity for pump miniaturization for the application to be achieved is promising.

### *Heating and cooling strategy for the MD system*

Although MD has some technical potentials over RO in terms of permeate flux (for the high-salinity plasma filtration), it has several limitations (e.g., wetting, fouling, temperature polarization, and high energy consumption) which should be overcome [270], [434]–[436].

Due to the safety of the device, the feed solution of Membrane 2 system should be not much higher than 70 °C for convenience in cooling down; and to ensure high temperature polarization between feed and permeate solutions (which results in high flux) the permeate solution should be as much lower temperature as possible (e.g., 0°C). A thermoelectric device (TEC) can be the ideal choice for a portable MD system. This device can convert battery-based electrical energy to heat (high temperature) at one side and cold electrode (low temperature) at the other side. For example, with current requirement for the MD test, an energy of 603 W (for MD scaled up model with equation (6-20)) is needed for heating the feed, assuming Coefficient of performance (COP) is 1 and the TEC device supplies 71 W [437]; the minimum number of TEC needed can be estimated as 9. Heat and mass transfer equations together with this thermal electrical device is presented in the recent literature [389]. This device, thus, can reduce the need of heating and cooling equipmement [438].

The energy from the permeate vapor channel in the MD system also can be further used for pumping/ useful energy in recyling the feed or controling the valve in the system [353], [393].

## 6.6 Chapter Outcomes

This Chapter demonstrates new approaches for mimicking the natural kidney's tubules filtration functions (via an integrated Membrane 2 in the proposed system). Membrane technologies were shown to have the potential for integration into portable artificial kidney (pAK) systems (e.g., reverse osmosis and membrane distillation) since they can achieve the required toxin removal while also reclaiming clean water.

The Chapter provides background of reverse osmosis and membrane distillation technologies in the literature specific for the task in pAK system. RO and MD systems

for testing salt and urea rejection and water adsorption have been successfully designed, fabricated and setup. For RO membrane system, the experiments revealed the urea rejection of 76% (and salt rejection reached 85%) and water reabsorption rate (per membrane area) up to 7.08 $L.m^{-2}.h^{-1}$ with 5-Bar feed pressure and at 1.2 L. $min^{-1}$ feed flowrate. For the MD membrane system, only by raising the feed temperature from 37 to ~70°C, urea rejection rate reached to 99% (same as salt rejection) and water reabsorption rate (per membrane area) up to 10.04 $L.m^{-2}.h^{-1}$. Although these results are still far from the superior water reabsorption rate 52.5 $L.m^{-2}.h^{-1}$ (with only 120 mL. $min^{-1}$ input flowrate) of nature tubules, higher urea rejection rate and the possibility to miniaturize the system make RO and MD systems promising compared to hemodialysis in term of portable kidney development.

The RO system requires high feed (input) pressure (5 Bar) and MD system requires high feed temperature (about 50-70 °C) to get a reasonable reabsorption rate but the high pressure and heat conditions are acceptable for multi-step filtration strategy where the cells, proteins and bio-components has been rejected completely before this step. The MD system allows the filtration and recycling of higher salinity fluid (e.g., protein-free plasma), without the need for increased input pressure compared to RO. However, MD and RO rejects salt which needed to be compensated by supplement injection solutions (e.g., saline) or tablets.

Several areas of future work were identified. The removal of waste metabolites and reclaiming clean water may be improved by recycling feed solution and using high urea adsorptive materials. Together with miniaturization and real blood tests, these are the future works before clinical evaluations.

# Chapter 7

# Discussions and Conclusions

## 7.1 Discussion and Conclusions

This thesis is an investigation of a new micro-engineered filtration system design to meet the needs of portable artificial kidneys (pAK). The final design's innovation stems from its use of advanced fabrication techniques (i.e., the use of microfluidic and additive manufacturing) and the membrane advances which mitigate the need for a dialysate system (i.e., via two stage of filtration to recycle water). The system was analyzed numerically and experimentally in detail to determine its feasibility for parallel, continuous operation with the natural kidney, aiming to reduce the frequency of clinical dialysis treatments. As is shown in Fig. 7-1, the overall system (and the thesis) was broken down into the several essential steps, each of which must consider flow rates and pressures from adjoining steps/stages.

Step 2 of the proposed system mimics artificial glomerular filtration and was found to improve filtration performance by utilizing microspacers which promote three-dimensional mixing in the narrow filtration channels. Another feature of the design, Step 3 in Fig. 7-1, is that it the two filtration stages much be connected despite a requisite mismatch in outlet/inlet pressures. To overcome this, small-scale valves were developed which enable a high level of fluidic control between filtration stages in the portable system. For the second stage of the filtration process, the goal is high urea rejection and a high percentage of water reabsorption. For this step, a reverse osmosis

membrane—and an alternative design using membrane distillation—were analyzed, designed, and tested.

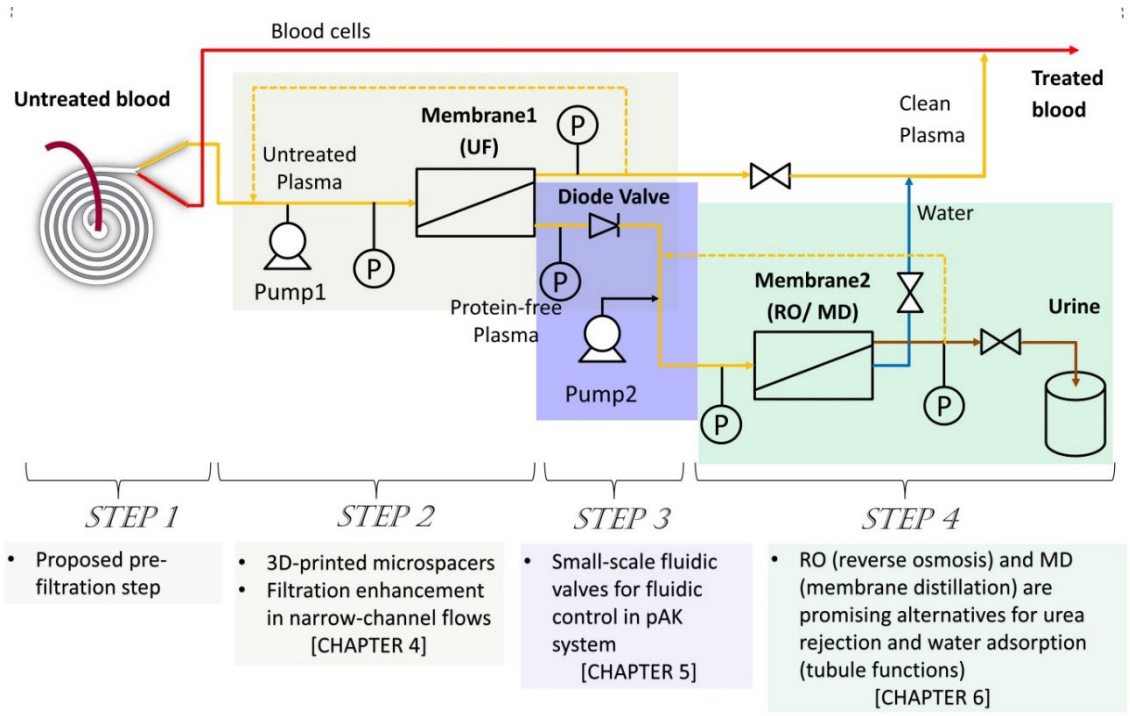


**Figure 7-1. Schematic representation of the background works done in this thesis for the multi-step non-cell-based portable artificial kidney.**

Chapter 2 provided a comprehensive review of the state-of-the-art of artificial kidneys, including the supporting technologies that could be brought into the field (e.g., microfluidics, fabrication techniques and advanced membrane designs). Chapter 2 concluded that while stem-cell-based kidneys represent the ultimate solution to kidney failure, while non-cell-based wearable, portable, and implantable devices represent a promising and—perhaps—more near-term artificial kidney solution. These insights motivated this work to target microfluidic-based devices which employ a multi-step filtration mechanism. That is, an engineering approach was adopted in the thesis work where several functional units were developed and tested (e.g., membranes, microspacers, microvalves, etc.) and tested for integration as a portable artificial kidney platform. The platform was also guided for future experimental testing of components such as micropumps and electronic microsensors.

Chapter 3 presented the materials and methods used in the experiments and simulations for each step of the proposed filtration system. For design and fabrication, this Chapter was the discussion of the rationale of the multi-step filtration system design and went into two different microfabrication methods for the modules. In the first method, photolithography was tested for the fabrication of the small-scale filtration platform. Different photomask designs and materials can be used to produce the dimensions of the capillaries found in the glomerulus. However, most of these only allow 2D microchannels with several limitations on the cross-sectional morphology of microchannels. Moreover, with the membrane attached in the device layer in the experiment, input pressure was limited under 40 kPa, permeate flux was constrained at µL scale and leaking and bubble-generation problems happened.

As an alternative to traditional micofabrication techniques, it is now possible to use 3D printing to achieve micro-scale geometries. This approach is intriguing for artificial kidney applications because complex three-dimensional channel/ spacer designs. The method also allows mechanical fastening for higher input pressures and flowrates. In addition, 3D printing also allows for much more rapid prototyping for progressively introducing design modifications.

In addition to details on fabrication, Chapter 3 also described the testing platform that was produced during this work. The platform was designed to be versatile over the range of flow rates and pressures expected for the components of the system shown in Fig. 7-1, namely 0-5 Bar and 0-1200 mL/min. Depending on the membrane configuration and its corresponding setup, different choices of tubings, connectors and wider-range sensors were used. For example, for Membrane 1 ultrafiltration configuration requires pressure 0-3 Bar while Membrane 2 with RO membrane requires operating pressures around 2-5 Bar. Last but not least, the details on experimental measurement (e.g., roughness, pressure, flow rate, nanoparticle concentration) and CFD simulation analysis methods were also presented in the chapter.

Chapter 4 presented the work on enhancing Membrane 1 hemofiltration (Step 2 in Fig. 7-1) by integrating 3D-printed microspacers in the feed channels of the filtration module.

A few promising microspacer designs (with feature sizes of 100 µm), including two herringbone geometries and a gyroid structure, were integrated into narrow channels and 3D-printed. The module was then experimentally tested to determine if these features could affect the overall flux and concentration polarization.

The result showed that adding microspacers into narrow-channel flows can indeed significantly enhanced filtration with the net benefit (of flux enhancement) relative to the cost (the increase of pressure drop). Under different flowrates (80-130 $mL.min^{-1}$) and for the two solutions used (i.e., BMS and PMS), all the microspacer designs boosted the permeate flux. Among the microspacers, the gyroid design achieved the highest permeate flux enhancement (i.e., 81% and 93% above a plain channel for the blood mimicking and plasma mimicking solution tests, respectively). This far exceeded the enhancement achieved by the herringbone designs. Although the gyroid microspacer incurred a 23% higher pressure drop than the plain channel, this represents an ~4X net benefit (on a percentage basis).

This Chapter also reported CFD results which agreed well with the experimental measurements. The CFD results indicated that 3D flow profiles and more mixing were created in the microspacer-integrated channels. According to CFD result, the gyroid design has the highest shear stress on its membrane surface, followed by herringbone designs with 32-59% lower shear stress, and non-spacer channel with 70% lower shear stress. In addition, it seems the spacer designs eliminate the small remaining low flow zones inside the filtration unit and aid in diffusing shear stress to reduce concentration polarization near the membrane surface.

The hydrodynamic performance in longer tests (e.g., 30 hours) for plasma mimicking solution revealed the relative performance difference between the microspacer and the plain channel was maintained over time. This result is meaningful for Membrane 1 filtration and for the designs of membrane modules for portable kidney system.

Chapter 5 described a full geometrical characterization and operational analysis of small-scale valves for Step 3 (i.e., the connection between Membrane 1 and Membrane 2) of the proposed portable artificial kidney system. It employed normally-closed (NC) microvalves and one-way microfluidic diode valves (MDV), along with a control system for the valves. A 3D-printed fabrication method was presented to quickly and reliably produce these microvalves.

Firstly, the effects of valve design parameters (e.g., valve sizes, valve-seat size, membrane thickness, coating materials) on the critical parameter (e.g., opening threshold pressure ($P_{thO}$)) were revealed. It was found that $P_{thO}$ reduced with increasing valve size, thinner valve-seat size and with a simple biomolecular surface coating material. Based on these results, these valves can now be designed and fabricated with a certain range of $P_{thO}$ and can be effectively controlled based upon the valves' desired open and closed states. Next, sequential and parallel fluidic controlling logics were developed for an integrated microfluidic-logic system. This study proved the potential of using these valves in portable systems (generally) where the integration of complex permeate liquid handling (mixing, measurement, or detection) is required.

Based on the characterization of the general valving unit, microfluidic diode valves were successfully fabricated and analyzed for the Connection part (Step 3 as shown in Fig. 7-1). The valve successfully performed a diode-like function, up to 4 bar (about 80% of the maximum target pressure for using RO membrane filtration ~5 Bar). These findings revealed these valses can be used for connecting Membrane 1 with Membrane 2 (RO or MD system) in the next filtration step.

Chapter 6 presented the work on new approaches for mimicking the filtration function of the natural kidney's tubules (Step 4/ Membrane 2 of the proposed system as shown in Fig. 7-1). Reverse osmosis and membrane distillation technologies were tested for urea (and salt) removal and water reclamation.

Two experimental systems were built and tested in this Chapter (for RO and MD) and both tested the molecule rejection rate and water re-adsorption potential. For the RO membrane system, the experimental urea rejection was 76% and the salt rejection was

85%. The water reabsorption rate (per unit of membrane area) was up to 7.08 $L.m^{-2}.h^{-1}$ with a 5-bar feed pressure and at 1.2 L. $min^{-1}$ feed flowrate. For the MD membrane system, with a feed temperature ~70°C, the urea and salt rejection rates were ~99% and water reabsorption rate (per membrane area) was up to 10.04 $L.m^{-2}.h^{-1}$. Although these values are relatively low compared to the superior water reabsorption rate of 52.5 $L.m^{-2}.h^{-1}$ (with only 120 mL. $min^{-1}$ input flowrate) of nature tubules, they did achieve a higher urea rejection rate. The drawback of these systems, however, is that they require either a high feed (input) pressure (up to 5 bar) and or high feed temperature (about 50-70 °C) to get a reasonable water reclamation rate. Those issues notwithstanding, these designs were deemed as promising because of their potential for further miniaturization and integration into a portable kidney development.

MD has one advantage over RO in this it allows for filtration of high salinity blood fluid, enabling higher recovery ratios. But MD also faces more issues on energy consumption and portability compared to RO system.

## 7.2 Original Contributions

The original contributions of this work, can be summarized as follows:

1- To overcome some of the limitations of traditional clinic-based, one-step with hemodialysis, this thesis proposed the first micro-engineered multi-step, dialysate-free filtration process which: (a) mimics the two-step filtration of the natural kidney (e.g., the glomerular filtration and tubule's reabsorption), (b) has potential to be made portable and continuous, (c) allows pressure-driven (e.g., reverse osmosis) or thermal-driven (e.g., membrane distillation) membrane processes.

2- This thesis introduced microfluidics design advances into this application, including micro-valves, micro-scale fluidic management, the potential for other micro-components (e.g., micropumps, microsensors, separation device) to be integrated into a portable artificial kidney platform.

3- This thesis demonstrated microfabrication methods could be applied to develop artificial kidney devices. 3D printing was selected as a more convenient rapid prototyping option, allowing more complex three-dimensional designs.

4- This thesis introduced the concept of micro-spacers to promote 3D fluid mixing at narrow-channel domains for small-scale filtration.

5- This thesis provided fundamental insights into the hydrodynamic behavior and the local shear stresses for the tested spacer designs. The trade-off between flux enhancement and pressure drop was revealed for simulated biological filtration (using plasma and blood mimicking solutions).

6- This thesis demonstrated that a microfluidic diode valve can negate backflow from one side of the valve, allowing to store diode pressure on other side up to 4 bar (exceeding the pressure requirement for running an MD membrane and reaching about 80% of the maximum target pressure for using RO membrane filtration).

7- This thesis demonstrated the potential to reclaim water and remove urea and toxic substances by using reverse osmosis at an ordinary pressure of 5 bar.

8- As an alternative approach, this thesis also demonstrating the use of membrane distillation to remove urea and toxic substances at low feed-temperature from 50-70 °C.

9- This thesis providing a comprehensive review of the state-of-the-art of artificial kidneys, near-term device considerations, and some background on technology which could be used to advance the field.

## 7.3 Outlook and Future Work

Although the current thesis has extended the state-of-the-art in a few different directions, it also exposed several under-developed topics that could be studied further to achieve a viable portable device for commercial use.

### *To Improve System Filtration Performance*

As can be seen in Fig. 7-2, the performance of testing system is far behind natural kidneys. Without recycling the concentrate from its filtration steps, current Membrane 1 and Membrane 2 can only produce approximately 4% and 1-2% of the permeate flux achieved by the natural glomerulus and tubules at the same feed flowrate, respectively.

Specifically, as shown in Fig. 7-2 A and B, nature glomerulus can generate 120 mL/ min filtrate from 1L/min whole blood input using glomerular membrane (molecular cut-off of around 68 kDa, ~5-7 nm pore-size). Meanwhile, the experiment with Membrane 1 just used a plasma input and a microfiltration membrane (220nm pore-size) but can generate only around 5 mL/min filtrate at the same level input flowrate (Note that this is just a proof-of-concept test for microspacer in narrow channels; the choice of membrane did not reflect the actual needed membrane type). As shown Fig. 7-2D, natural tubules can reabsorb 119 mL/min of water out of 120 mL/min filtrate and still reject most of urea. RO and MD membranes, in the other hand, use higher input flowrate and can also only reach to the water reclamation rate of 7.08 and 10.04 $L.m^{-2}.h^{-1}$, which account for 13 and 19% of the reabsorption rate of natural kidney, respectively. Further comparison of the RO and MD systems performance compared to hemodialysis was presented in detail in Chapter 6 (at 6.5.2. and Table 6-4).

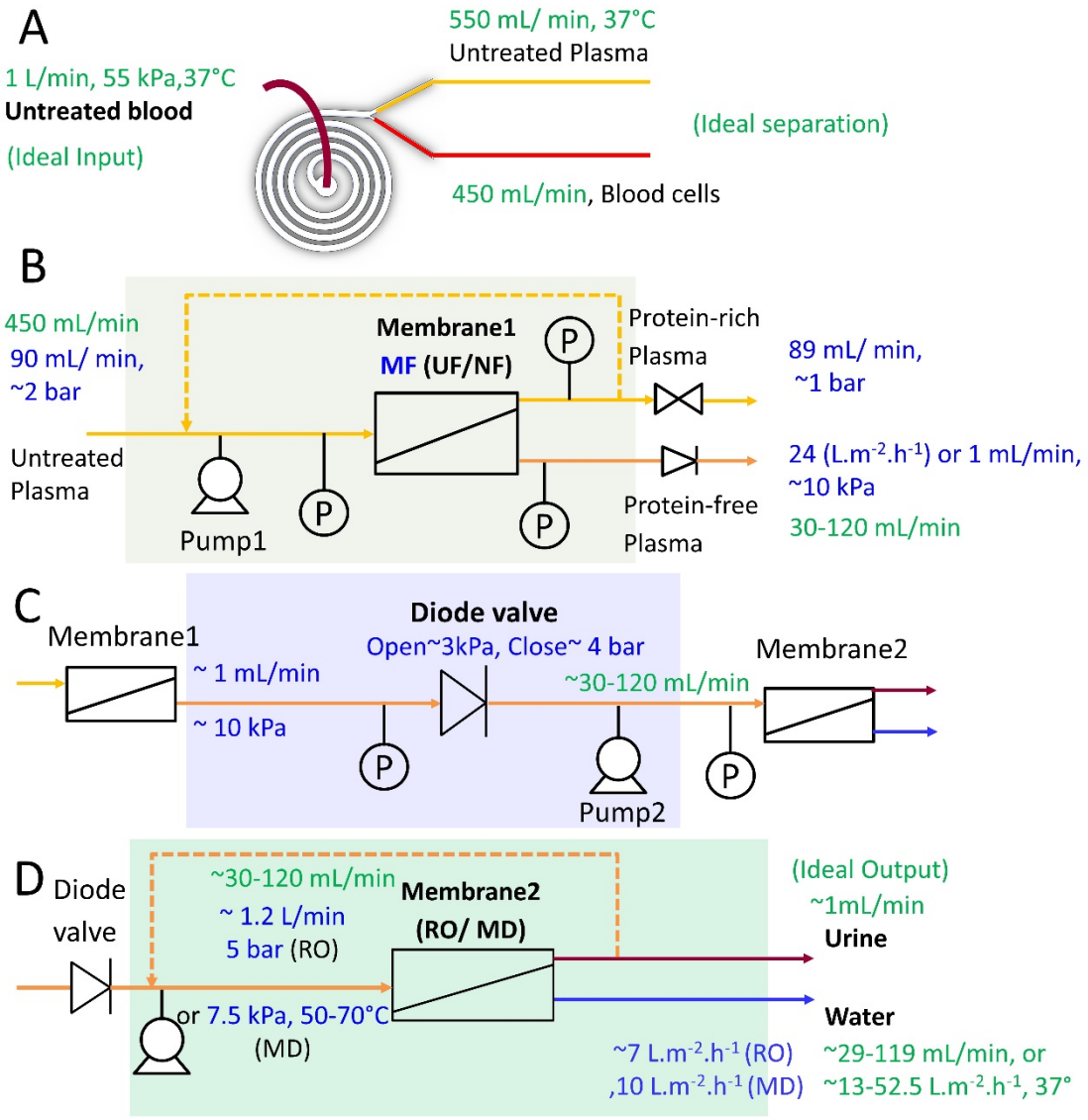


**Figure 7-2. Ideal kidney parameters and the experimental conditions.** The ideal kidney parameters (inspired from natural kidney, in green text) as compared to the experimental conditions of this work (blue text).

Therefore, further work to improve system performance is needed with the topics below:

- In Membrane 1, further tests are needed for different types of membrane with appropriate molecular cut-off ranges reducing from 68 kDa down to several kDa. It is crucial selectivity and permeate flux.
- In Membrane 1 part, is there another way to improve flux than just spacer? Based on the effective hydrodynamic effects in the filtration of 3D microspacers design which contains lot of fluidics turns, 3D-printed membrane (glomerulus-

like structure) can be expected to be a future development direction for Membrane 1.

- In Membrane 2 part, it is a high demand to improve water reabsorption rate by recycling feed solution. With high salinity fluid such as plasma, MD is favored over RO for recycling feed solution that salinity will increase after every cycle. Forward osmosis membrane can be also considered for solving the water recovery challenge [419], [425]. The number of recycling should be calculated carefully depending on Membrane 1's permeate flux and the requirement for feed flowrate for Membrane 2. This was discussed in detail in Chapter 6. 5.3.
- In Membrane 2 part, water reabsorption rate and toxic removal can also be improved by using of urea adsorptive and bio-cleaning materials [8], [14], [79]. The future work may need to find if any further advanced materials can be added in the system to reclaim not only water but also glucose, amino acids, hormones and any other valuable substances without taking also urea and creatinine back to blood stream [361]. This was also discussed in Chapter 6.5.3.
- The mismatch of flow rate between components in the proposed pAK system also remained as a future work to adjust. This is due to: (1) the capacity of microfluidic diode valve; (2) the choices of membranes and insufficient working area of Membrane 1 and Membrane 2; (3) the input pressure/ flowrate applied for experiment. As discussed in Chapter 5.5.4, the valve has potential to use/ be redesigned for the wider range of flow rate (e.g., several hundreds mL/min), and other types of one-way valves (e.g., ball/ spring, diaphragm check valves...), will also be able to fit to the purpose of pAK system if they are compact/ small and easy to operate. Due to the portable system will be running continuously (compared to hemodialysis), the actual filtrate flow rate in a fully developed pAK can be much lower in comparison to the natural glomerulus filtrate flow (e.g., at the range of target flow rate from 30-120 mL/min). Further experiment should consider the stack structure of membranes to supply sufficient membrane area for filtration.

- Since the thesis uses an engineering approach to the design and testing of portable artificial kidney systems, more physiological evaluations with the help from medical doctors and nephrologists is still needed.

### *Improve 3D Printing Resolution*

The fluidic management performance of microspacers in Membrane 1 was limited with the 3D-printed minimum features of ~100µm and the current deviation of up to 39% [380]. Recent printers such as ProJet® MJP 5600 and ProX 950 with minimum layer of 12.5 µm allows the potential for printing smaller spacers and larger area. This was discussed in detail in Chapter 4.4.5.

Further study in Chapter 5 showed that by higher printed resolution and surface roughness, the diode valve's tolerance pressure could be improved. With the rapid development of 3D printing, future smaller features and higher resolution will be achieved. 3D-printed materials for bio-printings [97], [98], [439] and 3D membrane printing will be a fascinating further study for Membrane 2 which can improve both filtration and adsorption activities of the pAK device.

### *Biocompatibility, Blood, Animal and Clinical Trials*

Other aspects such as pressure control for RO membrane filtration; heat and cooling strategy for MD filtration, biocompatibility, and safety measures for both should be studied. For example, one of the heating and cooling strategies is to use thermal electrical device (TEC) [389], [438], a device can convert to heat (high temperature) at one side and cold (low temperature) at the other side electrode. This can reduce the burden of MD energy consumption. More details have been discussed in detail in Chapter 6.5.3.

Experimental trials with real blood tests, animal and clinical trials on patients need to be carefully conducted before the device can be commercial.

# Appendix A

## Miniaturization Consideration

Miniaturization represented a main challenge for the application of the proposed system. Although most of the information has been discussed in Chapter 6.5.3, further details are considered in this part to specify which is needed to reduce in sizes to make the system portable.

The pie-chart Fig. B-4 shows the estimated miniaturization compounds/ factor. This estimation is rough calculation based on the lab-scale equipment. As can be seen in part A of the figure, the miniaturization of RO membrane system depends mostly on the miniaturization of stacked membrane module size (40%), the feed pump (35%), and the power supply for the feed pump (20%). The data was estimated by calculations based on the Table 6-5 in Chapter 6.5.2.

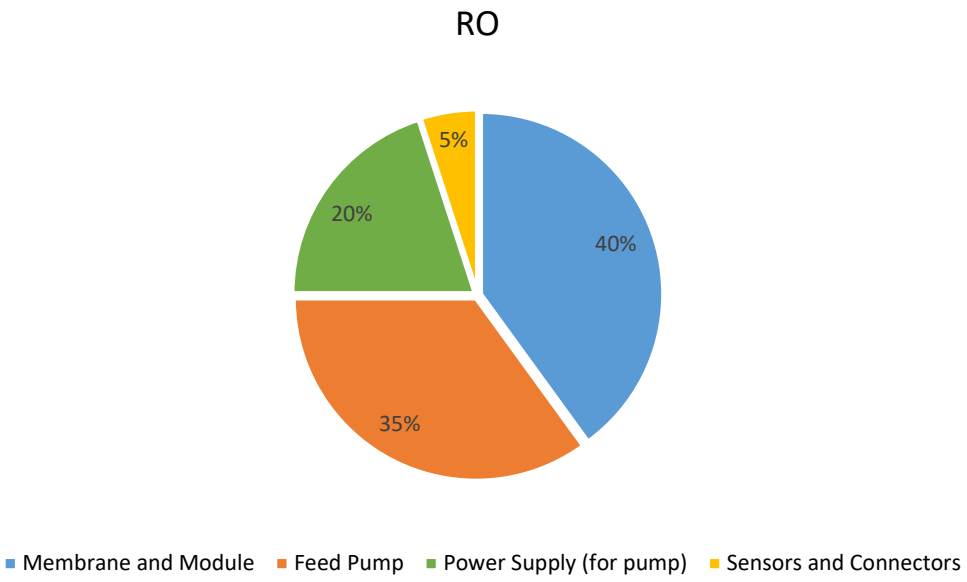

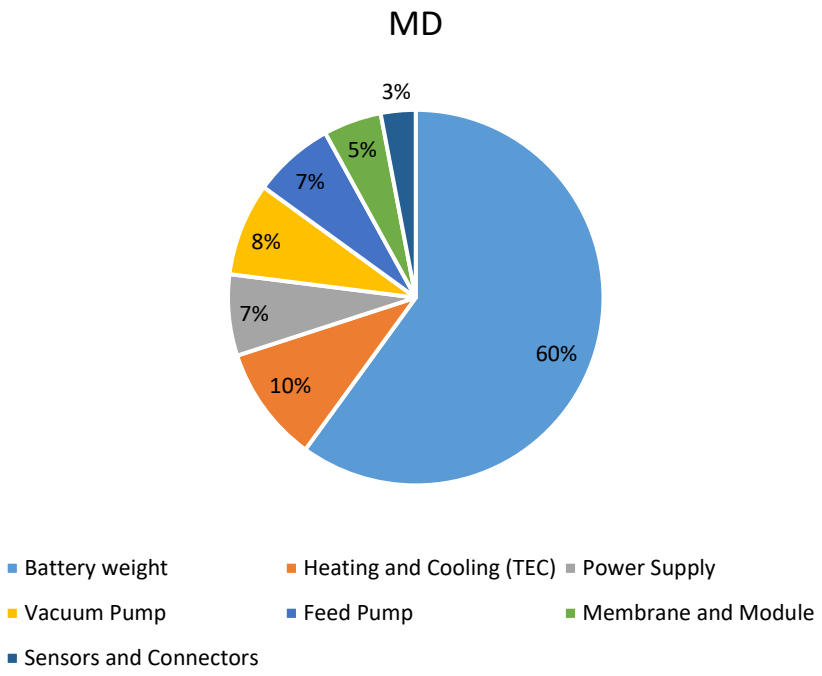


**Figure A-1. Estimated Miniaturization Compounds.** (A) RO miniaturization, (B) MD miniaturization.

Meanwhile, as can be seen in 2nd part of the figure, MD membrane system miniaturization depends on more factors including the battery weight (60%), the heat and cooling device (e.g, TEC) (10%), vacuum pump (8%), feed pump (7%), power supply (7%) and some more factors, which poses substantially greater challenges than RO.

# Appendix B

## Urea Concentration Measurement

The urea assay kit (Sigma-Aldrich) was used since it is best way for measure urea concentration in our lab. The measurement method has been discussed in Chapter 6.2.5. However, due to the kit inappropriate quality (confirmed by manufacturer), the result of the initial tests for absorbance value (shown as optical density (O.D.) at 570 nm in Fig. B-2B) was inconsistent when compared to Urea standard curve (Fig. B-2A) stated by manufacturer. Due to the effect of Covid-19 pandemic on chemical supply, it was impossible to repeat the experiments with the new replacement kits in the limited time fame of this thesis. It remains future work to confirm experimentally urea concentration as discussed in Chapter 6.3, 6.4.

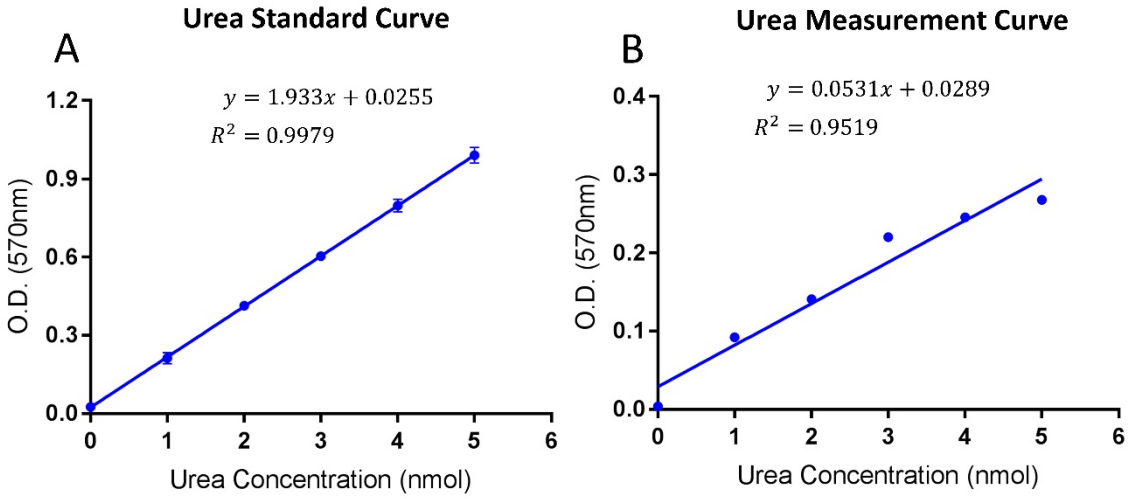


**Figure B-2. Urea concentration measurement with urea assay kit.** (A) Urea-Absorbance standard curve from manufacturer, (B)Urea-Absorbance curve by experimental measurement.

For the estimation of urea rejection based on corresponded salt rejection rate in Chapter 6, the detail references are shown in the bellow table.

**Table B-1. Urea and salt rejection of Polyamide Membranes.**

| Polyamide Membrane Types (with polymer additives) | Name | Salt Rejection (%) | Urea Rejection (%) | Ref. | Test condition Urea (ppm), NaCl (ppm), Pressure (psi) | Permeate (L/ m2.day) |
|---|---|---|---|---|---|---|
| DA-2 | Membrane 1 | 97 | 78 | [365] | 10,000/ 5,000/ 730 | 151 |
| DA-4 | Membrane 2 | 97 | 66 | [365] | 10,000/ 5,000/ 730 | N/A |
| MM-1 | Membrane 3 | 99 | 86 | [365] | 10,000/ 5,000/ 730 | 71.2 |
| MM-2 | Membrane 4 | 99 | 91 | [365] | 10,000/ 5,000/ 730 | 40 |
| MMP-1 | Membrane 5 | 99 | 91 | [365] | 10,000/ 5,000/ 730 | 88.2 |
| MMP-2 | Membrane 6 | 99 | 85 | [365] | 10,000/ 5,000/ 730 | 52.2 |
| MMP-2 (2nd) | Membrane 7 | 99 | 90 | [365] | 10,000/ 5,000/ 730 | 71.2 |
| MPM-3 | Membrane 8 | 97 | 92 | [365] | 10,000/ 5,000/ 730 | 92.4 |
| MPM-4 | Membrane 9 | 97 | 78 | [365] | 10,000/ 5,000/ 730 | 151 |
| MPM-4 (2nd) | Membrane 10 | 97 | 86 | [365] | 10,000/ 5,000/ 730 | N/A |
| MPM-5 | Membrane 11 | 95 | 77 | [365] | 10,000/ 5,000/ 730 | N/A |
| MPM-5 | Membrane 12 | 97 | 84 | [365] | 10,000/ 5,000/ 730 | N/A |
| MPM-9 | Membrane 13 | 95 | 64 | [365] | 10,000/ 5,000/ 730 | N/A |
| MPM-10 | Membrane 14 | 96 | 80 | [365] | 10,000/ 5,000/ 730 | N/A |
| MPM-10 (2nd) | Membrane 15 | 95 | 75 | [365] | 10,000/ 5,000/ 730 | N/A |
| Aromatic Polyamide | Membrane 16 | 99 | 92 | [378] | 18,000/ 4640/ 600 | 250-290 |
| Aromatic Polyamide | Membrane 17 | 99 | 70 | [377] | 10,000/ 10,000/ 600 | 25.2 |
| FO (Cellulose Triacetate) (Reference) | Membrane 18 | 97.4 | 78 | [425] | N/A | N/A |

* DA: 3,5-diaminobenzoic acid; MM: chemically identical to “Nomex”@ polymer [365]; MPM is obtained by condensing m-phenylenediamine with a 1:1 mixture of iso- and terephthaloyl chloride.

# References


[1] T. Liyanage *et al.*, “Worldwide access to treatment for end-stage kidney disease: A systematic review,” *Lancet*, vol. 385, no. 9981, pp. 1975–1982, 2015.

[2] A. Grassmann, S. Gioberge, S. Moeller, and G. Brown, “ESRD patients in 2004: Global overview of patient numbers, treatment modalities and associated trends,” *Nephrol. Dial. Transplant.*, vol. 20, no. 12, pp. 2587–2593, 2005.

[3] M. Noordzij and K. J. Jager, “Survival comparisons between haemodialysis and peritoneal dialysis,” *Nephrol. Dial. Transplant.*, vol. 27, no. 9, pp. 3385–3387, 2012.

[4] “Organ Donation and Transplantation Activities, 2016 Report,” 2018.

[5] J. Jansen, M. Fedecostante, M. J. Wilmer, L. P. van den Heuvel, J. G. Hoenderop, and R. Masereeuw, “Biotechnological challenges of bioartificial kidney engineering,” *Biotechnol. Adv.*, vol. 32, no. 7, pp. 1317–1327, 2014.

[6] V. Gura *et al.*, “A wearable hemofilter for continuous ambulatory ultrafiltration,” *Kidney Int.*, vol. 73, no. 4, pp. 497–502, 2008.

[7] M. Hueso, E. Navarro, D. Sandoval, and J. M. Cruzado, “Progress in the Development and Challenges for the Use of Artificial Kidneys and Wearable Dialysis Devices,” *Kidney Dis.*, pp. 1–8, 2018.

[8] F. Meng *et al.*, “MXene Sorbents for Removal of Urea from Dialysate: A Step toward the Wearable Artificial Kidney,” *ACS Nano*, p. acsnano.8b06494, 2018.

[9] H. D. Humes, D. Buffington, A. J. Westover, S. Roy, and W. H. Fissell, “The bioartificial kidney: Current status and future promise,” *Pediatr. Nephrol.*, vol. 29, no. 3, pp. 343–351, 2014.

[10] C. Attanasio, M. T. Latancia, L. E. Otterbein, and P. A. Netti, “Update on Renal

Replacement Therapy: Implantable Artificial Devices and Bioengineered Organs," *Tissue Eng. Part B Rev.*, vol. 22, no. 4, pp. 330–340, 2016.

[11] J. J. Song, J. P. Guyette, S. E. Gilpin, G. Gonzalez, J. P. Vacanti, and H. C. Ott, "Regeneration and experimental orthotopic transplantation of a bioengineered kidney," *Nat. Med.*, vol. 19, no. 5, pp. 646–651, 2013.

[12] N. To *et al.*, "Water-Permeable Dialysis Membranes for Multi-Layered Microdialysis System," *Front. Bioeng. Biotechnol.*, vol. 3, no. June, pp. 1–7, 2015.

[13] B. Van Dang, R. A. Taylor, A. J. Charlton, P. Le-Clech, and T. J. Barber, "Towards portable artificial kidneys: The role of advanced microfluidics and membrane technologies in implantable systems," *IEEE Rev. Biomed. Eng.*, vol. 13, no. 1, pp. 261–279, 2019.

[14] W. K. Cheah, K. Ishikawa, R. Othman, and F. Y. Yeoh, "Nanoporous biomaterials for uremic toxin adsorption in artificial kidney systems: A review," *J. Biomed. Mater. Res. - Part B Appl. Biomater.*, vol. 105, no. 5, pp. 1232–1240, 2017.

[15] G. M. Whitesides, "The origins and the future of microfluidics," *Nature*, vol. 442, no. 7101, pp. 368–373, 2006.

[16] A. C. Fernandes, K. V. Gernaey, and U. Krühne, "Connecting worlds – a view on microfluidics for a wider application," *Biotechnol. Adv.*, vol. 36, no. 4, pp. 1341–1366, 2018.

[17] X. Hou *et al.*, "Interplay between materials and microfluidics," *Nat. Rev. Mater.*, vol. 2, no. 5, 2017.

[18] R. Dong, Y. Liu, L. Mou, J. Deng, and X. Jiang, "Microfluidics-Based Biomaterials and Biodevices," *Adv. Mater.*, vol. 1805033, p. 1805033, 2018.

[19] B. Van Dang *et al.*, "Microfluidic actuation via 3D-printed molds towards multiplex biosensing of cell apoptosis," *ACS Sensors*, 2019.

[20] R. S. Pawell, D. W. Inglis, T. J. Barber, and R. A. Taylor, "Manufacturing and wetting low-cost microfluidic cell separation devices," *Biomicrofluidics*, vol. 7, no. 5, 2013.

[21] J. Luo, J. Fan, and S. Wang, “Recent Progress of Microfluidic Devices for Hemodialysis,” *Small*, no. 1904076, pp. 1–14, 2019.

[22] T. Yan, M. Cempini, C. M. Oddo, and N. Vitiello, “Review of assistive strategies in powered lower-limb orthoses and exoskeletons,” *Rob. Auton. Syst.*, vol. 64, pp. 120–136, 2015.

[23] B. Pelletier *et al.*, “System overview of the fully implantable destination therapy--ReinHeart-total artificial heart,” *Eur. J. cardio-thoracic Surg.*, vol. 47, no. 1, pp. 80–86, 2015.

[24] H. Liu, Y. Huang, and H. Jiang, “Artificial eye for scotopic vision with bioinspired all-optical photosensitivity enhancer,” *Proc. Natl. Acad. Sci.*, vol. 113, no. 15, pp. 3982–3985, 2016.

[25] N. Patel and P. Gohil, “A review on biomaterials: scope, applications & human anatomy significance,” *Int. J. Emerg. Technol. Adv. Eng.*, vol. 2, no. 4, pp. 91–101, 2012.

[26] B. Cheong, R. Muthupillai, M. F. Rubin, and S. D. Flamm, “Normal values for renal length and volume as measured by magnetic resonance imaging,” *Clin. J. Am. Soc. Nephrol.*, vol. 2, no. 1, pp. 38–45, 2007.

[27] F. Roch-Ramel, H. M. K. Besseghir, and E. E. Windhager, *Renal Physiology*. New York: Oxford University Press, 1992.

[28] L. Sherwood, *Human Physiology: From Cells to Systems*, 4th ed. Brooks/Cole, 2001.

[29] N. Kamaly, J. C. He, D. A. Ausiello, and O. C. Farokhzad, “Nanomedicines for renal disease: current status and future applications,” *Nat. Rev. Nephrol.*, vol. 12, no. 12, pp. 738–753, 2016.

[30] M. W. Taal, G. M. Chertow, P. A. Marsden, K. Skorecki, A. S. L. Yu, and B. M. Brenner, *Brenner & Rector’s the kidney*, 9th ed. Saunders Elsevier, 2011.

[31] C. O’Callaghan, *The renal system at a glance*, 3rd ed. John Wiley & Sons, 2009.

[32] O. Smithies, “Why the kidney glomerulus does not clog: a gel

permeation/diffusion hypothesis of renal function.," *Proc. Natl. Acad. Sci. U. S. A.*, vol. 100, no. 7, pp. 4108–13, 2003.

[33] R. Paoli and J. Samitier, "Mimicking the kidney: A key role in organ-on-chip development," *Micromachines*, vol. 7, no. 7, 2016.

[34] S. M. Bagshaw *et al.*, "Current state of the art for renal replacement therapy in critically ill patients with acute kidney injury," *Intensive Care Med.*, vol. 43, no. 6, pp. 841–854, 2017.

[35] G. M. Fleming, "Renal replacement therapy review," *Organogenesis*, vol. 7, no. 1, pp. 2–12, 2011.

[36] A. S. Levey, "Assessing Kidney Function — Measured and Estimated Glomerular Filtration Rate," *N. Engl. J. Med.*, vol. 354, pp. 2473–2483, 2006.

[37] "Blood & Urine Tests," *2018*. [Online]. Available: https://lifeoptions.org/learn-about-kidney-disease/blood-and-urine-tests/.

[38] U. Riserus, W. C. Willett, and F. B. Hu, "Dietary fats and prevention of type 2 diabetes," *Progress. Lipid Res.*, vol. 48, no. 1, pp. 44–51, 2010.

[39] O. K. Duru, T. Middleton, M. K. Tewari, and K. Norris, "The Landscape of Diabetic Kidney Disease in the United States," *Curr. Diab. Rep.*, vol. 18, no. 3, p. 14, 2018.

[40] A. K. Bello *et al.*, "Global overview of health systems oversight and financing for kidney care," *Kidney Int. Suppl.*, vol. 8, no. 2, pp. 27–29, 2018.

[41] V. Jha *et al.*, "Chronic kidney disease: Global dimension and perspectives," *Lancet*, vol. 382, no. 9888, pp. 260–272, 2013.

[42] B. Nguyen and F. Fukuuchi, "Survival rates and causes of death in Vietnamese chronic hemodialysis patients," *Ren. Replace. Ther.*, vol. 3, no. 22, 2017.

[43] "United States Renal Data System. 2017 USRDS annual data report: Epidemiology of kidney disease in the United States," Bethesda, MD, 2017.

[44] F. K. Port, R. A. Wolfe, E. A. Mauger, D. P. Berling, and K. Jiang, "Comparison of survival probabilities for dialysis patients vs cadaveric renal transplant recipients," *Jama*, vol. 270, no. 11, pp. 1339–1343, 1993.

[45] G. Wong *et al.*, “Comparative survival and economic benefits of deceased donor kidney transplantation and dialysis in people with varying ages and Co-Morbidities,” *PLoS One*, vol. 7, no. 1, pp. 1–9, 2012.

[46] “US Department of Health and Human Services. OPTN: Data Organ Procurement and Transplantation Network,” 2019. [Online]. Available: https://optn.transplant.hrsa.gov/data.

[47] R. Sinnakirouchenan and J. L. Holley, “Peritoneal dialysis versus hemodialysis: Risks, benefits, and access issues,” *Adv. Chronic Kidney Dis.*, vol. 18, no. 6, pp. 428–432, 2011.

[48] S. S. A. Fenton *et al.*, “Hemodialysis versus peritoneal dialysis: A comparison of adjusted mortality rates,” *Am. J. Kidney Dis.*, vol. 30, no. 3, pp. 334–342, 1997.

[49] J. Ehrman, P. Gordon, P. Visich, and S. Keteyian, *Clinical Exercise Physiology. Human Kinetics*, 2th ed. 2008.

[50] W. R. Clark, “Hemodialyzer membranes and configurations: a historical perspective,” *Semin Dial*, vol. 13, no. 5, pp. 309–311, 2000.

[51] K. Sakai, “Dialysis membranes for blood purification,” *Front. Med. Biol. Eng.*, vol. 10, no. 2, pp. 117–129, 2000.

[52] U. Buoncristiani, “Fifteen years of clinical experience with daily haemodialysis,” *Nephrol. Dial. Transplant.*, vol. 13, pp. 148–151, 1998.

[53] A. P. Heidenheim, N. Muirhead, L. Moist, and R. M. Lindsay, “Patient quality of life on quotidian hemodialysis,” *Am. J. Kidney Dis.*, vol. 42, no. 1, pp. 36–41, 2003.

[54] R. Saran *et al.*, “Longer treatment time and slower ultrafiltration in hemodialysis: Associations with reduced mortality in the DOPPS,” *Kidney Int.*, vol. 69, no. 7, pp. 1222–1228, 2006.

[55] G. Chertow *et al.*, “In-Center Hemodialysis Six Times per Week versus Three Times per Week,” *Perspective*, vol. 363, pp. 2287–2300, 2010.

[56] G. M. Chertow *et al.*, “Long-Term Effects of Frequent In-Center Hemodialysis,” *J. Am. Soc. Nephrol.*, vol. 27, no. 6, pp. 1830–1836, 2015.

[57] M. R. Marshall *et al.*, “Home hemodialysis and mortality risk in Australian and New Zealand populations,” *Am. J. Kidney Dis.*, vol. 58, no. 5, pp. 782–793, 2011.

[58] E. D. Weinhandl, K. M. Nieman, D. T. Gilbertson, and A. J. Collins, “Hospitalization in daily home hemodialysis and matched thrice-weekly in-center hemodialysis patients,” *Am. J. Kidney Dis.*, vol. 65, no. 1, pp. 98–108, 2014.

[59] J. A. Morfín, A. Yang, E. Wang, and B. Schiller, “Transitional dialysis care units: A new approach to increase home dialysis modality uptake and patient outcomes,” *Semin. Dial.*, 2017.

[60] S. Kim, W. H. Fissell, D. H. Humes, and S. Roy, “Current strategies and challenges in engineering a bioartificial kidney.,” *Front. Biosci.*, vol. 7, no. 2, pp. 215–28, 2015.

[61] J. Leupolz, A. Habermaier, and W. Reif, “Quantitative and qualitative safety analysis of a hemodialysis machine with S#,” *J. Softw. Evol. Process*, no. October 2017, pp. 1–14, 2018.

[62] D. A. Rose, E. Sonaike, and K. Hughes, *Hemodialysis access*, vol. 93, no. 4. 2013.

[63] J. E. Flythe *et al.*, “Association of intradialytic blood pressure variability with increased all-cause and cardiovascular mortality in patients treated with long-term hemodialysis,” *Am. J. Kidney Dis.*, vol. 61, no. 6, pp. 966–974, 2013.

[64] R. M. Hakim *et al.*, “Iron Overload and Mobilization in Long-Term Hemodialysis Patients,” *Am. J. Kidney Dis.*, vol. 10, no. 4, pp. 293–299, 1987.

[65] S. Wagner, C. Rode, R. Wojke, and B. Canaud, “Observation of microbubbles during standard dialysis treatments,” *Clin. Kidney J.*, vol. 8, no. 4, pp. 400–404, 2015.

[66] F. Farrokhi, N. Abedi, J. Beyene, P. Kurdyak, and S. V. Jassal, “Association between depression and mortality in patients receiving long-term dialysis: A systematic review and meta-analysis,” *Am. J. Kidney Dis.*, vol. 63, no. 4, pp. 623–635, 2014.

[67] D. L. Mapes *et al.*, “Health-related quality of life as a predictor of mortality and hospitalization: The dialysis outcomes and practice patterns study (DOPPS),” *Kidney Int.*, vol. 64, no. 1, pp. 339–349, 2003.

[68] B. Ogutmen *et al.*, “Health-related quality of life after kidney transplantation in comparison intermittent hemodialysis, peritoneal dialysis, and normal controls,” *Transplant. Proc.*, vol. 38, no. 2, pp. 419–421, 2006.

[69] W. H. Fissell and S. Roy, “The implantable artificial kidney,” *Semin. Dial.*, vol. 22, no. 6, pp. 665–670, 2009.

[70] M. Nowacki *et al.*, “Is regenerative medicine a new hope for kidney replacement?,” *J. Artif. Organs*, vol. 17, no. 2, pp. 123–134, 2014.

[71] G. S. Prihandana *et al.*, “Antithrombogenicity of fluorinated diamond-like carbon films coated nano porous polyethersulfone (PES) membrane,” *Materials (Basel).*, vol. 6, no. 10, pp. 4309–4323, 2013.

[72] T. Ota, N. To, Y. Kanno, and N. Miki, “Evaluation of biofouling for implantable micro dialysis system,” *Proc. Annu. Int. Conf. IEEE Eng. Med. Biol. Soc. EMBS*, vol. 2016-Octob, pp. 1942–1945, 2016.

[73] T. Ota, N. To, Y. Kanno, and N. Miki, “Evaluation of biofouling in stainless microfluidic channels for implantable multilayered dialysis device,” *Jpn. J. Appl. Phys.*, vol. 56, no. 6, 2017.

[74] T. Ota, M. Nakayama, Y. Kanno, T. Suzuki, and N. Miki, “In vitro and in vivo tests of nanoporous membrane coated with biocompatible fluorine-doped diamond-like carbon for hemofiltration treatment,” *Proc. IEEE Int. Conf. Micro Electro Mech. Syst.*, no. January, pp. 412–414, 2018.

[75] C. Kensinger *et al.*, “First implantation of silicon nanopore membrane hemofilters,” *ASAIO J.*, vol. 62, no. 4, pp. 491–495, 2016.

[76] Kim *et al.*, “Diffusive silicon nanopore membranes for hemodialysis applications,” *PLoS One*, vol. 11, no. 7, pp. 1–20, 2016.

[77] A. K. W. Buck *et al.*, “Original article submission: Platelet stress accumulation analysis to predict thrombogenicity of an artificial kidney,” *J. Biomech.*, vol. 69, pp. 26–33, 2018.

[78] I. R. Ausri, E. M. Feygin, C. Q. Cheng, Y. Wang, Z. Y. (William) Lin, and X. (Shirley) Tang, “A highly efficient and antifouling microfluidic platform for portable

hemodialysis devices," *MRS Commun.*, pp. 1–6, 2018.

[79] J.-B. Fan *et al.*, "Bioinspired Microfluidic Device by Integrating a Porous Membrane and Heterostructured Nanoporous Particles for Biomolecule Cleaning," *ACS Nano*, p. acsnano.9b03918, 2019.

[80] H. Di, G. J. O. Martin, and D. E. Dunstan, "A microfluidic system for studying particle deposition during ultrafiltration," *J. Memb. Sci.*, vol. 532, no. March 2017, pp. 68–75, 2017.

[81] E. Garreta *et al.*, "Tissue engineering by decellularization and 3D bioprinting," *Mater. Today*, vol. 20, no. 4, pp. 166–178, 2017.

[82] S. Yamanaka and T. Yokoo, "Current bioengineering methods for whole kidney regeneration," *Stem Cells Int.*, vol. 2015, 2015.

[83] N. Poornejad, L. B. Schaumann, E. M. Buckmiller, B. L. Roeder, and A. D. Cook, "Current Cell-Based Strategies for Whole Kidney Regeneration," *Tissue Eng. Part B Rev.*, vol. 22, no. 5, pp. 358–370, 2016.

[84] C. Legallais, D. Kim, S. M. Mihaila, and M. Figliuzzi, "Bioengineering organs for blood detoxification : artificial , bioartificial and tissue engineered kidney and liver," *Adv. Healthc. Mater.*, no. October, 2018.

[85] I. K. Ko *et al.*, "Enhanced re-endothelialization of acellular kidney scaffolds for whole organ engineering via antibody conjugation of vasculatures," *Technology*, vol. 02, no. 03, pp. 243–253, 2014.

[86] J. P. Zambon, "Kidney regeneration: Where we are and future perspectives," *World J. Nephrol.*, vol. 3, no. 3, p. 24, 2014.

[87] J. J. Song and H. C. Ott, "Organ engineering based on decellularized matrix scaffolds," *Trends Mol. Med.*, vol. 17, no. 8, pp. 424–432, 2011.

[88] K. H. Nakayama, C. A. Batchelder, C. I. Lee, and A. F. Tarantal, "Decellularized Rhesus Monkey Kidney as a Three-Dimensional Scaffold for Renal Tissue Engineering," *Tissue Eng. Part A*, vol. 16, no. 7, pp. 2207–2216, 2010.

[89] D. C. Sullivan *et al.*, "Decellularization methods of porcine kidneys for whole

organ engineering using a high-throughput system," *Biomaterials*, vol. 33, no. 31, pp. 7756–7764, 2012.

[90] R. P. Lanza *et al.*, "Generation of histocompatible tissues using nuclear transplantation," *Nat. Biotechnol.*, vol. 20, no. July, pp. 689–696, 2002.

[91] P. M. Baptista, M. M. Siddiqui, G. Lozier, S. R. Rodriguez, A. Atala, and S. Soker, "The use of whole organ decellularization for the generation of a vascularized liver organoid," *Hepatology*, vol. 53, no. 2, pp. 604–617, 2011.

[92] R. Katari *et al.*, "Renal bioengineering with scaffolds generated from human kidneys," *Nephron - Exp. Nephrol.*, vol. 126, no. 2, pp. 119–124, 2014.

[93] R. Chang, J. Nam, and W. Sun, "Effects of Dispensing Pressure and Nozzle Diameter on Cell Survival from Solid Freeform Fabrication–Based Direct Cell Writing," *Tissue Eng. Part A*, vol. 14, no. 1, pp. 41–48, 2008.

[94] M. Salvatori *et al.*, "Semi-xenotransplantation: The regenerative medicine-based approach to immunosuppression-free transplantation and to meet the organ demand," *Xenotransplantation*, vol. 22, no. 1, pp. 1–6, 2015.

[95] J. A. Fishman, L. Scobie, and Y. Takeuchi, "Xenotransplantation-associated infectious risk: A WHO consultation," *Xenotransplantation*, vol. 19, no. 2, pp. 72–81, 2012.

[96] T. Yokoo *et al.*, "Xenobiotic Kidney Organogenesis from Human Mesenchymal Stem Cells Using a Growing Rodent Embryo," *J Am Soc Nephrol*, vol. 17, no. 7, pp. 1026–1034, 2006.

[97] S. V. Murphy and A. Atala, "3D bioprinting of tissues and organs," *Nat. Biotechnol.*, vol. 32, no. 8, pp. 773–785, 2014.

[98] S. Turunen, S. Kaisto, I. Skovorodkin, V. Mironov, and T. Kalpio, "3D bioprinting of the kidney — hype or hope ?," vol. 2, no. May, pp. 119–162, 2018.

[99] G. Gao, B. S. Kim, J. Jang, and D. W. Cho, "Recent Strategies in Extrusion-Based Three-Dimensional Cell Printing toward Organ Biofabrication," *ACS Biomater. Sci. Eng.*, vol. 5, no. 3, pp. 1150–1169, 2019.

[100] H. D. Humes, S. M. MacKay, A. J. Funke, and D. A. Buffington, “Tissue engineering of a bioartificial renal tubule assist device: In vitro transport and metabolic characteristics,” *Kidney Int.*, vol. 55, no. 6, pp. 2502–2514, 1999.

[101] H. D. Humes, D. A. Buffington, S. M. MacKay, A. J. Funke, and W. F. Weitzel, “Replacement of renal function in uremic animals with a tissue-engineered kidney.,” *Nat. Biotechnol.*, vol. 17, no. 5, pp. 451–455, 1999.

[102] H. D. Humes *et al.*, “Metabolic replacement of kidney function in uremic animals with a bioartificial kidney containing human cells,” *Am. J. Kidney Dis.*, vol. 39, no. 5, pp. 1078–1087, 2002.

[103] H. D. Humes *et al.*, “Initial clinical results of the bioartificial kidney containing human cells in ICU patients with acute renal failure,” *Kidney Int.*, vol. 66, no. 4, pp. 1578–1588, 2004.

[104] J. Tumlin *et al.*, “Efficacy and Safety of Renal Tubule Cell Therapy for Acute Renal Failure,” *J. Am. Soc. Nephrol.*, vol. 19, no. 5, pp. 1034–1040, 2008.

[105] H. D. Humes, J. T. Sobota, F. Ding, and J. H. Song, “A selective cytopheretic inhibitory device to treat the immunological dysregulation of acute and chronic renal failure,” *Blood Purif.*, vol. 29, no. 2, pp. 183–190, 2010.

[106] C. J. Pino, A. S. Yevzlin, J. Tumlin, and H. D. Humes, “Cell-based strategies for the treatment of kidney dysfunction: A review,” *Blood Purif.*, vol. 34, no. 2, pp. 117–123, 2012.

[107] D. A. Buffington, C. J. Pino, L. Chen, A. J. Westover, G. Hageman, and H. D. Humes, “Bioartificial Renal Epithelial Cell System (BRECS): A Compact, Cryopreservable Extracorporeal Renal Replacement Device,” *Cell Med.*, vol. 4, no. 1, pp. 33–44, 2012.

[108] C. J. Pino and H. D. Humes, “Stem cell technology for the treatment of acute and chronic renal failure,” *Transl. Res.*, vol. 156, no. 3, pp. 161–168, 2010.

[109] J. Jansen *et al.*, “Human proximal tubule epithelial cells cultured on hollow fibers: living membranes that actively transport organic cations,” *Sci. Rep.*, vol. 5, no. 1, p. 16702, 2015.

[110] C. J. Pino, A. J. Westover, K. A. Johnston, D. A. Buffington, and H. D. Humes, "Regenerative Medicine and Immunomodulatory Therapy: Insights From the Kidney, Heart, Brain, and Lung," *Kidney Int. Reports*, vol. 3, no. 4, pp. 771–783, 2018.

[111] W. H. Fissell, A. J. Fleischman, H. D. Humes, and S. Roy, "Development of continuous implantable renal replacement: past and future," *Transl. Res.*, vol. 150, no. 6, pp. 327–336, 2007.

[112] W. H. Fissell, S. Manley, A. Westover, H. D. Humes, A. J. Fleischman, and S. Roy, "Differentiated growth of human renal tubule cells on thin-film and nanostructured materials," *ASAIO J.*, vol. 52, no. 3, pp. 221–227, 2006.

[113] A. T. Conlisk, S. Datta, W. H. Fissell, and S. Roy, "Biomolecular transport through hemofiltration membranes," *Ann. Biomed. Eng.*, vol. 37, no. 4, pp. 722–736, 2009.

[114] W. H. Fissell, A. Dubnisheva, A. N. Eldridge, A. J. Fleischman, A. L. Zydney, and S. Roy, "High-performance silicon nanopore hemofiltration membranes," *J. Memb. Sci.*, vol. 326, no. 1, pp. 58–63, 2009.

[115] D. M. Kanani, W. H. Fissell, S. Roy, A. Dubnisheva, A. Fleischman, and A. L. Zydney, "Permeability-selectivity analysis for ultrafiltration: Effect of pore geometry," *J. Memb. Sci.*, vol. 349, no. 1–2, pp. 405–410, 2010.

[116] L. Muthusubramaniam *et al.*, "Hemocompatibility of silicon-based substrates for biomedical implant applications," *Ann. Biomed. Eng.*, vol. 39, no. 4, pp. 1296–1305, 2011.

[117] W. H. Fissell, S. Roy, and A. Davenport, "Achieving more frequent and longer dialysis for the majority: wearable dialysis and implantable artificial kidney devices," *Kidney Int.*, vol. 84, no. 2, pp. 256–264, 2013.

[118] V. Gura *et al.*, "A wearable artificial kidney for patients with end-stage renal disease," *JCI Insight*, vol. 1, no. 8, pp. 1–15, 2016.

[119] A. Davenport, V. Gura, C. Ronco, M. Beizai, C. Ezon, and E. Rambod, "A wearable haemodialysis device for patients with end-stage renal failure: a pilot study,"

*Lancet*, vol. 370, no. 9604, pp. 2005–2010, 2007.

[120] V. Gura, M. Beizai, C. Ezon, and E. Rambod, “Continuous Renal Replacement Therapy for Congestive Heart Failure: The Wearable Continuous Ultrafiltration System,” *ASAIO J.*, vol. 52, no. 1, pp. 59–61, 2006.

[121] V. Gura, A. S. Macy, M. Beizai, C. Ezon, and T. A. Golper, “Technical breakthroughs in the wearable artificial kidney (WAK),” *Clin. J. Am. Soc. Nephrol.*, vol. 4, no. 9, pp. 1441–1448, 2009.

[122] V. Gura, A. Davenport, M. Beizai, C. Ezon, and C. Ronco, “β2-Microglobulin and Phosphate Clearances Using a Wearable Artificial Kidney: A Pilot Study,” *Am. J. Kidney Dis.*, vol. 54, no. 1, pp. 104–111, 2009.

[123] C. Ronco, A. Davenport, and V. Gura, “The future of the artificial kidney: moving towards wearable and miniaturized devices,” *Nefrologia*, vol. 31, no. 1, pp. 9–16, 2011.

[124] V. Gura, C. Ronco, and A. Davenport, “The wearable artificial kidney, why and how: From holy grail to reality,” *Semin. Dial.*, vol. 22, no. 1, pp. 13–17, 2009.

[125] D. G. Johnson *et al.*, “Ultrathin Silicon Membranes for Wearable Dialysis,” *Adv. Chronic Kidney Dis.*, vol. 20, no. 6, pp. 508–515, 2013.

[126] W. Zhu, J. Li, and J. Liu, “The cell engineering construction and function evaluation of multi-layer biochip dialyzer,” *Biomed. Microdevices*, vol. 15, no. 5, pp. 781–791, 2013.

[127] C. P. Ng, Y. Zhuang, A. W. H. Lin, and J. C. M. Teo, “A Fibrin-Based Tissue-Engineered Renal Proximal Tubule for Bioartificial Kidney Devices: Development, Characterization and In Vitro Transport Study,” *Int. J. Tissue Eng.*, vol. 2013, pp. 1–10, 2013.

[128] Y. Sakuta, I. Takehara, K. Tsunoda, and K. Sato, “Development of a microfluidic system comprising dialysis and secretion components for a bioassay of renal clearance,” *Anal. Sci.*, pp. 1–5, 2018.

[129] M. Ahmadi, “Implantable Renal Replacement Therapy,” 2018.

[130] F. Li, R. M. Guijt, and M. C. Breadmore, “Nanoporous membranes for microfluidic concentration prior to electrophoretic separation of proteins in urine,” *Anal. Chem.*, vol. 88, no. 16, pp. 8257–8263, 2016.

[131] R. F. Jeffrey *et al.*, “A Comparison of Molecular Clearance Rates During Continuous Hemofiltration and Hemodialysis with a Novel Volumetric Continuous Renal Replacement System,” *Artif. Organs*, vol. 18, no. 6, pp. 425–428, 1994.

[132] A. J. Conde *et al.*, “A polymer chip-integrable piezoelectric micropump with low backpressure dependence,” *RSC Adv.*, vol. 5, no. 62, pp. 49996–50000, 2015.

[133] M. Kawecki *et al.*, “A review of decellurization methods caused by an urgent need for quality control of cell-free extracellular matrix’ scaffolds and their role in regenerative medicine,” *J. Biomed. Mater. Res. - Part B Appl. Biomater.*, vol. 106, no. 2, pp. 909–923, 2018.

[134] A. C. Castro, M. Neri, A. Nayak Karopadi, A. Lorenzin, N. Marchionna, and C. Ronco, “Wearable artificial kidney and wearable ultrafiltration device vascular access—future directions,” *Clin. Kidney J.*, pp. 1–8, 2018.

[135] C. Koch, V. Remcho, and J. Ingle, “PDMS and tubing-based peristaltic micropumps with direct actuation,” *Sensors Actuators, B Chem.*, vol. 135, no. 2, pp. 664–670, 2009.

[136] E. Weinberg, M. Kaazempur-Mofrad, and J. Borenstein, “Concept and computational design for a bioartificial nephron-on-a-chip,” *Int. J. Artif. Organs*, vol. 31, no. 6, pp. 508–514, 2008.

[137] K.-J. Jang and K.-Y. Suh, “A multi-layer microfluidic device for efficient culture and analysis of renal tubular cells,” *Lab Chip*, vol. 10, no. 1, pp. 36–42, 2010.

[138] K.-J. Jang *et al.*, “Human kidney proximal tubule-on-a-chip for drug transport and nephrotoxicity assessment,” *Integr. Biol.*, vol. 5, no. 9, p. 1119, 2013.

[139] M. J. Wilmer, C. P. Ng, H. L. Lanz, P. Vulto, L. Suter-Dick, and R. Masereeuw, “Kidney-on-a-Chip Technology for Drug-Induced Nephrotoxicity Screening,” *Trends Biotechnol.*, vol. 34, no. 2, pp. 156–170, 2016.

[140] T. T. G. Nieskens and M. J. Wilmer, “Kidney-on-a-chip technology for renal proximal tubule tissue reconstruction,” *Eur. J. Pharmacol.*, vol. 790, pp. 46–56, 2016.

[141] S. Musah *et al.*, “Mature induced-pluripotent-stem-cell-derived human podocytes reconstitute kidney glomerular-capillary-wall function on a chip,” *Nat. Biomed. Eng.*, vol. 1, no. 5, p. 0069, 2017.

[142] V. B. Dang and S.-J. Kim, “Water-head-driven microfluidic oscillators for autonomous control of periodic flows and generation of aqueous two-phase system droplets,” *Lab Chip*, vol. 17, no. 2, pp. 286–292, 2017.

[143] G. Kim, B. Van Dang, and S. Kim, “Stepwise waveform generator for autonomous microfluidic control,” *Sensors Actuators B. Chem.*, vol. 266, pp. 614–619, 2018.

[144] S. Kim *et al.*, “Pharmacokinetic profile that reduces nephrotoxicity of gentamicin in a perfused kidney-on-a-chip,” *Biofabrication*, vol. 8, no. 015021, 2016.

[145] L. Wang, T. Tao, W. Su, H. Yu, Y. Yu, and J. Qin, “A disease model of diabetic nephropathy in a glomerulus-on-a-chip microdevice,” *Lab Chip*, vol. 17, no. 10, pp. 1749–1760, 2017.

[146] X. Chen, J. Shen, Z. Hu, and X. Huo, “Manufacturing methods and applications of membranes in microfluidics,” *Biomed. Microdevices*, vol. 18, no. 6, p. 104, 2016.

[147] B. Mosadegh *et al.*, “Integrated elastomeric components for autonomous regulation of sequential and oscillatory flow switching in microfluidic devices,” *Nat. Phys.*, vol. 6, no. 6, pp. 433–437, 2010.

[148] V. B. Dang and S. J. Kim, “Modular fluidic resistors to enable widely tunable flow rate and fluidic switching period in a microfluidic oscillator,” *Electrophoresis*, vol. 38, no. 7, pp. 977–982, 2017.

[149] K. A. Homan *et al.*, “Bioprinting of 3D Convoluted Renal Proximal Tubules on Perfusable Chips,” *Sci. Rep.*, vol. 6, no. 1, p. 34845, 2016.

[150] R. D. Sochol, N. R. Gupta, and J. V. Bonventre, “A Role for 3D Printing in Kidney-on-a-Chip Platforms,” *Curr. Transplant. Reports*, vol. 3, no. 1, pp. 82–92, 2016.

[151] X. Fan *et al.*, “A microfluidic chip integrated with a high-density PDMS-based microfiltration membrane for rapid isolation and detection of circulating tumor cells,” *Biosens. Bioelectron.*, vol. 71, pp. 380–386, 2015.

[152] M. Rafeie, J. Zhang, M. Asadnia, W. Li, and M. E. Warkiani, “Multiplexing slanted spiral microchannels for ultra-fast blood plasma separation,” *Lab Chip*, vol. 16, no. 15, pp. 2791–2802, 2016.

[153] M. Shakeel Syed, M. Rafeie, R. Henderson, D. Vandamme, M. Asadnia, and M. Ebrahimi Warkiani, “A 3D-printed mini-hydrocyclone for high throughput particle separation: application to primary harvesting of microalgae,” *Lab Chip*, vol. 17, no. 14, pp. 2459–2469, 2017.

[154] A. J. Mach and D. di Carlo, “Continuous scalable blood filtration device using inertial microfluidics,” *Biotechnol. Bioeng.*, vol. 107, no. 2, pp. 302–311, 2010.

[155] T. Salafi, K. K. Zeming, and Y. Zhang, “Advancements in microfluidics for nanoparticle separation,” *Lab Chip*, vol. 17, no. 1, pp. 11–33, 2017.

[156] M. Rafeie, S. Hosseinzadeh, R. A. Taylor, and M. E. Warkiani, “New insights into the physics of inertial microfluidics in curved microchannels. I. Relaxing the fixed inflection point assumption,” *Biomicrofluidics*, vol. 13, no. 034117, 2019.

[157] P. Dhananchezhiyan and S. S. Hiremath, “Improving the performance of micro pumps by reduction of flow pulsation for drug delivery application,” *Adv. Mater. Process. Technol.*, vol. 0698, pp. 1–15, 2018.

[158] J. Sateesh, K. G. Sravani, R. A. Kumar, and K. Guha, “Design and Flow Analysis of MEMS based Piezo-electric Micro Pump,” *Microsyst. Technol.*, vol. 24, no. 3, pp. 1609–1614, 2018.

[159] Y. Wang and L. Fu, “Micropumps and biomedical applications – A review,” *Microelectron. Eng.*, vol. 195, pp. 121–138, 2018.

[160] S. Cheng and Z. Wu, “Microfluidic stretchable RF electronics,” *Lab Chip*, vol. 10, no. 23, p. 3227, 2010.

[161] S. Xu *et al.*, “Soft Microfluidic Assemblies of for the Skin,” *Science (80-. ).*, vol. 344, no. April, pp. 70–74, 2014.

[162] R. Sobot, “Implantable systems - Retrospective tutorial review,” *Microelectronics J.*, no. June, pp. 1–9, 2017.

[163] M. N. Dakurah, C. Koo, W. Choi, and Y. H. Joung, “Implantable bladder sensors: A methodological review,” *Int. Neurourol. J.*, vol. 19, no. 3, pp. 133–141, 2015.

[164] A. Sonawane, P. Manickam, and S. Bhansali, “Stability of Enzymatic Biosensors for Wearable Applications,” *IEEE Rev. Biomed. Eng.*, vol. 10, pp. 174–186, 2017.

[165] T. Thorsen, S. J. Maerkl, and S. R. Quake, “Microfluidic large-scale integration,” *Science (80-. ).*, vol. 298, no. 5593, pp. 580–584, 2002.

[166] J. Shin, H. Park, V. B. Dang, C.-W. Kim, and S.-J. Kim, “Elastomeric microfluidic valve with low, constant opening threshold pressure,” *RSC Adv.*, vol. 5, no. 30, pp. 23239–23245, 2015.

[167] J. W. Stansbury and M. J. Idacavage, “3D printing with polymers: Challenges among expanding options and opportunities,” *Dent. Mater.*, vol. 32, no. 1, pp. 54–64, 2016.

[168] H.-G. Yi, H. Lee, and D.-W. Cho, “3D Printing of Organs-On-Chips,” *Bioengineering*, vol. 4, no. 1, p. 10, 2017.

[169] A. Bonyár, H. Sántha, B. Ring, M. Varga, J. G. Kovács, and G. Harsányi, “3D Rapid Prototyping Technology (RPT) as a powerful tool in microfluidic development,” *Procedia Eng.*, vol. 5, pp. 291–294, 2010.

[170] H. Wei *et al.*, “Particle sorting using a porous membrane in a microfluidic device,” *Lab Chip*, vol. 11, no. 2, pp. 238–245, 2011.

[171] S. Zheng *et al.*, “Membrane microfilter device for selective capture, electrolysis and genomic analysis of human circulating tumor cells,” *J. Chromatogr. A*, vol. 1162, no. 2 SPEC. ISS., pp. 154–161, 2007.

[172] A. A. S. Bhagat, H. Bow, H. W. Hou, S. J. Tan, J. Han, and C. T. Lim, “Microfluidics for cell separation,” *Med. Biol. Eng. Comput.*, vol. 48, no. 10, pp. 999–1014, 2010.

[173] M. M. Wang *et al.*, “Microfluidic sorting of mammalian cells by optical force switching,” *Nat. Biotechnol.*, vol. 23, no. 1, pp. 83–87, 2005.

[174] P. Y. Chiou, A. T. Ohta, and M. C. Wu, “Massively parallel manipulation of single cells and microparticles using optical images,” *Nature*, vol. 436, no. 7049, pp. 370–372, 2005.

[175] I. Doh and Y. H. Cho, “A continuous cell separation chip using hydrodynamic dielectrophoresis (DEP) process,” *Sensors Actuators, A Phys.*, vol. 121, no. 1, pp. 59–65, 2005.

[176] W. Hoffmann, W. Werner, R. Steinert, and R. Kaufmannt, “Cell electrophoresis for diagnostic purposes. I. Diagnostic value of the electrophoretic mobility test (EMT) for the detection of gynaecological malignancies,” *Br. J. Cancer*, vol. 43, pp. 588–597, 1981.

[177] M. Zborowski, G. R. Ostera, L. R. Moore, S. Milliron, J. J. Chalmers, and A. N. Schechter, “Red blood cell magnetophoresis,” *Biophys. J.*, vol. 84, no. 4, pp. 2638–2645, 2003.

[178] K. H. Han and A. B. Frazier, “Paramagnetic capture mode magnetophoretic microseparator for high efficiency blood cell separations,” *Lab Chip*, vol. 6, no. 2, pp. 265–273, 2006.

[179] F. Petersson, L. Åberg, A. M. Swärd-Nilsson, and T. Laurell, “Free flow acoustophoresis: Microfluidic-based mode of particle and cell separation,” *Anal. Chem.*, vol. 79, no. 14, pp. 5117–5123, 2007.

[180] A. A. S. Bhagat, S. S. Kuntaegowdanahalli, and I. Papautsky, “Inertial microfluidics for continuous particle filtration and extraction,” *Microfluid. Nanofluidics*, vol. 7, no. 2, pp. 217–226, 2009.

[181] N. Pamme, “Continuous flow separations in microfluidic devices,” *Lab Chip*, vol. 7, no. 12, pp. 1644–1659, 2007.

[182] L. R. Huang, E. C. Cox, R. H. Austin, and J. C. Sturm, “Continous particle separation through deterministic lateral displacement,” *Science (80-. ).*, vol. 304, no. 5673, pp. 987–991, 2004.

[183] K. Loutherback, J. D’Silva, L. Liu, A. Wu, R. H. Austin, and J. C. Sturm, “Deterministic separation of cancer cells from blood at 10 mL/min,” *AIP Adv.*, vol.

2, no. 4, 2012.

[184] H. N. Joensson, M. Uhlén, and H. A. Svahn, “Droplet size based separation by deterministic lateral displacement—separating droplets by cell-induced shrinking,” *Lab Chip*, vol. 11, no. 7, p. 1305, 2011.

[185] B. H. Wunsch *et al.*, “Nanoscale lateral displacement arrays for the separation of exosomes and colloids down to 20nm,” *Nat. Nanotechnol.*, vol. 11, no. 11, pp. 936–940, 2016.

[186] M. E. Warkiani, L. Wu, A. K. P. Tay, and J. Han, “Large-Volume Microfluidic Cell Sorting for Biomedical Applications,” *Annu. Rev. Biomed. Eng.*, vol. 17, no. 1, pp. 1–34, 2015.

[187] X. Chen, D. F. Cui, C. C. Liu, and H. Li, “Microfluidic chip for blood cell separation and collection based on crossflow filtration,” *Sensors Actuators, B Chem.*, vol. 130, no. 1, pp. 216–221, 2008.

[188] X. Lu and X. Xuan, “Continuous Microfluidic Particle Separation via Elasto-Inertial Pinched Flow Fractionation,” *Anal. Chem.*, vol. 87, no. 12, pp. 6389–6396, 2015.

[189] P. Wilding, L. J. Kricka, J. Cheng, G. Hvichia, M. A. Shoffner, and P. Fortina, “Integrated cell isolation and polymerase chain reaction analysis using silicon microfilter chambers,” *Anal. Biochem.*, vol. 257, no. 2, pp. 95–100, 1998.

[190] M. Faivre, M. Abkarian, K. Bickraj, and H. A. Stone, “Geometrical focusing of cells in a microfluidic device: An approach to separate blood plasma,” *Biorheology*, vol. 43, no. 2, pp. 147–159, 2006.

[191] S. C. Hur, A. J. Mach, and D. Di Carlo, “High-throughput size-based rare cell enrichment using microscale vortices,” *Biomicrofluidics*, vol. 5, no. 2, 2011.

[192] G. Guan *et al.*, “Spiral microchannel with rectangular and trapezoidal cross-sections for size based particle separation,” *Sci. Rep.*, vol. 3, pp. 1–9, 2013.

[193] A. Nejat, F. Kowsary, A. Hasanzadeh-Barforoushi, and S. Ebrahimi, “Unsteady pulsating characteristics of the fluid flow through a sudden expansion microvalve,” *Microfluid. Nanofluidics*, vol. 17, no. 4, pp. 623–637, 2014.

[194] Y. Daghighi and D. Li, “Micro-valve using induced-charge electrokinetic motion of Janus particle,” *Lab Chip*, vol. 11, no. 17, pp. 2929–2940, 2011.

[195] J. Kim, M. Kang, E. C. Jensen, and R. A. Mathies, “Lifting gate polydimethylsiloxane microvalves and pumps for microfluidic control,” *Anal. Chem.*, vol. 84, no. 4, pp. 2067–2071, 2012.

[196] D. Copic and A. J. Hart, “Corrugated paraffin nanocomposite films as large stroke thermal actuators and self-activating thermal interfaces,” *ACS Appl. Mater. Interfaces*, vol. 7, no. 15, pp. 8218–8224, 2015.

[197] M. A. Unger, H. P. Chou, T. Thorsen, A. Scherer, and S. R. Quake, “Monolithic microfabricated valves and pumps by multilayer soft lithography,” *Science (80-. ).*, vol. 288, no. 5463, pp. 113–116, 2000.

[198] J. A. Weaver, J. Melin, D. Stark, S. R. Quake, and M. A. Horowitz, “Static control logic for microfluidic devices using pressure-gain valves,” *Nat. Phys.*, vol. 6, no. 3, pp. 218–223, 2010.

[199] W. H. Grover, A. M. Skelley, C. N. Liu, E. T. Lagally, and R. A. Mathies, “Monolithic membrane valves and diaphragm pumps for practical large-scale integration into glass microfluidic devices,” *Sensors Actuators, B Chem.*, vol. 89, no. 3, pp. 315–323, 2003.

[200] R. Mohan, B. R. Schudel, A. V. Desai, J. D. Yearsley, C. A. Apblett, and P. J. A. Kenis, “Design considerations for elastomeric normally closed microfluidic valves,” *Sensors Actuators B Chem.*, vol. 160, no. 1, pp. 1216–1223, 2011.

[201] J. Kim, A. M. Stockton, E. C. Jensen, and R. A. Mathies, “Pneumatically actuated microvalve circuits for programmable automation of chemical and biochemical analysis,” *Lab Chip*, vol. 16, no. 5, pp. 812–819, 2016.

[202] B. Van Dang, G. Kim, and S. J. Kim, “Anomalous pulse change in gravity-driven microfluidic oscillator and its application to photodiode switching,” *Microfluid. Nanofluidics*, vol. 22, no. 2, pp. 1–6, 2018.

[203] M. Wehner *et al.*, “An integrated design and fabrication strategy for entirely soft, autonomous robots,” *Nature*, vol. 536, no. 7617, pp. 451–455, 2016.

[204] Z. Li and S. Kim, “Pulsatile micromixing using water-head-driven microfluidic oscillators,” *Chem. Eng. J.*, vol. 313, pp. 1364–1369, 2017.

[205] N. Xiang and Z. Ni, “High-throughput blood cell focusing and plasma isolation using spiral inertial microfluidic devices,” *Biomed. Microdevices*, vol. 17, no. 6, pp. 1–11, 2015.

[206] N. Inoue, Y. Koya, N. Miki, and H. Onoe, “Graphene-Based Wireless Inline Pressure Sensor for in Vivo Blood Pressure Monitoring,” *Micromachines*, vol. 10, no. 2, p. 139, 2019.

[207] F. A. Gotch and J. A. Sargent, “A mechanistic analysis of the National Cooperative Dialysis Study (NCDS),” *Kidney Int.*, vol. 28, no. 3, pp. 526–534, 1985.

[208] A. S. Bode and J. H. M. Tordoir, *Vascular access for hemodialysis therapy*, vol. 404, no. January 2013. 2013.

[209] M. E. Warkiani *et al.*, “Slanted spiral microfluidics for the ultra-fast, label-free isolation of circulating tumor cells,” *Lab Chip*, vol. 14, no. 1, pp. 128–137, 2014.

[210] P. K. Das and A. B. M. T. Hasan, “Mechanical micropumps and their applications: A review,” *AIP Conf. Proc.*, vol. 1851, no. June, 2017.

[211] C. Ronco and A. R. Nissenson, “Does nanotechnology apply to dialysis?,” *Blood Purif.*, vol. 19, no. 4, pp. 347–352, 2001.

[212] J. T. Daugirdas and A. A. Bernardo, “Hemodialysis effect on platelet count and function and hemodialysis- associated thrombocytopenia,” *Kidney Int.*, vol. 82, no. 2, pp. 147–157, 2012.

[213] J. Himmelfarb, P. Stenvinkel, T. A. Ikizler, and R. M. Hakim, “The elephant in uremia: Oxidant stress as a unifying concept of cardiovascular disease in uremia,” *Kidney Int.*, vol. 62, no. 5, pp. 1524–1538, 2002.

[214] L. Del Vecchio, F. Locatelli, and M. Carini, “What We Know About Oxidative Stress in Patients with Chronic Kidney Disease on Dialysis-Clinical Effects, Potential Treatment, and Prevention,” *Semin. Dial.*, vol. 24, no. 1, pp. 56–64, 2011.

[215] G. a Kaysen, “The microinflammatory state in uremia: causes and potential

consequences.," *J. Am. Soc. Nephrol.*, vol. 12, no. 17, pp. 1549–1557, 2001.

[216] L. Li, R. E. Marchant, A. Dubnisheva, S. Roy, and W. H. Fissell, "Anti-biofouling sulfobetaine polymer thin films on silicon and silicon nanopore membranes," *J. Biomater. Sci. Polym. Ed.*, vol. 22, no. 1–3, pp. 91–106, 2011.

[217] J. Zhu and R. E. Marchant, "Dendritic saccharide surfactant polymers as antifouling interface materials to reduce platelet adhesion," *Biomacromolecules*, vol. 7, no. 4, pp. 1036–1041, 2006.

[218] K. C. Popat and T. A. Desai, "Poly(ethylene glycol) interfaces: An approach for enhanced performance of microfluidic systems," *Biosens. Bioelectron.*, vol. 19, no. 9, pp. 1037–1044, 2004.

[219] S. Roy *et al.*, "Silicon nanopore membrane technology for an implantable artificial kidney," *TRANSDUCERS 2009 - 15th Int. Conf. Solid-State Sensors, Actuators Microsystems*, pp. 755–760, 2009.

[220] G. Kotzar *et al.*, "Evaluation of MEMS materials of construction for implantable medical devices," *Biomaterials*, vol. 23, no. 13, pp. 2737–2750, 2002.

[221] S. Sharma and T. Desai, "Nanostructured Antifouling Poly(ethylene glycol) Films for Silicon-Based Microsystems," *J. Nanosci. Nanotechnol.*, vol. 5, no. 2, pp. 235–243, 2005.

[222] S. Sharma, R. W. Johnson, and T. A. Desai, "Evaluation of the Stability of Nonfouling Ultrathin Poly(ethylene glycol) Films for Silicon-Based Microdevices," *Langmuir*, vol. 20, no. 2, pp. 348–356, 2004.

[223] W. H. Fissell *et al.*, "Ficoll is not a rigid sphere," *AJP Ren. Physiol.*, vol. 293, no. 4, pp. F1209–F1213, 2007.

[224] W. Zhang, J. Luo, L. Ding, and M. Y. Jaffrin, "A review on flux decline control strategies in pressure-driven membrane processes," *Ind. Eng. Chem. Res.*, vol. 54, no. 11, pp. 2843–2861, 2015.

[225] H. D. Humes, W. H. Fissell, and K. Tiranathanagul, "The future of hemodialysis membranes," *Kidney Int.*, vol. 69, no. 7, pp. 1115–1119, 2006.

[226] Y. Kang, S. Zheng, C. Finnerty, M. J. Lee, and B. Mi, “Regenerable Polyelectrolyte Membrane for Ultimate Fouling Control in Forward Osmosis,” *Environ. Sci. Technol.*, vol. 51, no. 6, pp. 3242–3249, 2017.

[227] Y. R. Chang, Y. J. Lee, and D. J. Lee, “Membrane fouling during water or wastewater treatments: Current research updated,” *J. Taiwan Inst. Chem. Eng.*, vol. 0, pp. 1–9, 2018.

[228] N. Wisniewski, F. Moussy, and W. M. Reichert, “Characterization of implantable biosensor membrane biofouling,” *Fresenius J. Anal. Chem.*, vol. 366, no. 6–7, pp. 611–621, 2000.

[229] L. Deng *et al.*, “Biofouling and control approaches in membrane bioreactors,” *Bioresour. Technol.*, vol. 221, pp. 656–665, 2016.

[230] K. I. Yamamoto, M. Hiwatari, F. Kohori, K. Sakai, M. Fukuda, and T. Hiyoshi, “Membrane fouling and dialysate flow pattern in an internal filtration-enhancing dialyzer,” *J. Artif. Organs*, vol. 8, no. 3, pp. 198–205, 2005.

[231] J. Paris, P. Guichardon, and F. Charbit, “Transport phenomena in ultrafiltration: A new two-dimensional model compared with classical models,” *J. Memb. Sci.*, vol. 207, no. 1, pp. 43–58, 2002.

[232] X. Li, Y. Mo, J. Li, W. Guo, and H. H. Ngo, “In-situ monitoring techniques for membrane fouling and local filtration characteristics in hollow fiber membrane processes: A critical review,” *J. Memb. Sci.*, vol. 528, no. December 2016, pp. 187–200, 2017.

[233] X. Zhang, P. Gao, V. Hollimon, D. S. Brodus, A. Johnson, and H. Hu, “Surface thiolation of silicon for antifouling application,” *Chem. Cent. J.*, vol. 12, no. 1, pp. 1–7, 2018.

[234] H. Waheed, F. T. Minhas, and A. Hussain, “Cellulose acetate/sericin blend membranes for use in dialysis,” *Polym. Bull.*, vol. 75, no. 9, pp. 3935–3950, 2018.

[235] X. Zhao and C. Liu, “Efficient preparation of a novel PVDF antifouling membrane based on the solvent-responsive cleaning properties,” *Sep. Purif. Technol.*, vol. 210, no. August 2018, pp. 100–106, 2019.

[236] K. J. Hwang and C. Y. Ku, “Model development for estimating microfiltration performance of bio-ethanol fermentation broth,” *J. Taiwan Inst. Chem. Eng.*, vol. 45, no. 4, pp. 1233–1240, 2014.

[237] R. M. Hakim, D. T. Fearon, and J. M. Lazarus, “Biocompatibility of dialysis membranes: Effects of chronic complement activation,” *Kidney Int.*, vol. 26, no. 2, pp. 194–200, 1984.

[238] D. E. Chenoweth, A. K. Cheung, and L. W. Henderson, “Anaphylatoxin formation during hemodialysis: Effects of different dialyzer membranes,” *Kidney Int.*, vol. 24, no. 6, pp. 764–769, 1983.

[239] P. R. Craddock, J. Fehr, A. P. Dalmasso, K. L. Brighan, and H. S. Jacob, “Hemodialysis leukopenia. Pulmonary vascular leukostasis resulting from complement activation by dialyzer cellophane membranes,” *J. Clin. Invest.*, vol. 59, no. 5, pp. 879–888, 1977.

[240] J. C. Hempel *et al.*, “Distinct in vitro Complement Activation by Various Intravenous Iron Preparations,” *Am. J. Nephrol.*, vol. 45, no. 1, pp. 49–59, 2017.

[241] M. Abe, T. Hamano, A. Wada, S. Nakai, and I. Masakane, “Effect of dialyzer membrane materials on survival in chronic hemodialysis patients: Results from the annual survey of the Japanese nationwide dialysis registry,” *PLoS One*, vol. 12, no. 9, pp. 1–18, 2017.

[242] F. Poppelaars *et al.*, “The complement system in dialysis: A forgotten story?,” *Front. Immunol.*, vol. 9, no. JAN, pp. 1–12, 2018.

[243] D. Kirmizis, A. Papagianni, G. Efstratiadis, and D. Memmos, “Impact of inflammation on anti-oxidative effects of vitamin E-coated membrane dialyzer in patients on chronic hemodialysis,” *Hemodial. Int.*, vol. 18, no. 4, pp. 751–757, 2014.

[244] X. Yu *et al.*, “High performance thin-film nanofibrous composite hemodialysis membranes with efficient middle-molecule uremic toxin removal,” *J. Memb. Sci.*, vol. 523, no. May 2016, pp. 173–184, 2017.

[245] K. Kokubo *et al.*, “Effects of increased surface coverage of polyvinylpyrrolidone

over a polysulfone hemofilter membrane on permeability and cell adhesion during continuous hemofiltration," *J. Artif. Organs*, vol. 18, no. 3, pp. 257–263, 2015.

[246] G. L. Morini, "Single-phase convective heat transfer in microchannels: A review of experimental results," *Int. J. Therm. Sci.*, vol. 43, no. 7, pp. 631–651, 2004.

[247] M. E. Steinke and S. G. Kandlikar, "Single-phase liquid friction factors in microchannels," *Int. J. Therm. Sci.*, vol. 45, no. 11, pp. 1073–1083, 2006.

[248] A. R. Da Costa, A. G. Fane, C. J. D. Fell, and A. C. M. Franken, "Optimal channel spacer design for ultrafiltration," *J. Memb. Sci.*, vol. 62, no. 3, pp. 275–291, 1991.

[249] A. G. Fane, R. Wang, and M. X. Hu, "Synthetic membranes for water purification: Status and future," *Angew. Chemie - Int. Ed.*, vol. 54, no. 11, pp. 3368–3386, 2015.

[250] Q. Yang, T. S. Chung, and Y. E. Santoso, "Tailoring pore size and pore size distribution of kidney dialysis hollow fiber membranes via dual-bath coagulation approach," *J. Memb. Sci.*, vol. 290, no. 1–2, pp. 153–163, 2007.

[251] J. Y. Lee *et al.*, "The potential to enhance membrane module design with 3D printing technology," *J. Memb. Sci.*, vol. 499, pp. 480–490, 2016.

[252] M. Goldstein, M. Carrillo, and S. Ghai, "Continuous ambulatory peritoneal dialysis-a guide to imaging appearances and complications," *Insights Imaging*, vol. 4, no. 1, pp. 85–92, 2013.

[253] M. Kersaudy-Kerhoas and E. Sollier, "Micro-scale blood plasma separation: From acoustophoresis to egg-beaters," *Lab Chip*, vol. 13, no. 17, pp. 3323–3346, 2013.

[254] S. Kerdi, A. Qamar, J. S. Vrouwenvelder, and N. Ghaffour, "Fouling resilient perforated feed spacers for membrane filtration," *Water Res.*, vol. 140, pp. 211–219, 2018.

[255] N. Sreedhar *et al.*, "Mass transfer analysis of ultrafiltration using spacers based on triply periodic minimal surfaces: Effects of spacer design, directionality and voidage," *J. Memb. Sci.*, vol. 561, no. March, pp. 89–98, 2018.

[256] C. A. Schneider, W. S. Rasband, and K. W. Eliceiri, “NIH Image to ImageJ: 25 years of image analysis,” *Nat. Methods*, vol. 9, no. 7, pp. 671–675, 2012.

[257] Y. SANO, “Operating Conditions for the Hemodialysis Treatment Based on the Volume Averaging Theory,” *Interdiscip. Inf. Sci.*, vol. 22, no. 2, pp. 215–227, 2016.

[258] J. Liu, A. Iranshahi, Y. Lou, and G. Lipscomb, “Static mixing spacers for spiral wound modules,” *J. Memb. Sci.*, vol. 442, pp. 140–148, 2013.

[259] L. F. Greenlee, D. F. Lawler, B. D. Freeman, B. Marrot, and P. Moulin, “Reverse osmosis desalination: Water sources, technology, and today’s challenges,” *Water Res.*, vol. 43, no. 9, pp. 2317–2348, 2009.

[260] A. Alkhudhiri, N. Darwish, and N. Hilal, “Membrane distillation: A comprehensive review,” *Desalination*, vol. 287, pp. 2–18, 2012.

[261] A. M. Walker, C. R. Johnston, and D. E. Rival, “On the characterization of a non-newtonian blood analog and its response to pulsatile flow downstream of a simplified stenosis,” *Ann. Biomed. Eng.*, vol. 42, no. 1, pp. 97–109, 2014.

[262] S. Gaudry *et al.*, “Initiation Strategies for Renal-Replacement Therapy in the Intensive Care Unit,” *N. Engl. J. Med.*, vol. 375, no. 2, pp. 122–133, 2016.

[263] C. C. Chen *et al.*, “Correlation between breath ammonia and blood urea nitrogen levels in chronic kidney disease and dialysis patients,” *J. Breath Res.*, vol. 14, no. 3, 2020.

[264] L. Eykens, K. De Sitter, C. Dotremont, L. Pinoy, and B. Van der Bruggen, “Membrane synthesis for membrane distillation: A review,” *Sep. Purif. Technol.*, vol. 182, pp. 36–51, 2017.

[265] R. Bian, K. Yamamoto, and Y. Watanabe, “The effect of shear rate on controlling the concentration polarization and membrane fouling,” *Desalination*, vol. 131, no. 1–3, pp. 225–236, 2000.

[266] I. Sutzkover, D. Hasson, and R. Semiat, “Simple technique for measuring the concentration polarization level in a reverse osmosis system,” *Desalination*, vol. 131, no. 1–3, pp. 117–127, 2000.

[267] X. Du, Z. Zhang, K. H. Carlson, J. Lee, and T. Tong, “Membrane fouling and reusability in membrane distillation of shale oil and gas produced water: Effects of membrane surface wettability,” *J. Memb. Sci.*, vol. 567, no. September, pp. 199–208, 2018.

[268] Z. X. Wang, C. H. Lau, N. Q. Zhang, Y. P. Bai, and L. Shao, “Mussel-inspired tailoring of membrane wettability for harsh water treatment,” *J. Mater. Chem. A*, vol. 3, no. 6, pp. 2650–2657, 2015.

[269] M. Rezaei, D. M. Warsinger, J. H. Lienhard V, M. C. Duke, T. Matsuura, and W. M. Samhaber, “Wetting phenomena in membrane distillation: Mechanisms, reversal, and prevention,” *Water Res.*, vol. 139, pp. 329–352, 2018.

[270] M. Rezaei, D. M. Warsinger, J. H. Lienhard V, and W. M. Samhaber, “Wetting prevention in membrane distillation through superhydrophobicity and recharging an air layer on the membrane surface,” *J. Memb. Sci.*, vol. 530, no. February, pp. 42–52, 2017.

[271] A. C. M. Franken, J. A. M. Nolten, M. H. V. Mulder, D. Bargeman, and C. A. Smolders, “Wetting criteria for the applicability of membrane distillation,” *J. Memb. Sci.*, vol. 33, no. 3, pp. 315–328, 1987.

[272] X. Chen and J. Shen, “Review of membranes in microfluidics,” *J. Chem. Technol. Biotechnol.*, vol. 92, no. 2, pp. 271–282, 2017.

[273] D. Huh, B. D. Matthews, A. Mammoto, H. Y. Hsin, and D. E. Ingber, “Reconstituting Organ-Level Lung Functions on a Chip,” *Science (80-. ).*, vol. 328, pp. 1662–1668, 2010.

[274] D. S. Y. Lin, F. Guo, and B. Zhang, “Modeling organ-specific vasculature with organ-on-a-chip devices,” *Nanotechnology*, 2018.

[275] M. Rhee and M. A. Burns, “Microfluidic pneumatic logic circuits and digital pneumatic microprocessors for integrated microfluidic systems,” *Lab Chip*, vol. 9, no. 21, pp. 3131–3143, 2009.

[276] V. B. Dang and S. J. Kim, “Water-head-driven microfluidic oscillators for autonomous control of periodic flows and generation of aqueous two-phase

system droplets," *Lab Chip*, vol. 17, no. 2, pp. 286–292, 2017.

[277] F. Allioux *et al.*, "Electro-capture of heavy metal ions with carbon cloth integrated micro fluidic devices," *Sep. Purif. Technol.*, vol. 194, pp. 26–32, 2018.

[278] U. Novak, A. Pohar, I. Plazl, and Z. Polona, "Ionic liquid-based aqueous two-phase extraction within a microchannel system," *Sep. Purif. Technol.*, vol. 97, pp. 172–178, 2012.

[279] J. P. Dijkshoorn, M. A. I. Schutyser, R. M. Wagterveld, C. G. P. H. Schroën, and R. M. Boom, "A comparison of microfiltration and inertia-based microfluidics for large scale suspension separation," *Sep. Purif. Technol.*, vol. 173, pp. 86–92, 2017.

[280] X. Su *et al.*, "A low cost, membranes based serum separator modular," *Biomicrofluidics*, vol. 12, no. 2, 2018.

[281] S. Sun, Y. Yue, X. Huang, and D. Meng, "Protein adsorption on blood-contact membranes," *J. Memb. Sci.*, vol. 222, no. 1–2, pp. 3–18, 2003.

[282] K. Hill *et al.*, "Second Generation Nanoporous Silicon Nitride Membranes for High Toxin Clearance and Small Format Hemodialysis," *Adv. Healthc. Mater.*, vol. 1900750, pp. 1–10, 2020.

[283] W. R. Clark, D. Gao, M. Neri, and C. Ronco, "Solute Transport in Hemodialysis: Advances and Limitations of Current Membrane Technology," *Contrib. Nephrol.*, vol. 191, pp. 84–99, 2017.

[284] M. H. V. Mulder, "Polarization phenomena and membrane fouling," in *Membrane Separations Technology*, 1st ed., vol. 2, no. C, R. . Stern and S. . Noble, Eds. Elsevier, 1995, pp. 45–84.

[285] A. H. Haidari, S. G. J. Heijman, and W. G. J. Van Der Meer, "Optimal design of spacers in reverse osmosis," *Sep. Purif. Technol.*, vol. 192, pp. 441–456, 2018.

[286] Y. Gao, S. Haavisto, C. Y. Tang, J. Salmela, and W. Li, "Characterization of fluid dynamics in spacer-filled channels for membrane filtration using Doppler optical coherence tomography," *J. Memb. Sci.*, vol. 448, pp. 198–208, 2013.

[287] J. Schwinge, P. R. Neal, D. E. Wiley, D. F. Fletcher, and A. G. Fane, "Spiral wound

modules and spacers: Review and analysis," *J. Memb. Sci.*, vol. 242, no. 1–2, pp. 129–153, 2004.

[288] S. Bucs, N. Farhat, J. C. Kruithof, C. Picioreanu, M. C. M. van Loosdrecht, and J. S. Vrouwenvelder, "Review on strategies for biofouling mitigation in spiral wound membrane systems," *Desalination*, vol. 434, no. February, pp. 189–197, 2018.

[289] H. S. Abid, D. J. Johnson, R. Hashaikeh, and N. Hilal, "A review of efforts to reduce membrane fouling by control of feed spacer characteristics," *Desalination*, vol. 420, no. July, pp. 384–402, 2017.

[290] S. Y. Lim, Y. Y. Liang, G. A. Fimbres Weihs, D. E. Wiley, and D. F. Fletcher, "A CFD study on the effect of membrane permeance on permeate flux enhancement generated by unsteady slip velocity," *J. Memb. Sci.*, no. 556, pp. 138–145, 2018.

[291] Z. X. Low, Y. T. Chua, B. M. Ray, D. Mattia, I. S. Metcalfe, and D. A. Patterson, "Perspective on 3D printing of separation membranes and comparison to related unconventional fabrication techniques," *J. Memb. Sci.*, vol. 523, no. October 2016, pp. 596–613, 2017.

[292] W. S. Tan, S. R. Suwarno, J. An, C. K. Chua, A. G. Fane, and T. H. Chong, "Comparison of solid, liquid and powder forms of 3D printing techniques in membrane spacer fabrication," *J. Memb. Sci.*, vol. 537, no. May, pp. 283–296, 2017.

[293] N. Yanar *et al.*, "Investigation of the performance behavior of a forward osmosis membrane system using various feed spacer materials fabricated by 3D printing technique," *Chemosphere*, vol. 202, pp. 708–715, 2018.

[294] A. Shrivastava, S. Kumar, and E. L. Cussler, "Predicting the effect of membrane spacers on mass transfer," *J. Memb. Sci.*, vol. 323, no. 2, pp. 247–256, 2008.

[295] C. Fritzmann, M. Wiese, T. Melin, and M. Wessling, "Helically microstructured spacers improve mass transfer and fractionation selectivity in ultrafiltration," *J. Memb. Sci.*, vol. 463, pp. 41–48, 2014.

[296] F. Li, W. Meindersma, A. B. De Haan, and T. Reith, "Novel spacers for mass transfer enhancement in membrane separations," *J. Memb. Sci.*, vol. 253, no. 1–

2, pp. 1–12, 2005.

[297] A. Siddiqui *et al.*, “Development and characterization of 3D-printed feed spacers for spiral wound membrane systems,” *Water Res.*, vol. 91, pp. 55–67, 2016.

[298] G. A. Fimbres-Weihs and D. E. Wiley, “Numerical study of mass transfer in three-dimensional spacer-filled narrow channels with steady flow,” *J. Memb. Sci.*, vol. 306, no. 1–2, pp. 228–243, 2007.

[299] G. A. Fimbres-Weihs and D. E. Wiley, “Review of 3D CFD modeling of flow and mass transfer in narrow spacer-filled channels in membrane modules,” *Chem. Eng. Process. Process Intensif.*, vol. 49, no. 7, pp. 759–781, 2010.

[300] J. Schwinge, D. E. Wiley, and D. F. Fletcherb, “A CFD study of unsteady flow in narrow spacer-filled channels for spiral-wound membrane modules,” *Desalination*, vol. 146, no. 2002, pp. 195–201, 2002.

[301] S. Mitrouli, A. J. Karabelas, A. Karanasiou, and M. Kostoglou, “Incipient calcium carbonate scaling of desalination membranes in narrow channels with spacers-experimental insights,” *J. Memb. Sci.*, vol. 425–426, pp. 48–57, 2013.

[302] C. P. Koutsou and A. J. Karabelas, “Shear stresses and mass transfer at the base of a stirred filtration cell and corresponding conditions in narrow channels with spacers,” *J. Memb. Sci.*, vol. 399–400, pp. 60–72, 2012.

[303] S. L. Stott *et al.*, “Isolation of circulating tumor cells using a microvortex-generating herringbone-chip.,” *Proc. Natl. Acad. Sci. U. S. A.*, vol. 107, no. 43, pp. 18392–7, 2010.

[304] N. T. Nguyen, M. Hejazian, C. H. Ooi, and N. Kashaninejad, “Recent advances and future perspectives on microfluidic liquid handling,” *Micromachines*, vol. 8, no. 6, 2017.

[305] N. Thomas, N. Sreedhar, O. Al-Ketan, R. Rowshan, R. K. Abu Al-Rub, and H. Arafat, “3D printed triply periodic minimal surfaces as spacers for enhanced heat and mass transfer in membrane distillation,” *Desalination*, vol. 443, no. March, pp. 256–271, 2018.

[306] O. Al-Ketan, M. Adel Assad, and R. K. Abu Al-Rub, “Mechanical properties of

periodic interpenetrating phase composites with novel architected microstructures," *Compos. Struct.*, vol. 176, pp. 9–19, 2017.

[307] N. Sreedhar *et al.*, "3D printed feed spacers based on triply periodic minimal surfaces for flux enhancement and biofouling mitigation in RO and UF," *Desalination*, vol. 425, no. July 2017, pp. 12–21, 2018.

[308] J. Calejo, D. Pinho, F. J. Galindo-Rosales, R. Lima, and L. Campo-Deaño, "Particulate blood analogues reproducing the erythrocytes cell-free layer in a microfluidic device containing a hyperbolic contraction," *Micromachines*, vol. 7, no. 1, pp. 1–12, 2016.

[309] S. H. Ye, J. Watanabe, Y. Iwasaki, and K. Ishihara, "Antifouling blood purification membrane composed of cellulose acetate and phospholipid polymer," *Biomaterials*, vol. 24, no. 23, pp. 4143–4152, 2003.

[310] J. Seo and J. H. Seo, "Fabrication of an Anti-Biofouling Plasma-Filtration Membrane by an Electrospinning Process Using Photo-Cross-linkable Zwitterionic Phospholipid Polymers," *ACS Appl. Mater. Interfaces*, vol. 9, no. 23, pp. 19591–19600, 2017.

[311] H. A. Balogun, R. Sulaiman, S. S. Marzouk, A. Giwa, and S. W. Hasan, "3D printing and surface imprinting technologies for water treatment: A review," *J. Water Process Eng.*, vol. 31, no. October 2018, p. 100786, 2019.

[312] J. Schwinge, D. E. Wiley, and A. G. Fane, "Novel spacer design improves observed flux," *J. Memb. Sci.*, vol. 229, no. 1–2, pp. 53–61, 2004.

[313] S. Armbruster, O. Cheong, J. Lölsberg, S. Popovic, S. Yüce, and M. Wessling, "Fouling mitigation in tubular membranes by 3D-printed turbulence promoters," *J. Memb. Sci.*, vol. 554, no. February, pp. 156–163, 2018.

[314] S. Kerdi, A. Qamar, A. Alpatova, J. S. Vrouwenvelder, and N. Ghaffour, "Membrane filtration performance enhancement and biofouling mitigation using symmetric spacers with helical filaments," *Desalination*, vol. 484, no. April, p. 114454, 2020.

[315] M. L. Christensen, T. V. Bugge, B. H. Hede, M. Nierychlo, P. Larsen, and M. K.

Jørgensen, “Effects of relaxation time on fouling propensity in membrane bioreactors,” *J. Memb. Sci.*, vol. 504, pp. 176–184, 2016.

[316] W. Beattie, X. Qin, L. Wang, and H. Ma, “Clog-free cell filtration using resettable cell traps,” *Lab Chip*, vol. 14, no. 15, pp. 2657–2665, 2014.

[317] E. A. Ottesen, J. W. Hong, S. R. Quake, and J. R. Leadbetter, “Microfluidic Digital PCR Enables Multigene Analysis of Individual Environmental Bacteria,” *Science (80-. ).*, vol. 314, pp. 1464–1467, 2006.

[318] Z. Xu *et al.*, “Design and Construction of a Multi-Organ Microfluidic Chip Mimicking the in vivo Microenvironment of Lung Cancer Metastasis,” *ACS Appl. Mater. Interfaces*, vol. 8, no. 39, pp. 25840–25847, 2016.

[319] A. Hassanzadeh-Barforoushi *et al.*, “A rapid co-culture stamping device for studying intercellular communication,” *Sci. Rep.*, vol. 6, pp. 1–11, 2016.

[320] K. E. Bates and H. Lu, “Optics-integrated microfluidic platforms for biomolecular analyses,” *Biophys. J.*, vol. 110, no. 8, pp. 1684–1697, 2016.

[321] M. H. Shamsi, K. Choi, A. H. C. Ng, M. D. Chamberlain, and A. R. Wheeler, “Electrochemiluminescence on digital microfluidics for microRNA analysis,” *Biosens. Bioelectron.*, vol. 77, pp. 845–852, 2015.

[322] M. H. Wu, S. Bin Huang, and G. Bin Lee, “Microfluidic cell culture systems for drug research,” *Lab Chip*, vol. 10, no. 8, pp. 939–956, 2010.

[323] J. Zhang, J. Wu, H. Li, Q. Chen, and J.-M. Lin, “An in vitro liver model on microfluidic device for analysis of capecitabine metabolite using mass spectrometer as detector,” *Biosens. Bioelectron.*, vol. 68, pp. 322–328, 2015.

[324] H. Stefen *et al.*, “A Novel Microfluidic Device-Based Neurite Outgrowth Inhibition Assay Reveals the Neurite Outgrowth-Promoting Activity of Tropomyosin Tpm3.1 in Hippocampal Neurons,” *Cell. Mol. Neurobiol.*, vol. 38, no. 8, pp. 1557–1563, 2018.

[325] A. Hassanzadeh-Barforoushi *et al.*, “Static droplet array for culturing single live adherent cells in an isolated chemical microenvironment,” *Lab Chip*, vol. 18, no. 15, pp. 2156–2166, 2018.

[326] A. Reece, B. Xia, Z. Jiang, B. Noren, R. McBride, and J. Oakey, “Microfluidic techniques for high throughput single cell analysis,” *Curr. Opin. Biotechnol.*, vol. 40, pp. 90–96, 2016.

[327] A. B. Wang *et al.*, “A novel lab-on-a-chip design by sequential capillary-gravitational valves for urinary creatinine detection,” *Sensors Actuators, B Chem.*, vol. 222, pp. 721–727, 2016.

[328] N. T. Nguyen and Z. Wu, “Micromixers - A review,” *J. Micromechanics Microengineering*, vol. 15, no. 2, 2005.

[329] Z. Tak For Yu *et al.*, “Rapid, automated, parallel quantitative immunoassays using highly integrated microfluidics and AlphaLISA,” *Sci. Rep.*, vol. 5, no. 1, pp. 1–12, 2015.

[330] R. Zhou, F. Bai, and C. Wang, “Magnetic separation of microparticles by shape,” *Lab Chip*, vol. 17, no. 3, pp. 401–406, 2017.

[331] X. Ding *et al.*, “Cell separation using tilted-angle standing surface acoustic waves,” *Proc. Natl. Acad. Sci.*, vol. 111, no. 36, pp. 12992–12997, 2014.

[332] B. Lee, S. H. Jin, Y. M. Noh, S. G. Jeong, H. H. Jeong, and C. S. Lee, “Scalable static droplet array for biochemical assays based on concentration gradients,” *Sensors Actuators, B Chem.*, vol. 273, no. July, pp. 1572–1578, 2018.

[333] R. Ortiz, J. L. Chen, D. C. Stuckey, and T. W. J. Steele, “Poly(methyl methacrylate) Surface Modification for Surfactant-Free Real-Time Toxicity Assay on Droplet Microfluidic Platform,” *ACS Appl. Mater. Interfaces*, vol. 9, no. 15, pp. 13801–13811, 2017.

[334] M. Rafeie, M. Welleweerd, A. Hassanzadeh-Barforoushi, M. Asadnia, W. Olthuis, and M. E. Warkiani, “An easily fabricated three-dimensional threaded lemniscate-shaped micromixer for a wide range of flow rates,” *Biomicrofluidics*, vol. 11, no. 1, 2017.

[335] A. K. Au, W. Huynh, L. F. Horowitz, and A. Folch, “3D-Printed Microfluidics,” *Angew. Chemie - Int. Ed.*, vol. 55, no. 12, pp. 3862–3881, 2016.

[336] A. K. Au, N. Bhattacharjee, L. F. Horowitz, T. C. Chang, and A. Folch, “3D-printed

microfluidic automation," *Lab Chip*, vol. 15, no. 8, pp. 1934–1941, 2015.

[337] H. Gong, A. T. Woolley, and G. P. Nordin, "High density 3D printed microfluidic valves, pumps, and multiplexers," *Lab Chip*, vol. 16, no. 13, pp. 2450–2458, 2016.

[338] Y. S. Lee, N. Bhattacharjee, and A. Folch, "3D-printed Quake-style microvalves and micropumps," *Lab Chip*, vol. 18, no. 8, pp. 1207–1214, 2018.

[339] Y. Hwang, O. H. Paydar, and R. N. Candler, "3D printed molds for non-planar PDMS microfluidic channels," *Sensors Actuators, A Phys.*, vol. 226, pp. 137–142, 2015.

[340] R. Amin *et al.*, "3D printed microfluidic devices," *Biofabrication*, vol. 8, no. 2, pp. 103–113, 2016.

[341] C. C. Glick *et al.*, "Rapid assembly of multilayer microfluidic structures via 3D-printed transfer molding and bonding," *Microsystems Nanoeng.*, vol. 2, no. April, p. 16063, 2016.

[342] L. Ren *et al.*, "An enzymatic immunoassay microfluidics integrated with membrane valves for microsphere retention and reagent mixing," *Biosens. Bioelectron.*, vol. 35, no. 1, pp. 147–154, 2012.

[343] S. Fornera, P. Kuhn, D. Lombardi, A. D. Schlüter, P. S. Dittrich, and P. Walde, "Sequential immobilization of enzymes in microfluidic channels for cascade reactions," *Chempluschem*, vol. 77, no. 2, pp. 98–101, 2012.

[344] R. J. Jimenez-Valdes, R. Rodriguez-Moncayo, D. F. Cedillo-Alcantar, and J. L. Garcia-Cordero, "Massive Parallel Analysis of Single Cells in an Integrated Microfluidic Platform," *Anal. Chem.*, vol. 89, no. 10, pp. 5210–5220, 2017.

[345] R. A. Kellogg, R. Gómez-Sjöberg, A. A. Leyrat, and S. Tay, "High-throughput microfluidic single-cell analysis pipeline for studies of signaling dynamics," *Nat. Protoc.*, vol. 9, no. 7, pp. 1713–1726, 2014.

[346] S. J. Maerkl and S. R. Quake, "A Systems Approach to Measuring the Binding Energy Landscapes of Transcription Factors," *Science (80-. ).*, vol. 315, no. January, pp. 233–237, 2007.

[347] H. Van Nguyen, V. D. Nguyen, E. Y. Lee, and T. S. Seo, “Point-of-care genetic analysis for multiplex pathogenic bacteria on a fully integrated centrifugal microdevice with a large-volume sample,” *Biosens. Bioelectron.*, vol. 136, no. January, pp. 132–139, 2019.

[348] M. Park and T. S. Seo, “An integrated microfluidic device with solid-phase extraction and graphene oxide quantum dot array for highly sensitive and multiplex detection of trace metal ions,” *Biosens. Bioelectron.*, vol. 126, no. November 2018, pp. 405–411, 2019.

[349] E. C. Jensen, W. H. Grover, and R. A. Mathies, “Micropneumatic digital logic structures for integrated microdevice computation and control,” *J. Microelectromechanical Syst.*, vol. 16, no. 6, pp. 1378–1385, 2007.

[350] I. D. Johnston, D. K. McCluskey, C. K. L. Tan, and M. C. Tracey, “Mechanical characterization of bulk Sylgard 184 for microfluidics and microengineering,” *J. Micromechanics Microengineering*, vol. 24, no. 3, 2014.

[351] Y. Yoon and R. M. Lueptow, “Reverse osmosis membrane rejection for ersatz space mission wastewaters,” *Water Res.*, vol. 39, no. 14, pp. 3298–3308, 2005.

[352] J. Xu, X. Feng, and C. Gao, “Surface modification of thin-film-composite polyamide membranes for improved reverse osmosis performance,” *J. Memb. Sci.*, vol. 370, no. 1–2, pp. 116–123, 2011.

[353] F. Mahmoudi, M. E. Pishbin, A. Date, and A. Akbarzadeh, “A unique permeate gap membrane distillation system for combined fresh water and power production,” *Energy Procedia*, vol. 160, no. 2018, pp. 170–177, 2019.

[354] T. Pan, S. J. McDonald, E. M. Kai, and B. Ziaie, “A magnetically driven PDMS micropump with ball check-valves,” *J. Micromechanics Microengineering*, vol. 15, no. 5, pp. 1021–1026, 2005.

[355] P. Nandy *et al.*, “Evaluation of one-way valves used in medical devices for prevention of cross-contamination,” *Am. J. Infect. Control*, vol. 45, no. 7, pp. 793–798, 2017.

[356] T. Mazzocchi, L. Ricotti, N. Pinzi, and A. Menciassi, “Parametric design,

fabrication and validation of one-way polymeric valves for artificial sphincters," *Sensors Actuators, A Phys.*, vol. 233, pp. 184–194, 2015.

[357] J. F. Kennedy, "0 Low -Dead -Volume Inlet for Vacuum Chamber Simple Check Valves for Microfluidic Devices A Capillary-Based Static Phase Separator for Highly Variable Wetting Conditions," no. May, pp. 24–25, 2010.

[358] F. A. Da Silva Rahal and C. K. Saul, "Symmetrical ball check-valve based rotation-sensitive pump," *J. Fluids Eng. Trans. ASME*, vol. 135, no. 11, pp. 1–9, 2013.

[359] T. D. Ngo, A. Kashani, G. Imbalzano, K. T. Q. Nguyen, and D. Hui, "Additive manufacturing (3D printing): A review of materials, methods, applications and challenges," *Compos. Part B Eng.*, vol. 143, no. February, pp. 172–196, 2018.

[360] F. Li, N. P. Macdonald, R. M. Guijt, and M. C. Breadmore, "Increasing the functionalities of 3D printed microchemical devices by single material, multimaterial, and print-pause-print 3D printing," *Lab Chip*, vol. 19, no. 1, pp. 35–49, 2019.

[361] H. D. Lehmann, R. Marten, and C. A. Gullberg, "How To Catch Urea? Considerations on Urea Removal from Hemofiltrate," *Artif. Organs*, vol. 5, no. 3, pp. 278–285, 1981.

[362] N. A. Mew, M. B. Pappa, and A. L. Gropman, *Urea Cycle Disorders*, Fifth Edit. Elsevier Inc., 2014.

[363] M. K. van Gelder *et al.*, "Urea removal strategies for dialysate regeneration in a wearable artificial kidney," *Biomaterials*, vol. 234, no. July 2019, p. 119735, 2020.

[364] H. Lehmann, R. Marten, I. Fahrner, and C. Gullberg, "Urea Elimination Using a Cold Activated-Carbon Artificial TUbulus for Hemofiltration," *Artif. Organs*, vol. 5, no. 4, pp. 351–356, 1981.

[365] M. A. Kraus, M. A. Frommer, M. Nemas, and R. Gutman, "Urea-rejecting membranes and their application in the development of a miniature artificial kidney," *J. Memb. Sci.*, vol. 1, no. C, pp. 115–127, 1976.

[366] C. Fritzmann, J. Löwenberg, T. Wintgens, and T. Melin, "State-of-the-art of reverse osmosis desalination," *Desalination*, vol. 216, no. 1–3, pp. 1–76, 2007.

[367] M. Qasim, M. Badrelzaman, N. N. Darwish, N. A. Darwish, and N. Hilal, “Reverse osmosis desalination: A state-of-the-art review,” *Desalination*, vol. 459, no. February, pp. 59–104, 2019.

[368] Perry, R.H. and D. W. Green, *Perry’s Chemical Engineers’ Handbook*. New York.: McGraw Hill, 1997.

[369] R. B. Bird, W. E. Stewart, and E. N. Lightfoot, *Transport Phenomena*. New York: John Wiley & Sons, Inc., 2002.

[370] W. R. Bowen and J. S. Welfoot, “Modelling the performance of membrane nanofiltration-critical assessment and model development,” *Chem. Eng. Sci.*, vol. 57, no. 7, pp. 1121–1137, 2002.

[371] J. A. Otero *et al.*, “Three independent ways to obtain information on pore size distributions of nanofiltration membranes,” *J. Memb. Sci.*, vol. 309, no. 1–2, pp. 17–27, 2008.

[372] O. Kedem and V. Freger, “Determination of concentration-dependent transport coefficients in nanofiltration: Defining an optimal set of coefficients,” *J. Memb. Sci.*, vol. 310, no. 1–2, pp. 586–593, 2008.

[373] H. K. Lonsdale, U. Merten, and R. L. Riley, “Transport properties of cellulose acetate osmotic membranes,” *J. Appl. Polym. Sci.*, vol. 9, no. 4, pp. 1341–1362, 1965.

[374] D. R. Paul, “Reformulation of the solution-diffusion theory of reverse osmosis,” *J. Memb. Sci.*, vol. 241, no. 2, pp. 371–386, 2004.

[375] J.G. Wijmans and R. W. Baker, “The solution-diffusion model: a review,” *J. Memb. Sci.*, vol. 107, pp. 1–21, 1995.

[376] S. Jiang, Y. Li, and B. P. Ladewig, “A review of reverse osmosis membrane fouling and control strategies,” *Sci. Total Environ.*, vol. 595, pp. 567–583, 2017.

[377] T. Wydeven and M. Leban, “Performance of cellulose acetate butyrate membranes in hyperfiltration of sodium chloride and urea feed solution,” *J. Appl. Polym. Sci.*, vol. 17, no. 7, pp. 2277–2287, 1973.

[378] R. McKinney, “Reverse Osmosis Separations With Aromatic Polyamide Films and Hollow Fibers,” *Sep. Purif. Rev.*, vol. 1, no. 1, pp. 31–115, 1972.

[379] M. A. Kraus, M. Nemas, and M. A. Frommer, “The effect of low molecular weight additives on the properties of aromatic polyamide membranes,” *J. Appl. Polym. Sci.*, vol. 23, no. 2, pp. 445–452, 1979.

[380] B. Van Dang *et al.*, “Can 3D-printed spacers improve filtration at the microscale?,” *Sep. Purif. Technol.*, vol. 256, no. July 2020, p. 117776, 2021.

[381] N. M. Krivitski, “Theory and validation of access flow measurement by dilution technique during hemodialysis,” *Kidney Int.*, vol. 48, no. 1, pp. 244–250, 1995.

[382] G. Amy *et al.*, “Membrane-based seawater desalination: Present and future prospects,” *Desalination*, vol. 401, pp. 16–21, 2017.

[383] L. M. Camacho *et al.*, “Advances in membrane distillation for water desalination and purification applications,” *Water*, vol. 5, no. 1, pp. 94–196, 2013.

[384] J. Kim, H. Kwon, S. Lee, S. Lee, and S. Hong, “Membrane distillation (MD) integrated with crystallization (MDC) for shale gas produced water (SGPW) treatment,” *Desalination*, vol. 403, pp. 172–178, 2017.

[385] G. Zakrzewska-Trznadel, M. Harasimowicz, and A. G. Chmielewski, “Concentration of radioactive components in liquid low-level radioactive waste by membrane distillation,” *J. Memb. Sci.*, vol. 163, no. 2, pp. 257–264, 1999.

[386] U. Kesieme, A. Chrysanthou, M. Catulli, and C. Y. Cheng, “A review of acid recovery from acidic mining waste solutions using solvent extraction,” *J. Chem. Technol. Biotechnol.*, vol. 93, no. 12, pp. 3374–3385, 2018.

[387] A. Criscuoli, J. Zhong, A. Figoli, M. C. Carnevale, R. Huang, and E. Drioli, “Treatment of dye solutions by vacuum membrane distillation,” *Water Res.*, vol. 42, no. 20, pp. 5031–5037, 2008.

[388] P. Loganathan, G. Naidu, and S. Vigneswaran, “Mining valuable minerals from seawater: A critical review,” *Environ. Sci. Water Res. Technol.*, vol. 3, no. 1, pp. 37–53, 2017.

[389] Q. Li *et al.*, “Improving the performance of vacuum membrane distillation using a 3D-printed helical baffle and a superhydrophobic nanocomposite membrane,” *Sep. Purif. Technol.*, vol. 248, no. May, p. 117072, 2020.

[390] J. A. Andrés-Mañas, A. Ruiz-Aguirre, F. G. Acién, and G. Zaragoza, “Assessment of a pilot system for seawater desalination based on vacuum multi-effect membrane distillation with enhanced heat recovery,” *Desalination*, vol. 443, no. May, pp. 110–121, 2018.

[391] Q. Li *et al.*, “The potential of hollow fiber vacuum multi-effect membrane distillation for brine treatment,” *Appl. Energy*, vol. 276, no. July, p. 115437, 2020.

[392] B. L. Pangarkar, M. G. Sane, and M. Guddad, “Reverse Osmosis and Membrane Distillation for Desalination of Groundwater: A Review,” *ISRN Mater. Sci.*, vol. 2011, pp. 1–9, 2011.

[393] F. Mahmoudi, A. Date, and A. Akbarzadeh, “Combined fresh water production and power generation using membrane distillation technology,” in *Chemeca Conference*, 2018, no. October, pp. 1–12.

[394] F. E. Ahmed, B. S. Lalia, R. Hashaikeh, and N. Hilal, “Alternative heating techniques in membrane distillation: A review,” *Desalination*, vol. 496, no. August, p. 114713, 2020.

[395] M. A. Isla, H. A. Irazoqui, and C. M. Genoud, “Simulation of a Urea Synthesis Reactor. 1. Thermodynamic Framework,” *Ind. Eng. Chem. Res.*, vol. 32, no. 11, pp. 2662–2670, 1993.

[396] B. Claudel, E. Brousse, and G. Shehadeh, “Novel thermodynamic and kinetic investigation of ammonium carbamate decomposition into urea and water,” *Thermochim. Acta*, vol. 102, no. C, pp. 357–371, 1986.

[397] Y. Shahebrahimi and A. Fazlali, “Vapor-Liquid Equilibrium of Aqueous Urea Solution from Dynamic Vapor Sorption Measurements at 283.15-343.15 K,” *J. Chem. Eng. Data*, vol. 65, no. 7, pp. 3528–3535, 2020.

[398] M. R. Rahimpour, “A non-ideal rate-based model for industrial urea thermal hydrolyser,” *Chem. Eng. Process. Process Intensif.*, vol. 43, no. 10, pp. 1299–1307,

2004.

[399] G. Folesani *et al.*, “Urea in exhaled breath condensate of uraemics and patients with chronic airway diseases,” *Acta Biomed. l’Ateneo Parm.*, vol. 79, no. SUPPL. 1, pp. 79–86, 2008.

[400] E. Urbanczyk, M. Sowa, and W. Simka, “Urea removal from aqueous solutions—a review,” *J Appl Electrochem*, vol. 46, pp. 1011–1029, 2016.

[401] A. Yokozeki, “Osmotic pressures studied using a simple equation-of-state and its applications,” *Appl. Energy*, vol. 83, no. 1, pp. 15–41, 2006.

[402] C. Bartels, R. Franks, S. Rybar, M. Schierach, and M. Wilf, “The effect of feed ionic strength on salt passage through reverse osmosis membranes,” *Desalination*, vol. 184, no. 1–3, pp. 185–195, 2005.

[403] S. Choi, Z. Yun, S. Hong, and K. Ahn, “The effect of co-existing ions and surface characteristics of nanomembranes of the removal of nitrate and fluoride,” *Desalination*, vol. 133, no. 1, pp. 53–64, 2001.

[404] N. Hilal, H. Al-Zoubi, N. A. Darwish, A. W. Mohammad, and M. Abu Arabi, “A comprehensive review of nanofiltration membranes: Treatment, pretreatment, modelling, and atomic force microscopy,” *Desalination*, vol. 170, no. 3, pp. 281–308, 2004.

[405] A. Hirano *et al.*, “Evaluation of Dialyzer Jacket Structure and Hollow-Fiber Dialysis Membranes to Achieve High Dialysis Performance,” *Ther. Apher. Dial.*, vol. 15, no. 1, pp. 66–74, 2011.

[406] B. Nicolaisen, “Developments in membrane technology for water treatment,” *Desalination*, vol. 153, no. 1–3, pp. 355–360, 2003.

[407] B. Lian, Y. Wang, P. Le-Clech, V. Chen, and G. Leslie, “A numerical approach to module design for crossflow vacuum membrane distillation systems,” *J. Memb. Sci.*, vol. 510, pp. 489–496, 2016.

[408] Q. Chen, M. Kum Ja, Y. Li, and K. J. Chua, “Thermodynamic optimization of a vacuum multi-effect membrane distillation system for liquid desiccant regeneration,” *Appl. Energy*, vol. 230, no. April, pp. 960–973, 2018.

[409] J. Swaminathan, H. W. Chung, D. M. Warsinger, and J. H. Lienhard V, “Energy efficiency of membrane distillation up to high salinity: Evaluating critical system size and optimal membrane thickness,” *Appl. Energy*, vol. 211, no. November 2017, pp. 715–734, 2018.

[410] J. I. Mengual, M. Khayet, and M. P. Godino, “Heat and mass transfer in vacuum membrane distillation,” *Int. J. Heat Mass Transf.*, vol. 47, no. 4, pp. 865–875, 2004.

[411] C. A. Yunus and J. G. Afshin, *Heat and Mass Transfer: Fundamentals and Applications*. New Delhi, India: McGraw-Hill Education, 2011.

[412] “Pump power calculation.” [Online]. Available: https://neutrium.net/equipment/pump-power-calculation/.

[413] A. Criscuoli, M. C. Carnevale, and E. Drioli, “Evaluation of energy requirements in membrane distillation,” *Chem. Eng. Process. Process Intensif.*, vol. 47, no. 7, pp. 1098–1105, 2008.

[414] P. Datt, “Latent Heat of Condensation,” in *Encyclopedia of Snow, Ice and Glaciers*, V. P. Singh, P. Singh, and U. K. Haritashya, Eds. Dordrecht: Springer Netherlands, 2011, pp. 702–703.

[415] “Water-vapor saturation pressure.” [Online]. Available: https://www.engineeringtoolbox.com/water-vapor-saturation-pressure-d_599.html.

[416] A. Omar, Q. Li, A. Nashed, J. Guan, P. Dai, and R. A. Taylor, “Experimental and numerical investigation of a new hollow fiber-based multi-effect vacuum membrane distillation design,” *Desalination*, vol. 501, no. December 2020, p. 114908, 2021.

[417] H. C. Duong, P. Cooper, B. Nelemans, T. Y. Cath, and L. D. Nghiem, “Evaluating energy consumption of air gap membrane distillation for seawater desalination at pilot scale level,” *Sep. Purif. Technol.*, vol. 166, pp. 55–62, 2016.

[418] “RO Flat-Sheet Performance Comparison by Manufacture,” *SterliTech*. [Online]. Available: https://www.sterlitech.com/tm-73ha-reverse-osmosis-ro-membrane-

457-x-457-mm-size.html.

[419] P. Dou, S. Zhao, S. Xu, X. M. Li, and T. He, “Feasibility of osmotic dilution for recycling spent dialysate: Process performance, scaling, and economic evaluation,” *Water Res.*, vol. 168, p. 115157, 2020.

[420] J. Kim, K. Park, D. R. Yang, and S. Hong, “A comprehensive review of energy consumption of seawater reverse osmosis desalination plants,” *Appl. Energy*, vol. 254, no. April, p. 113652, 2019.

[421] G. Zuo, R. Wang, R. Field, and A. G. Fane, “Energy efficiency evaluation and economic analyses of direct contact membrane distillation system using Aspen Plus,” *Desalination*, vol. 283, pp. 237–244, 2011.

[422] N. Ghaffour, S. Soukane, J. G. Lee, Y. Kim, and A. Alpatova, “Membrane distillation hybrids for water production and energy efficiency enhancement: A critical review,” *Appl. Energy*, vol. 254, no. February, p. 113698, 2019.

[423] K. Bridger *et al.*, “High-pressure magnetostrictive pump development: a comparison of prototype and modeled performance,” *Smart Struct. Mater. 2004 Ind. Commer. Appl. Smart Struct. Technol.*, vol. 5388, no. July 2004, p. 246, 2004.

[424] Y. Y. Lu, Y. D. Hu, X. L. Zhang, L. Y. Wu, and Q. Z. Liu, “Optimum design of reverse osmosis system under different feed concentration and product specification,” *J. Memb. Sci.*, vol. 287, no. 2, pp. 219–229, 2007.

[425] P. Dou, D. Donato, H. Guo, S. Zhao, and T. He, “Recycling water from spent dialysate by osmotic dilution: Impact of urea rejection of forward osmosis membrane on hemodialysis duration,” *Desalination*, vol. 496, no. September, p. 114605, 2020.

[426] A. Credi, “A Molecular Cable Car for Transmembrane Ion Transport,” *Angew. Chemie - Int. Ed.*, vol. 58, no. 13, pp. 4108–4110, 2019.

[427] L. A. Baker and S. P. Bird, “Nanopores: A makeover for membranes,” *Nat. Nanotechnol.*, vol. 3, no. 2, pp. 73–74, 2008.

[428] J. De Vos, K. Broeckhoven, and S. Eeltink, “Advances in Ultrahigh-Pressure Liquid Chromatography Technology and System Design,” *Anal. Chem.*, vol. 88, no. 1, pp.

262–278, 2016.

[429] S. Sharma *et al.*, “Hand-Portable Gradient Capillary Liquid Chromatography Pumping System,” *Anal. Chem.*, vol. 87, no. 20, pp. 10457–10461, 2015.

[430] A. Ishida *et al.*, “A portable liquid chromatograph with a battery-operated compact electroosmotic pump and a microfluidic chip device with a reversed phase packed column,” *Anal. Sci.*, vol. 31, no. 11, pp. 1163–1169, 2015.

[431] A. Górecka-Drzazga, “Miniature and MEMS-type vacuum sensors and pumps,” *Vacuum*, vol. 83, no. 12, pp. 1419–1426, 2009.

[432] M. Doms and J. Müller, “Design, fabrication, and characterization of a micro vapor-jet vacuum pump,” *J. Fluids Eng. Trans. ASME*, vol. 129, no. 10, pp. 1339–1345, 2007.

[433] A. P. Taylor and L. F. Velásquez-García, “Miniaturized diaphragm vacuum pump by multi-material additive manufacturing,” *J. Microelectromechanical Syst.*, vol. 26, no. 6, pp. 1316–1326, 2017.

[434] Q. Li *et al.*, “Improving the performance of vacuum membrane distillation using a 3D-printed helical baffle and a superhydrophobic nanocomposite membrane,” *Sep. Purif. Technol.*, vol. 248, no. November 2019, p. 117072, 2020.

[435] L. Li and K. K. Sirkar, “Studies in vacuum membrane distillation with flat membranes,” *J. Memb. Sci.*, vol. 523, no. August 2016, pp. 225–234, 2017.

[436] H. S. Abid, D. J. Johnson, R. Hashaikeh, and N. Hilal, “A review of efforts to reduce membrane fouling by control of feed spacer characteristics,” *Desalination*, vol. 420, no. June, pp. 384–402, 2017.

[437] “Thermoelectric Device.” [Online]. Available: https://www.digikey.com.au/product-detail/en/marlow-industries,-inc/LCC12-8-16LS/1681-1022-ND/6159070?utm_adgroup=General&utm_source=google&utm_medium=cpc&utm_campaign=Smart Shopping_Product_Zombie SKUS&utm_term=&productid=6159070&gclid=Cj0KCQiApY6BBhCsAR.

[438] R. A. Taylor and G. L. Solbrekken, “Comprehensive system-level optimization of

thermoelectric devices for electronic cooling applications," *IEEE Trans. Components Packag. Technol.*, vol. 31, no. 1, pp. 23–31, 2008.

[439] S. Patra and V. Young, "A Review of 3D Printing Techniques and the Future in Biofabrication of Bioprinted Tissue," *Cell Biochem. Biophys.*, vol. 74, no. 2, pp. 93–98, 2016.